Observation of Single-Molecule Rotational Diffusion at Microsecond Timescales by Polarized Fluorescence Correlation Spectroscopy

Thesis by

Ian R. Shapiro

In Partial Fulfillment of the Requirements

for the Degree of

Doctor of Philosophy

California Institute of Technology

Pasadena, California

2009

(Defended June 2, 2009)

To all my friends and family; past, present and future.

Acknowledgements

Abstract

This work presents a series of experimental and numerical studies of macromolecular organic, inorganic and biological structures, in all instances focusing on the behavior characteristic of individual discrete molecular elements. Chapters 1 and 2, beginning on pages 1 and 31, respectively, describe fabrication, use and numerical analysis of of single-walled carbon nanotube probes for amplitude-modulation atomic force microscopy. These studies reach the conclusion that the molecular structure and nanoscale surface interaction potential unique to carbon nanotubes collectively give rise to atomic force microscopy imaging artifacts manifesting as apparent lateral topographic resolution significantly better than that predicted by the probe and sample structures.

Chapter 3 (p. 61) presents a brief review of single-molecule microscopy, describes a generalized mathematical formalism for focusing polarized visible-spectrum electromagnetic radiation, and delineates the construction of a custom two-channel scanning confocal fluorescence microscope system with single-photon detection capability for spectral- and polarization-resolved studies of individual mobile fluorophores. This Chapter includes a theory-based optical analysis of the confocal probe volume structure and photoluminescence collection efficiency from 3D-polarized single-dipole emitters. The latter analysis was aided by introducing a modified Jones formalism using non-square matrix representation for polarization state changes in the specific context of confocal optics. Proper calculation of the expected confocal probe vol-

ume dimensions was essential for accurately interpreting experimental data in the following chapter. Additionally, the quantitative understanding that followed from analysis of 3D polarization state measurement by orthogonally polarized detection channels was critical to both the interpretation of experimental data and the numerical generation of simulated data in Chapter 5.

Chapter 4 (p. 125) presents a generalized formalism for correlation analysis of the fluorescence signal collected using the two-channel microscopy system described in Chapter 3. Particular focus was directed toward the theoretical auto- and cross-correlation traces anticipated from polarization-sensitive bivariate time series of photoluminescence emission from freely-rotating transition dipoles. Chapter 4 also presents population-resolved data collected from single Förster resonance energy transfer fluorphore pairs conjugated to DNA oligomers as they undergo cleavage by restriction endonucleases. The endonuclease enzyme Michaelis constants K_M measured for EcoRI and BglI via fluorescence burst analysis were in agreement with prior literature. The success of these experiments provide concrete confirmation of the microscope's fluorescence emission sensitivity and detection channel selectivity in the context of single-molecule experiments.

Chapter 5 describes a polarized fluorescence correlation spectroscopy (PFCS) investigation of liquid phase rotational diffusion by colloidal CdSe semiconductor nanocrystals possessing two-dimensional nondegenerate photoluminescence transition dipoles, as well as red fluorescent protein (monomeric DsRed) and rhodamine-labeled phospholipids that possess more conventional one-dimensional fluorescence transition dipoles. The experimental PFCS data collected from these samples is in close agreement with simulated PFCS data produced by a Monte Carlo rotational diffusion numerical routine that incorporates the microscope 3D polarization state sensitivity

calculated in Chapter 3.

Appendices beginning on page 221 include a matrix-based description of arbitrary 3D rotation that was used in the rotational diffusion simulations, Matlab code transcripts (p. 227), and an additional mathematical formalism based on information theoretic precepts (p. 242) for assessing directed causal relationships in bivariate time series data.

Contents

Chapter 1

Development of a Method for Rapid Fabrication of Single-Wall Carbon Nanotube AFM Probes, and Correlation of Probe Morphology with Subsequent Amplitude-Feedback Topographic Image Resolution

Abstract

This Chapter presents a methodology for facile, high-throughput fabrication of single-walled carbon nanotube (SWNT) probes for use in topographic atomic force microscopy (AFM) image acquisition using oscillation amplitude feedback. Various methods for SWNT growth, probe mounting and shortening were compared and refined into a single optimal process. This process utilized the following steps: 1.) Thermal chemical vapor deposition (CVD) growth of carbon nanotubes on Si/SiO_2

substrates using ferritin-derived catalytic iron nanoparticles and CH_4/H_2 gas feedstock at 950°C. 2.) SWNTs were 'picked-up' directly from the CVD substrate onto conventional silicon AFM cantilevers, and the same substrate was also used for the following three steps to minimize fabrication time. 3.) Nanotube lengths protruding past the end of the silicon probe pyramid were measured from force/amplitude approach curves. 4.) Shortening of the protruding carbon nanotubes to a length appropriate for topographic imaging was performed by a combination of push-shortening for small length changes and electrical pulse-shortening for large length changes. 5.) SWNT probes were characterized for topographic resolution by collecting images of prone nanotubes by amplitude-feedback AFM imaging. 6.) The fabricated probes were imaged by transmission electron microscopy (TEM), and using these images the carbon nanotube size and orientation were correlated with the measured AFM resolution. We found that in many cases the observed topographic imaging resolution was significantly better than the value expected from the probe nanotube diameter, in one case being just 5Å, the highest reported resolution for a carbon nanotube AFM probe.

Associated Publication

Correlating AFM Probe Morphology to Image Resolution for Single-Wall Carbon Nanotube Tips.[1]

Associated Patent

Selective functionalization of carbon nanotube tips allowing fabrication of new classes of nanoscale sensing and manipulation tools.[2]

1.1 Introduction

1.1.1 Scanning Probe Microscopy

All forms of scanning probe microscopy (SPM), of which there are scores of specific varieties, rely upon parametric scanning of a sample in two spatial dimensions $\{x = X(t), y = Y(t)\}$ using piezoelectric actuators of sub-Å precision while iterating a variable feedback loop encompassing both the third spatial dimension Z and an additional state value Q. Within this feedback loop one of $\{Z, Q\}$ is actively adjusted as an independent variable, while the other is continuously measured as the dependent variable. The contrast source is the set of independent variable values to which the feedback loop converges at each scan point $\{x, y\}$.

All specific SPM varieties simply correspond to different state value measurement types $\{Q\}$ and which variable of $\{Z, Q\}$ is selected for measurement while the other is actively adjusted in the feedback loop. For example in scanning tunneling microscopy (STM), the earliest type of scanning probe microscope, I_t is the electron tunneling current I_t (at a given voltage).[3,4] In constant-current STM the tunneling current I_t is measured at each scan point $\{x, y\}$ and the height Z adjusted by piezoelectric extension to maintain I_t at a user-specified set-point value:$I_t = I_{sp}$. The resulting image is topography $Z\big(x, y, I_{sp}\big)$ that depends on the chosen current set-point. In constant-height STM the height Z is measured at each scan point, the current $I_t$adjusted to maintain Z at its set-point value $Z = Z_{sp}$ and the resulting image $I_t\big(x, y, Z_{sp}\big)$. Scanning tunneling microscopy has long yielded electronic structure information at atomic scale due to the extremely steep nonlinear response of the electron tunneling current to the probe-sample separation.

In contact atomic force microscopy (AFM), first reported over 20 years ago,[5] the measured value Q is the perpendicular component of the repulsive force F_{ts} between the sample and a microfabricated cantilever having a sharpened point, determined from the cantilever deflection. At each scan point the height Z is adjusted to maintain constant cantilever deflection $F_{ts} = F_{sp}$ and the resulting image corresponds closely to three-dimensional topography $Z\big(x, y, F_{sp}\big)$.

AFM can also be performed in a variety of other modes, the most common of which is amplitude-modulation topographic imaging (AM-AFM). This measurement mode involves mechanically exciting the probe cantilever with constant power at a frequency ω close to its resonant frequency ω_0, and the time-dependent probe position $z(t)$ approximated by that of a simple damped-driven harmonic oscillator. At each scan point $\{x, y\}$ the feedback loop measures the oscillation amplitude A to which the cantilever converges and actively adjusts the cantilever's equilibrium resting height Z_r until $A = A_{sp}$ with all other parameters remaining constant. The resulting image $Z_r\big(x, y, A_{sp}\big)$ roughly represents the sample topography, although as will be discussed extensively in Chapter 2 (p. 31) the exact interpretation of $Z_r\big(x, y, A_{sp}\big)$ requires intimate understanding of the force field between the probe tip and the sample.

Contact AFM and AM-AFM acquire image contrast primarily from van der Waals force fields between the probe and sample, which exhibit a much more gradual change with separation than electron tunneling current in STM. As a result, although the vertical (z) topographic resolution is sub-Å, limited by the thermal fluctuations and actuator precision of the piezoelectric scanning elements, the lateral ($x-y$) resolution is governed by the radius of curvature of the probe tip (Figure 1.4c, p. 18). This

curvature varies widely between probes based upon their manufacturing methods, but in most cases is limited to at least a few nanometers in dimension, an order of magnitude larger than the vertical resolution. In special circumstances, however, sub-nanometer lateral resolution been observed even for relatively soft samples such as biological macromolecules under physiological conditions.[6–13]

Alternately, in frequency-modulation AFM (FM-AFM) the cantilever's fundamental oscillation frequency ω_f is measured at each scan point $\{x, y\}$ and the height Z_r adjusted so that $\omega_f = \omega_{sp}$. The image topography $Z_r\big(x, y, \omega_{sp}\big)$ obtained by FM-AFM is significantly better than that obtained by AM-AFM, achieving true atomic resolution of crystalline samples in ultra-high vacuum conditions.[14–18] When higher-harmonic frequencies of the oscillating cantilever are included in the FM-AFM feedback measurement, atomic resolution is possible at room temperature,[19] and subatomic resolution can be achieved under cryogenic conditions.[20–22]

Several additional SPM varieties, too numerous to describe in detail, and their corresponding feedback-modulated measurement (in parentheses) are: electrostatic force microscopy, EFM[23] (oscillation phase shift ϕ); lateral force microscopy, LFM[24] (lateral cantilever deflection); magnetic force microscopy, MFM[25] (oscillation phase shift ϕ); scanning electrochemical microscopy, SECM[26–32] (electrochemical current). Single-molecule vibrational spectroscopy using STM-based inelastic tunneling current has been reported fo a variety of substrates, although these experiments are uniformly performed at cryogenic temperatures ($\leq$13K) under ultra-high vacuum.[33–36]

1.1.2 Carbon Nanotubes

Carbon nanotubes, being essentially one-dimensional conductive materials with molecular dimensions, have elicited a flurry of proposed uses since their initial discovery by Iijima and coworkers in 1991.[37,38] Carbon nanotubes can be either single-walled, having a structure consisting of a graphite sheet seamlessly rolled into a single tube 0.5–10 nm in diameter, or multi-walled, consisting of concentrically nested single-walled tubes with an outer diameter of up to 100 nm.[39] The structural and mechanical properties of carbon nanotubes can be accurately estimated by *ab inito* numerical methods based on graphene bonding.[40,41]

Each single wall carbon nanotube can be classified structurally by a pair of integers (n, m) that describe both the diameter of the tube and the orientation of its network of hexagonal graphene rings with respect to the tubes long axis. The relative values of n and m determine the carbon nanotubes electronic properties.[42] If $n = m$ the tube is metallic, with a conductivity of up to 10^9 A/cm^2, four orders of magnitude higher than ordinary metals.[43] If $n - m = 3k, k \in \mathbb{N}^+$, the tube is semiconducting with a small band gap. For all other values of n and m the nanotubetube is semiconducting, but the band gap is inversely proportional to the diameter.[44–46] The electronic properties of individual isolated SWNTs of varying structure have been measured by scanning tunneling microscopy and are in agreement with those predicted by *ab initio* quantum mechanical simulations.[47–49] The diameter and helicity of isolated SWNTs can also be determined by resonant Raman scattering measurement of the radial breathing mode frequency.[50] The electric density of states measured by STM reflects peaks arising from van Hove singularities caused by the quasi-one-dimensional nature of the tubes, as well as anomalous low-energy peaks attributed to the effects of the

changing structural curvature at the ends of closed tubes.[51]

This characteristic of electronic property dependence upon structure in carbon nanotubes represents a double-edged sword for researchers: despite a variety of accessible electronic properties, it is as yet impossible to rationally manufacture tubes with specific predetermined characteristics. The problem is further compounded for multi-wall nanotubes because each layer has its own geometry and corresponding properties. Despite this drawback, however, both SWNTs and MWNTs have been utilized in nanoscale electronic and sensing devices. Nanotubes can be employed as single-electron transistors,[52] and have been integrated into rewritable bistable memory bits[53] and simple logic elements.[54]

1.1.3 Synthesis of Carbon Nanotubes

Carbon nanotubes and other fullerenes can be grown from flame sources, high-voltage arc discharge between carbon electrodes, laser ablation of carbon samples, or chemical vapor deposition (both thermal and plasma-enhanced) using carbon-bearing gas sources and catalytic metal nanoparticles.[55–60] The latter methods permit the use of patterned and size-controlled catalyst to affect more specific CNT end products. Patterned CNT growth can also be achieved by uniform catalyst deposition followed by template-mediated transfer prior to CVD growth.[61] Thermal CVD nanotube growth is most commonly reported in the temperature range of 850–1000°C, while plasma-enhanced CVD permits permits slightly lower temperatures ($\approx$ 600°C and yields preferential growth of semiconducting SWNTs.[62,63] The catalytic metal nanoparticles used in CVD synthesis are most commonly iron-bearing but may also be composed of nickel, cobalt, molybdenum, platinum or alloys of in-

termediate compsition.[64,65] Metal source material can be introduced homogeneously in gas phase along with the carbon-bearing gas,[66] but are more commonly deposited from soluble inorganic precursors such as iron III nitrate,[67] electron beam-deposited metal,[68] evaporated metal or protein-derived metal clusters such as ferritin.[69]

Ab initio molecular dynamics and continuum numerical simulations of carbon nanotubes grown by CVD in the presence of mental nanoparticles have recently begun to elucidate the mechanism of catalytic growth.[70–73] At high temperatures, thermal dissociation of the carrier gas yields carbon atoms that associate via transient carbide bonding on the surface of the metal nanoparticles, although carbon dissolution into the metal does not occur. The carbon atoms on the metal surface form small covalently linked clusters, and eventually form a small sp^2-bonded graphitic network capping the nanoparticle. The sp^2-bonded atoms at the center of the cell shell interact weakly but non-negligibly with the metallic iron surface, although the carbon atoms at the shell edges form covalent Fe-C bonds. Further carbon atoms associating with the metal nanoparticle form C-C bonds with the edges of the graphitic shell, eventually extruding as a long capped tube with a diameter roughly determined by that of the original catalytic nanoparticle, corroborating experimental observations.[1,69] With nanoparticles composed predominantly of a different metal such as gold, the sp^2-bonded atoms have negligible attraction to the metal surface and the atoms at the edge of the newly-formed graphitic cap do not establish stable metal-carbon bonds. The small carbon cluster quickly detaches from the particle and no closed fullerene structures form.

1.1.4 Carbon Nanotube Functionalization

Both single- and multi-wall carbon nanotubes can be end- or sidewall-functionalized with varying specificity using a variety of chemical and biochemical species. Sidewall functionalization of carbon nanotubes generally displays less specificity but alters their material properties including solubility, conductivity and compatibility biological environments.[74–76] Additionally the very ends of MWNT probes can be modified to present simple chemical functional groups such as amines and carboxylic acids by application of brief electrical pulses in the presence of varying gas atmospheres.[77,78] Under well controlled reaction conditions it is possible to covalently attach a single biotin moiety to the end of a single-wall carbon nanotube presented at the apex of an AFM cantilever. This permits further attachment of individual streptavidin-conjugated macromolecules and subsequent spatial positioning using an AFM piezoelectric scanning element.[79]

Plasma deposition techniques can also coat carbon nanotubes with nanoscale polymer films[80] or silicon oxide.[81] Sputter-coating SWNT AFM probes with gold has been reported to produce 30nm thick nanowires,[82] and SWNTs can also be filled with conductive liquid-phase mercury by electrowetting.[83] Lastly, bulk carbon nanotube electrodes have been used for biologically-relevant electrochemistry.[74,84–89] SWNT-based electrochemical probes can make direct redox contact with glucose oxidase flavin cofactors, with retention of enzymatic activity, and in some cases a significant *increase* in redox turnover rate.[90–94] Taken collectively these developments in manipulation, functionalization and use of single-wall carbon nanotubes suggest a future wealth of experimental possibilities.[2]

1.1.5 Carbon Nanotube Probes for Amplitude-Modulation Atomic Force Microscopy and Other Scanning Probe Techniques

Single-wall carbon nanotubes have shown great potential as high-resolution AFM imaging probes.[95–97] Commercially available silicon probes have tip radii of 5–15nm, effectively limiting the degree of lateral resolution possible for both single molecule imaging and force transduction. The finest commercially available silicon tips are very delicate, leading to substantial variation in tip shape and size even between successive images. In contrast single-wall carbon nanotubes have diameters between 1.5 and 5 nm, providing the potential for topographic image resolution comparable to molecular scale dimensions. Additionally they are chemically and mechanically robust, having axial Youngs moduli in excess of 10^{12} Pa,[98] resulting in a probe structure that is geometrically stable for prolonged imaging periods. Lastly, SWNT AFM probes can be functionalized uniquely at their very ends, permitting a broad array of applications in nanotechnology and biotechnology.[77–79]

Nevertheless, it has proven difficult to assemble large quantities of high-quality single-wall nanotube AFM probes reproducibly. Realizing the full promise of these probes for high-resolution AFM necessitates better physical understanding of how the geometry of the mounted SWNT on its AFM tip support affects image quality. Successfully fabricating a probe suitable for AFM imaging in air involves several steps: attaching the nanotube to a conventional silicon AFM tip, shortening it sufficiently to enable high resolution imaging, characterizing its quality, and storing it for later use. Building upon previously reported techniques, we have conducted a comparative survey of fabrication methods to produce a protocol that routinely re-

sults in high quality probes. The quality of the AFM images taken with the resultant probes was used to distinguish between the several approaches studied. In addition, SEM and TEM images of hundreds of nanotube AFM probes were used to evaluate the efficacy of different probe attachment and shortening techniques, and to improve the accuracy of our interpretation of AFM imaging and force calibration results. For the first time, the AFM resolution achieved when imaging with nanotube probes was directly correlated to TEM images taken of these same probes. This allowed us to carry out a rigorous examination of nanotube morphology and its influence on image resolution and quality, by directly correlating nanotube geometry, as determined with TEM imaging, with their performance as AFM probes. As a result, we gained significant new insights that are important for research groups performing AFM imaging with SWNT probes.

1.2 Experimental Methods

1.2.1 Equipment and Hardware

Digital Instruments BioScope and Multimode atomic force microscopes were used with Nanoscope IV controllers for this work. Transmission electron microscopy was performed with a Phillips EM430, and scanning electron microscopy was performed with a Hitachi 4100. Chemical vapor deposition was performed using a 22 mm inner diameter Lindberg/Blue M quartz tube furnace with a single heating zone 312 mm long. CVD gases were comprised of Argon (Matheson, 99.9995% purity), H_2 (Matheson, research grade) and CH_4 (Air Liquide, Ultra High Purity). Unless otherwise noted, all AFM probes were NanoDevices TESP silicon probes with a resonant frequency of $\approx 50kHz$ and a spring constant of $4.8Nm^{-1}$.

1.2.2 Chemical Vapor Deposition

All chemical vapor deposition was carried out in a quartz tube furnace using mixtures of Argon, hydrogen and methane gas as illustrated in figure 1.1. CVD substrates were square, 500 μm thick Si/SiO_2 wafers with lateral dimensions between 4 mm and 8 mm, and either native oxide coating or 300nm thick oxide. In the CVD furnace five wafers were positioned 12.5 mm apart in a specially designed quartz holder, oriented vertically and with the catalyst-coated side facing away from the direction of the incoming gas. A significant advantage of this holder is that it enables up to three small substrates to be mounted side-by-side in each slot for parallel comparison of growth results under nearly identical temperature and gas flow conditions. The location of the quartz holder relative to the end of the furnace tube is critical for optimal growth.

CVD substrates were prepared for carbon nanotube growth by first depositing catalytic iron nanoparticles by one of four methods: spin coating with solution of $Fe(NO_3)_3{\cdot}9H_2O$ in isopropyl alcohol, thermal evaporation of iron, electron beam deposition of iron, or incubation with ferritin. Silicon substrates were cleaved from full 3-inch wafers under cleanroom conditions, and cleaned by sonicating for 15 minutes at 25 °C in each of toluene, acetone, and electronics-grade isopropyl alcohol. To coat the substrates with catalytic iron nanoparticles, 6–12 drops of 100–600μg/mL $Fe(NO_3)_3{\cdot}9H_2O$ solution in electronics-grade isopropyl alcohol were applied while spinning substrates at 3000 r.p.m., waiting approximately 10 seconds between drops to permit the solvent to evaporate. Alternately, some silicon substrates were coated under high vacuum with 1/40 monolayer iron applied by thermal or e-beam evaporation. Other substrates were incubated overnight at 4 °C in a 44μM solution of

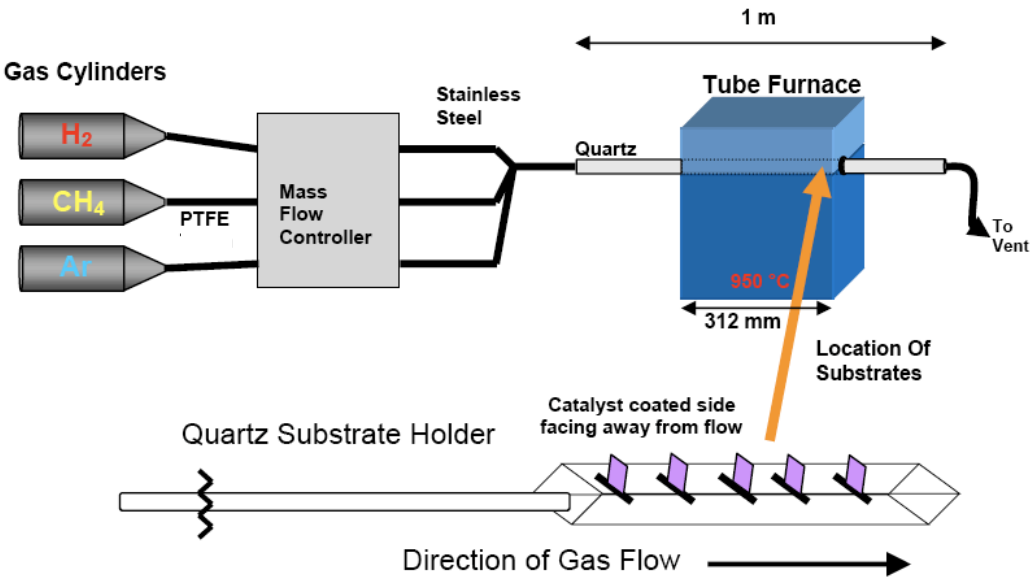

Figure 1.1: Diagram of CVD apparatus for production of nanotube substrates. Five wafers are positioned 12.5 mm apart in a specially designed quartz holder, oriented vertically and with the catalyst-coated side facing away from the direction of the incoming gas.

ferritin containing 200 Fe atoms/protein. For CVD growths in which the catalytic iron nanoparticles were prepared from ferritin deposition, the furnace was first heated to 800 °C in air and held at that temperature for 10 minutes. The purpose of this calcination step is to remove all organic material originating from the ferritin protein, leaving behind only nanoparticles of iron oxide. This step was not carried out for substrates bearing the other iron catalysts.

The following CVD procedure was found to produce quality carbon nanotubes with a high proportion of single-walled tubes less than 4nm in diameter: The quartz holder is positioned at the leeward end of the tube, with the last wafer approximately 2 cm from the end of the heating chamber. The quartz tube is then flushed for 15 minutes with 400 sccm Ar gas. The furnace is heated to 950°C over a period of 20 minutes, and then held at 950°C for 15 minutes under a flowing atmosphere of Ar (400 sccm) and 125 sccm H_2. The furnace is held at this temperature for 5 additional minutes while flushing with only Ar (400 sccm). Growth of nanotubes is then carried out for between one and two minutes at 950°C using 1080 sccm CH_4 and 125 sccm H_2. Following this growth step, the furnace is again flushed with Ar (400 sccm) and held at 950°C for 5 minutes before rapidly cooling to less than 250°C, after which the substrates are exposed to air and removed from the furnace. This growth procedure generates primarily SWNTs with diameters ranging from 1.6 to 4.0 nm and lengths between 100 nm and $5\mu m$, as imaged by SEM, TEM and atomic force microscopy. Some nanotube ropes were also observed. Most of the tubes were oriented horizontally with respect to the substrate surface, and could be imaged with standard AFM. The results from a typical growth are depicted in figure 1.2. Variations in growth density appear to be due primarily to variations in temperature. Note that the ≈900°C rise in gas temperature occurs in only 25 cm. Small changes

in position can make a significant change in the final gas and substrate temperature. Figure 1.2 shows an AFM topographic image of carbon nanotubes grown by CVD from a ferritin coated oxidized silicon substrate. This substrate was suitable for use in the 'pick-up' SWNT AFM probe fabrication method (p. 16).

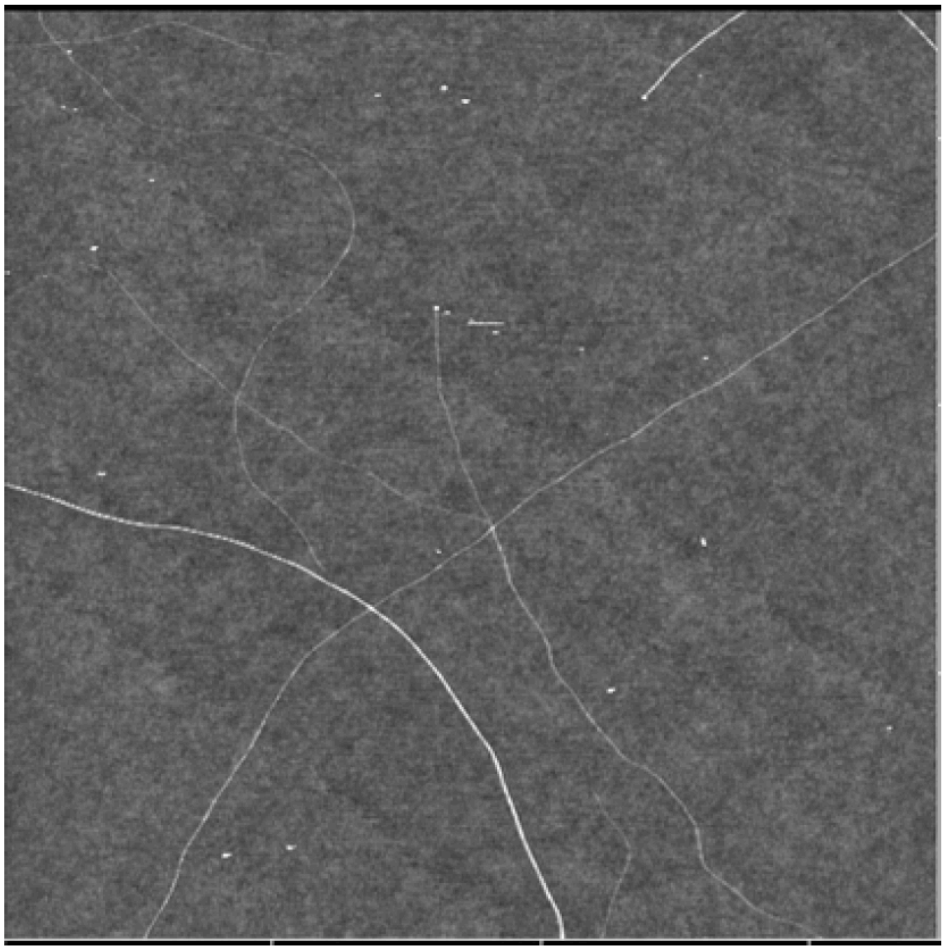

Figure 1.2: AFM height image of nanotubes grown from ferritin coated oxidized silicon substrate using the CVD apparatus shown in figure 1.1. Field of view is 3x3μm. The height range is 10 nm.

1.2.2.1 Direct CVD Growth of Carbon Nanotubes on AFM Probes

Some carbon nanotube AFM probes were fabricated by a 'direct growth' method, using the AFM probes as CVD substrates. For direct-growth probes, conventional silicon tapping AFM cantilevers were coated with iron catalyst by dipping for 2 seconds in 150 μg/mL $Fe(NO_3)_3{\cdot}9H_2O$ solution in electronics-grade isopropyl alcohol, followed by 2 seconds in HPLC-grade hexanes to induce precipitation of iron nanoparticles. The probes were then subjected to CVD following the aforementioned procedure.

1.2.3 Probe Fabrication

We compared three methods for attaching nanotubes to silicon AFM tips: manual assembly, direct growth, and pickup. Manual assembly of AFM probes was straightforward, although this method necessitates nanotube bundles or multi-wall carbon nanotubes large enough to be seen and manipulated under an optical microscope ($\gtrsim$ 25nm) and and therefore does not yield high-resolution probes.[77,99–113] While direct CVD growth of carbon nanotubes on AFM probes provides potential for large-scale parallel fabrication, we found that the yield of usable probes was quite low, primarily because of the lack of sufficiently fine control over the growth conditions necessary to produce probes with a single carbon nanotube protruding from probe apex.[114–117] Figure 1.3 shows two TEM images of a typical probe fabricated by the direct growth method. Carbon nanotubes frequently grew in ropes, bundles and loops, emerging from the silicon probe pyramid with a wide array of orientations.

Panels a and b of figure 1.4 illustrates steps associated with the 'pick-up' method of SWNT AFM probe fabrication.[1,118–122] The initial nanotube pick-up step was ac-

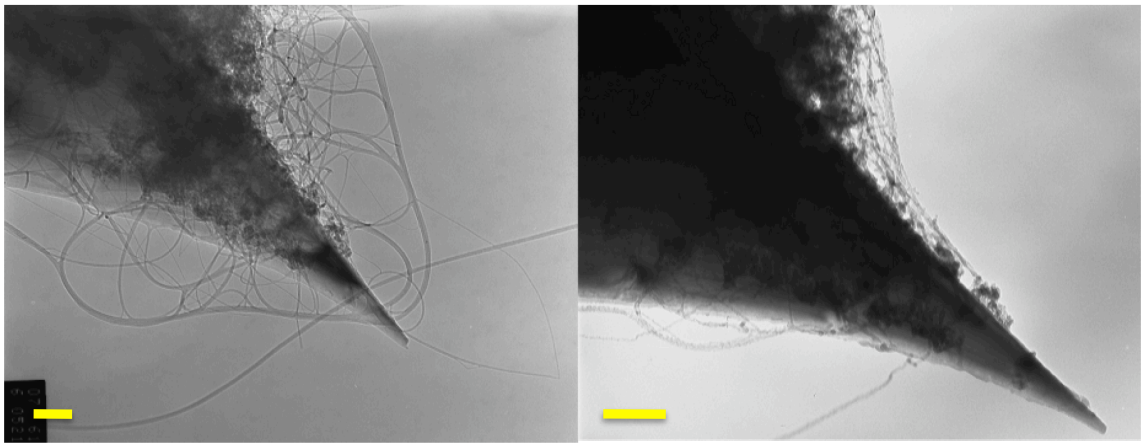

Figure 1.3: Transmission electron microscopy images representative of direct-growth nanotube AFM probes. The yellow scale bar in each image corresponds to 100nm.

complished by scanning a nanotube substrate by AFM in amplitude-feedback mode, as illustrated in figure 1.4a. CVD growth of carbon nanotubes on Si/SiO_2 by the method in Section 1.2.2 (Figure 1.2) yields a small but significant fraction of SWNTs oriented vertically on the substrate. When a conventional silicon AFM probe scans the substrate in amplitude-feedback imaging mode, a nanotube will occasionally bind to the side of the pyramidal AFM tip via attractive van der Waals forces, usually remaining attached firmly enough that it can be pressed repeatedly into and scanned across the substrate surface. The pick-up event is immediately apparent from a significant height discontinuity in the collected image. We found that it was important to reduce the field of view (e.g., from 10μm to 10nm) or retract the tip entirely from the surface as soon as a nanotube was successfully picked up in order to minimize the probability of picking up additional nanotubes. Multiple attached tubes or bundles can lead to AFM image artifacts.

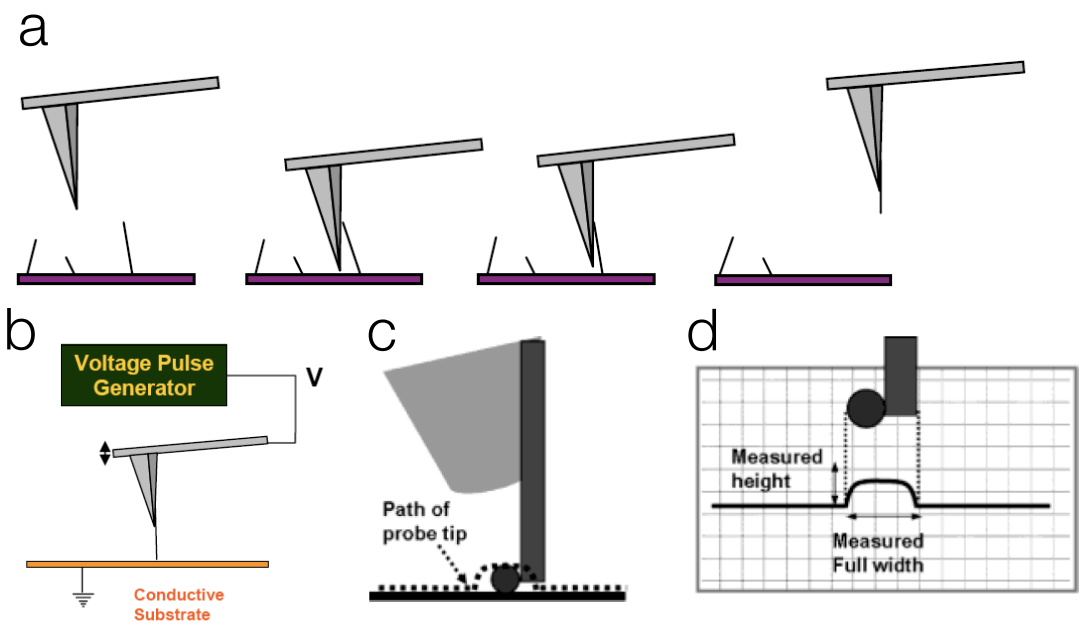

Figure 1.4: Fabrication and testing steps for SWNT AFM probes. **(a)** Illustration of the carbon nanotube 'pick-up' step. A conventional silicon AFM probe scans the CVD-grown nanotube substrate, which presents a small but significant fraction of SWNTs oriented vertically. When the silicon pyramid contacts a vertical nanotube Van der Waals attractive forces attach it stably to the surface of the probe. **(b)** Illustration of the electrical pulse-shortening step. A brief (100μs) 5–30V pulse is applied between the probe and a conductive substrate. **(c)** and **(d)** Schematic illustration of the relationship between probe diameter and lateral resolution in the hard-sphere paradigm. **(c)** shows a simple model for a SWNT probe imaging a prone nanotube on a flat surface. **(d)** shows the resulting cross-sectional profile, from which the width and height of the imaged nanotube are measured. In this simple model the full cross sectional width is equal to the sum of the diameters of the probe and sample nanotubes.

Following pick-up the nanotube length of protruding beyond the end of the silicon pyramid was inferred by observing the oscillation amplitude and deflection of the cantilever in force calibration mode (figure 1.5). In this step the AFM probe is lowered toward the substrate surface under constant mechanical excitation. The cantilever oscillation amplitude remains constant until the end of the carbon nanotube touches the surface of the substrate, dramatically reducing the effective quality factor of the cantilever and effectively damping oscillation. However, the carbon nanotube is of insufficient stiffness to deflect the silicon cantilever itself. Measurable deflection only occurs once the silicon probe pyramid itself contacts the surface. The height difference between the point at which the cantilever oscillation amplitude falls to zero and the point at which deflection occurs is considered to be the length of nanotube protruding from the end of the probe along the vertical dimension. As shown in figure 1.6, immediately following pick-up typically more than 100 nm of nanotube length protrudes beyond the end of the AFM tip. High-resolution imaging is not possible with such a long nanotube tip due to thermal fluctuations and bending.

Mounted nanotubes were then shortened by applying 5–30V, 100μs electrical pulses between the AFM probe and a conductive substrate, either gold coated silicon or p-doped silicon, as depicted in figure 1.4b.[118,122] In all cases the positive bias was on the AFM probe. Pulses were supplied from a Hewlett-Packard 8114A pulse generator and routed to the tip through a Digital Instruments Signal Access Module connected to the AFM. Additionally, push shortening could be accomplished by performing force calibration curves while gradually increasing the Z-start position in 5nm increments. When the protruding nanotube had been reduced to a suitable length it was then used for amplitude-feedback topographic imaging.

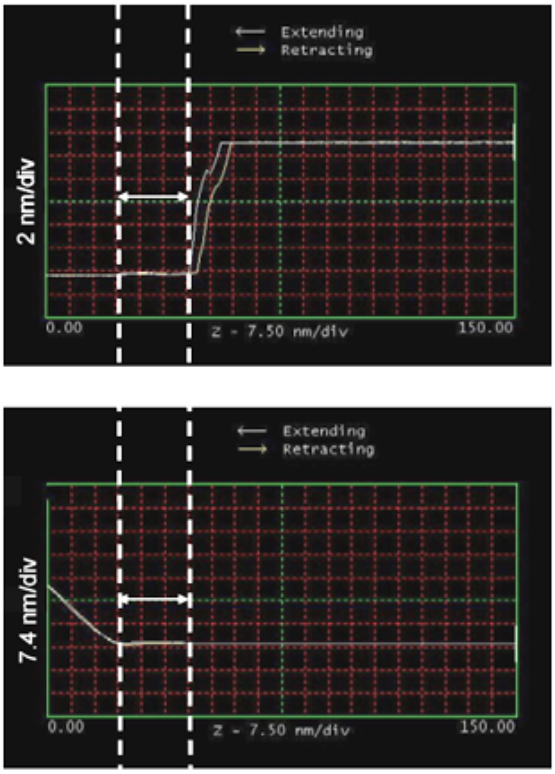

Figure 1.5: Force calibration of a SWNT AFM probe. The x-axis represents vertical cantilever position in nm. The top image shows the cantilever oscillation amplitude as a function of height above the substrate. The bottom image shows the corresponding cantilever deflection at each vertical position. When the carbon nanotube end contacts the hard substrate it damps the cantilever oscillation (top image), but is not sufficiently stiff to deflect the silicon cantilever itself. As the cantilever continues downward it eventually contacts the substrate surface with the silicon pyramid itself and causes cantilever deflection. The difference between the point of damped oscillation and the point of cantilever deflection represents the length of the protruding nanotube along the vertical axis. In this case the measured nanotube length was 22nm.

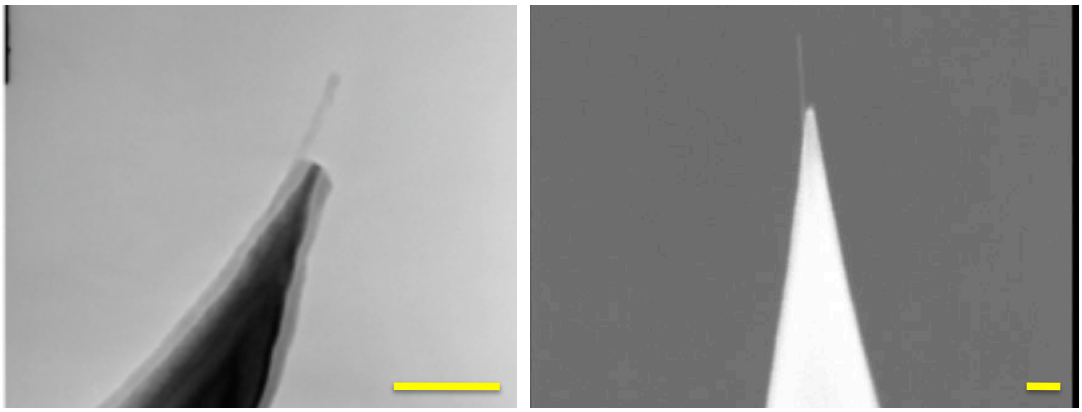

Figure 1.6: TEM (left) and SEM (right) images of two single-wall carbon nanotube probes mounted on AFM probes by the 'pick up' method, prior to any shortening steps. The yellow scale bar represents 100nm in both images.

1.3 Results and Discussion

Figure 1.7 presents the amplitude-feedback AFM image of a prone carbon nanotube on a flat Si/SiO_2 substrate, acquired using a SWNT probe fabricated by the pick-up and shortening method described above. The measured full width of the nanotube in the image is 2.1 nm and the measured height is 1.6 nm, yielding an apparent lateral resolution of 5Å. This resolution is significantly better than that predicted based on the diameter distribution observed for the SWNTs on a VCD-grown pick-up substrate (Figure 1.2, p. 15).

This phenomenon of smaller-than-expected $\left[\text{width}-\text{height}\right]$ value was observed repeatedly in images of prone nanotubes collected using SWNT probes, and was present consistently in sequential images obtained with the same probe. We termed this phenomenon 'super-resolution' and began acquiring TEM pictures of the SWNT AFM probes that had been used for AFM imaging in order to correlate the specific structure and orientation of the probe nanotube that produced each topographic

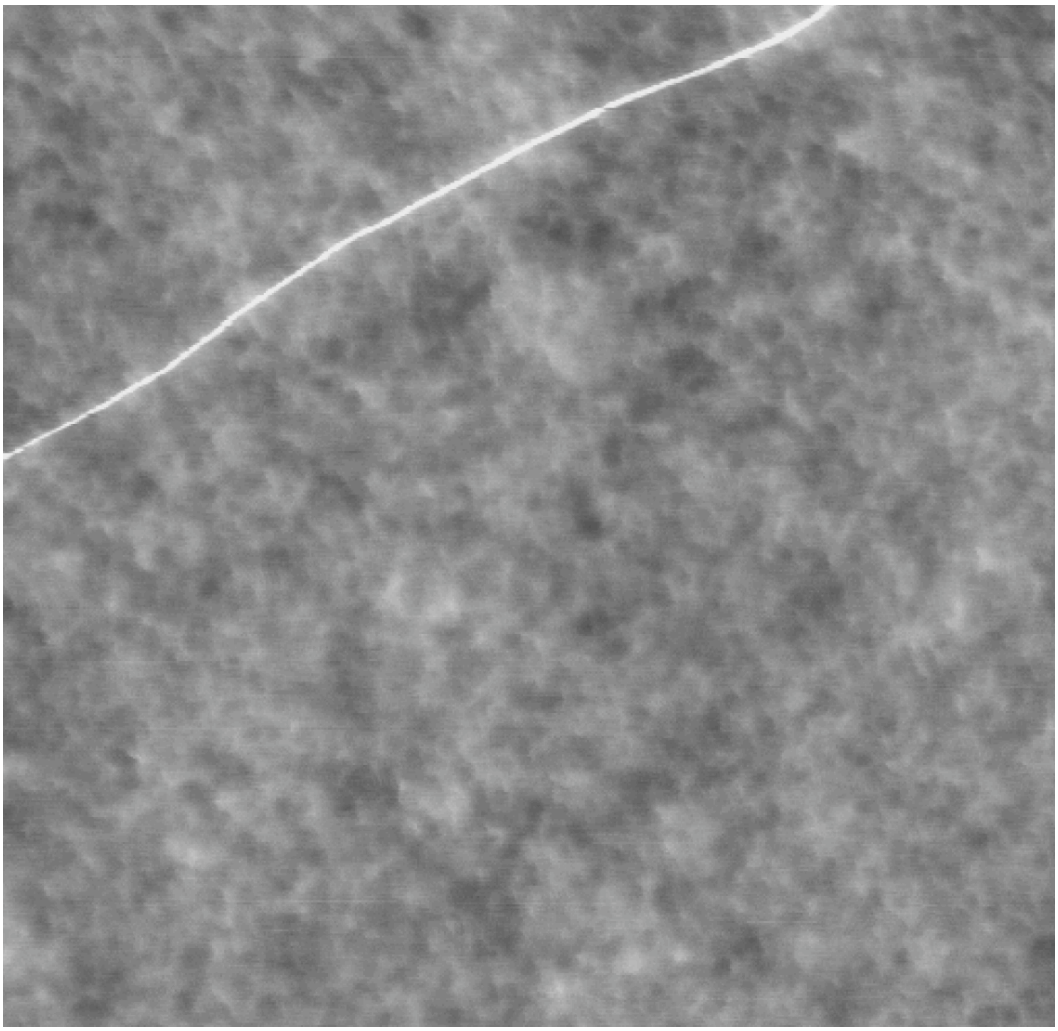

Figure 1.7: Topographic amplitude-feedback AFM image of a carbon nanotube lying prone on a silicon substrate, acquired using a SWNT probe fabricated by the full pick-up and shortening method described in this section. The measured full width of the nanotube is 2.1 nm and the measured height is 1.6 nm, giving an apparent lateral resolution of 5Å. Field of view of 358nm.

image. A representative TEM-AFM image correlation data set is shown in figure 1.8. This particular probe displayed super-resolution behavior, which was also observed in 5 of the 13 additional probes that were fully characterized by TEM-AFM image correlation.

Each data set consisted of transmission electron microscopy images of the SWNT probe at varying magnification (Figure 1.8 top row), and amplitude-feedback topographic AFM images of one or more prone nanotubes on Si/SiO_2 acquired with the SWNT probe (Figure 1.8 bottom left). The TEM images were used to measure the probe nanotube diameter, protruding length and orientation relative to the silicon cantilever. Height and width measurements of prone nanotubes in the AFM images acquired using the SWNT probe were used to calculate the effective lateral resolution.

Figure 1.9 displays histograms of topographic lateral image resolution for SWNT AFM probes fabricated by the pick-up method. The left histogram corresponds to probes fabricated from CVD pick-up substrates grown using iron nitrate-deposited catalytic nanoparticles. The right histogram corresponds to probes fabricated from CVD pick-up substrates grown using ferritin-deposited catalytic nanoparticles. We found that substrates grown from ferritin-deposited catalyst produced a greater fraction of probes of superior lateral image resolution (< 5nm). The variation in nanotube probe performance was greater than we expected based on previous reports. Leiber, *et al*, had examined the image quality of different nanotube types (MWNTs and SWNTs).[122] In contrast, we have compared 39 SWNTs made fromthe same iron nitrate-coated substrate and 40 from a ferritin substrate. The wide range in resolution found, between the two different kinds of substrate (ferritin vs iron nitrate),

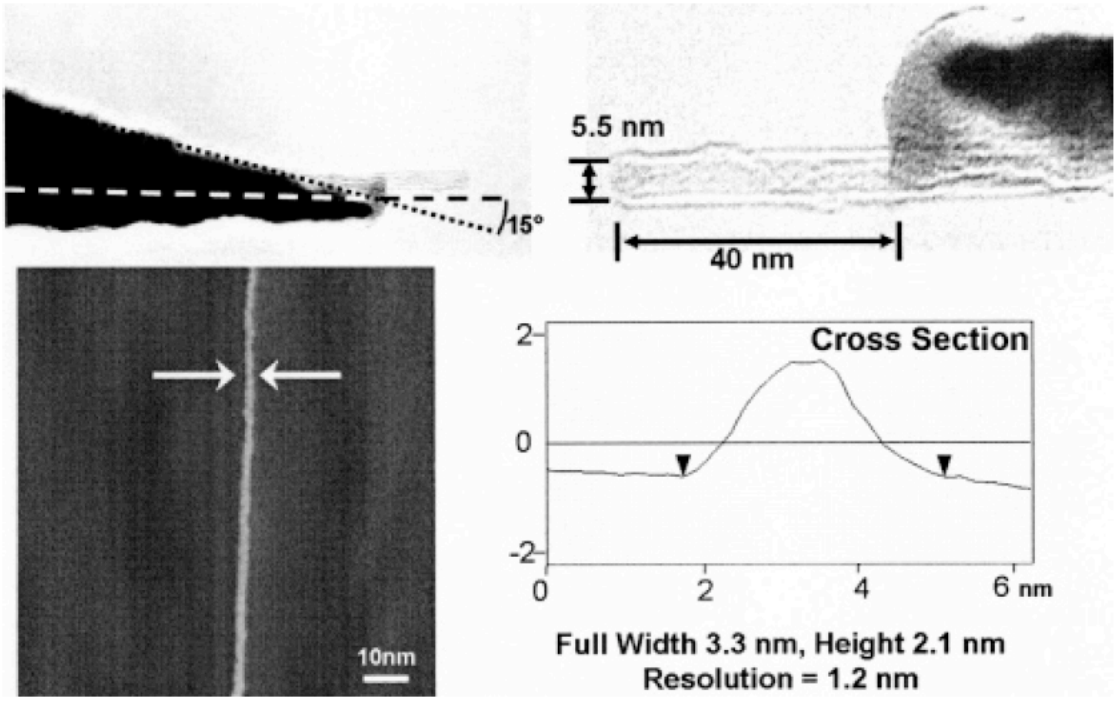

Figure 1.8: TEM and AFM data collected for each fabricated carbon nanotube AFM probe. Panels A and B are TEM images of the fabricated probe. The dashed green line in panel A is perpendicular to the sample surface when the probe is mounted in the AFM. Panel C is an AFM image of a nanotube in a flat silicon substrate taken using the probe in the TEM images. Panel D shows the cross section represented by the red line in panel C. This particular probe is rather striking because the effective lateral resolution is just 23% of the tube width.

as well as from the same substrate, underscores the importance of specific nanotube characteristicsin determining the maximum achievable resolution.

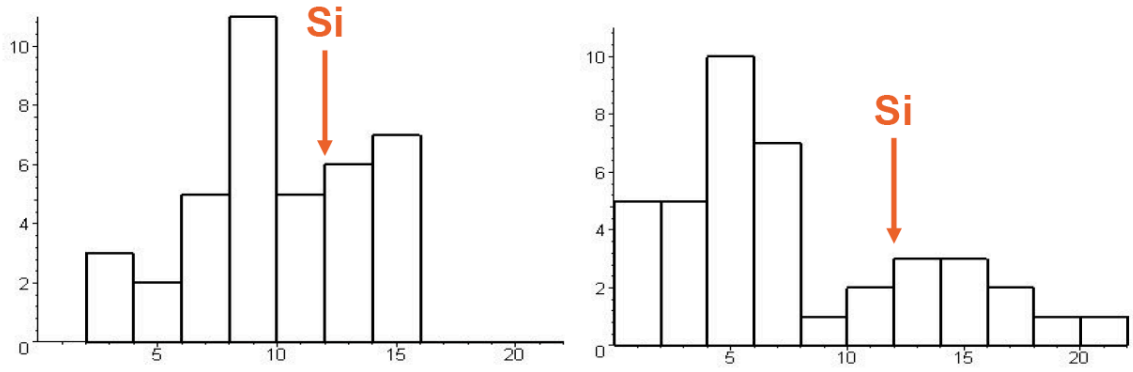

Figure 1.9: Histograms of lateral resolution in topographic imaging for all of the carbon nanotube AFM probes fabricated by the pick-up method. The two separate histograms correspond to probes fabricated from CVD-grown carbon nanotube substrates grown either from iron nitrate-deposited catalytic nanoparticles (left) or ferritin-deposited catalytic nanoparticles (right). The orange arrow in each histogram indicates the typical lateral resolution for a bare silicon AFM probe.

In figure 1.9 there is a clear shift in the distribution toward higher resolution probes when ferritin was used as the catalyst, consistent with a narrower catalyst size distribution. It is not clear how much technique improvements rather than the switch to ferritin from ferric nitrate coated substrates played in the comparative distribution. Most of the latter tips were fabricated using ferritin substrates. By that time, we were more careful to reduce the field of view immediately after pick-up to minimize bundle formation. This could explain why there are fewer 10-15 nm resolution tips. However, it is clear that significantly more probes with resolution better than 5 nm were fabricated using ferritin substrates.

Nearly 100 probes were imaged by TEM to characterize the efficacy of different fabrication techniques. Of these, fourteen SWNT probes imaged by TEM had previously been used for tapping-mode topographic imaging. Table 1.10 presents a summary of structural properties from these TEM-AFM image correlation data sets. Table entries in bold correspond to probes that demonstrated super-resolution.

AFM image quality is a function of many factors including tube diameter and length, contact angle, number of nanotubes extending past the silicon tip, thermal noise and contamination. These factors can lead to substantial variability in resolution. Lateral tip-sample forces can bend single-wall nanotubes or cause snap-to-contact behavior when the tubes exceed either a critical length or a critical angle relative to the substrate surface normal. These effects introduce a significant degree of broadening and the appearance of image artifacts.

If the nanotube is presented to the sample surface at an angle deviating from the surface normal by $\gtrsim 30^\circ$ poor resolution and obvious image artifacts result due to tip-sample forces having a significant component perpendicular to the nanotube axis. For example, figure 1.11 presents data sets for two probes that exhibited imaging artifacts. The upper data set shows a 19 nm long, 4 nm diameter nanotube projecting from the probe tip at an angle of 40°. This probe produced an image that contained a positive height shadowing artifact approximately 10 nm in width parallel to each sample nanotube. This artifact resulted from the nonideal orientation of the probe. Similar artifacts were seen with SWNT ropes (multiple SWNTs bundled together) for the same reason; the layered structure of a bundle of nanotubes attached to the AFM tip results in stiffness variation along the probe length. Additionally, the TEM images (Figure 1.11 top row) showed that the nanotube buckled near the silicon

tip type	tube diameter	tube length	aspect ratio	deviation from perpendicular	lateral resolution (full width-height)	lateral resolution/ probe diameter
SWNT	**4.2 nm**	**10 nm**	**2.4**	**10°**	**2.8 nm**	**0.67**
Bundle	**9.3 nm**	**77 nm**	**8.3**	**20°**	**4.0 nm**	**0.43**
SWNT	4.0 nm	112 nm	28	30°	10.4 nm	2.60
SWNT[a]	4.0 nm	19 nm	4.8	40°	4.6 nm	1.15
SWNT	**5.5 nm**	**40 nm**	**7.3**	**20°**	**1.2 nm**	**0.22**
Bundle	**8.0 nm**	**35 nm**	**4.4**	**15°**	**5.6 nm**	**0.70**
SWNT	3.7 nm	30 nm	8.1	30°	5.8 nm	1.56
SWNT[a,b]	4.2 nm	33 nm	7.9	20°	6.0 nm	1.43
SWNT	5.4 nm	38 nm	7.0	10°	5.9 nm	1.09
SWNT	3.5 nm	15 nm	4.3	20°	4.4 nm	1.26
Bundle	5.5 nm	51 nm	9.3	0°	21 nm	4.0
SWNT	**5.3 nm**	**55 nm**	**10.4**	**0°**	**3.9 nm**	**0.74**
SWNT	**6.5 nm**	**42 nm**	**6.5**	**0°**	**4.3 nm**	**0.66**
SWNT	5.4 nm	26 nm	4.8	10°	8.0 nm	1.48

[a] Probe showed a "shadowing" artifact. [b] Nanotube appeared buckled 16 nm from the end of the tube.

Figure 1.10: Summary of structural properties for 13 carbon nanotube AFM probes characterized by the comprehensive TEM and AFM image correlation data sets (figure 1.8, p. 24). Entries in bold correspond to probes that demonstrated lateral resolution less than the actual nanotube probe diameter.

tip. Previous reports have described reversible elastic buckling of the nanotube that did not have a serious impact on image quality, although TEM images indicate that buckling may under some circumstances be inelastic and result in irreversible structural changes and corresponding image artifacts.[123]

SWNTs must also have aspect ratios $\lesssim 10$ in order to be adequate for amplitude-modulation AFM imaging. The lower data set in figure 1.11 shows a 4 nm diameter nanotube protruding 112 nm from the end of the AFM tip, but at an angle deviating from the surface normal by only 20°. The resulting lateral resolution was 2.5 times the probe tube diameter. This broadening of the image is due only in small part to thermal vibrations. Mechanical modeling studies have indicated that for a nanotube of this geometry, the root-mean-squared thermal vibrations of the end of the tube should be less than 2Å. Nanotube bending due to lateral tip-sample forces is most likely the principal contribution to the degraded resolution

It is also important to note that the ambient humidity appeared to affect the efficiency of the pickup method. We found it nearly impossible to pick-up nanotubes from a substrate under high humidity conditions. Enclosing the AFM in a glovebag under a flow of dry nitrogen for about 30 min rejuvenated the process. We speculate that an increase in the relative humidity makes it more difficult to pick-up nanotubes for two main reasons: First, at higher humidity values, it is harder to overcome capillary forces due to the build up of a surface layer of water on the growth substrate. More force is necessary to pry a nanotube off the surface due to increased adhesion. Second, increasing water build up on the tip decreases the attractive interactions of the nanotube to the silicon surface of the AFM tip during pick up. It is known that the van der Waals interactions at the nanotube-AFM tip interface are not strong

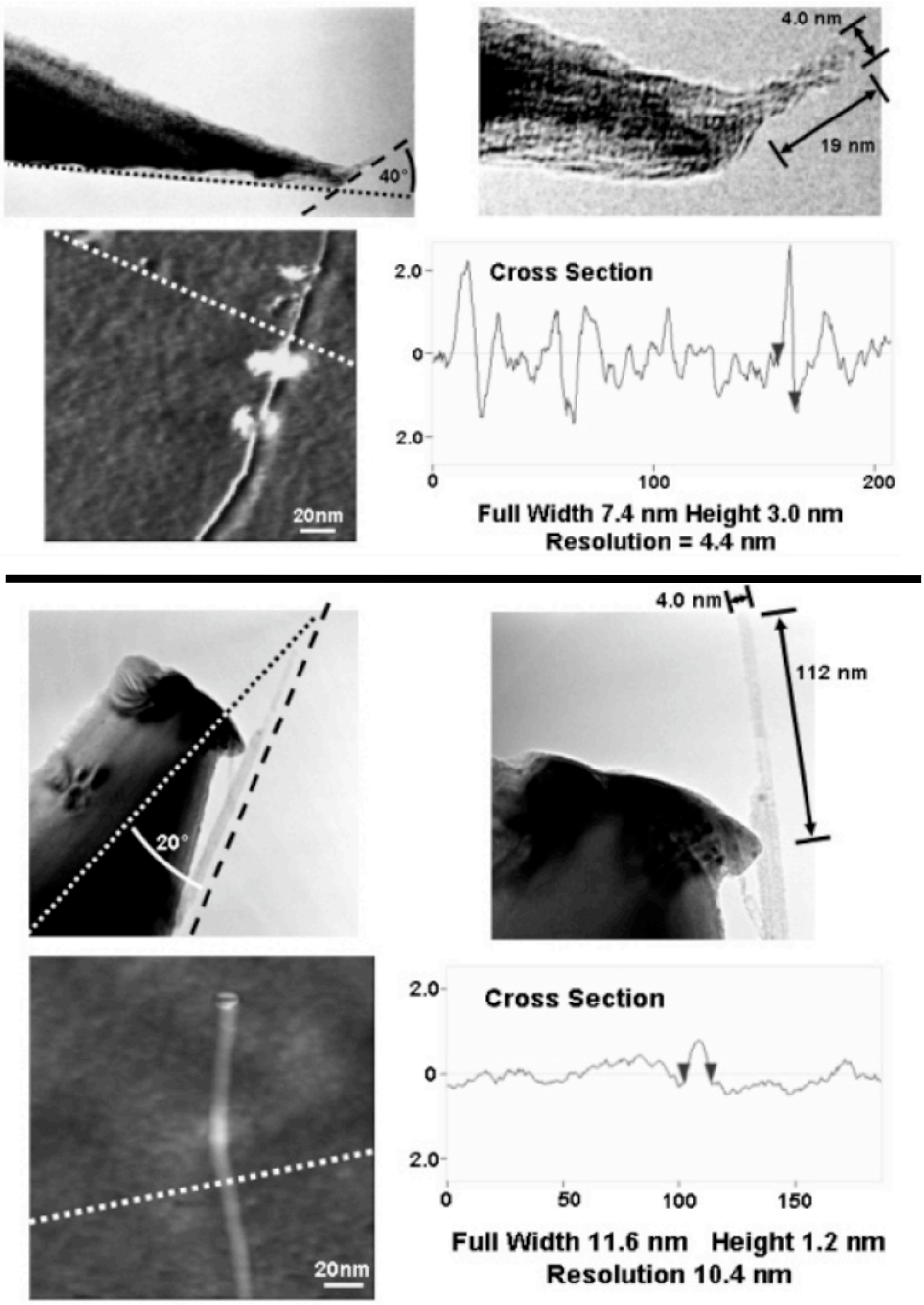

Figure 1.11: TEM and AFM data data sets corresponding to two probes that exhibited imaging artifacts. The upper image correlation data set shows an artifact due to large contact angle with substrate. Additionally, this nanotube appears to be buckled near the silicon tip. The dotted black line in the upper left image is perpendicular to the substrate. The lower image correlation data set illustrates image artifacts due to bending, which are significant for long nanotubes. Note that there are a number of picked up nanotubes at the base of this tip. The damage to the silicon tip probably occurred during repeated force calibrations.

enough to keep the tube attached to the tip in liquid water. Nanoscale condensation of water between the AFM tip and the growth substrate at high relative humidity may have an analogous effect on the success rate for picking up a nanotube.

Overall, we have found AFM image quality to be consistently and significantly better with nanotube tips used in amplitude-feedback mode than with the best silicon AFM tips. Correlation of TEM images of SWNT probes with the effective lateral resolution obtained when using these probes for topographical imaging with AFM indicates that approximately one-third of the probes demonstrate resolution better than the diameter of the nanotube probe itself when imaging nanotubes on a smooth substrate. The explanation for this phenomenon follows in the next Chapter.

Chapter 2

Influence of Elastic Deformation on Single-Wall Carbon Nanotube Atomic Force Microscopy Probe Resolution

Abstract

The preceding chapter and an earlier publication[1] describe a method for fabricating single-walled carbon nanotube probes for use in amplitude-feedback AFM imaging. One surprising feature of these probes was frequent instances of 'super-resolution' (p. 21) when they were used to topographically image isolated carbon nanotubes lying prone on a flat Si/SiO_2 substrate. The following numerical approach was carried out to assess the mechanism underlying this phenomenon: we first constructed atomic models of a sample nanotube, a Si/SiO_2 substrate, a typical Si/SiO_2 pyramidal AFM probe, and the probe nanotube, basing the latter on high-resolution TEM and AFM images collected for a single well-characterized SWNT AFM probe that had displayed super-resolution in amplitude-feedback topographic imaging (Figure 1.8, p. 24). The models were then used in rigorous *ab initio* molecular dynamics

simulations to numerically measure the one-dimensional potential energy profile and corresponding tip-sample force field at eleven evenly spaced points along the sample nanotube cross section. Force field data sets were combined with the known mechanical properties of the AFM cantilever and integrated in a classical mechanics simulation of the amplitude-feedback imaging algorithm that generated Figure 1.8. The resulting simulated cross-sectional data was in close agreement with that observed by experiment, including the appearance of lateral resolution better than that expected from the diameters of the carbon nanotube probe and sample. This phenomenon arises due to the strong attractive surface forces between the conjugated sp^2-bonded graphitic carbon atoms of the probe and sample. This causes the tubes to deform elastically and slip past one another when the applied force exceeds a threshold value governed by their relative positions. The slipping behavior is absent for an ordinary pyramidal silicon AFM probe due not only to geometric dissimilarity with the SWNT probe, but also because of the fundamentally different different tip-sample potential energy profile.

Associated Publication

Influence of Elastic Deformation on Single-Wall Carbon Nanotube Atomic Force Microscopy Probe Resolution.[124]

2.1 Atomic Force Microscopy Using Carbon Nanotube Probes

2.1.1 Imaging with CNT AFM probes

To date several publications have described the preparation of both multi-wall and single-wall carbon nanotube atomic force microscopy probes.[78,95,108,118,125,126] Carbon nanotube probes offer topographic imaging resolution superior to that of conventional silicon AFM tips by virtue of their unique chemical and mechanical properties, high aspect ratios, and molecular-scale dimensions.[96,97,99,104,105,127] Both contact-mode force-feedback and oscillating-probe amplitude-feedback imaging have been reported using carbon nanotube AFM probes.[121,127] Experimental evidence suggests that image artifacts will arise from inelastic buckling of CNT probe tips under conditions of high-repulsive-force imaging.[128,129] However, even under less forceful imaging conditions adhesive attraction encountered by the end of the SWNT probe tip introduce experimental artifacts. This occurs even when imaging hard, flat surfaces presenting no lateral probe-sample forces.[123,130] These dissipative processes are more prominent for graphite surfaces than for oxidized silicon, indicating that the material-specific force field plays a significant role in the efficacy of SWNT AFM probes.[131] Additional artifacts arising from lateral attraction between long MWNT probes and high-aspect-ratio solid structures have also been reported.[132]

We have previously described an efficient SWNT probe fabrication methodology and correlated probe structure with the consequent quality of images they produced when used to image probe SWNTs on Si/SiO_2 in amplitude-feedback AFM.[1] As discussed in Chapter 1, by comparing the observed AFM resolution with the diameter

of the probe nanotube measured from the TEM image, we found that the lateral resolution is on average 1.2 times the nanotube probe diameter. This value approaches the expected ideal ratio of unity in the absence of thermal vibrations and bending effects of the probe. This simplified model, in which which the probe and sample are considered to be incompressible objects, has commonly been used to describe AFM resolution.[78,105,118] However, simple geometrical arguments alone cannot explain the subdiameter resolution we observed. The potential for SWNT AFM probes to be used as common research tools requires a more thorough understanding of how the physical, chemical, and mechanical properties of SWNT probes affect image resolution.

To these ends, we present here a numerical study of SWNT AFM probe behavior in the context of amplitude-feedback topographic imaging, using a combination of molecular dynamics and classical mechanics simulations. The dimensions of the probes and samples are on the order of 1–50 nm, placing them within the range of atomistic simulations. To elucidate the specific tip-sample interactions that give rise to the observed phenomena, we have used TEM-AFM correlation data to construct realistic molecular models of an open-ended SWNT probe interacting with a prone SWNT sample on a flat hydroxyl-terminated silicon surface. These models were used to generate potential energy curves at different positions of the probe relative to the sample. Integration of the resulting forces into the equation of motion for an oscillating cantilever yielded a simulated topographic cross-section profile that corroborate the experimental results. These simulations indicate that, under the AFM conditions employed, both probe bending and localized deformations of the probe and sample SWNTs strongly influence the topographic profile measured by AFM. The reversible elastic nature of these deformations is demonstrated both experimentally

and in simulations.

An AFM cantilever operated in dynamic mode closely approximates a damped driven harmonic oscillator, described formally in Section 2.2 (p. 36). Briefly, upon encountering an external force field from the sample being imaged, the result is a change in the oscillator parameters and consequently a shift in the fundamental frequency of the system. If the encountered force is linear, the combined cantilever-sample system continues to oscillate at the driving frequency, albeit with a different amplitude than before. This oscillation amplitude is used as the feedback measurement in AM-AFM (p. 4).

If the encountered force deviates significantly from linearity, however, the combined system becomes that of a nonlinear driven oscillator, which universally generates higher harmonics at integer multiples of the fundamental frequency. (equations 2.9−2.10 in Section 2.2, p. 43) Therefore, measuring the amplitude changes in the higher harmonics of the cantilever yields sensitive information about the force field present at the sample surface, a relationship that is utilized for the feedback measurement in FM-AFM (p. 5). In general, oscillating-probe force microscopy may be interpreted as an inversion problem: the time-dependent signal consisting of probe tip position $\boldsymbol{z}$ yields information regarding both the time-independent cantilever-substrate force field F_{ts} and the time-dependent rate of energy dissipation.[133]

In the following section we present a rigorous framework for oscillating-probe atomic force microscopy that is amenable to numerical simulation. The model equation for cantilever motion (equation 2.4, p. 39) was combined with force field data from atomistic MD simulations and used to generate a simulated cross-sectional pro-

file of the sample nanotube in Figure 1.7 (p. 22) under the conditions identical to those used in the experimental image acquisition. The resulting simulated data matches the measured experimental data closely and provides a phenomenological explanation for the topographic super-resolution we observed repeated from SWNT AFM probes: elastic deformation of both the probe and sample nanotubes results in the tubes slipping past one another under ordinary imaging conditions. The apparent resolution is therefore a much more complex convolution of probe and sample interactions than the simple hard-sphere model usually used to describe AFM image resolution.

2.2 Formal Description of Amplitude-Modulation Atomic Force Microscopy

As described in Section 1.1.1, amplitude-modulation atomic force microscopy (AM-AFM) for topographic imaging involves mechanically exciting a probe cantilever to a specified oscillation amplitude A_0 in the absence of any sample forces acting on the probe. The oscillation amplitude is measured using a laser reflected off the cantilever's top surface onto a position-sensitive photodetector. The mechanical excitation has frequency ω and driving power p_d specified independently by the experimenter. ω is generally chosen to be close to the cantilever's resonant frequency ω_0 and excitation power is specified at a value insufficient to cause significant deviation from harmonic-oscillator approximation for the cantilever. When the cantilever approaches sufficiently close to the surface to encounter tip-sample forces the oscillation amplitude A drops from the initial isolated-oscillation amplitude A_0. A piezoelectric actuator then scans the cantilever parametrically across the sample surface in two

lateral dimensions $\left\{(\hat{\boldsymbol{x}}, \hat{\boldsymbol{y}})\,; x = X(t), y = Y(t)\right\}$ with Å-level resolution, although the lateral precision is usually significantly worse than that for the vertical position. The experimenter specifies an oscillation amplitude set-point $A_{sp} < A_0$, and at each scan point $\{x, y\}$ the feedback loop measures the cantilever oscillation amplitude A and actively adjusts the cantilever's vertical position until $A = A_{sp}$ with all other parameters remaining constant.

The independent variable in this process is the cantilever's equilibrium rest position Z_r (measured at the very end of the pyramidal probe tip) in the absence of mechanical excitation. This value is independently controlled using a piezoelectric linear actuator with sub-Åposition resolution, its precision being limited primarily by thermal vibration of the cantilever and piezoelectric element. The vertical-dimension $(\hat{\boldsymbol{z}})$ actuator precision is universally better than that of the lateral actuator, in part because the lateral actuator must be longer in order to span a larger spatial scanning range, and in part by design since the AFM lateral image is usually limited by the size of the probe tip (fig. 1.4c, p.18). The height changes ΔZ_r necessary to maintain the $A = A_{sp}$ condition are the source of contrast. The resulting image $Z_r\big(x, y, A_{sp}\big)$ roughly represents the sample topography, although the exact interpretation of $Z_r\big(x, y, A_{sp}\big)$ requires an intimate understanding of the three-dimensional force field between the probe tip and the sample.

Starting at a height sufficient to avoid any forces between the probe tip and the sample surface, the cantilever is mechanically excited using a vibrating piezoelectric element with constant driving power p_d and driving frequency ω in the range $10^3 \lesssim \omega \lesssim 10^6 Hz$. The driving frequency and power induce oscillation of the cantilever with amplitude A governed by a variety of independent parameters including

the mechanical excitation power (user-specified so that $1nm \lesssim A \lesssim 100nm$), the viscosity of the surrounding medium, and the cantilever's size, shape, mass and resonance 'quality factor' Q.[†] In isolation from other interacting forces the probe tip then has time-dependent instantaneous position $\boldsymbol{z}$ governed by the cantilever oscillation amplitude, mechanical excitation frequency and equilibrium probe rest point:

$$\boldsymbol{z} = z(A, \omega, Z_r, t) \tag{2.1}$$

$$= Z_r + A\cos(\omega t)\,. \tag{2.2}$$

In general the cantilever motion in most imaging contexts is best described by that of a damped-driven harmonic oscillator encountering an external force.[134–140]

$$m\frac{d^2}{dt^2}\boldsymbol{z} = -k\boldsymbol{z} - m\frac{\omega_0}{Q}\frac{d}{dt}\boldsymbol{z} + F_{ts}(\boldsymbol{z}) + F_0\cos(\omega t) \tag{2.3}$$

where m is the cantilever mass, k is the cantilever spring constant, ω_0 is the resonant frequency of the cantilever in isolation, Q is the cantilever quality factor, $\boldsymbol{z} = z(Z_r, t)$ is the instantaneous time-dependent probe tip position, F_{ts} is the vertical component of the probe-tip force field, and F_0 is the driving force amplitude corresponding to the driving power p_d.

Equation 2.3 describes harmonic oscillation and only holds analytically in the special case where $F_{ts}(\boldsymbol{z})$ is linear. This linear requirement of $F_{ts}(\boldsymbol{z})$ is essentially never rigorously fulfilled for any real-world systems, and in addition the cantilever is a stiff-beam oscillator of finite length L_c that will deviate from a constant restoring

[†]Q is a dimensionless parameter corresponding to the number of periods it takes for oscillation amplitude to fall to e^{-1} of its initial value.

force factor (k) unless its displacement is small ($A \lesssim L_c/1000$).

In the context of AFM imaging, however, the harmonic approximation is usually sufficient to describe the oscillating cantilever probe, at least in cases of small driving amplitudes ($A_0 \lesssim 100nm$). Integrating equation 2.3 using a numerical routine commonly applied for solving ordinary differential equations (e.g., common 4^{th} order Runge Kutta) yields, after dissipation of transients, a cantilever oscillating at the same frequency as the driving force ω, albeit with a phase shift ϕ and and at an amplitude lower than A_0. For a specified cantilever rest position Z_r and an isolated oscillation amplitude A_0 (specified indirectly via p_d) the steady-state solution takes the form of equation 2.4.

$$\boldsymbol{z} = z(Z_r, A_0, t) = Z_r + \boldsymbol{A}\cos\big(\omega t - \boldsymbol{\phi}\big) \tag{2.4}$$

where $\boldsymbol{A} = A\big(Z_r, A_0\big)$ and $\boldsymbol{\phi} = \phi\big(Z_r, A_0\big)$ are both governed by the specified parameters.

The phase term is $\phi = \frac{\pi}{2}$ when the cantilever is isolated from the sample, the value expected for an underdamped oscillator. Experimentally, the measured phase shift ϕ is indicative of whether the predominant tip-sample interaction is attractive ($\phi > \frac{\pi}{2}$) or repulsive ($0 \leq \phi < \frac{\pi}{2}$). The force field landscape between any two solid-state materials almost universally includes regions of both attractive and repulsive. The Lennard-Jones potential, a representative approximation for the van der Waals potential energy profile between molecules, corresponds to mutual repulsion at short distances and mutual attraction at moderate distances, asymptotically approaching zero for large separation. Depending on the cantilever's mechanical driving force

and its equilibrium rest position, the predominant probe-sample interaction force may be either attractive or repulsive. For small cantilever oscillation amplitude A, the steady-state solution to equation 2.4 in the presence of amplitude feedback corresponds to predominantly long-range attractive forces, and conversely for large cantilever amplitude the predominant probe-sample interaction in the steady-state solution is repulsive. These two solutions have been labeled the 'attractive' and 'repulsive' imaging regimes, respectively.[134–137] At intermediate oscillation amplitudes the result is bifurcation of the steady-state solution for the cantilever amplitude, with discontinuous jumps between the two imaging regimes and corresponding image artifacts induced unpredictably by small system perturbations.[141,142]

This scenario is frequently prominent with soft matter such as biological macromolecules, although it is true even when both the probe and sample are rigid crystalline materials (e.g., both having a silicon oxide surface). Multistability is a ubiquitous property of nonlinear systems, the nonlinearity in the context of AFM being a tip-sample force field $F_{ts}(\boldsymbol{z})$ containing both attractive and repulsive components. Multistability with greater than two possible amplitude solutions arises in the presence of more complex tip-sample force fields.[128,143–145] Addition of a second feedback control loop, such as a force modulation feedback motif, can reduce the incidence of image artifacts arising from bi- and multi-stability, although this comes at the expense of slower data acquisition.[146,147]

An additional repercussion of nonlinear $F_{ts}(\boldsymbol{z})$ in equation 2.4 is the phase shift value, $\phi > \frac{\pi}{2}$ indicating attractive regime imaging and $0 \leq \phi < \frac{\pi}{2}$ indicating repulsive regime imaging. Measuring the value of ϕ also permits separation of the cantilever equation of motion (equation 2.3) into conservative elastic and dissipative inelas-

tic components of the tip-sample interaction by calculating the effective resonance frequency ω_{eff} and quality factor Q_{eff} using equations 2.5−2.8.

$$\frac{d^2}{dt^2}\boldsymbol{z} = \omega_{eff}\boldsymbol{z} - \frac{\omega_0}{Q_{eff}}\frac{d}{dt}\boldsymbol{z} + \frac{F_o}{m}\cos\omega t \tag{2.5}$$

$$\omega_{eff} = \omega_0^2 - \frac{d}{dz}F_{ts}(\boldsymbol{z}) \tag{2.6}$$

$$= \sqrt{\omega^2 + \frac{\omega_0^2}{Q}\frac{A}{A_0}\cos\phi} \tag{2.7}$$

$$Q_{eff} = Q\frac{A}{A_o}\frac{\omega}{\omega_0}\frac{1}{\sin\phi} \tag{2.8}$$

where the three separate frequencies ω, ω_0 and ω_{eff} correspond to the driving frequency, isolated-cantilever resonant frequency, and effective cantilever resonant frequency, respectively.

The ω_{eff}-dependent term in equation 2.5 corresponds to the elastic component of the tip-sample interaction, with the Q_{eff}-dependent term corresponding to the inelastic component. The empirical values for ω_{eff} and Q_{eff} can be calculated solely using experimentally-accessible measurements and equations 2.7−2.8. Inelastic energy dissipation dependence upon the probe and sample material composition has been thoroughly modeled by numerical methods.[139,148–157] Experimentally, inelastic dissipation has been measured from oscillating-probe AFM both on inorganic substrates such as crystalline silicon,[152,154] gold[158] and silver[159] and on soft biological materials. The phase value also yields material contrast in samples that are otherwise topologically smooth.[148,149]

Separation of elastic and dissipative components of the probe-sample interaction via analyses similar to equation 2.5 have also been applied to mechanical unfolding and refolding of proteins,[160–165] nucleic acids[166] and other biologically relevant polymers such as dextran chains[167] over a broad spectrum of mechanical cycle rates. At sufficiently high rates ($\gtrsim 1kHz$) the macromolecular extension and unfolding by force microscopy occurs by non-equilibrium pathways.[168,169] These experiments have described behavior similar to relaxation dynamics of tethered molecules released from nonequilibrium prepared states via optical trapping methods, and generallly corroborate the phenomenon of numerous nonequilibrium measurements eventually converging to an average that is in agreement with equilibrium statistical mechanics.[170–172]

Additionally, 'Q control' methods have been reported that permit low-force ($\lesssim 100pN$) imaging in liquid environments as well as increased sensitivity to inelastic energy dissipation.[140] In Q-controlled AFM a piezoelectric actuator integrated into the probe cantilever introduces an additional independent force term $gk\boldsymbol{z}(t-\tau)$ (g being the gain, and τ being an empirical phase-shifting parameter) to equation 2.3.[173–177]

Lastly, deviation of the oscillating cantilever from harmonic behavior, which is nonzero in all cases except when the trip-sample force field F_{ts} is perfectly linear with z, and is prominent in cases where F_{ts} includes sharp changes, induces higher-order oscillatory modes in the cantilever's steady-state motion. These modes can be measured as higher harmonics in the frequency spectrum of $z(t)$ at predictable integer-multiples of ω_0. $\boldsymbol{z}(t)$ may then be described using the Fourier series shown in equation 2.9, with harmonic coefficients a_n determined by integral convolution of all tip-sample force field gradients with a semicircular weighting function over the full

range of cantilever motion $\left[Z_r - A, Z_r + A\right]$.[20]

$$\boldsymbol{z}(t) = \sum_{n=0}^{\infty} a_n \cos(n\omega t) \tag{2.9}$$

$$a_n = \frac{2A^n}{k\pi} \frac{1}{1-n^2} \frac{1}{\prod_{m=1}^{m=n}\left(2m-1\right)} \int_{-1}^{1} \frac{d^n}{dz^n}\left[F_{ts}\left(Z_r + Au\right)\right]\left(1-u^2\right)^{\left(n-\frac{1}{2}\right)} du \tag{2.10}$$

If the tip-sample force field $F_{ts}(z)$ is known (or estimable), equation 2.10 will provide the expected higher harmonic coefficients for a given cantilever rest position Z_r and oscillation amplitude A. The method in equation 2.10 for calculating the harmonic weighting from an arbitrary force field represents a direct analogy to the Born approximation for determining wavefunction time-evolution in a perturbed quantum-mechanical harmonic oscillator.[178]

Alternately, given an experimentally measured cantilever position signal of sufficient time resolution, Fourier transformation of $z(t)$ (the inverse process of equation 2.9) will indicate the relative weights of each higher-order harmonic term. Numerical deconvolution of these coefficients from equation 2.10 can yield a profile of the corresponding tip-sample force field.[21,179,180]

The higher harmonic terms of the cantilever oscillation have been reported experimentally to reveal compositional contrast because the probe-sample force field will differ between materials.[20,21,156,180–184] Harmonic responses in many cases also display significantly better lateral spatial resolution than the fundamental cantilever frequency signal because they correspond to higher-order derivatives of the probe-sample force field. In general this process is slower than conventional topographic imaging using only the fundamental cantilever frequency, although Solares *et al.*

have very recently proposed utilizing the fundamental and harmonic cantilever frequencies simultaneously in independent feedback control loops to streamline topographic tracking while simultaneously acquiring information about the tip-sample force field.[185]

2.3 Methods

2.3.1 Experimental Methods

Fabrication, characterization, and imaging with SWNT AFM probes has been described previously.[1] The effective lateral resolution of each probe was obtained by imaging, under ambient conditions, a carbon nanotube lying prone on a flat native-oxide silicon surface. To acquire accurate sample height and width measurements by use of amplitude-modulation AFM, it was necessary to first carefully calibrate the response of the system over a wide range of operational parameters, most importantly, the oscillation amplitude of the SWNT probe. For example, to understand the effects that vertical compression of a sample nanotube by the AFM probe had on the lateral resolution, repeated measurements of the sample nanotube height as a function of probe oscillation amplitude were performed for both conventional silicon and SWNT AFM tips. In all cases, the driving amplitudes employed were kept below the limit corresponding to a 10% reduction in the apparent height of the sample nanotube due to compression. In addition we measured repeated force calibration curves, which consist of scans of the damped oscillation amplitude as a function of the average tip-sample separation for a given cantilever driving force. The force calibration curves revealed the presence of coexisting attractive and repulsive tip-sample interaction regimes.[134,137] Bistable switching of the cantilever oscillation between the

two regimes manifests itself as sudden changes in the observed sample height and width.[136] In general we avoided these amplitude instabilities and the concomitant experimental artifacts by operating the AFM cantilever with a driving force sufficient to give a free-air oscillation amplitude greater than 20 nm. Consequently, all AFM data presented here can be considered in the repulsive imaging regime.

2.3.2 Molecular Dynamics Simulations

Molecular dynamics (MD) simulations were carried out with Cerius2 molecular simulations software (Accelrys, San Diego, CA).[¶] The MD force-field parameters were optimized by fitting the material bulk and surface properties such as elasticity moduli, vibrational frequencies, and surface geometry both to experimental data and to rigorous quantum mechanics calculations on clusters representative of the silicon and graphene systems under study. Realistic atomistic models were constructed for the SWNT probe used for amplitude-feedback AFM imaging. Every effort was made to match the model structures and simulation conditions as closely as possible to corresponding experimental values, including the nanotube probe diameter, length, angle relative to the substrate normal, and the fine structure at the probe end. All silicon surfaces were (100) and were terminated with hydroxyl groups. The probe was a $(40, 40)$[§] armchair SWNT (5.4 nm diameter, 45 nm length, with 5 nm of fixed atoms at one end of the probe to simulate its attachment site at the AFM tip) constructed from approximately 25,000 carbon atoms. The sample was a $(16, 16)$ armchair SWNT (2.2 nm diameter, 10 nm length) constructed from approximately 2600 carbon atoms. The sample SWNT was kept fixed at both ends during the calculations to simulate a very long nanotube, which is unlikely to displace laterally

[¶]All molecular dynamics simulations were performed by Santiago Solares.

[§]The (n, m) designation of SWNT structure is discussed in Section 1.1.2, p. 6.

during imaging. Similar models were generated for a conventional silicon tip interacting with the sample nanotube. The 11 scan point positions and MD simulation snapshots illustrating the relative probe and sample nanotube positions for several scan points are shown in Figure 2.1.

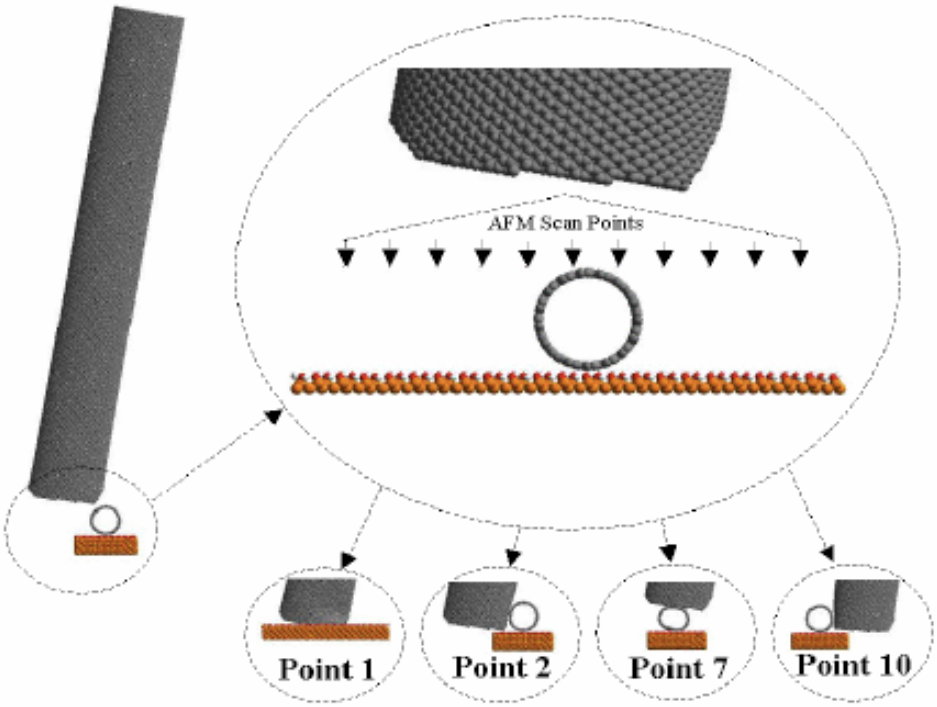

Figure 2.1: Illustration of the atomistic models used to construct the tip-sample interaction profile. Lateral positions of the 11 scan points are indicated by the arrows. Atomistic models were constructed on the basis of experimental TEM and AFM data.[1] The final tip position reached in the subsequent classical-mechanics AFM scan (fig. 2.3, p. 51) is shown for four of these points. The corresponding force curves for all 11 scan points are shown in Figure 2.2 (p. 50).

The tip-sample interaction potentials were constructed by vertically approaching the sample with the probe nanotube at 0.05 nm intervals, at each point optimizing the

system geometry by minimization of the potential energy. Additional calculations performed at 300K showed that the potentials did not significantly change with inclusion of thermal vibrations at room temperature. The gradient of this energy-position function with respect to the vertical tip position is the tip-sample interaction force ($F_{ts}(\boldsymbol{z})$ in equation 2.3).

To reduce the computational cost of the MD simulations each model of a nanotube on the surface included only a small section of the silicon substrate, sufficient to obtain an accurate description of the SWNT probe interactions with the sample. This does not give an accurate description of the interaction of the tip with the silicon surface for the cases in which the SWNT tip deforms and slips against one side of the sample nanotube and makes contact with the underlying substrate. To correct this, another model was constructed *without* a sample nanotube on the substrate to obtain the interaction forces between the tip and the bare silicon surface. Deformation of the probe structure was considered in all cases when the relative position of the surface and the end of the tip was calculated for each scan point.

2.3.3 Classical Mechanics Simulations

Oscillating-probe AFM was modeled by classical mechanics numerical methods, following the well-established theoretical framework in which the cantilever is approximated as a damped-driven harmonic oscillator.[139,148–157] Our simulations use a separate coordinate $\boldsymbol{z_{ts}}$ for the probe tip position relative to the *origin* of the probe-sample force. This is because the force fields determined using the *ab intio* molecular dynamics simulations are measured as a function of tip-sample separation, while the cantilever restoring force $-k\boldsymbol{z}$ is calculated a function of displacement away

from its equilibrium rest position. Both of these forces ($-k\boldsymbol{z}$ and $F_{ts}(\boldsymbol{z_{ts}})$) are time-dependent due to the time-varying position of the driven oscillating cantilever. The link between the two force sources arises from the fact that the cantilever oscillation yields a time-varying distance between the probe tip and sample, and this tip-sample distance consequently determines the force encountered by the cantilever in addition to its endogenous harmonic restoring force.

Parameter	Value
Cantilever spring constant	$k = 4.8N/m$
Cantilever quality factor	$Q = 150$
Cantilever resonant frequency	$\omega/2\pi = 47.48kHz$
Isolated oscillation amplitude	$A_0 = 39nm$
Amplitude set-point	$A_{sp} = 15.4nm$
Excitation force	$F_0 = 1.25nN$

Table 2.1: Amplitude-feedback AFM imaging parameters used in acquisition of the experimental image in Figure 1.7 (p. 22) and in the classical mechanics simulations described in this section.

Simulation of the AFM probe tip motion was carried out by numerical integration of equation 2.3 at each of the 11 scan points along the sample, using the experimental imaging parameter values shown in Table 2.1 and tip-sample force fields $F_{ts}(\boldsymbol{z})$ obtained from the atomistic simulations (fig. 2.2), using the Verlet algorithm to fourth-order accuracy for the tip position and second-order accuracy for the tip velocity.[186] Although the actual dynamics of the oscillating cantilever in the presence of the probe-sample interactions are nonlinear, the validity of the harmonic approximation for modeling conventional amplitude-feedback AFM imaging in air

has been demonstrated by both theory and experiment for the range of parameters used here.[135,137–139,187] Integration of equation 2.3 was performed for values of the cantilever equilibrium rest position relative to the substrate, Z_r, ranging from 50 to 0 nm, At each scan point and tip position, equation 2.3 was integrated numerically for a total time of 0.02s using a 100ps integration step to determine the steady-state oscillation amplitude of the cantilever as a function of its vertical rest position: $A(Z_r)$. For each integration the initial tip position was its equilibrium rest position and its initial velocity was set to zero in all cases. The simulated cross section (Figure 2.3) is then the locus of Z_r values that resulted in convergence to $A = A_{sp}$ at each scan point.

2.3.4 Results and Discussion

Probe-sample force curves for all 11 scan points are shown in Figure 2.2 (p. 50). The separation between adjacent points was 1 nm. The abscissa on all graphs in Figure 2.2 corresponds to the distance between the lowest atom on the SWNT tip and the highest atom of the Si(100)-OH surface. Negative values on this axis correspond to elastic deformations in nanotube and surface geometry, including local deformation of the probe, as well as slight deformation of the Si-OH surface.

The result of each classical mechanics simulation was a curve showing the cantilever equilibrium oscillation amplitude as a function of the average vertical position of the tip for each point along the scan direction: $A(Z_r, x)$. Two of these curves are shown as insets in Figure 2.3. The simulated cross-section trace in Figure 2.3 was constructed by plotting the locus of tip rest position values which maintained the oscillation amplitude at the set-point value of 15.4 nm. Note that the average tip-

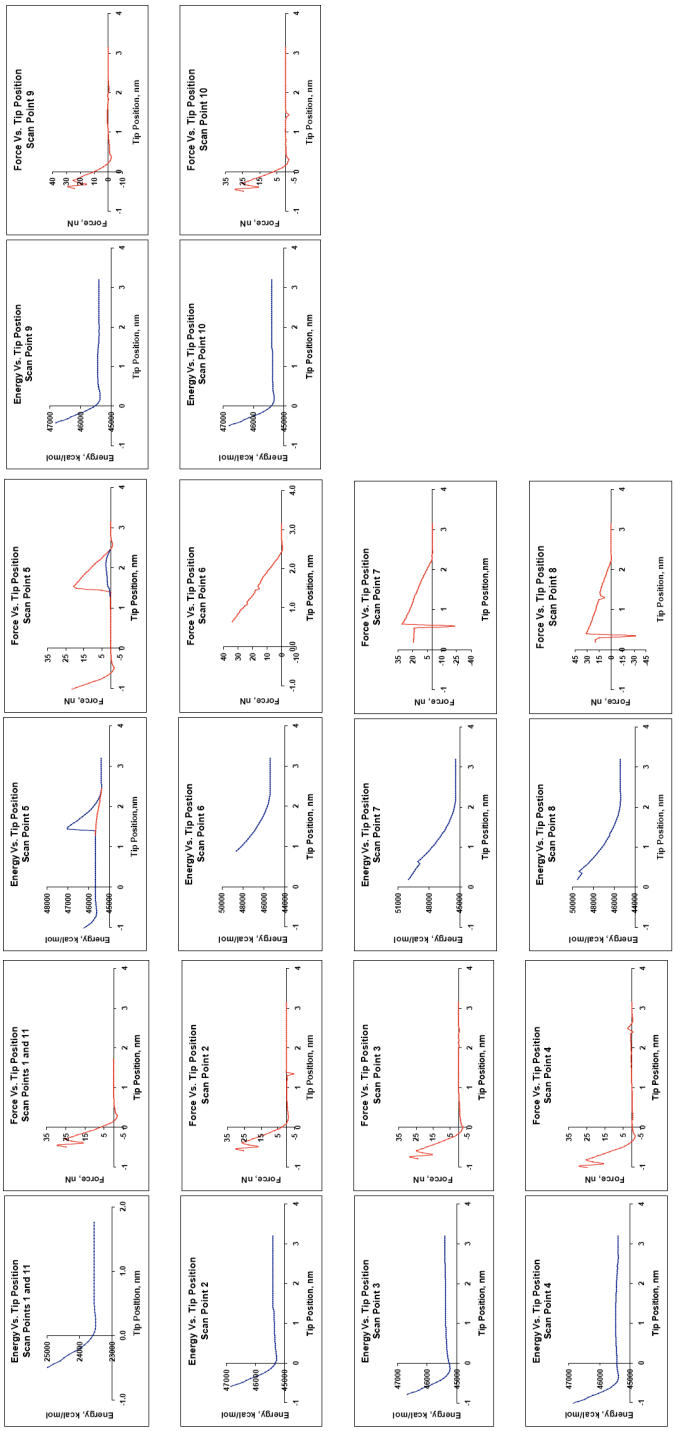

Figure 2.2: Energy profiles and tip-sample force fields at all 11 scan points of the simulation

sample separation for each scan point is given relative to the value obtained when imaging the bare silicon oxide substrate.

The final result of the combined *ab initio* MD and classical mechanics amplitude-feedback imaging simulation is shown in Figure 2.3 and overlaid with the experimentally obtained cross-section data for comparison.

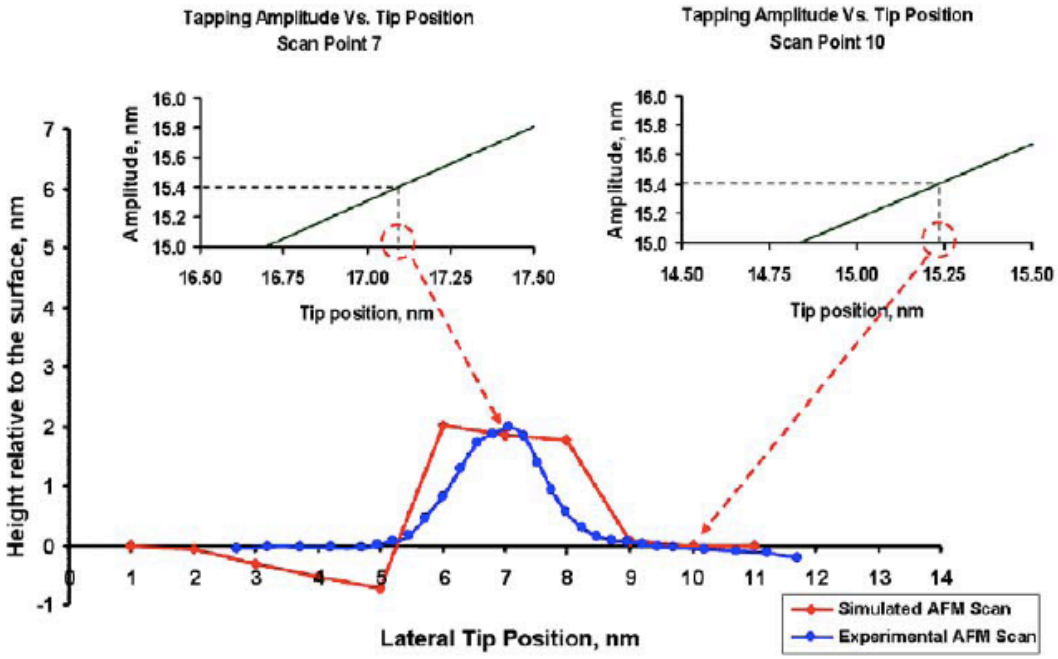

Figure 2.3: Schematic depiction of the construction of an AFM scan from molecular and AFM dynamics simulations. The two inset amplitude-distance curves illustrate how the measured height is obtained for each scan point at an amplitude set-point of 15.4 nm. The resulting AFM cross-sectional height is given relative to the average tip separation from the bare SiO_2 surface. The horizontal axis corresponds to the scan points shown in Figure 2.2. For comparison, the cross section from experimental data (1.7 p. 22) has been overlaid on the same scale with its center point arbitrarily positioned to match up with the center of the simulated cross section.

The construction of tip-sample interaction force curves through MD simulations of large finite systems underestimates the long-range attractive forces present in the system. This is because the calculation of nonbonded interaction energies between pairs of atoms is generally limited to a cutoff radius on the order of 1 nm or less to reduce the cost of the computation (the number of nonbonded interactions, which scales with the square of the number of atoms in the simulation, can account for over 90% of the computation costs of a typical system). Underestimating the long-range attractive forces, and hence the region of positive force gradient, can alter the predicted regions of amplitude bistability.[137] However, at the free oscillation amplitude employed here ($A_0 = 39$nm, Table 2.1), the average force will be determined almost exclusively by the repulsive part of the tip-sample interaction potential,[135] and thus the underestimation of the attractive contribution has negligible influence on the simulated topographic profile.

Under ambient conditions, a thin film of water is adsorbed on hydrophilic surfaces such as SiO_2. The formation of a meniscus or liquid bridge between the surface and the probe will result in an additional attractive capillary force that depends on probe-sample distance.[137] We did not include the effects of adsorbed water in our model. We do not expect that inclusion of these effects will significantly change the nanoscale interactions between the probe and sample nanotubes predicted by the simulations. Future work will address this issue.

Simple models of AFM resolution assume that the probe is a rigid, incompressible cylinder with a flat or hemispherical end. In practice this is not the case. High-magnification TEM images show that the ends of the probe nanotubes are generally open due to ablation from the electrical etching procedure used to shorten the

nanotube probes to useful length.[78,118] Purely geometric arguments suggest that an open-ended tube with protruding asperities could, for extremely low-relief samples, potentially provide resolution comparable to the asperity diameter rather than the full diameter of the probe, in direct analogy to ultra-high resolution results published using silicon probes.[6] However, probe asperities are unlikely to be important when imaging a sample nanotube that has a diameter comparable to that of the probe nanotube.

The Youngs moduli of single-wall carbon nanotubes are $\approx 10^{12}$ Pa along the tube axis.[98] Due to this very high stiffness, only a small amount of longitudinal compression of the tube occurs during AFM imaging. However, published results have shown that SWNT probes are susceptible to bending due to their high aspect ratio if not oriented vertically relative to a surface.[130] Image artifacts from bending can be minimized by shortening the nanotube probe so that it protrudes less than 100 nm beyond the supporting silicon tip.

Although SWNTs have exceptional longitudinal stiffness, radially they are far more compliant, a characteristic that permits localized deformation of the nanotube walls.[98] The likelihood of deformation is further increased due to the structural discontinuity at the opened end of the nanotube probe. The susceptibility of nanotubes to radial deformation is predicated upon two competing effects: the energy cost associated with strain of the nanotube as it is deformed from its equilibrium cylindrical geometry, and the stabilization that a compressed nanotube gains due to increased interlayer van der Waals attractions. These two competing effects scale in opposite directions with increased nanotube diameter, such that larger SWNTs are easier to deform radially than smaller diameter tubes. We have previously observed

that SWNTs attached to silicon AFM tips via the 'pick-up' method tend to be 3–5 nm, which is larger than the tubes observed lying prone upon the pick-up substrate (1–3 nm, Figure. 1.2, p. 15).[1] We postulated that the increase in net binding energy with larger diameter nanotubes stems from the interplay between van der Waals forces and the geometric stiffness of a nanotube. The resulting radial compliance of these larger nanotubes not only increases the energy with which they bind to a silicon probe during pick-up but also has significant implications when they are subsequently used for AFM imaging.

Our MD simulations show lateral slipping of the probe nanotube relative to the sample nanotube, due both to bending along the length of the probe and to localized radial deformation of the probe and sample at the point of contact, as shown in Figure 2.4 (p. 55). This behavior is a function of the structures and relative orientations of the probe and sample nanotubes, the applied tip-sample force, and the lateral position (in the $x-y$ plane) of the probe nanotube relative to the sample nanotube. The smaller the lateral distance between the center of the probe tube and the axis of the sample tube, the larger the force required to deform the nanotubes and cause them to slip past one another. That is, when the probe presses on the edge of the sample nanotube, a smaller amount of force is required to cause it to slip laterally than when it presses on the crown of the sample nanotube. The simulations show this deformation behavior to be completely reversible and elastic. Experimentally, the elasticity is demonstrated by the fact that we have not observed the topographic cross sections to change significantly during imaging at a given amplitude set-point, and the TEM images taken of each probe after AFM imaging show no alterations of the nanotube structure, such as kinks or buckles.

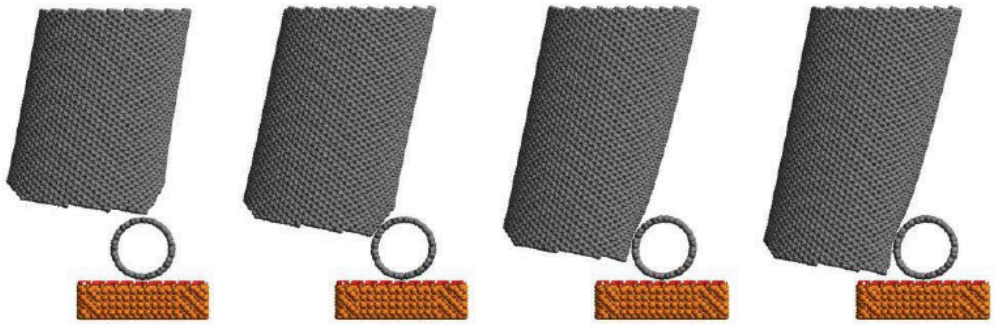

Figure 2.4: Illustration of the slipping phenomenon of the SWNT probe past the SWNT sample for scan point 3. Both bending along the length of the probe and local deformation contribute to slipping. The picture shows that the simulated probe is more susceptible to deformation, although the sample nanotube does deform slightly. This is due to the larger diameter of the probe (5.4 vs 2.2 nm) and the fact that its end is opened, which decreases its radial rigidity.

This lateral slipping and deformation of the probe nanotube explains the observation of sub-probe-diameter effective resolution. In amplitude-feedback AFM, modulation of the cantilever oscillation amplitude depends on the average strength of the tip-sample forces.[138] As discussed in Section 1.1.1 (p. 4) the AFM controller adjusts the extension of the $\hat{\boldsymbol{z}}$ piezoelectric actuator in order to hold the amplitude of the cantilever oscillation at the fixed value designated by the amplitude set-point, an independent variable set by the user. The resulting z-piezo voltage corrections are converted to units of length and output as the topographic height data. If the probe and sample deform negligibly under the associated tapping forces, the sample height can be measured accurately to within the precision of the piezoelectric element, typically $\lesssim$ 1Å. However, if either material is significantly deformable, the resultant height data represents a more complex convolution of probe and sample structure.

The simulations conducted here indicate that when the probe SWNT is tapping on an edge of the sample SWNT, the subsequent repulsive forces deform both nanotubes sufficiently to allow them to slip past one another without significantly influencing the cantilever oscillation amplitude. In fact, when the very edges of the probe and sample tubes come into contact, the net tip-sample force is actually *attractive* rather than repulsive, due to the large area of favorable contact between the graphitic surfaces. This is illustrated in the force curves for scan points 2 and 10 by the fact that the net force is negative between the two local minima, corresponding to the region in which the probe and the sample slide past one another. Once lateral slipping takes place, the resulting tip-sample interaction is dominated by the repulsive forces between the probe SWNT and the Si/SiO_2 surface. Thus, for that particular (x, y) position, the AFM controller does not 'see' the sample nanotube. Only when the probe SWNT is positioned closer to the crown of the prone sample SWNT are the interaction forces between the probe and sample nanotubes high enough to cause sufficient damping of the cantilever oscillation amplitude. At scan point 7 (fig. 2.2), which corresponds to the probe tapping on the crown of the sample nanotube, no slipping can take place under the imaging conditions given in Table 2.1 because the maximum tip-sample repulsive force does not exceed the necessary threshold of ≈ 30nN. Here, the cantilever amplitude is damped by the sample nanotube and the AFM records the interaction. The net result is that the topographic data indicates an apparent nanotube width that is smaller than the sum of the probe and sample SWNT diameters.

A quantitative representation of this phenomenon is illustrated in Figure 2.3 (p. 51). The lower half of the figure shows the effective cross section of a sample nanotube, calculated from the MD and AFM dynamics simulations, obtained when

a SWNT probe is used under the repulsive tapping conditions given in Table 2.1. This scan shows two important features that are also observed experimentally. First, the apparent probe resolution for this simulation is 2.0 nm, 37% of the probe diameter. Additionally, the simulated cross section is asymmetric, which is a direct consequence of the specific SWNT probe geometry, particularly the tilt angle, that favors probe-sample slipping more on one side of the sample than on the other.

In contrast, MD simulations have shown that a conventional silicon probe does not slip under the same imaging conditions. This is because the rigidity of the silicon probe requires higher forces to induce deformation, while the larger radius of curvature of the probe tip actually generates smaller lateral forces compared to a SWNT probe. Additionally, the different behavior is also due to the chemical properties of crystalline silicon, which strongly influence the surface-surface interactions with the SWNT sample, as well as the attractive van der Waals forces between the larger silicon tip and the silicon surface. These two interaction parameters in particular, probe compressibility and adhesion forces, are transformed in a highly nonlinear way by the response of the oscillating tip.[141] Thus, SWNT probes perform in a fundamentally different manner than silicon probes, not merely when imaging prone carbon nanotubes but for a variety of samples.

Because previous reports have described nanotube probes in the 1–3 nm diameter range,[78,95,99] we have also simulated a smaller diameter SWNT probe. Smaller diameter nanotube probes should be far less susceptible to localized radial deformation, due to their increased resistance against compression (as seen with the sample nanotube in Figure 2.4, p. 55). However, the bending mode along the length of a thinner probe is actually softer, since the flexural rigidity scales as r^4.[82] The probe was a

(16, 16) armchair SWNT (2.2 nm diameter, 20 nm length) that had approximately the same aspect ratio as the larger 5.4 nm probe used in this study. As before, the probe nanotube was oriented at 15° relative to the surface normal and the sample nanotube was 2.2 nm in diameter and 10 nm in length. Images from the simulation (not shown) indicate that slipping also occurs for the thinner probe when tapping on the edge of the sample nanotube. For this probe, the slipping is almost entirely due to bending and not to local sidewall deformation. The corresponding tip-sample force curve indicates that the force opposing the slipping motion of the probe was negligible.

Previous reports have indicated that a conventional silicon AFM probe will vertically compress a 1.4 nm single-wall nanotube lying on a flat surface as a function of driving amplitude in repulsive regime imaging, resulting in decreased apparent height.[49] This experimental observation is consistent with previously reported experimental measurements and molecular dynamics simulations, which described radial deformation of 1–3 nm single-wall carbon nanotubes by both van der Waals forces and external static loads.[41] Here we have shown that in amplitude-feedback AFM, the associated forces deform the *probe* nanotube in addition to the sample nanotube, strongly influencing the subsequently measured effective lateral resolution.

Our molecular dynamics simulations confirm that some vertical compression of a prone sample nanotube occurs under standard amplitude-feedback AFM conditions, for both conventional silicon AFM probes and SWNT probes. However the simulations predict that this effect is, at most, 10% of the sample tube diameter for 1–3 nm SWNTs and occurs primarily when the probe nanotube is positioned over the crown of the sample nanotube (e.g., scan point 7 in Figure 2.2). This corre-

sponds well with our experimental calibration of sample tube compression under the amplitude-feedback operating parameters employed. The enhanced lateral resolution, on the other hand, is due to the highly localized deformation and bending of the probe nanotube along the *edges* of the sample nanotube, and is therefore not affected significantly by vertical compression.

2.3.5 Summary

By correlating experimental data with atomistic molecular dynamics simulations, we have characterized how the unique properties of SWNT AFM probes can strongly influence topographic imaging fidelity. Probe bending and mutual local deformation of both the probe and sample nanotubes under typical amplitude-feedback AFM forces results in a reduction of the measured width of the sample tube, and consequently an ostensive improvement of the lateral resolution, to the extent that the resolution can appear to be better than expected from the measured diameter of the nanotube probe. We are interested in determining whether a similar improvement of apparent resolution is observed when imaging less compliant samples of different material composition, such as metallic or semiconducting nanoparticles.

Given the interest in nanoscale physical and biological phenomena, SWNT probes are likely to evolve into a more common research tool. A complete understanding of probe behavior in the context of atomic force microscopy is therefore critical. It is important to note that the lateral resolution reported here is an apparent value, arising from the simplified definition set forth in Section 2.1, and was studied for the specific case of 4–6 nm diameter open-ended SWNT probes imaging 2–3 nm diameter SWNTs adsorbed on a flat surface. In practice, the structural resolving power of

an AFM probe is dependent upon the experimental context. It is of particular importance to determine whether the observed deformation phenomenon results in a net gain or loss of structural information when SWNT probes are used to image soft nanoscale samples, such as biological macromolecules. The improvement in the apparent resolution due to deformation of the probe and sample nanotubes in this study was a consequence of the relatively high driving forces applied to the AFM cantilever. Amplitude-feedback AFM imaging performed in this repulsive regime with conventional probes has been shown to damage biomolecules.[134] In addition, resolution less than the probe diameter could complicate interpretation of AFM images quantitatively.

The combination of probe structure determination, characterization of imaging resolution, and simulated dynamic behavior described here has highlighted practical differences between carbon nanotube probes and conventional silicon probes. This work also underscores the usefulness of atomistic simulations in describing the dynamic nanoscale interactions involved in scanning probe microscopy.

Chapter 3

Construction of a Multichannel Scanning Confocal Microscope with Single-Photon Sensitivity for Fluorescence Correlation Spectroscopy and Imaging of Macromolecules

Abstract

This chapter begins with a brief a review of contemporary fluorescence microscopy as it pertains to single-molecule imaging. The following section presents a rigorous formalism for epifluorescence microscopy using high-numerical-aperture optics for both the focus of a coherent excitation source and the collection of fluorescent emission. This chapter includes a theory-based optical analysis of the confocal probe volume structure and photoluminescence collection efficiency from 3D-polarized single-dipole emitters. The latter analysis was aided by introducing a modified Jones formalism using non-square matrix representation for polarization state changes in

the specific context of confocal optics. Proper calculation of the expected confocal probe volume dimensions was essential for accurately interpreting experimental data in the following chapter. Additionally, the quantitative understanding that followed from analysis of 3D polarization state measurement by orthogonally polarized detection channels was critical to both the interpretation of experimental data and the numerical generation of simulated data in Chapter 5. The chapter concludes with a description of the components and free-space construction of a customizable multichannel scanning confocal microscope with single-photon sensitivity for fluorescence fluctuation spectroscopy and imaging of individual fluorophores.

Associated Publication

'In the Laboratory': Single Molecule Fluorescence Observation and Analysis. **(Manuscript in review)**[188]

3.1 Fluorescence Microscopy

Fluorescence microscopy is one of the most powerful analytic tools in contemporary biology, chemistry and biophysics.[189,190] The ready availability of solid-state laser excitation sources, sharp-cutoff spectral bandpass filters and room-temperature phototedectors with single-photon sensitivity have made data collection from individual tagged enzymes, signaling proteins, nucleic acids and other biological nanomachinery commonplace.[191–195] Confocal optics, evanescent field excitation,[196–210] laser trapping,[211–218] and near-field optical scanning tools,[219,220] have extended the spatial resolution of optical microscopy to distances well below 100nm. Label-free optical detection of single molecules has also been demonstrated by surface-enhanced

Raman scattering[221–223] and surface adhesion within a high-Q photonic microcavity resonator.[224] It is now possible to integrate numerous fully-optical single-molecule manipulation and observation techniques onto a single microscopy platform, including differential interference contrast, temporal and image correlation spectroscopy, through-objective and external prism-based evanescent excitation, and dynamic holographic optical trapping.[225–228] Recent studies have also combined additional non-optical tools such as atomic force microscopy, nanomechanical resonators and magnetic tweezers with optical microscopy systems to yield additional dimensions of measurement and manipulation to current single-molecule experiments.[229–232]

3.1.1 Single Molecule Fluorescence

Observation and manipulation of single molecules, whether by optical methods or otherwise, is in itself a powerful scientific tool, not merely by representing sensitivity at the smallest level of material structure, but also because it reveals both static and dynamic population information that is otherwise inherently lost via ensemble averaging in bulk measurements. For example, time series analysis of a single two-state fluorescence system will produce the probability distribution function for 'on times' and 'off times', a measurement that cannot be determined by bulk experiments.[233,234] In a pair of recent reports, laser-induced interconversion between dark and bright states in a single defect center of a diamond crystal have measured the distribution of non-equilibrium work functions and transient violations of the second law of thermodynamics, the latter phenomenon of which is reconciled with classical statistical mechanics by time- and population-averaging.[235,236]

Single-molecule experiments on proteins using endogenous fluorescent cofactors, genetically-encoded fluorescent peptide fusions or synthetically conjugated dyes has expanded the scope of enzymology to the observation of individual biochemical reaction steps and structural changes.[237–242] Among the wide array of published specific single-molecule investigations are real-time measurements of topoisomerase activity,[243] RNA folding and catalytic function,[244,245] binding of DNA by RecA,[246,247] Rep helicase,[248] and Staphylococcal nuclease,[195] RNA polymerase enzymatic action,[249,250] protein folding,[251–253] dynamics of nucleic acid Holladay Junctions,[254–256] hairpin ribozyme function and folding,[257–259] SNARE-complex formation,[260] F_0F_1-ATP synthase catalytic action,[261,262] ribosomal RNA binding,[263] cooperative Cadherin binding,[264] and numerous studies of nucleic acid structural fluctuations.[265–272]

3.1.2 Challenges in Single Molecule Fluorescence Microscopy

All of the above fluorescence microscopy investigations hold in common a handful of unifying challenges present in many single-molecule experiments. Foremost among these is the separation, discrimination and quantification of an extremely small optical signal in the presence of enormous background sources. It is not sufficient to possess sensitive light measurement tool capable of single-photon detection if all the tool has to measure is glaring background. In many instances the background source is not physically or spectrally separable from the desired signal, as is case with both endogenous intracellular autofluorescence and inelastic Raman scattering induced by the excitation light. Every individual fluorophore possesses a maximum rate of photoluminescence excitation/decay cycling, placing an upper bound on its inherent brightness, while in contrast the background noise level is potentially unlimited. All optical single-molecule experiments are therefore restricted to a maximum practical

signal strength.

A second prominent challenge is signal granularity introduced by performing state measurements via an inherently quantized transmission source: collected photons.[273] This statistical 'photon shot noise' represents a fundamental limitation in all optical single-molecule experiments by placing a lower bound on the useful minimum signal strength.[274] Additional issues in single molecule fluorescence experiments include potential sample contamination by invisibly small amounts of undesired material, competing non-equilibrium photoinduced processes such as inter-system crossing to nonradiative triplet-states, and the irreversible destruction of fluorophores by excitation-induced photobleaching.

Most experimental tools, methods and innovations specific to single-molecule fluorescence have evolved to directly address the challenges described above. Confocal optics, evanescent-field excitation, high-collection-efficiency objective lenses, steep-bandpass spectral filters and photonic waveguides all seek to increase the desired photon signal and reduce the unwanted background. Effectively utilizing the roles many of these tools play in facilitating single-molecule microscopy begins with a comprehensive understanding of optical microscopy.

3.2 Fundamentals of Optical Microscopy

3.2.1 Focusing Electromagnetic Radiation

The electromagnetic field arriving from a spectrally pure infinitely-distant radiation point source takes the form of an infinite **plane wave** of uniform intensity. Assuming the plane wave to have amplitude $\mathcal{E}_o$, temporal frequency ω, spatial frequency

ν, and propagation direction $\vec{\boldsymbol{k}} = (k_x\hat{\boldsymbol{x}} + k_y\hat{\boldsymbol{y}} + k_z\hat{\boldsymbol{z}})$, the wave function $\psi(\vec{\boldsymbol{r}}, t)$ describing its time-dependece at a location $\vec{r}$ in 3-space is then:

$$\begin{aligned}\psi(\vec{\boldsymbol{r}}, t) &= \mathcal{E}_o e^{i\left(\omega t - \nu\left\langle\vec{\boldsymbol{r}},\vec{\boldsymbol{k}}\right\rangle\right)} \\ &= \mathcal{E}_o e^{-i(\omega t - \nu(k_x x + k_y y + k_z z))}\end{aligned} \tag{3.1}$$

Without loss of generality, we can orient the coordinate axes of our Cartesian coordinate system so that $\vec{\boldsymbol{k}}$ is aligned with the z-axis of the laboratory reference frame. The wave function describing the propagation of this plane wave then simplifies to:

$$\psi(z, t) = \mathcal{E}_o e^{-i(\omega t - \nu k_z z)} \tag{3.2}$$

and for additional clarity we will generally use the scalar value $k = \nu\langle\vec{\boldsymbol{k}}, \hat{\boldsymbol{z}}\rangle$ to implicitly indicate the component and spatial frequency of $\vec{\boldsymbol{k}}$ aligned with the reference frame z-axis. Then the wave function is simply $\psi(z, t) = \mathcal{E}_o e^{-i(\omega t - kz)}$ (or ψ_z in shorthand notation).

Consider the scenario illustrated in Figure 3.1 (p. 67), in which an opaque infinite barrier of negligible thickness $\boldsymbol{\sigma}_0$ is coincident with the $z = 0$ plane ($\boldsymbol{\sigma_0}$) of the reference axes, and contains a single opening $\boldsymbol{\mathcal{A}}$ defined by the arbitrary parametric closed curve $f_{\mathcal{A}}(x) + g_{\mathcal{A}}(y) + c_{\mathcal{A}} = 0$. A plane wave propagating parallel to the z-axis, $\psi(z, t)$, incident upon $\boldsymbol{\sigma}_0$ will transmit a fraction of the light through the opening $\boldsymbol{\mathcal{A}}$ to the other side of the barrier. This set of diffracted waves $\left\{\psi_{\mathcal{A}}\right\}$ generates in an interference pattern $\mathcal{I}(\rho, \phi, +\infty)$ convergent upon an infinitely distant image plane $\boldsymbol{\sigma}_{+\boldsymbol{\infty}}$. At a point (x, y, z) in the $z > 0$ half space, for which $r = (x^2 + y^2 + z^2)^{\frac{1}{2}}$ is large compared to the dimensions of $\boldsymbol{\mathcal{A}}$, the resulting electromagnetic field intensity

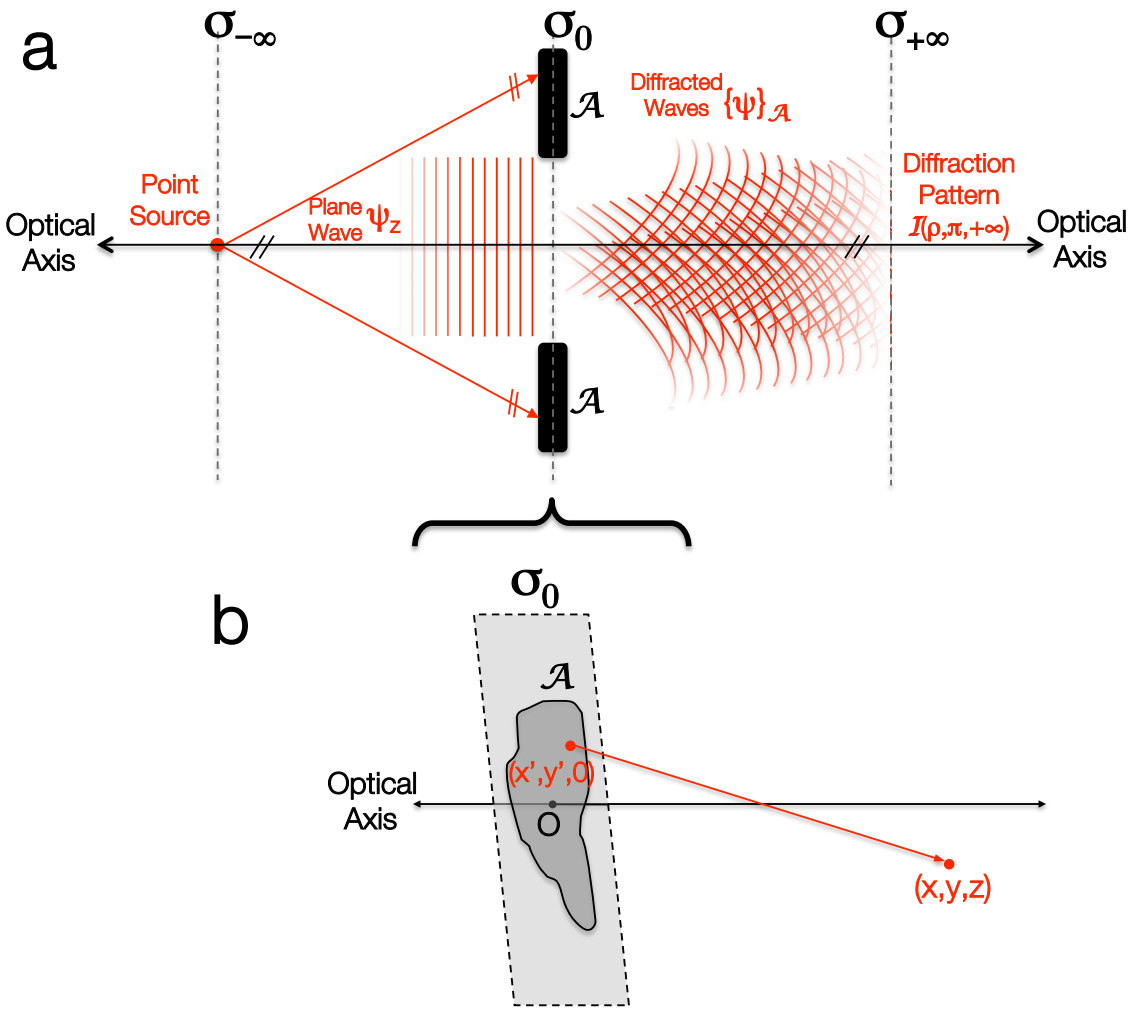

Figure 3.1: Diffraction of a plane wave $\psi(z,t) = \mathcal{E}_o e^{-i(\omega t - kz)}$ arising from an infinitely-distant point source located on $\boldsymbol{\sigma_{-\infty}}$ by the aperture $\boldsymbol{\mathcal{A}}$ in $\boldsymbol{\sigma_0}$. **(a)**: The wave incident upon $\boldsymbol{\sigma}_0$ will transmit a fraction of the light through $\boldsymbol{\mathcal{A}}$ to the other side of the barrier. This set of diffracted waves $\{\psi\}_{\mathcal{A}}$ generates an interference pattern $\mathcal{I}(\rho,\phi,+\infty)$ convergent upon an infinitely distant image plane $\boldsymbol{\sigma_{+\infty}}$. **(b)**: The electromagnetic field $I_{\mathcal{E}}(x,y,z,t)$ at any point (x,y,z) in the $z > 0$ half space, for which $r = (x^2+y^2+z^2)^{\frac{1}{2}}$ is large compared to the dimensions of $\boldsymbol{\mathcal{A}}$, may be calculated by integral convolution of incident radiation arriving from all point sources $(x',y',0)$ in $\boldsymbol{\mathcal{A}}$ using equation 3.3.

$I_{\mathcal{E}}(x, y, z, t)$ can be calculated by integral convolution of incident radiation arriving from all point sources $(x', y', 0)$ (Figure 3.1b) within the closed curve $f_{\mathcal{A}}(x') + g_{\mathcal{A}}(y') + c_{\mathcal{A}} = 0$ describing $\boldsymbol{\mathcal{A}}$:

$$I_{\mathcal{E}}(x, y, z, t) = \epsilon_{\mathcal{A}} \frac{e^{-i(\omega t - kr)}}{r} \iint_{\mathcal{A}} dx'\, dy' e^{\left(\frac{ik\langle [x,y],[x'y'] \rangle}{r}\right)} \tag{3.3}$$

where $r = (x^2 + y^2 + z^2)^{1/2}$ and $\epsilon_{\mathcal{A}}$ is the electromagnetic field amplitude of ψ_z at $\boldsymbol{\sigma}_0$, assumed (for the time being) to be spatially uniform across the opening $\boldsymbol{\mathcal{A}}$.

The **irradiance** $\mathcal{I}(x, y, z)$ represents the time-invariant optical energy associated with the oscillating electromagnetic field $I_{\mathcal{E}}(x, y, z, t)$, calculated from:

$$\begin{aligned} \mathcal{I}(x, y, z) &= \frac{1}{2} I_{\mathcal{E}}(x, y, z, t) \cdot I^*_{\mathcal{E}}(x, y, z, t) \\ &= \left\langle \left(Real\left(I_{\mathcal{E}}(x, y, z, t) \right) \right)^2 \right\rangle \end{aligned} \tag{3.4}$$

In nearly all real-world experimental cases we can consider opening $\boldsymbol{\mathcal{A}}$ to be a **circular aperture** of radius $r_{\mathcal{A}}$, an assumption that greatly simplifies the integral term in equation 3.3. Casting the system in cylindrical coordinates (ρ, ϕ, z) we can as before, without loss of generality, locate the origin $O = (0, \phi, 0)$ at the center of aperture $\boldsymbol{\mathcal{A}}_{circ}$ and define z as the **optical axis**, parallel to the direction of ψ_z propagation ($\vec{\boldsymbol{k}}$) as in Figure 3.2 (p. 70). Equation 3.3 then simplifies to:

$$I_{\mathcal{E}}(\rho, \phi, z, t) = \epsilon_{\mathcal{A}} \frac{e^{-i(\omega t - kD)}}{D} \int_{\rho'=0}^{a} \rho' d\rho' \int_{\phi'=0}^{2\pi} d\phi' e^{i\left(\frac{k\rho' \rho \cos \phi'}{D}\right)} \tag{3.5}$$

where $D = (\rho^2 + z^2)^{1/2}$ and $\epsilon_{\mathcal{A}}$ is the uniform amplitude of ψ_z across $\boldsymbol{\mathcal{A}}_{circ}$ as before.

Equation 3.5 describes a radially symmetric diffraction pattern convergent upon an infinitely distant image plane $\boldsymbol{\sigma}_{+\infty}$. As illustrated in Figure 3.2 (p. 70), placing a circular lens $\boldsymbol{\mathcal{L}}_f$ of negligible thickness and focal length f inside circular aperture $\boldsymbol{\mathcal{A}}_{circ}$ transforms the plane wave ψ_z incident on the aperture into a converging partial spherical wave ψ_f, thereby focusing the transmitted light onto a plane $\boldsymbol{\sigma}_f$ at a finite distance f from the aperture (Figure 3.2a). This plane is also referred to as the **image plane**, $\boldsymbol{\sigma}_{\mathcal{I}}$.

The irradiance intensity pattern $\boldsymbol{\mathcal{I}}$ formed at $\boldsymbol{\sigma}_f$ consists of the integral convolution of individual every electromagnetic wave function $\psi_{\mathcal{A}}$ originating from a point $P = (\rho, \phi)$ inside $\boldsymbol{\mathcal{A}}$, $\big((\rho_P, \phi_P, 0)$ in cylindrical coordinates$\big)$and propagating to a point Q in $\boldsymbol{\sigma}_f$, $\big((\rho_Q, \phi_Q, f)$ in cylindrical coordinates$\big)$, as shown in Figure 3.2b. The path length $L_Q(P)$ of ψ_A between P and Q is given by:

$$\begin{aligned} L_Q(P) &= L(\rho_P, \phi_P, \rho_Q, \phi_Q) \\ &= \sqrt{(\rho_P \cos\phi_P - \rho_Q \cos\phi_Q)^2 + (\rho_P \sin\phi_P - \rho_Q \sin\phi_Q)^2 + f^2}\,. \end{aligned} \tag{3.6}$$

Each path-length $L_Q(P)$ contains $L(\rho_P, \phi_P, \rho_Q, \phi_Q)\omega/c$ wavelengths λ of the monochromatic radiation, λ being the spatial frequency inverse ν^{-1} (or k^{-1}). If the path lengths $L_Q(P)$ and $L_Q(P')$ from two different points $\big\{P = (x, y), P' = (x', y') \in \boldsymbol{\mathcal{A}}\big\}$, to the same point (ρ_Q, ϕ_Q) in image $\boldsymbol{\mathcal{I}}$ fulfill the condition $\big\{\Delta L_Q = L_Q(P) - L_Q(P') = \pm N\lambda : N \in \mathbb{Z}\big\}$, the result is **constructive wave interference** and consequently bright irradiance at (ρ_Q, ϕ_Q). Correspondingly, if $\Delta L_Q = (\pm N + \frac{1}{2})\lambda$ the result is **destructive interference** and net absence of irradiance. Intermediate values for ΔL_Q yield intermediate degrees of interference and intermediate irradiance at Q. Therefore the intensity profile $\mathcal{I}(\rho, \phi)$ forming image $\boldsymbol{\mathcal{I}}$ in optical system consists of

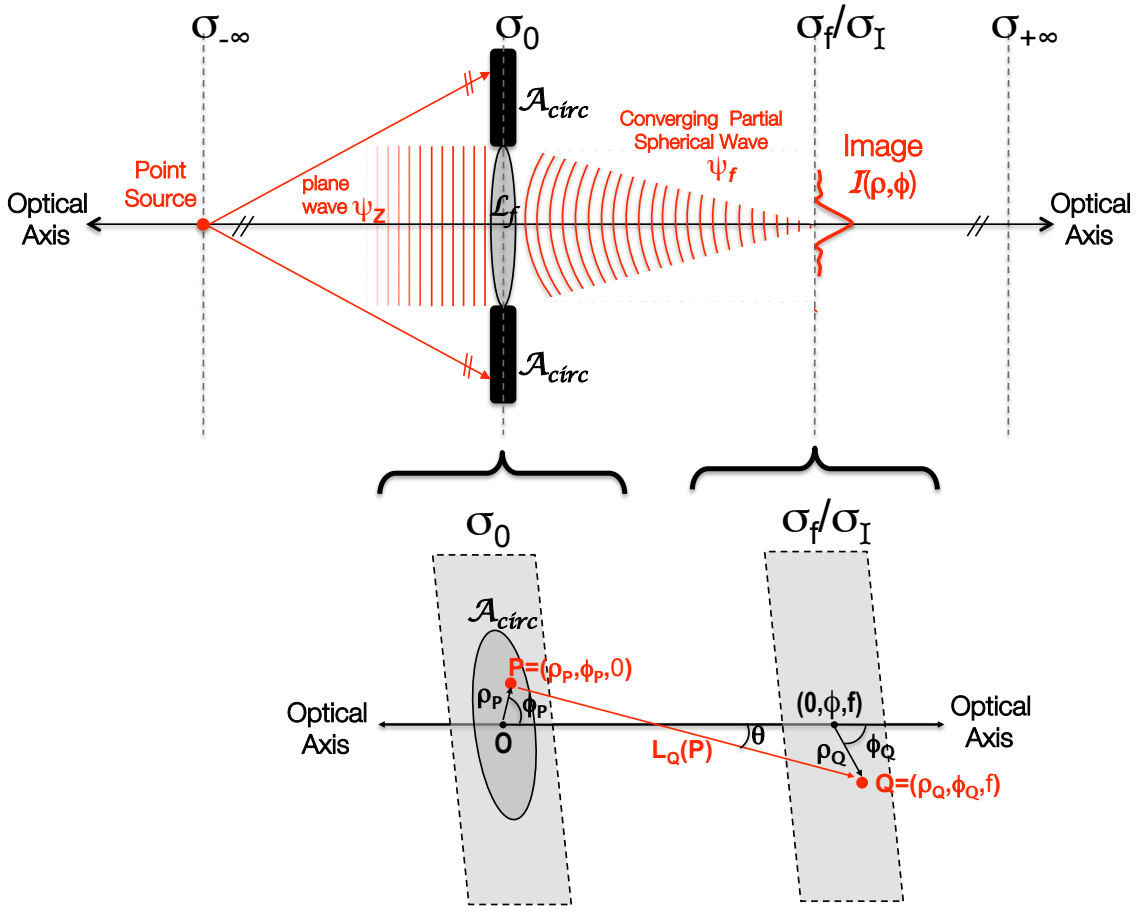

Figure 3.2: **(a)**: A simple system for focusing a plane wave $\psi(z,t) = \mathcal{E}_o e^{-i(\omega t - kz)}$ incident upon a circular aperture $\boldsymbol{\mathcal{A}}_{circ}$ using a lens of focal length f. The resulting focused wave ψ_f is a converging partial spherical wavefront that forms a diffraction pattern on the image plane $\boldsymbol{\sigma_f}$. The converging partial spherical wavefront is equivalent to a set of individual wave functions propagating from points in $\boldsymbol{\mathcal{A}}$: $\psi_f \equiv \{\psi\}_{\mathcal{A}}$ **(b)**: The path length $L_Q(P)$ of all individual component wave functions $\psi \in \{\psi\}_{\mathcal{A}}$ between any point P in $\boldsymbol{\mathcal{A}}_{circ}$ and any point Q in $\boldsymbol{\sigma_f}$ is given by equation 3.6. The resulting image $\mathcal{I}(\rho,\phi)$ formed at $\boldsymbol{\sigma_f}$ may be determined using equations 3.5 and 3.4 to calculate the irradiance intensity distribution in $\boldsymbol{\sigma_f}$.

a pattern of bright and dark regions determined by the net radiation from all points in $\boldsymbol{\mathcal{A}}$ projected by $\boldsymbol{\mathcal{L}}_f$ onto $\boldsymbol{\sigma}_f$.

For each point (ρ_Q, ϕ_Q) in the image plane $\boldsymbol{\sigma}_f$ there corresponds a set of all *pairs* of points $\{P, P'\}$ selected from $\boldsymbol{\mathcal{A}}$ which satisfy the condition $\{L(P) - L(P') = \pm N\lambda\}$ and yield bright irradiance. This set $\mathcal{S}^+(Q) \subset \{\boldsymbol{\mathcal{A}} \times \boldsymbol{\mathcal{A}}\}$ is defined by:

$$\mathcal{S}^+(Q) \equiv \Big\{(P, P') : L(\rho, \phi, \rho_Q, \phi_Q) - L(\rho', \phi', \rho_Q, \phi_Q) = \pm N\lambda; N \in \mathbb{Z}; \forall\,(P, P') \in \boldsymbol{\mathcal{A}}\Big\}$$

$$\equiv \Big\{\{(\rho, \phi), (\rho', \phi')\} : \big[(\rho\cos\phi - \rho_Q\cos\phi_Q)^2 + (\rho\sin\phi - \rho_Q\sin\phi_Q)^2 + f^2\big]^{\frac{1}{2}}$$
$$- \big[(\rho'\cos\phi' - \rho_Q\cos\phi_Q)^2 + (\rho'\sin\phi' - \rho_Q\sin\phi_Q)^2 + f^2\big]^{\frac{1}{2}} = \pm N\lambda;$$
$$N \in \mathbb{Z}; \forall\{(\rho, \phi), (\rho', \phi')\} \in \boldsymbol{\mathcal{A}}\Big\}. \tag{3.7}$$

Because point pairs are chosen according to their path length *differences*, the set $\mathcal{S}^+(Q)$ can also be thought of as corresponding to a characteristic **spatial frequency** $\omega(Q)$ across $\boldsymbol{\sigma_0}$ that gives rise to bright irradiance at point Q. The diffractive pattern transmitted with lens $\boldsymbol{\mathcal{L}}_f$ in place is nearly equivalent to that for the aperture $\boldsymbol{\mathcal{A}}$ alone, the key alteration being the *removal* of spatial frequency components $\omega(Q)$ of ψ_z at plane $\boldsymbol{\sigma_0}$ that are *below* a frequency threshold. This threshold value is determined by the dimensions of $\boldsymbol{\mathcal{A}}$, which also governs the range of angles (relative to the optical axis $\hat{\boldsymbol{z}}$) that $\boldsymbol{\mathcal{L}_f}$ is capable of focusing onto the image plane, with the remaining below-threshold spatial frequency components of ψ_z discarded. The angular range $0 \leq \theta \leq \phi_{max}$ (Figure 3.2b) exerts a strong influence over the resulting image formed at $\boldsymbol{\sigma}_f$, as will be discussed in greater detail beginning on page 81. A similar set of all point pairs yielding absence of irradiance at point Q, $\mathcal{S}^-(Q)$ can be constructed by substituting $(N + \frac{1}{2})$ for N in equation 3.7.

This concept of $\boldsymbol{\mathcal{L}}_f$ mapping spatial frequency at $\boldsymbol{\sigma}_0$ to spatial intensity at $\boldsymbol{\sigma}_f$ is illustrated more clearly by returning to a Cartesian coordinate reference system with $\hat{\boldsymbol{z}}$ aligned with the propagation direction of ψ_z and $\boldsymbol{\mathcal{A}}$ and $\boldsymbol{\mathcal{L}}_f$ in the $z = 0$ plane. For all points $\{P = (x, y), P' = (x', y') \in \boldsymbol{\mathcal{A}}\}$ and $\{Q = (x_Q, y_Q) \in \boldsymbol{\sigma}_f\}$, equations 3.8 and 3.9 correspond to 3.6 and 3.7 used to calculate ΔL_Q in cylindrical coordinates:

$$L_Q(P) = L(x, y, x_Q, y_Q) = \left[(x - x_Q)^2 + (y - y_Q)^2 + f^2\right]^{\frac{1}{2}} \tag{3.8}$$

$$\begin{aligned}\mathcal{S}^+(Q) &\equiv \left\{(P, P') : L(x, y, x_Q, y_Q) - L(x', y', x_Q, y_Q) = \pm N\lambda; N \in \mathbb{Z}; (P, P') \in \boldsymbol{\mathcal{A}}\right\} \\ &\equiv \Bigg\{ \left\{(x, y), (x', y')\right\} : \sqrt{(x - x_Q)^2 + (y - y_Q)^2 + f^2} \\ &\qquad \sqrt{(x' - x_Q)^2 + (y' - y_Q)^2 + f^2} = \pm N\lambda; N \in \mathbb{Z}, \\ &\qquad \forall\{(x, y), (x', y')\} \in \boldsymbol{\mathcal{A}} \Bigg\}. \end{aligned} \tag{3.9}$$

In addition to length $L_Q(P)$ (equation 3.8), each path between a radiation point source $P \in \boldsymbol{\mathcal{A}}$ and a focal point $Q \in \boldsymbol{\sigma}_f$ also possesses a characteristic angle θ relative to optical axis $\hat{\boldsymbol{z}}$. Calling the corresponding value for a second point (P') θ', the path length difference $\Delta L_Q = L(x, y) - L(x', y')$ can then be estimated closely from focal length f of lens $\boldsymbol{\mathcal{L}}_f$ and the angular difference ($\Delta\theta = \theta - \theta'$): $\Delta L_Q = f\Delta\theta$. Inversely, $\Delta\theta$ may be calculated from the 2D distance ΔP between points P and P' in plane $\boldsymbol{\sigma}_0$. The overall result is that for each point $Q \in \boldsymbol{\sigma_f}$ the path length difference between any two points in $\boldsymbol{\mathcal{A}}$ is a function of the focal length and the point separation: $\Delta L_Q = f\Delta P$.

We can derive this relationship easily by utilizing several simplifying approximations, based upon the condition $\left\{\{(x-x'),(y-y')\} \ll f; \forall \{(x,y),(x',y')\} \in \mathcal{A}\right\}$ which follows from the original requirement that the dimensions of the aperture be small relative to the focal length of the lens.

Continuing in Cartesian coordinates, the path length $L_Q(P)$ is determined from:

$$L_Q(P) = \left[(x_Q - x)^2 + (y_Q - y)^2 + f^2\right]^{\frac{1}{2}} \tag{3.10}$$

$$= f\left[1 + \frac{x^2+y^2}{f^2} - 2\frac{xx_Q + yy_Q}{f^2}\right]^{\frac{1}{2}} \tag{3.11}$$

$$\approx f\left[1 - 2\frac{xx_Q + yy_Q}{f^2}\right]^{\frac{1}{2}} \tag{3.12}$$

with elimination of the $(x^2+y^2)/f^2$ term being valid because $(x^2+y^2) \ll f^2$. Binomial expansion of equation 3.12, discarding the higher order terms then yields:

$$L_Q(P) \approx f\left(1 - \frac{xx_Q + yy_Q}{f^2}\right). \tag{3.13}$$

Similarly, for the second point source P':

$$L_Q(P') \approx f\left(1 - \frac{x'x_Q + y'y_Q}{f^2}\right). \tag{3.14}$$

from which we can now calculate the path length difference ΔL_Q:

$$\begin{aligned}\Delta L_Q &= L_Q(P) - L_Q(P') \\ &= L - L' \\ &= \frac{x_Q(x' - x) + y_Q(y' - y)}{f}\,. \end{aligned} \tag{3.15}$$

The consequence of equation 3.15 is that for each point $(x_Q, y_Q, f) \in \boldsymbol{\sigma}_f$, constructive interference and consequently bright irradiance occurs if:

$$x_Q(x' - x) + y_Q(y' - y) = fN\lambda; N \in \mathbb{Z}\,. \tag{3.16}$$

Similarly, destructive interference with corresponding absence of irradiance occurs if:

$$x_Q(x' - x) + y_Q(y' - y) = f(N + \frac{1}{2})\lambda; N \in \mathbb{Z}\,. \tag{3.17}$$

In our Cartesian coordinate system, however, x and y correspond to independent and orthogonal vector component values. Given point $P = (x, y)$, the vector from the origin to P is $\vec{\boldsymbol{P}} = \left(x\hat{\boldsymbol{x}} + y\hat{\boldsymbol{y}}\right)$. Given a second point $P' = (x', y')$ the vector from P to P' is $\vec{\boldsymbol{P'P}} = \left((x - x')\,\hat{\boldsymbol{x}} + ((y - y')\,\hat{\boldsymbol{y}}\right)$. If we hold the y terms in equations 3.16 and 3.17 constant under the condition $y_Q(y' - y) = fN\lambda$ (i.e. the $\hat{\boldsymbol{y}}$-component of $\vec{\boldsymbol{P'P}}$ is zero), and also maintain the requirement $(y' - y) \ll f$, then we can construct alternative simplified definitions for $\mathcal{S}^+(Q)$ and $\mathcal{S}^-(Q)$ dependent *solely* upon the x

coordinate in $\boldsymbol{\sigma}_0$:

$$\mathcal{S}^{+}_{\boldsymbol{x}}(Q) \equiv \left\{(x,x') : x - x' = \frac{fN\lambda}{x_Q}; \forall N \in \mathbb{Z}\right\}$$
$$\mathcal{S}^{-}_{\boldsymbol{x}}(Q) \equiv \left\{(x,x') : x - x' = \frac{f(N+\frac{1}{2})\lambda}{x_Q}; \forall N \in \mathbb{Z}\right\}.$$

Similarly, holding the x terms in equations 3.16 and 3.17 constant under the conditions $x_Q(x'-x) = fN\lambda$ and $(x-x') \ll f$ yields:

$$\mathcal{S}^{+}_{\boldsymbol{y}}(Q) \equiv \left\{(y,y') : y - y' = \frac{fN\lambda}{y_Q}; \forall N \in \mathbb{Z}\right\}$$
$$\mathcal{S}^{-}_{\boldsymbol{y}}(Q) \equiv \left\{(y,y') : y - y' = \frac{f(N+\frac{1}{2})\lambda}{y_Q}; \forall N \in \mathbb{Z}\right\}.$$

We can now come to several important conclusions regarding the nature of the image $\mathcal{I}(x,y)$ formed at the lens focal plane $\boldsymbol{\sigma}_f$ by transformation of wavefuntion ψ_z via the $\boldsymbol{\mathcal{L}}_f/\boldsymbol{\mathcal{A}}$ system. The radiation pattern depends upon both the 2D spatial frequency of radiation point sources in $\boldsymbol{\mathcal{A}}$ and the focal length f. Up to now we have assumed that the electromagnetic wave amplitude of ψ_z at plane $\boldsymbol{\sigma}_0$ has constant value ϵ_A across the entire aperture. However, because calculating the net irradiance at $\boldsymbol{\sigma}_f$ now corresponds to transformation of spatial frequency across $\boldsymbol{\sigma}_0$, we can permit the radiation amplitude to vary according to a spatial mapping $\{\epsilon : P \mapsto \epsilon(P); \forall P = (x,y,z) \in \boldsymbol{\sigma}_0\}$. The effect of the aperture $\boldsymbol{\mathcal{A}}$ is to mask $\epsilon(x,y,z)$ so that the mapping function becomes $\{\epsilon : P \mapsto 0; \forall P = (x,y,z) \notin \boldsymbol{\mathcal{A}}\}$. Additionally, since $\boldsymbol{\sigma}_0$ constrains the z value to 0, the intensity map is essentially two dimensional:

$$\epsilon : (x,y) \mapsto \epsilon_{\mathcal{A}}(x,y) \in \mathbb{R}; \forall (x,y) \in \boldsymbol{\sigma_0}\,. \tag{3.18}$$

The process by which lens-aperture system $\boldsymbol{\mathcal{L}}_f/\boldsymbol{\mathcal{A}}$ focuses ψ_z onto $\boldsymbol{\sigma}_f$ can therefore be thought of as a two-dimensional Fourier transform of $\epsilon_{\mathcal{A}}(x,y)$. In Cartesian coordinates $\{P=(x_P,y_P,0)\,;Q=(x_Q,y_Q,f)\}$, given a spatial mapping (equation 3.18) describing the the electromagnetic radiation intensity of ψ_z across $\boldsymbol{\mathcal{A}}$, the electromagnetic radiation intensity $I_{\mathcal{E}}(x_Q,y_Q)$ for all points $(x_Q,y_Q)\in\boldsymbol{\sigma}_f$ may be calculated from the functional mapping $\mathcal{F}_{Cart.}$:

$$\mathcal{F}_{Cart.}\colon\{Q,\boldsymbol{\mathcal{A}}\}\mapsto\iint_{\boldsymbol{\mathcal{A}}}\epsilon_{\mathcal{A}}(P)e^{-2\pi i\frac{\lambda}{f}\langle P,Q\rangle}d\mathcal{A} \tag{3.19}$$

where $\langle\rangle$ denotes vector dot product and the differential area element is $d\mathcal{A}=dx\cdot dy$ In cylindrical coordinates the most significant difference is the the differential area element $d\mathcal{A}=\rho\cdot d\rho\cdot d\phi$ and the nature of the vector dot product $\langle\rangle$, which for the planar 2-vectors $\{P=(\rho_P,\phi_P)\,;Q=(\rho_Q,\phi_Q)\}$ will be:

$$\langle P,Q\rangle=\rho_P\rho_Q\cos\left(\phi_P-\phi_Q\right)\,. \tag{3.20}$$

The radiation intensity $I_{\mathcal{E}}(\rho_Q,\phi_Q)$ for all points $(\rho_Q,\phi_Q)\in\boldsymbol{\sigma}_f$ may then be calculated using the functional mapping $\mathcal{F}_{Cyl.}$:

$$\mathcal{F}_{Cyl.}\colon\{Q,\mathcal{A}\}\mapsto\frac{1}{2\pi}\iint_{\boldsymbol{\mathcal{A}}}\epsilon_{\mathcal{A}}(\rho_P,\phi_P)e^{-i\frac{\lambda}{f}\rho_P\rho_Q\cos(\phi_P-\phi_Q)}d\mathcal{A}\,. \tag{3.21}$$

Notably, the functional mapping of equation 3.21 does *not* represent an ordinary two-dimensional Fourier transform. Regardless of the coordinate system, however, the irradiance $\mathcal{I}(Q)$ in $\boldsymbol{\sigma}_f$ is then calculated from:

$$\mathcal{I}(Q)=\frac{1}{2}\left(Real\Big[\mathcal{F}\{Q,\boldsymbol{\mathcal{A}}\}\Big]\right)^2\,. \tag{3.22}$$

In the context of this optical system (Figure 3.2), the most pertinent aspect of equations 3.19 and 3.21 is the range over which the double integral is performed, determined by the aperture. For arbitrarily shaped apertures $\boldsymbol{\mathcal{A}}$, neither equation 3.19 nor equation 3.21 will be straightforward or have an analytical solution. Fortunately, knowing that $I_{\mathcal{E}}(Q)$ is determined by Fourier transformation of the radiation intensity spatial frequency across $\boldsymbol{\mathcal{A}}$ provides an important insight into the $\boldsymbol{\mathcal{L}_f/\mathcal{A}}$ system. The dimensions of aperture $\boldsymbol{\mathcal{A}}$ relative to the wavelength λ place a *lower* bound on the spatial frequency range that lens $\boldsymbol{\mathcal{L}}_f$ transforms to generate image $\boldsymbol{\mathcal{I}}$. The smaller the smaller the dimensions of $\boldsymbol{\mathcal{A}}$ (or the larger the value of λ), the more low-frequency terms are lost in performing the integral over the ρ range for $\boldsymbol{\mathcal{A}}$. As will be seen, the consequence of this truncation directly leads to the spatial resolution of the resulting image $\boldsymbol{\mathcal{I}}$.

Two additional important mathematical phenomena providing some insight into the optical transform in cylindrical coordinates are the complex exponential of the dot product (equation 3.20), the expansion of which is given in equation 3.23, and integrals taking the form of the radial/angular double integral in equation 3.21.

$$\begin{aligned} e^{i\langle P,Q\rangle} &= e^{i\cdot\left[\rho_P\rho_Q\cos\left(\phi_P-\phi_Q\right)\right]} \\ &= \sum_{n=-\infty}^{+\infty} i^n J_n\left(\rho_P\rho_Q\right)e^{in\left(\phi_P-\phi_Q\right)} \end{aligned} \tag{3.23}$$

$$J_n(x) = \frac{i^{-n}}{2\pi}\int_{\phi=0}^{2\pi} e^{i(n\phi+x\cos\phi)}d\phi \tag{3.24}$$

where equation 3.24 is the Bessel function of order n. Additionally, the generalized form of the double integral in functional mapping $\mathcal{F}_{Cyl.}$ (equation 3.21) represents

a Fourier series of the angle variable ϕ and a Hankel transform of order n ($\mathcal{H}_n$, equation 3.25) of the radial variable ρ:

$$\mathcal{H}_n \colon \{\rho, f\} \mapsto \int_0^\infty f(\rho) J_n(x\rho)\, \rho\, d\rho \tag{3.25}$$

The Hankel transform, not coincidentally, is also formulated in terms of the Bessel function $J_n(x\rho)$ (equation 3.24).[275]

Additional simplification of the optical system depicted in Figure 3.2 is still necessary to identify an analytical solution for the 2D intensity distribution $\boldsymbol{\mathcal{I}}$ on the focal plane $\boldsymbol{\sigma_f}$. First, consider the simplified but experimentally realistic imaging system in which ψ_z is a perfectly collimated laser illumination source with wavelength λ, uniform beam intensity ϵ_{obj}, and beam diameter larger than the aperture. The lens/aperture pair $\boldsymbol{\mathcal{A}}/\boldsymbol{\mathcal{L}}$ is an infinity-corrected microscope objective oriented parallel to optical axis z with front focal length f_{obj}, front aperture radius r_{obj} and the aperture located at $z = 0$. This complete image formation system $\{\psi, \boldsymbol{\mathcal{A}}, \boldsymbol{\mathcal{L}}\}$ has cylindrical symmetry, and we can conclude that image $\boldsymbol{\mathcal{I}}$ at $z = f_{obj}$ will have radial symmetry. It is therefore reasonable to return to a cylindrical coordinate system (ρ, ϕ, z) and assume $\boldsymbol{\mathcal{I}} = \mathcal{I}(\rho)$.

Using 3.21 to determine the diffraction image $\boldsymbol{\mathcal{I}}$ generated by the objective, the radiation amplitude function $\epsilon(\rho)$ is simply a constant ϵ_{obj} for all values of $\rho \leq r_{obj}$. Since ϵ_{obj} has no dependence upon ϕ, we can declare $\phi_P = 0$ to simplify the double

integral, which then becomes:

$$\begin{aligned}\mathcal{I}(\rho) &= \frac{I_{\mathcal{E}}(t,\rho)\cdot I_{\mathcal{E}}(t,\rho)^{*}}{2} \\ &= \frac{1}{2}\Big[Real\Big(\epsilon_{obj}\frac{1}{2\pi}\int_{\rho'=0}^{r_{obj}}\rho' d\rho'\int_{\phi'=0}^{2\pi} d\phi' e^{-i\frac{\lambda}{f}\rho\rho'\cos\phi}\Big)\Big]^{2}. \qquad (3.26)\end{aligned}$$

The solution to the double integral in equation 3.26 takes the form of a first-order Bessel function of ρ scaled by the factor $\left(\frac{r_{obj}}{\lambda f_{obj}}\right)$:

$$\mathcal{I}(\rho) = \left[\frac{2\pi\epsilon_{obj}r_{obj}}{\lambda\rho}J_1\left(\frac{\rho r_{obj}}{\lambda f_{obj}}\right)\right]^{2} \qquad (3.27)$$

$$= \mathcal{I}(0)\left[\frac{J_1(x)}{x}\right]^{2} \qquad (3.28)$$

Equations 3.27 and 3.27 for the irradiance $\mathcal{I}(\rho)$ at the focal plane $\boldsymbol{\sigma}_f$ describe a radially symmetric pattern of concentric rings of decreasing intensity surrounding a bright central spot called the **Airy disk**, as shown in Figure 3.3. The Airy disk has a radius determined by the smallest value of ρ for which $J_1\left(\frac{2\pi\rho r_{obj}}{\lambda f_{obj}}\right) = 0$, which occurs when $\left(\frac{\pi\rho r_{obj}}{\lambda f_{obj}}\right)$=3.83. The radius of this disk, defined as an Airy unit, is therefore $\frac{3.83}{\pi}\frac{\lambda f_{obj}}{r_{obj}} = .61\left(\frac{\lambda f_{obj}}{r_{obj}}\right)$.

The integral performed over ρ' in equation 3.26 can also be thought of as an integral over the full angular range of paths $0 < \theta < \phi_{max}$ (relative to the optical axis) between every point $P \in \boldsymbol{\mathcal{A}}$ and a specified point $Q \in \boldsymbol{\sigma}_f$. As long as we maintain the conditions that $r_{\mathcal{A}} \ll f$, quantitatively the only necessary change to equation 3.26 is the substitution $\theta = \rho/f$ (and $d\theta = d\rho/f$). For microscope objectives, ϕ_{max} is

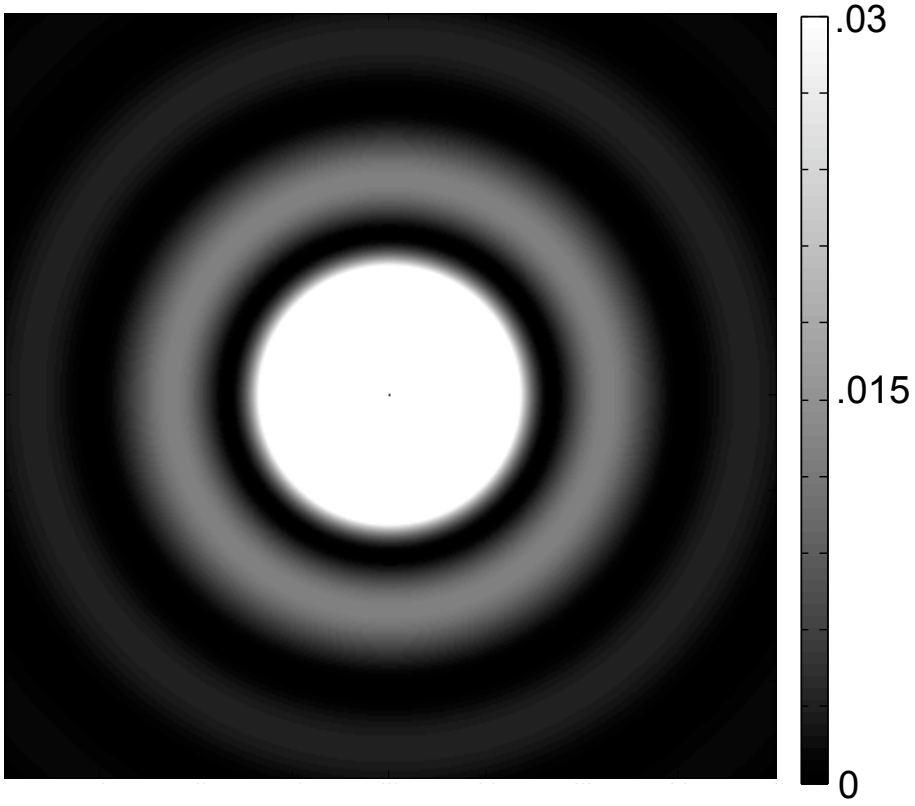

Figure 3.3: Radially symmetric irradiance pattern $\mathcal{I}(\rho/\frac{\lambda}{\pi NA})$ (equation 3.27) resulting from diffraction of a uniform plane wave by a circular aperture (as in Figure 3.2). Irradiance intensity has been scaled to highlight the first and second ring maxima surrounding the central spot, which occur at $\rho = \{5.14, 8.42\} \cdot \left(\frac{\lambda}{\pi NA}\right)$ with intensity values $\{.0175, .0042\} \cdot \mathcal{I}(0)$, respectively. The lateral range of the image is $\pm 3\pi$. The bright central spot represents the **Airy disk**. The numerical aperture NA is defined according to equation 3.29.

governed by an important figure of merit, the numerical aperture (NA):

$$NA = n_0 \sin \phi_{max} \tag{3.29}$$

which, for $\phi_{max} \ll 1$ may be approximated by:

$$NA \approx \left(\frac{n_0 r_{obj}}{f_{obj}} \right)$$

where n_0 is the refractive index of the surrounding medium, and f_{obj} and r_{obj} are the focal length and radius of the objective lens, respectively. Using this parameter, the diameter of the Airy disk (3.3) is $1.22\lambda/NA$.

Of important consequence in confocal microscopy, particularly for determining the confocal observation volume dimensions and subsequent correlation traces in fluorescence correlation spectroscopy (discussed extensively in chapter 4) is the fact that the Fourier transform of a Gaussian function yields a Gaussian function with variance inversely proportional to the variance of the original Gaussian function. This important conclusion based on this fact is that a cylindrical non-divergernt beam having a radially symmetric Gaussian intensity profile will produce a 2D point spread function also having a radially symmetric Gaussian irradiance distribution, in contrast to the multiple-minima diffraction pattern produced by a uniform beam (Figure 3.3).

3.2.2 2D Point Spread Function and Lateral Optical Resolution

The image $\mathcal{I}(\rho)$ (Figure 3.3) formed by diffraction of a uniform plane wave through aperture $\boldsymbol{\mathcal{A}}$, focused by lens $\boldsymbol{\mathcal{L}}_f$ also describes the 2D **point spread function (*psf*)** of the $\boldsymbol{\mathcal{A}}/\boldsymbol{\mathcal{L}}_f$ optical system. The processes of focusing of a monochromatic plane wave wave ψ_z to a diffraction-limited point in $\boldsymbol{\sigma}_{\mathcal{I}}$ and collection of radiation emitted from a point source in $\boldsymbol{\sigma}_{\mathcal{I}}$ by a microscope objective lens $\mathcal{L}_{obj}$ are functionally equivalent procedures. This is because the wave function paths between $\boldsymbol{\sigma}_f$ and $\boldsymbol{\sigma}_i$ are irrespective of the direction of wave propagation.

The equivalence of focus and collection processes is illustrated in particular clarity by modern 'infinity-corrected' fluorescence microscopy systems. Figure 3.4 illustrates an epifluorescence microscopy scheme utilizing an 'infinity-corrected' objective lens, $\mathcal{L}_{obj}$. Each lens in the system, $\mathcal{L}_{obj}$, $\mathcal{L}_{tel}$, and $\mathcal{L}_{tube}$ performs equivalent complementary transformations: 1.) Transformation of a point source into a collimated beam (a partial plane wavefront). 2.) Transformation of a collimated beam into a point spread function. Each transformation corresponds to a spatial-frequency Fourier transform (equations 3.19 and 3.21), with transformation 2 being the inverse of transformation 1.

Within the 'infinity space' of the system ($\boldsymbol{S}_{\boldsymbol{\infty}}$ and $\boldsymbol{S}'_{\boldsymbol{\infty}}$), all wave functions passing through a single focal point in the sample plane $\boldsymbol{\sigma}_{sample}$ are plane waves with zero divergence. The laser excitation pathway (discussed in experimental detail in Section 3.3) includes a spatial filter pinhole P_{sf} in plane $\boldsymbol{\sigma}_{sf}$, as well as a beam expansion telescope with final lens $\mathcal{L}_{tel}$ of focal length f_{tel}. $\mathcal{L}_{tel}$ transforms the divergent partial

spherical wavefront emerging from point P_{sf} into a collimated beam with diameter d_{ex}. The beam passes through a dichroic beamsplitter in the infinity space $\boldsymbol{S}_{+\infty}$ is cropped by the back aperture $\mathcal{A}_{back}$ of the objective. $\mathcal{L}_{obj}$ subsequently focused the beam to a diffraction-limited point spread function at point P_{focus} in $\boldsymbol{\sigma}_{sample}$ at focal distance f_{obj} from $\mathcal{L}_{obj}$.

In the inverse process, emission from the point P_{focus} is transformed by $\mathcal{L}_{obj}$ into a collimated beam with a diameter equal to that of the back aperture $\mathcal{A}_{back}$. In the infinity space the emission beam reflects off the primary dichroic and is then focused to a point spread function at point P_{img} in image plane $\boldsymbol{\sigma}_{img}$ by a tube lens $\mathcal{L}_{tube}$ having focal length f_{tube}. Signal collection is subsequently affected by detection system that measures the irradiance intensity at P_{img}.

In the microscopy system shown in Figure 3.4, $\boldsymbol{\sigma}_{sf}, \boldsymbol{\sigma}_{sample}$, and $\boldsymbol{\sigma}_{img}$ are conjugate focal planes; a image generated at one plane can be projected by the system into an image at one of the other planes, taking into consideration the spectral selectivity of the dichroic beamsplitter mirror. The points P_{sf}, P_{sample}, and P_{img} are conjugate focal points; a true point source at one of these points will be transformed into a point spread function at the other points, again accounting for the spectral selectivity of the dichroic mirror. The magnifying power of each plane relative to the others is determined by the ratio of the lens focal lengths. The excitation pathway magnification is f_{tel}/f_{obj}, and the magnification of the emission pathway is f_{tube}/f_{obj}. Due to the non-divergent nature of both excitation and emission beam paths between $\mathcal{L}_{obj}$, $\mathcal{L}_{tel}$, and $\mathcal{L}_{tube}$, additional planar optical elements (such as filters or polarization wave-plates) can be added to the infinity spaces $\boldsymbol{S}_{\infty}$ and $\boldsymbol{S}'_{\infty}$ without altering the positions of conjugate focal planes or equivalent points.

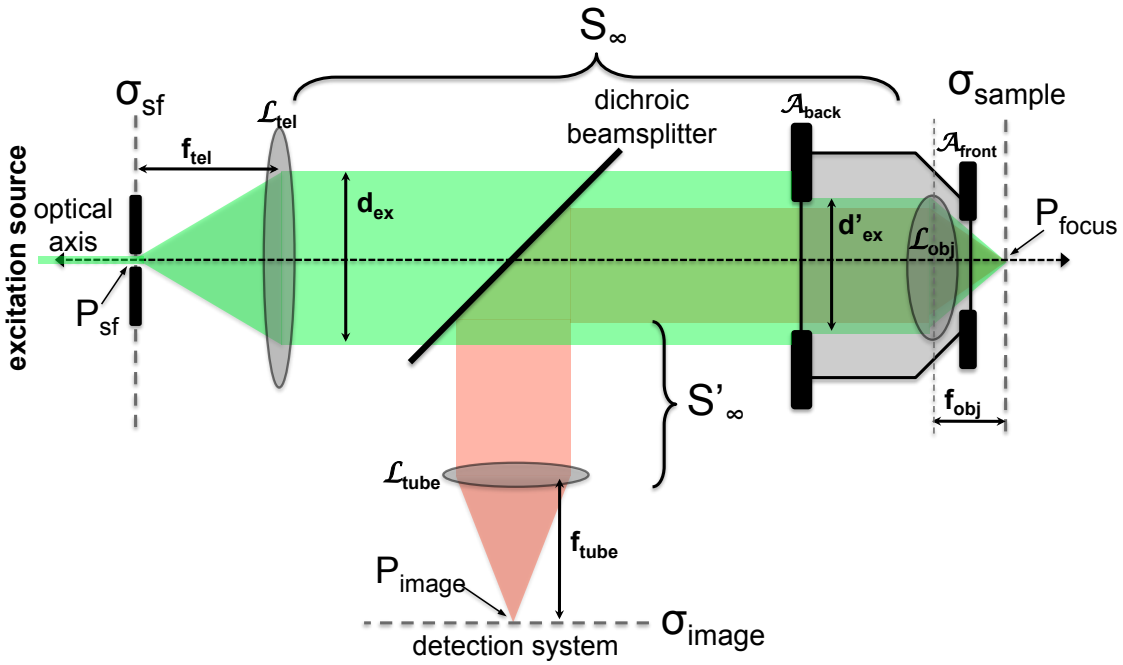

Figure 3.4: Focus of a collimated laser excitation source (green) and collection of emitted fluorescence (red) by the same 'infinity corrected' objective lens ($\mathcal{L}_{obj}$) in an epifluorescence microscopy system. The laser excitation source passes through a spatial filter with pinhole P_{sf} (discussed in Section 3.3) into a beam expansion telescope having a second lens $\mathcal{L}_{tel}$ of focal length f_{tel} to yield a collimated beam with diameter d_{ex}. The beam path between $\mathcal{L}_{tel}$ and $\mathcal{L}_{obj}$ constitutes the 'infinity space' $\boldsymbol{S_\infty}$, with a complementary space, $\boldsymbol{S'_\infty}$, corresponding to the path of the collimated emission beam between the dichroic beamsplitter and tube lens $\mathcal{L}_{tube}$. The collimated excitation beam passes through the high-pass dichroic beamsplitter and is cropped by the back aperture of the objective, $\mathcal{A}_{back}$ to a diameter d'_{ex} before being focused by the objective lens $\mathcal{L}_{obj}$ with focal length f_{obj} to a point spread function at point P_{focus} in the sample plane $\boldsymbol{\sigma}_{sample}$. The optical signal emitted from point P_{focus} (red) is collected by the objective lens and transformed into a collimated beam with diameter d'_{ex}. The emission beam reflects off the dichroic beamsplitter, entering the complementary infinity space $\boldsymbol{S'_\infty}$, and is focused by lens $\mathcal{L}_{tube}$ of focal length f_{tube} into point spread function at P_{img} in the image plane $\boldsymbol{\sigma}_{img}$. Signal collection is subsequently undertaken by detection system that does not influence the illustrated optical pathway.

The *psf* represents both the 2D pattern formed at the focal plane $\boldsymbol{\sigma}_f$ by diffraction-limited focus of a uniform collimated laser beam (Figure 3.2a) as well as the pattern formed at the conjugate image plane $\boldsymbol{\sigma}_i$ by collection of optical signal using radiation wavelength λ_{obs} from a true point-source (an object with dimensions $d \ll \lambda_{obs}$). The *psf* also determines the spatial resolution limit for discriminating objects of identical intensity in the focal plane at a specified level of contrast (commonly 50%). The irradiance intensity, determined using equation 3.27), at the point exactly between a pair of point sources separated by distance d_{res} in the focal plane follows the function $2 \cdot \mathcal{I}(\frac{d_{res}}{2})$. Using a contrast criterion $0 < c < 1$, the two objects will be successfully resolved when the irradiance amplitude exactly between them is less than c times its maximum:

$$
\begin{aligned}
2 \cdot \mathcal{I}\left(\frac{d_{res}}{2}\right) &\leq c \cdot \left(\mathcal{I}(0) + \mathcal{I}\left(d_{res}\right)\right) \\
2 \cdot \mathcal{I}(0) \left[\frac{J_1\left(\frac{\pi N A d_{res}}{\lambda}\right)}{\left(\frac{\pi N A d_{res}}{\lambda}\right)}\right]^2 &\leq c \cdot \mathcal{I}(0) \left(1 + \left[\frac{J_1\left(\frac{2\pi N A d_{res}}{\lambda}\right)}{\left(\frac{2\pi N A d_{res}}{\lambda}\right)}\right]^2\right) \qquad (3.30) \\
\frac{2}{c} \cdot \left(\frac{J_1(x)}{x}\right)^2 &= \frac{1}{c}\left(1 + \left(\frac{J_1(2x)}{2x}\right)^2\right); d_{res} = \left(\frac{\lambda x}{\pi N A}\right). \qquad (3.31)
\end{aligned}
$$

Solving equation 3.30 by numerical methods yields the minimum point source spacing d_{res}versus the contrast criterion value c, as shown in Figure 3.6.

The point spread function of an imaging system is of practical relevance not merely for spatially resolving objects of sub-wavelength dimensions but also for accurately assessing the profile of larger objects. The variation of resolving power and the resulting image fidelity as a function of the NA of the optical system is illustrated in Figure 3.5 for an observation wavelength λ=500nm. At a low NA of 0.4 (Figure 3.5,

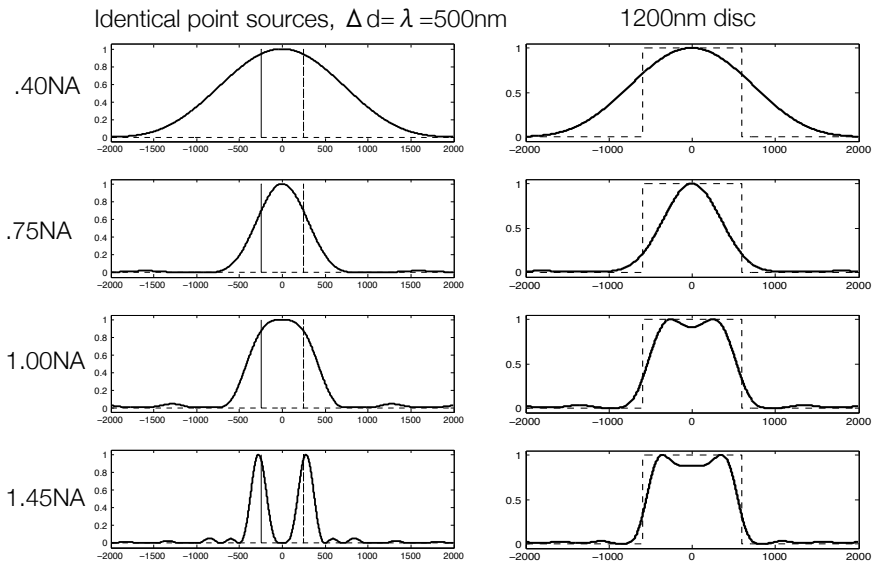

Figure 3.5: Radially symmetric irradiance intensity profile $\mathcal{I}(\rho)$ for two identical point sources separated by 500nm (left column) and for a single uniform-intensity 1200nm diameter disc (right column) at λ_{obs}=500nm and varying NA values

top row) two identical point sources 500nm apart are seen as a single broad *psf*, and a single 1200nm disc is not observed to have a uniform intensity profile. At high a NA of 1.45 (Figure 3.5, bottom row), the two points are easily resolved as separate objects even using the stringent contrast criterion $c > .9$, and the 1200nm disc appears to have a nearly uniform profile. The progressive resolution of two identical point sources is illustrated in Figure 3.7 as a function of separation using wavelength- and NA-normalized dimensionless units.

For conventional (non-confocal) optical imaging, d_{res} scales linearly with observation wavelength λ_{obs} and inversely with numerical aperture. Observation wavelength is often an independent parameter across the visible spectrum and into the near IR, 350nm$\lesssim \lambda_{obs} \lesssim$900nm, but may also be constrained tightly by experimental needs. The NA, however, is a function of the angular collection range $0 \leq \theta \leq \phi_{max}$ (equa-

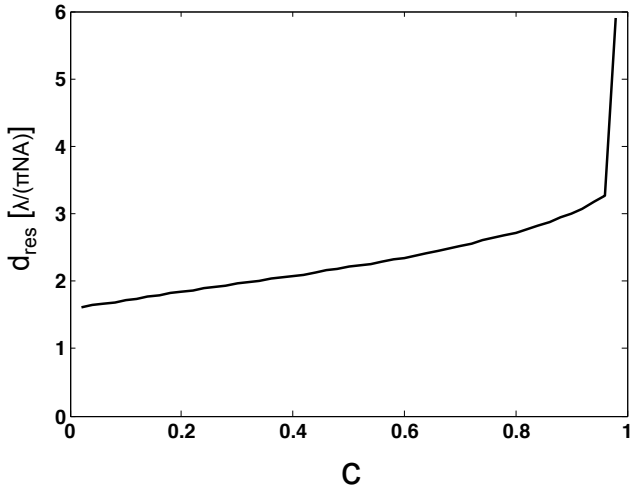

Figure 3.6: Minimum identical point source spacing d_{res} (in normalized dimensionless units $\rho \Big/ \left(\frac{\lambda}{\pi NA}\right)$ as a function of contrast criterion c. The slope discontinuity at $c \approx .98$ arises as a direct result of the secondary peak (the first ring-shaped local maximum) of the diffraction pattern (Figure 3.3).

tion 3.29), with $\sin(\phi_{max})$ constrained to ≤ 1. NA therefore has an upper bound determined by n_0. The refractive index for air is essentially unity, and so the highest NA possible for a light microscope having air situated between the objective lens and sample is 1.0. Dilute aqueous solutions have a refractive index of roughly 1.33, and so a light microscope using a water-immersion objective lens is limited to $NA \leq 1.33$. Most optical glasses have a refractive index of approximately 1.5, with borosilicate glass used to manufacture microscopy slides and coverslips commonly having $n_0 = 1.52$. Using a high-NA objective lens ($1.33 \leq NA \leq 1.52$) necessitates the use of an optical immersion oil with a refractive index $n_{oil} \geq NA$ in order to eliminate the presence of NA-limiting media such as air or water between the objective and sample. An index-matching oil ($n_{oil} = n_{glass}$) minimizes optical aberration and reflections introduced by refractive-index discontinuities. Microscope objectives

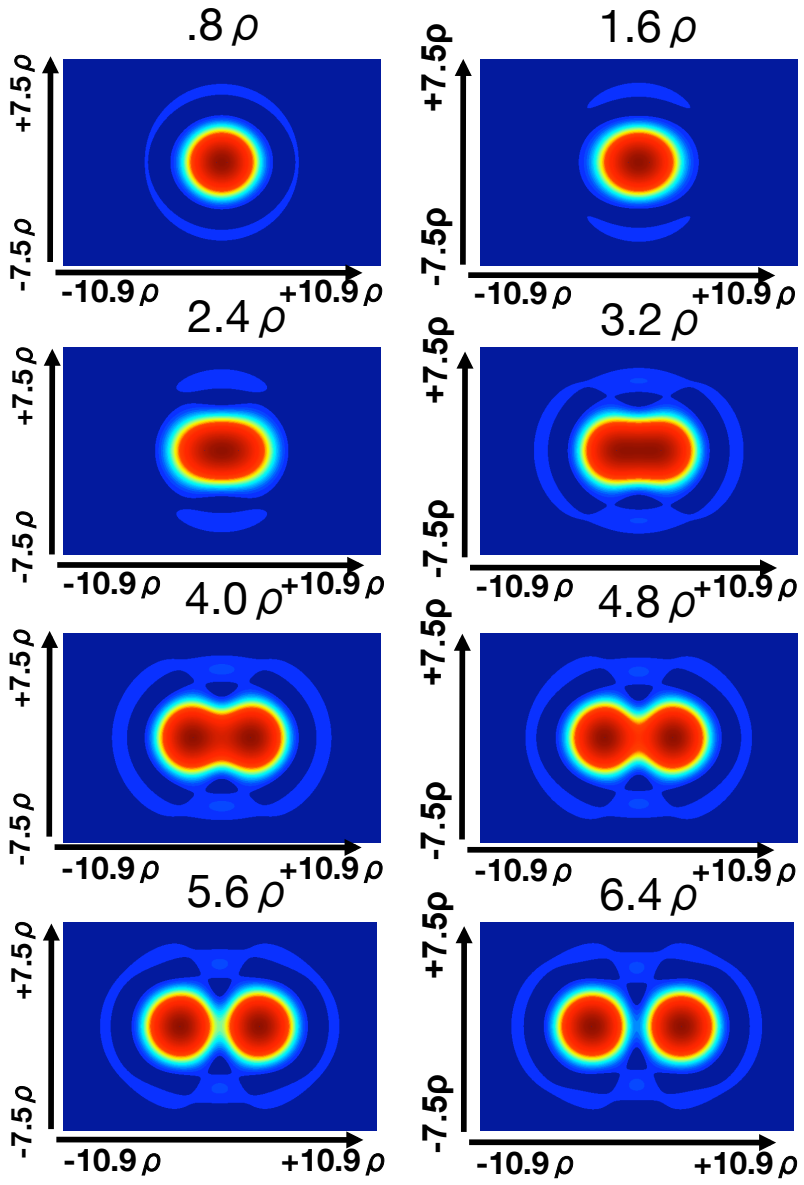

Figure 3.7: 2D irradiance intensity distribution for identical point sources separated by varying lateral spacing $\Delta d = 0.8 - 6.4$, in normalized dimensionless units $\rho \Big/ \left(\frac{\lambda}{\pi NA}\right)$, calculated using equation 3.27. Successful resolution with contrast criterion value $c = .5$ occurs for $\Delta d \approx \frac{4}{\pi}\frac{\lambda}{NA}$.

with numerical aperture values as high as 1.65 are available, but these necessitate the use of corresponding high-refractive-index sample windows (e.g., sapphire coverslips with $n_0 = 1.757$–1.779) and immersion liquids (e.g., diiodomethane immersion oil with n_{oil}=1.74) that are both expensive and more difficult to use than conventional materials.

3.2.3 Confocal Optics

Thus far we have only discussed the lateral profile and resolvability of the point spread function in the plane perpendicular to the optical axis. In almost all experimental instances, however, the sample under investigation has a significant 3-dimensional component, necessitating knowledge of the the depth of field or the *psf* profile and resolvability along the z axis for the optical system being used. As is the case for the lateral sample dimensions, the z-axial optical resolution of the microscope is directly proportional to the wavelength of light used, and also scales inversely (although not linearly) with the numerical aperture of the objective lens. In particular, as the desired resolving power progresses toward smaller and smaller dimensions, as is the case with single-molecule fluorescence microscopy and subcellular structural imaging, the need for high-NA optics with $n_o \sin \phi_{max} > 1$ vitiates the earlier assumption that $\frac{f_{obj}}{\mathcal{A}_{obj}} \ll 1$.

In addition to yielding improved spatial resolution, high-NA optics provide the essential feature of background reduction in single molecule fluorescence experiments. In contrast to samples with homogeneously distributed optical signal sources (such as those in a bulk fluorimeter), the signal collected from a single-molecule photon emitter does not scale with the observation volume. This is because the dimensions of

the emitter, typically 1-10nm, are much smaller than those of the optical point spread function, even in cases where the NA is high and the observation wavelength λ is at the blue end of the visible light spectrum. Background signal, however, usually arises principally from homogeneous sources, as is the case for inelastic photon scattering and autofluorescence from the sample medium, and therefore does scale linearly with the observation volume. In general the smaller this volume can be prepared the better the signal-to-background ratio of the collected data. High-NA objective lenses, in particular when combined with confocal optics or two-photon excitation, provide observation volumes on the scale of femotliters ($10^{-15} - 10^{-12}$ L) sufficient for single molecule experiments.

In the optical systems designed for single molecule microscopy, the mathematical simplifications used Section 3.2.2, which are reasonable approximations in the low-NA limit, become much less viable. Simultaneously, the need for accurate quantitative knowledge of the observation volume dimensions often arises, as in the case of fluorescence fluctuation microscopy. For optical systems with $n_o \sin \phi_{max} > 1$ calculation of the full 3D point spread function necessitates numerical methods. Fortunately, calculating the 3-dimensional *psf* for high-NA optical systems is rendered relatively facile by modern computational tools.

Using the model of a collimated laser beam focused by an objective lens, (Figure 3.4) we can continue to work in cylindrical coordinates (ρ, ϕ, z) because the optical system retains that symmetry irrespective of NA. However, instead of a 2D diffraction pattern (Figure 3.3), we now seek a 3D irradiance intensity function $\mathcal{I}(\rho, \phi, z)$ centered at the laser focus $(0, \phi, f)$.

A laborious and highly nontrivial derivation of the 3D wave function for a converging spherical electromagnetic wave has been provided by Born and Wolf.[276] The solution utilizes Lommel functions of the scaled dimensionless variables ζ and ρ in place of z and ρ. Lommel functions are infinite series of Bessel functions, a situation that follows directly from the Hankel transform component of the beam transformation in cylindrical coordinates (equations 3.23−3.25, p. 77) Following Born and Wolf's derivation, the 3D *psf* is given by:

$$\zeta = \left(\frac{2\pi NA^2}{n_o\lambda}\right) z$$

$$r = \left(\frac{2\pi NA}{\lambda}\right) \rho$$

the optical irradiance $\mathcal{I}(\zeta, r)$ at the objective lens focus is then given by equation 3.32.[276]

$$\mathcal{I}_{psf}(\zeta, r) = \mathcal{I}_{obj}\left(\frac{2\pi NA^2}{\lambda\zeta}\right)^2 \left\{ \left(\sum_{s=0}^{\infty} -1^s \left(\frac{\zeta}{r}\right)^{2s+1} J_{2s+1}(r)\right)^2 + \left(\sum_{s=0}^{\infty} -1^s \left(\frac{\zeta}{r}\right)^{2s+2} J_{2s+2}(r)\right)^2 \right\} \tag{3.32}$$

where I_{obj} is the total optical power exiting the objective.

R. H. Webb has provided an alternative equivalent expression (equation 3.33) using integral terms that are more amenable to rapid evaluation by high-level numerical

platforms such as Matlab.[277]

$$\mathcal{I}_{psf}(\zeta, r) = I_0(\zeta, r)I_0^*(\zeta, r) + I_1(\zeta, r)I_1^*(\zeta, r) + I_2(\zeta, r)I_2^*(\zeta, r) \tag{3.33}$$

$$I_0(\zeta, r) = \int_0^{\phi_{max}} J_0\left(\frac{r\sin\alpha}{\sin\phi_{max}}\right)\cos^{\frac{1}{2}}\alpha\sin\alpha\,(1+\cos\alpha)\,e^{\left(\frac{i\zeta\cos\alpha}{\sin^2\phi_{max}}\right)}d\alpha$$

$$I_1(\zeta, r) = \int_0^{\phi_{max}} J_0\left(\frac{r\sin\alpha}{\sin\phi_{max}}\right)\cos^{\frac{1}{2}}\alpha\sin^2\alpha e^{\frac{i\zeta\cos\alpha}{\sin^2\phi_{max}}}d\alpha$$

$$I_2(\zeta, r) = \int_0^{\phi_{max}} J_0\left(\frac{r\sin\alpha}{\sin\phi_{max}}\right)\cos^{\frac{1}{2}}\alpha\sin\alpha\,(1-\cos\alpha)\,e^{\frac{i\zeta\cos\alpha}{\sin^2\phi_{max}}}d\alpha\,.$$

Equation 3.33 was evaluated numerically in Matlab; a transcript of the code used is presented in the Appendix (A.2.1, p. 227). The resulting 3-dimensional point spread function is equivalent to equation 3.27 in the focal plane $\zeta = 0$. The 3-dimensional electromagnetic radiation amplitude is displayed versus the dimensionless parameters ζ and r (equations 3.32 and 3.32, respectively) for a $NA = 1.45$ objective lens in the top plot of Figure 3.8 (p. 95). The 3D irradiance intensity distribution point spread function is shown in the middle plot of Figure 3.8.

In a confocal optical setup, a pinhole corresponding to roughly 1–5 Airy units is located at the origin O' of the conjugate image plane $\boldsymbol{\sigma}_{img}$. The focusing of the collected irradiance at O' follows the same functional process as the focus of the incident irradiance at O. Therefore the resulting confocal point spread function is the 3D *convolution* of the original point spread function psf_0 and the pinhole: $psf_{conf} = \left\{psf_0 \otimes psf_{ph}\right\}$. For a pinhole of exactly 1 Airy unit, the confocal point spread function (shown for a $NA = 1.45$ objective lens in the bottom plot of Figure 3.8) is the square of the normalized conventional point spread function: $psf_{conf} = [psf_0]^2$.

The implications of this new *psf* are far-reaching and provide the indispensable foundation for all confocal microscopy. The electromagnetic field amplitude, conventional point spread function and confocal point spread function calculated from equation 3.33 are plotted versus the dimensionless parameters ζ and r (equations 3.32 and 3.32, respectively) for several numerical aperture values in Figure 3.9 (p. 96). In addition to scaling inversely in linear dimension with NA, the 3D *psf* shape also changes somewhat. The addition of a confocal pinhole results in a slight improvement in the lateral spatial resolution and a significant improvement in the axial spatial resolution. Notably, the axial (ζ) resolution has roughly double the dimensions of the lateral (ρ) resolution. Additionally, the background arising from the low-intensity but large-volume 'tails' of the conventional *psf* (the concentric rings in Figure 3.3, p. 80) are essentially eliminated. Analogously, the squared irradiance density-dependence of two-photon excitation processes also results in squaring of the original point spread function, with $\mathcal{I}_{2P} = [\mathcal{I}_{psf}]^2$. Combining two-photon excitation with confocal optics should in theory yield a point spread function equal to the cube of the original, $\mathcal{I}_{(2P,conf)} = [\mathcal{I}_{psf}]^3$, but this has not been reported in the literature.

The confocal observation volume, defined arbitrarily by the e^{-2} intensity contour surface of psf_{conf}, scales according to $\left(\frac{\lambda^3}{NA^4}\right)$, clearly highlighting the value of high-NA optics in single-molecule fluorescence microscopy. A $1.45NA$ objective lens provides nearly 4.5 times the signal-to-background of a $1.0NA$ lens. Under most imaging conditions the confocal point spread function can be approximated as a 3-dimensional Gaussian distribution having prolate ellipsoidal symmetry, with $\sigma_z \approx 2\sigma\rho$, instead of the complex density distributions shown in Figure 3.8. This approximation is essential for calculating the expected diffusional correlation function in fluorescence correlation spectroscopy, discussed in detail in Section 4.3.2 (p. 152).

3.2.4 Polarization in Optical Microscopy

Thus far we have not considered the effects of optical polarization on the excitation or emission processes in confocal fluorescence microscopy. In many experimental contexts the polarization state is not relevant as either a parameter or measurement, and the coherent excitation source is often circularly polarized prior to introduction into the epifluorescence optics specifically to avoid artifacts associated with linearly polarized excitation. Similarly, great care is often taken to avoid introducing optical elements to the emission pathway that exhibit polarization anisotropy or birefringence, specifically in order to avoid artifacts associated with unintended polarized emission. However, in a polarization-sensitive optical arrangement, particularly one employing high- NA lenses, the excitation and emission polarization states are of critical quantitative importance. Polarization sensitivity in either the excitation or emission optics alone is sufficient to introduce significant changes to the point spread functions associated with equations 3.3−3.33 (particularly 3.32 and 3.33) and Figures 3.3−3.9.

Using Müller-Stokes formalism,[278] the polarization states of an optical wave function $\boldsymbol{\psi}_{\mathcal{S}}$ propagating in three dimensions is represented is described by 4-element complex-valued state vectors $\{\boldsymbol{\mathcal{S}}_i\}$:

$$\boldsymbol{\mathcal{S}}_i = \begin{pmatrix} I_i \\ Q_i \\ U_i \\ V_i \end{pmatrix} = \begin{pmatrix} |E_{x,i}|^2 + |E_{y,i}|^2 \\ |E_{x,i}|^2 - |E_{y,i}|^2 \\ 2Real\left(E_{x,i}E_{y,i}^{*}\right) \\ 2Imag.\left(E_{x,i}E_{y,i}^{*}\right) \end{pmatrix} \tag{3.34}$$

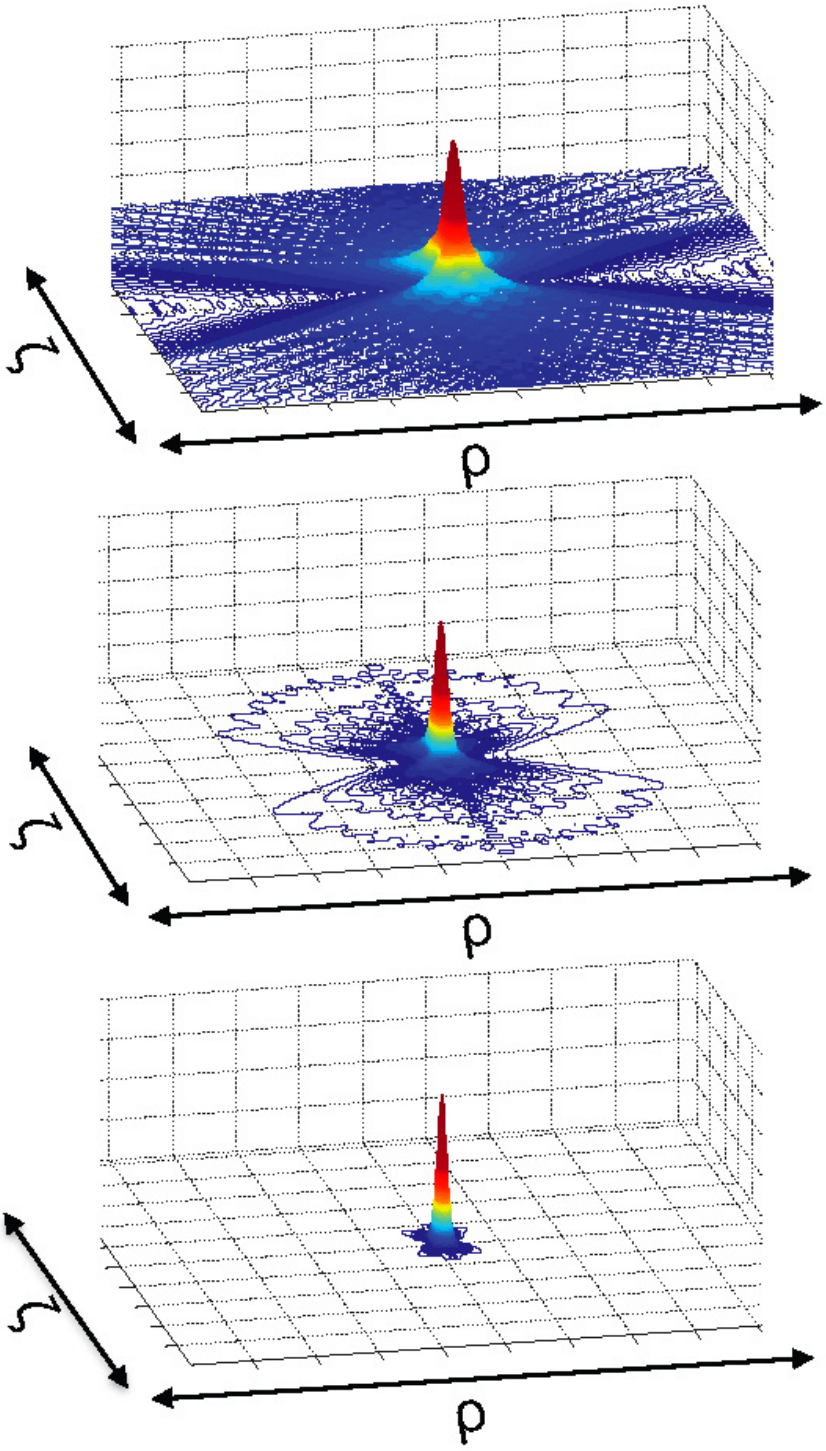

Figure 3.8: Electromagnetic field amplitude (top), conventional irradiance point spread function (middle) and confocal irradiance point spread function (bottom) for a 1.45NA optical system. Dimensionless parameters ρ and ζ are scaled by $\left(\frac{2\pi NA}{\lambda}\right)$ and $\left(\frac{2\pi NA^2}{n_o\lambda}\right)$ (equations 3.32 and 3.32, respectively.)

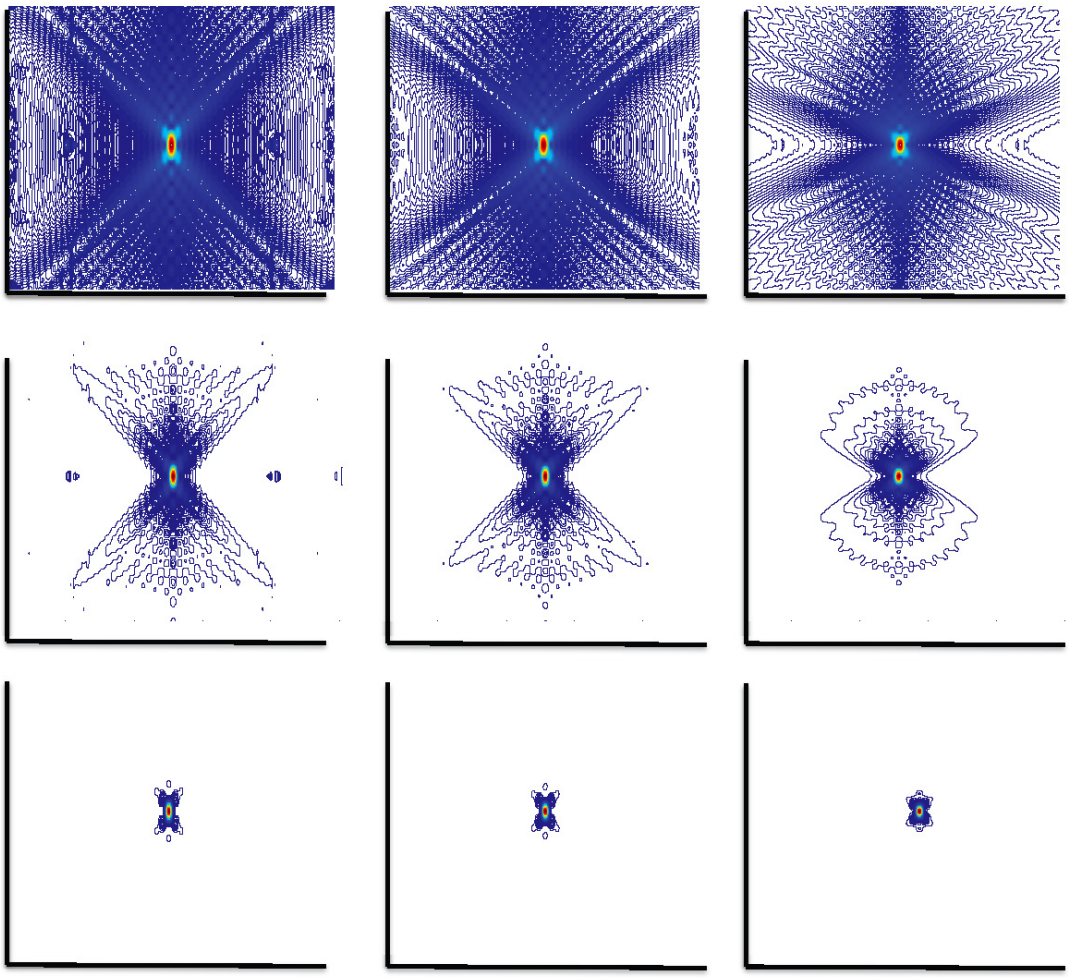

Figure 3.9: Electromagnetic field amplitudes (top row), conventional point spread functions (middle row) and confocal point spread functions (bottom row) for optical systems with 0.4NA (left column), 1.00NA (middle column), and 1.45NA (right column). The x-axis of each plot is the dimensionless parameter ρ over a range of $\pm 12\pi$, and the y-axis of each plot is the dimensionless parameter ζ over a range of $\pm 12\pi$ and ζ.

where $E_{x,i}$ is the electric field amplitude parallel to $\hat{\boldsymbol{x}}$, and $E_{y,i}$ the corresponding value parallel to $\hat{\boldsymbol{y}}$ for the i^{th} state of $\boldsymbol{\psi}_{\mathcal{S}}$ in the three-dimensional Cartesian reference frame $(\hat{\boldsymbol{x}}, \hat{\boldsymbol{y}}, \hat{\boldsymbol{z}})$ in which polarization measurements take place.

Each change in the polarization state $\boldsymbol{\psi}_i \rightarrow \boldsymbol{\psi}_{i+1}$, such as those induced by a retarder plate, polarizer or otherwise birefringent optical element, is fully described by a corresponding 4x4 transformation matrix $\boldsymbol{\mathcal{M}}_i$, with the $(i+1)^{\text{th}}$ state vector calculated from the product of the transformation matrix and the i^{th} state vector:

$$\boldsymbol{\mathcal{S}}_{i+1} = \boldsymbol{\mathcal{M}}_i \cdot \boldsymbol{\mathcal{S}}_i \tag{3.35}$$

$$\boldsymbol{\mathcal{M}}_i = \begin{bmatrix} m_{1,1,i} & m_{1,2,i} & m_{1,3,i} & m_{1,4,i} \\ m_{2,1,i} & m_{2,2,i} & m_{2,3,i} & m_{2,4,i} \\ m_{3,1,i} & m_{3,2,i} & m_{3,3,i} & m_{3,4,i} \\ m_{4,1,i} & m_{4,2,i} & m_{4,3,i} & m_{4,4,i} \end{bmatrix} . \tag{3.36}$$

The individual matrix element values $m_{(x,y,i)}$ of $\boldsymbol{\mathcal{M}}_i$ are determined by the specific optical element inducing each discrete polarization state change. The generalized polarization state of a light source in the excitation pathway ($\boldsymbol{S}_{\boldsymbol{\infty}}$, Figure 3.4) is elliptical with irradiance intensity I_o, eccentricity e, and azimuthal angle κ, yielding $\boldsymbol{\mathcal{S}}_{ex}$.

$$\boldsymbol{\mathcal{S}}_{ex} \in \left\{ \boldsymbol{\mathcal{S}} = \begin{pmatrix} I_o \\ Q \\ U \\ V \end{pmatrix} : \frac{1}{2}\tan^{-1}\left(\frac{V}{\sqrt{Q^2+U^2}}\right) = \tan^{-1}\left(\sqrt{1-e^2}\right); \frac{U}{Q} = \tan 2\kappa \right\} \tag{3.37}$$

However, because the laser excitation source consists of a completely polarized coherent plane wave, the polarization state can be represented much more simply

by a 2-element Jones vector (and 2x2 Jones transformation matrices) in place of the Müller-Stokes formalism. The 2-element Jones vector $\boldsymbol{\mathcal{E}}_i$ for a coherent excitation source is simply given by:

$$\boldsymbol{\mathcal{E}}_i = \begin{pmatrix} E_x e^{i\phi_x} \\ E_y e^{i\phi_y} \end{pmatrix} \in \mathbb{C}^{(2)} \tag{3.38}$$

with each discrete polarization state change corresponding to a 2x2 Jones matrix $\boldsymbol{\mathcal{J}}$:

$$\boldsymbol{\mathcal{J}}_i = \begin{bmatrix} j_{1,1} & j_{1,2} \\ j_{2,1} & j_{2,2} \end{bmatrix}_i ; j_{n,m} \in \mathbb{C} \tag{3.39}$$

$$\boldsymbol{\mathcal{E}}_{i+1} = \boldsymbol{\mathcal{J}}_i \cdot \boldsymbol{\mathcal{E}}_i \,. \tag{3.40}$$

We can further constrain the experimental conditions, however, by requiring that the excitation source be only circularly polarized or linearly polarized parallel to one cardinal axis ($\hat{\boldsymbol{x}}$ or $\hat{\boldsymbol{y}}$) of the laboratory reference frame. There are now only 4 possible states for the excitation source:

$$\boldsymbol{\mathcal{E}}_{ex} \in \left\{ E_o \begin{pmatrix} 1 \\ 0 \end{pmatrix}, E_o \begin{pmatrix} 0 \\ 1 \end{pmatrix}, \frac{E_o}{\sqrt{2}} \begin{pmatrix} 1 \\ -i \end{pmatrix}, \frac{E_o}{\sqrt{2}} \begin{pmatrix} 1 \\ i \end{pmatrix} \right\} .$$

These are, horizontal linear ($\hat{\boldsymbol{x}}$), vertical linear ($\hat{\boldsymbol{y}}$), clockwise circular ($\hat{\boldsymbol{\sigma}}_+$) and counterclockwise circular ($\hat{\boldsymbol{\sigma}}_-$), respectively.

To include polarization state representation in the optical wave function ψ_z, equation 3.2 must be modified to combine two independent orthogonal components: the vertical electric field intensity $\mathcal{E}_V(z,t)$, and the horizontal electric field intensity:

$\mathcal{E}_H(z,t)$. Without loss of generality, we can assign the 'horizontal' unit vector $\hat{\boldsymbol{h}}$ to the laboratory reference frame x-axis ($\hat{\boldsymbol{h}} = \hat{\boldsymbol{x}}$), and assign the 'vertical' unit vector $\hat{\boldsymbol{v}}$ to the y- axis ($\hat{\boldsymbol{v}} = \hat{\boldsymbol{y}}$).[‡] The representative equation for a polarized plane wave propagating in the $\hat{\boldsymbol{z}}$-direction is then:

$$\psi(z,t) = E_o\left(\xi\hat{\boldsymbol{h}} + \upsilon\hat{\boldsymbol{v}}\right)e^{-i(\omega t - kz)}. \tag{3.41}$$

and the irradiance intensity of the corresponding orthogonal polarization components is:

$$\mathcal{I}_h = \frac{1}{2}E_o^2\xi\xi^* \tag{3.42}$$

$$\mathcal{I}_v = \frac{1}{2}E_o^2\upsilon\upsilon^* \tag{3.43}$$

$$\mathcal{I}_{tot} = \frac{1}{2}E_o^2\left(|\xi|^2 + |\upsilon|^2\right). \tag{3.44}$$

If $\arg(\xi) = \arg(\upsilon) \pm \pi$ and $\arg(\xi), \arg(\upsilon) \neq 0$ (where $\arg : \zeta \in \mathbb{C} \mapsto \theta \in \mathbb{R}^+$ represents the angle θ between complex-valued ζ and the real-number line in the complex plane), then ψ_z is linearly polarized. If $\arg(\xi) = 0$, then ψ is vertically polarized (polarized in the the $\hat{\boldsymbol{y}}$-direction). If $\arg(\upsilon) = 0$, then ψ_z is horizontally polarized (polarized in the the $\hat{\boldsymbol{x}}$-direction). If $\xi\xi^* = \upsilon\upsilon^*$ and $\arg(\xi) = \arg(\upsilon) + \pi/2$, then ψ_z is circularly polarized with $\boldsymbol{\sigma}^+$ orientation. If $\xi\xi^* = \upsilon\upsilon^*$ and $\arg(\xi) = \arg(\upsilon) - \pi/2$, then ψ_z is circularly polarized with $\boldsymbol{\sigma}^-$ orientation. For *all* other cases of υ and ξ, ψ is elliptically polarized. Linear and circular polarization are both special cases of elliptical polarization for which the corresponding ellipse eccentricity

[‡]There is a third orthogonal polarization vector in 3-dimensional optical systems: the 'z-polarization', assigned to the reference frame z-axis ($\hat{\boldsymbol{z}}$). This component is by definition absent from a plane wave propagating in the $\hat{\boldsymbol{z}}$-direction, but will be discussed extensively in the context of adding together waves representing individual ray paths on page 109.

is 1 or 0, respectively.

A single one-dimensional dipole photon source emits radiation with polarization orientation $\vec{\boldsymbol{\rho}}_{\boldsymbol{em}}$ dependent upon the emission direction $\vec{\boldsymbol{k}}$ relative to its transition dipole vector $\vec{\boldsymbol{\rho}}_{\boldsymbol{d}}$.[†]

$$\vec{\boldsymbol{\rho}}_{\boldsymbol{em}} = \vec{\boldsymbol{k}} \times \vec{\boldsymbol{\rho}}_{\boldsymbol{d}} \times \vec{\boldsymbol{k}}\,. \tag{3.45}$$

Consider the optical arrangement illustrated in Figure 3.10, in which the radiation source is located at the focal plane $\boldsymbol{\sigma}_{sample}$ of objective lens $\mathcal{L}_{obj}$. The transition dipole $\vec{\boldsymbol{\rho}}_{\boldsymbol{d}}$ is a 3-space vector $(\rho_x\hat{\boldsymbol{x}} + \rho_y\hat{\boldsymbol{y}} + \rho_z\hat{\boldsymbol{z}})$ with an angle ϕ relative to the optical axis (z) given by:

$$\phi = \cos^{-1}\left(\frac{\rho_z}{\|\vec{\boldsymbol{\rho}}_{\boldsymbol{d}}\|}\right) \tag{3.46}$$

and an angle θ relative to the x-axis of the laboratory reference frame given by:

$$\theta = \cos^{-1}\left(\frac{\sqrt{\rho_x^2 + \rho_y^2}}{\|\vec{\boldsymbol{\rho}}_{\boldsymbol{d}}\|}\right)\,. \tag{3.47}$$

Lens $\mathcal{L}_{obj}$ collects radiation from every individual ray $\boldsymbol{\mathcal{R}}$ with direction $\vec{\boldsymbol{k}}$ and origin at the dipole vector $\vec{\boldsymbol{\rho}}_{\boldsymbol{d}}$, preserving its polarization components, and projects this onto the image plane $\boldsymbol{\sigma}_{img}$ in Figure 3.10. The polarization-sensitive emission pathway consists of a beamsplitter that separates $\vec{\boldsymbol{\rho}}_{img}$ into the $\hat{\boldsymbol{x}}$- and $\hat{\boldsymbol{y}}$-polarization components (corresponding to $\hat{\boldsymbol{h}}$- and $\hat{\boldsymbol{v}}$, respectively), which are then measured by separate photodetectors having a relative collection efficiency ratio $\gamma = C_x/C_y$.

[†]Each individual photon wave function $|\psi_i\rangle$ is a superposition of orthogonal quantum states: $|\psi\rangle_i = \xi|\boldsymbol{X}\rangle + \upsilon|\boldsymbol{Y}\rangle + \zeta|\boldsymbol{Z}\rangle$, normalized by the condition $\xi^2 + \upsilon^2 + \zeta^2 = 1$.

At the limit of low numerical aperture optics ($NA_{\mathcal{L}} \ll 1$), the image of $\vec{\boldsymbol{\rho}}_{\boldsymbol{d}}$ in $\boldsymbol{\sigma}_{img}$ is simply the projection of the 3-space vector $(\rho_x\hat{\boldsymbol{x}} + \rho_y\hat{\boldsymbol{y}} + \rho_z\hat{\boldsymbol{z}})$ onto the xy-plane, or $\vec{\boldsymbol{\rho}}_{\boldsymbol{img}} = (\rho_x\hat{\boldsymbol{x}} + \rho_y\hat{\boldsymbol{y}})$, which consequently displays a total dipole magnitude scaled by the factor $\cos\phi$, and has an angle θ relative to the x-axis given by $\theta = \sin^{-1}\left(\frac{\rho_y}{l\|\vec{\boldsymbol{\rho}}_{\boldsymbol{d}}\|}\right)$. The signal intensity measured by each polarization channel can be calculated from:

$$
\begin{aligned}
I_{det} &= \begin{pmatrix} I_x \\ I_y \end{pmatrix} \\
&= \begin{pmatrix} \langle \vec{\boldsymbol{\rho}}_{\boldsymbol{d}}, \hat{\boldsymbol{x}} \rangle^2 \\ \gamma \langle \vec{\boldsymbol{\rho}}_{\boldsymbol{d}}, \hat{\boldsymbol{y}} \rangle^2 \end{pmatrix} && (3.48) \\
&= \begin{pmatrix} \left(\frac{\rho_x}{\|\vec{\boldsymbol{\rho}}_{\boldsymbol{d}}\|}\right)^2 \\ \gamma \left(\frac{\rho_y}{\|\vec{\boldsymbol{\rho}}_{\boldsymbol{d}}\|}\right)^2 \end{pmatrix} && (3.49) \\
&= I_o \begin{pmatrix} (\sin\theta + \cos\theta)^2 \\ \gamma \left[\left(\sin\left(\frac{\pi}{2} - \theta\right) + \sin\left(\frac{\pi}{2} - \theta\right)\right)^2 \right] \end{pmatrix} && (3.50) \\
&= I_o \begin{pmatrix} \sin^2\theta + \cos^2\theta + 2\sin\theta\cos\theta \\ \gamma \left[\sin^2\left(\frac{\pi}{2} - \theta\right) + \cos^2\left(\frac{\pi}{2} - \theta\right) + 2\sin\left(\frac{\pi}{2} - \theta\right)\cos\left(\frac{\pi}{2} - \theta\right) \right] \end{pmatrix} && (3.51) \\
&= I_o \begin{pmatrix} 1 + \sin 2\theta \\ \gamma\,(1 - \sin 2\theta) \end{pmatrix} && (3.52)
\end{aligned}
$$

where I_o is the total signal intensity measured when $\vec{\boldsymbol{\rho}}_{\boldsymbol{d}}$ is oriented parallel to plane $\boldsymbol{\sigma}_{sample}$. The total intensity depends upon the angle ϕ of $\vec{\boldsymbol{\rho}}_{\boldsymbol{d}}$ relative to the optical axis:

$$I_{tot} = (I_x + I_y) \propto \cos^2\phi \tag{3.53}$$

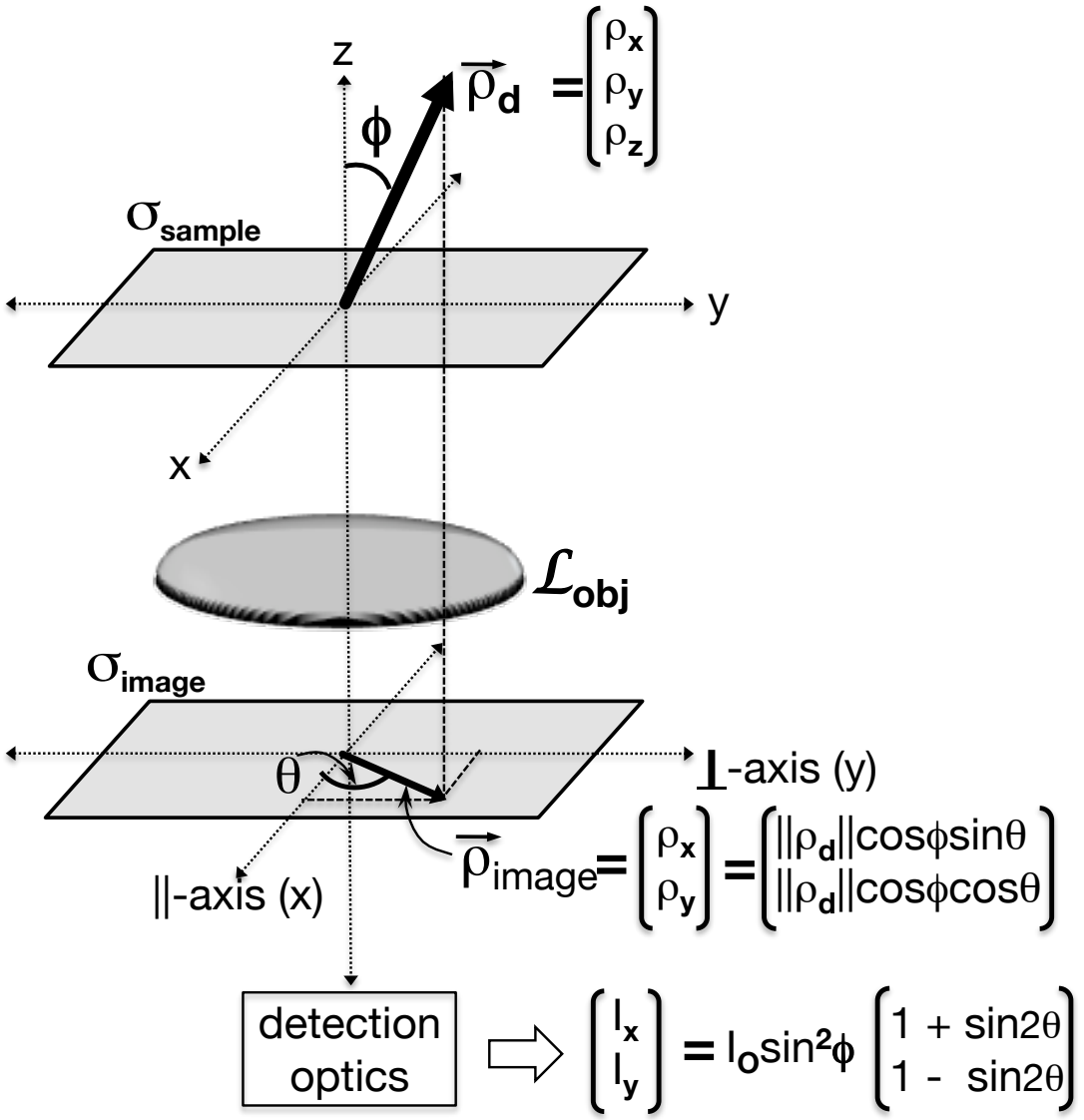

Figure 3.10: Imaging a 1D linear dipole with an optical system at the limit of low numerical aperture, $NA \ll 1$. $\vec{\boldsymbol{\rho}}_{\boldsymbol{d}}$ is a 3-space vector $\vec{\boldsymbol{\rho}}_{\boldsymbol{d}} = (\rho_x \hat{\boldsymbol{x}} + \rho_y \hat{\boldsymbol{y}} + \rho_z \hat{\boldsymbol{z}})$, with angle ϕ relative to the optical axis. The polarization state measured by this optical system is simply the projection of the 3-space vector $\vec{\boldsymbol{\rho}}_{\boldsymbol{d}}$ into the $xy-$plane, $\vec{\boldsymbol{\rho}}_{\boldsymbol{img}} = (\rho_x \hat{\boldsymbol{x}} + \rho_y \hat{\boldsymbol{x}})$, equivalent to discarding the ρ_z component of $\vec{\boldsymbol{\rho}}_{\boldsymbol{d}}$ entirely.

This low-NA approximation and equations 3.48−3.53 are useful for assessing macroscopic polarization, such as that performed by a bulk polarization anisotropy fluorimeter. However, in a real microscope having an appreciable NA, an additional polarization characteristic introduced to both the excitation and emission pathways is the effect of refraction by finite-focal length lenses, in particular the objective lens of the microscope. Every individual ray $\boldsymbol{\mathcal{R}_i}$ collected by the objective can be described uniquely by their propagation direction $\vec{\boldsymbol{k_i}}$ and any point through which they pass. Each discrete refraction event corresponds to a ray rotation in three dimensions. This rotation of incident rays by the objective lens alters their polarization state, to the extent of inducing a polarization component parallel to the optical axis $\hat{\boldsymbol{z}}$. In an infinity-corrected microscope system (Figure 3.4), the **back focal plane (BFP)** of the objective lens (Figure 3.11, inset) can be considered as the sole locus in which each ray $\boldsymbol{\mathcal{R}_i}$ from the excitation pathway undergoes a single discrete rotational transformation. Each point on the BFP maps incident rays to a unique emergence angle relative to the optical axis, and each incident angle on the BFP maps rays to a unique point on the focal plane, as shown in Figure 3.11. The inverse transformation also occurs in the emission pathway, with the objective lens BFP mapping each point on the focal plane to a specific ray emergence angle relative to the optical axis, and each ray angle in the sample plane to a unique point on the back focal plane.

It is therefore necessary to modify the 2-dimensional Jones formalism (equations 3.38 and 3.39) to permit 3- dimensional polarization representation at the sample plane in addition to non-square matrix transformations $\boldsymbol{\mathcal{J}}$ between 2-element polarization state vectors $\boldsymbol{\mathcal{E}}^{(2)} \in \mathbb{C}^{(2)}$ in the infinity spaces $\boldsymbol{S_\infty}/\boldsymbol{S'_\infty}$ and 3-element polarization state vectors $\boldsymbol{\mathcal{E}}^{(3)} \in \mathbb{C}^{(3)}$ at the sample plane $\boldsymbol{\sigma_s}$ (as well as at the conjugate image plane $\boldsymbol{\sigma_{img}}$). The modified Jones 3x2 matrices are functional mappings

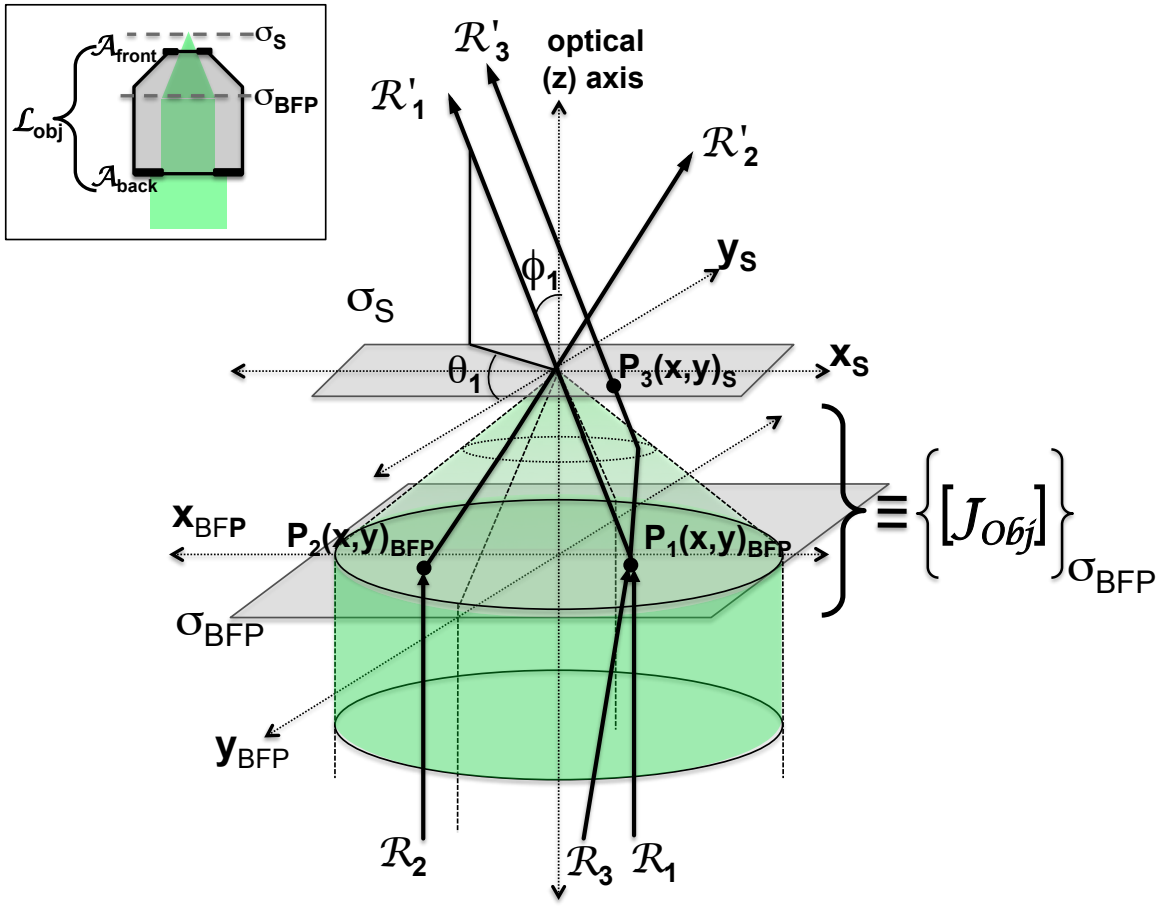

Figure 3.11: Spatial mapping between the objective back focal plane and sample plane. The objective lens (inset) is infinity-corrected, resulting in parallel rays $\{\boldsymbol{\mathcal{R}_i}\}$ within the infinity space corresponding to specific focal points on the image plane. A unique ray $\boldsymbol{\mathcal{R}_1}$ parallel to the optical axis ($\hat{\boldsymbol{z}}$), intersecting the back focal plane at a point $P_1(x,y)_{BFP}$, will emerge as ray $\boldsymbol{\mathcal{R}'_1}$ intersecting the origin of the sample plane (point $(0,0)_S$) at a unique azimuthal/axial angular orientation (ϕ_1, θ_1) dependent upon the coordinates of the intersection point $P_1(x,y)_{BFP}$ in $\boldsymbol{\sigma_{BFP}}$. A second ray $\boldsymbol{\mathcal{R}_2}$ also parallel to $\hat{\boldsymbol{z}}$ but intersecting $\boldsymbol{\sigma_{BFP}}$ at a different point $P_2(x,y)_{BFP}$ will emerge as a ray $\boldsymbol{\mathcal{R}'_2}$ that also intersects point $(0,0)_S$, but with a different orientation (ϕ_2, θ_2). A third ray $\boldsymbol{\mathcal{R}_3}$ that intersects the back focal plane at the same point as $P_1(x,y)_{BFP}$, but which is not parallel to the optical axis ($\hat{\boldsymbol{z}}$) will emerge as a ray $\boldsymbol{\mathcal{R}'_3}$ parallel to $\boldsymbol{\mathcal{R}'_1}$ (i.e. $(\phi_3, \theta_3) = (\phi_1, \theta_1)$) but intersecting a point $P_3(x,y)_S$ other than the origin $(0,0)_S$. Each transformation performed by the objective lens on a ray $\boldsymbol{\mathcal{R}_i}$ intersecting point (x,y) in the back focal plane is a 3x2 modified Jones matrix $\boldsymbol{\mathcal{J}_{Obj}}(x,y)$ (equation 3.56), the individual matrix elements of which are determined using equation 3.61 (p. 111).

$\boldsymbol{\mathcal{J}} : \mathbb{C}^{(2)} \mapsto \mathbb{C}^{(3)}$ representing the polarization transformations induced by lenses that have non-negligible numerical aperture, but which are otherwise non-birefringent optical elements.

$$\boldsymbol{\mathcal{E}}_{S_\infty} = \begin{pmatrix} E_1 \\ E_2 \end{pmatrix}_{xy} \in \mathbb{C}^{(2)} \tag{3.54}$$

$$\boldsymbol{\mathcal{E}}_{\boldsymbol{\sigma_{img}}} = \begin{pmatrix} E_1 \\ E_2 \\ E_3 \end{pmatrix}_{xyz} \in \mathbb{C}^{(3)} \tag{3.55}$$

$$\boldsymbol{\mathcal{J}}_{Obj} = \begin{bmatrix} j_{1,1} & j_{1,2} \\ j_{2,1} & j_{2,2} \\ j_{3,1} & j_{3,2} \end{bmatrix}; j_{n,m} \in \mathbb{C} \tag{3.56}$$

Each individual 3D polarized ray originating at the focal point is transformed by the objective lens into a 2D polarized ray propagating parallel to $\hat{\boldsymbol{z}}$ in $\boldsymbol{S_\infty}$ by the following:

$$\begin{pmatrix} E_1 \\ E_2 \\ E_3 \end{pmatrix}_{\boldsymbol{\sigma}_S} = \boldsymbol{\mathcal{J}}_{Obj} \cdot \begin{pmatrix} E_1 \\ E_2 \end{pmatrix}_{S_\infty} \tag{3.57}$$

$$\begin{pmatrix} E_1 \\ E_2 \end{pmatrix}_{S_\infty} = [\boldsymbol{\mathcal{J}}_{Obj}]^\dagger \cdot \begin{pmatrix} E_1 \\ E_2 \\ E_3 \end{pmatrix}_{\boldsymbol{\sigma}_S} . \tag{3.58}$$

Equation 3.57 describes the introduction of a polarization component parallel to $\hat{\boldsymbol{z}}$ caused by spatially-dependent refraction of collimated excitation beam. Equation 3.58 represents the collection of 3D-polarized emission from a dipole source at the focal plane and transformation of $\hat{\boldsymbol{z}}$- component polarization into a *radial* polarization component of the collimated emission beam. Since $\boldsymbol{\mathcal{J}}_{Obj}$ is a 3x2 matrix, $[\boldsymbol{\mathcal{J}}_{Obj}]^{\dagger} \cdot \boldsymbol{\mathcal{E}}^{(3)}_{xyz}$, corresponding to collection of a single emitted polarized ray$\boldsymbol{\mathcal{R}_i}$ originating from the objective focal point with propagation direction $\vec{\boldsymbol{k_i}}$, is a 2-element vector $\boldsymbol{\mathcal{E}}^{(2)}_{xy}$. Likewise, the product $\boldsymbol{\mathcal{J}}_{Obj} \cdot \boldsymbol{\mathcal{E}}^{(2)}_{xy}$, corresponding to the inverse is a 3-element vector $\boldsymbol{\mathcal{E}}^{(3)}_{xyz}$.

As illustrated in Figure 3.12, each individual 3x2 transformation matrix $\boldsymbol{\mathcal{J}}_{Obj}$ is itself is a function of both the azimuthal angle ϕ_s and the radial angle θ_s of the emitted ray $\boldsymbol{\mathcal{R}'}$ in the 3D spherical coordinate system with its origin at the laser focus, and also corresponds to a unique point of intersection with the objective back focal plane in its 2D coordinate system. Consider the focusing of a linearly polarized excitation source by the optical arrangement illustrated in Figure 3.13. An excitation beam with uniform polarization orientation $\vec{\boldsymbol{\rho}}_{\boldsymbol{S\infty}}$ may, for the purposes of visualization, be separated into the components $\left\{\vec{\boldsymbol{\rho}}_{\mathbf{1}}, \vec{\boldsymbol{\rho}}_{\mathbf{2}}, \vec{\boldsymbol{\rho}}_{\mathbf{3}}, \vec{\boldsymbol{\rho}}_{\mathbf{4}}\right\}$ corresponding to radial angles $\left\{\theta = \pi/2, \theta = \pi, \theta = 3\pi/2, \theta = 2\pi\right\}$in $\boldsymbol{\mathcal{S}_\infty}$, each of which is transformed uniquely by the modified Jones matrices $\boldsymbol{J}_{Obj}$ (equation 3.61) dependent upon its point of intersection with the back focal plane. The net polarization vector $\vec{\boldsymbol{\rho}}$ at the sample plane $\boldsymbol{\sigma_S}$ is then the superposition of each individually transformed component $\sum \vec{\boldsymbol{\rho}}_{\boldsymbol{i}}$. However, since all component vectors $\vec{\boldsymbol{\rho}}_{\boldsymbol{i}}$ are parallel in $\boldsymbol{S_\infty}$, and the transformations induced by all transformation matrices $\left\{\boldsymbol{J}_{Obj}(x,y); \forall (x,y) \in \boldsymbol{\sigma_{BFP}}\right\}$ are radially symmetric, the net polarization $\vec{\boldsymbol{\rho}}_{\boldsymbol{tot}}$ at the focal point is parallel to $\vec{\boldsymbol{\rho}}_{\boldsymbol{S\infty}}$, with no $\hat{\boldsymbol{z}}-$component.

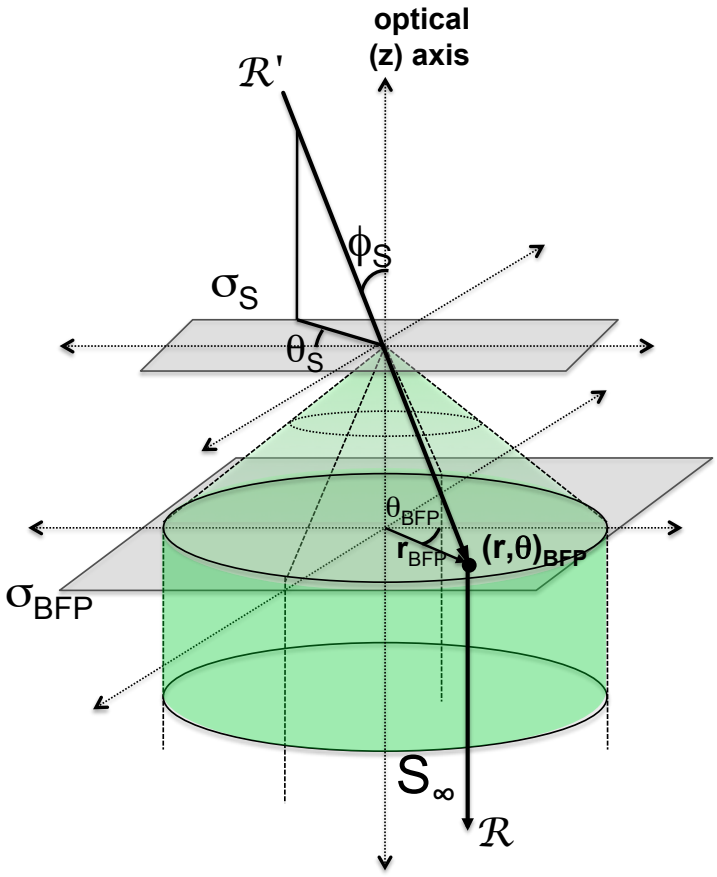

Figure 3.12: 3D rotational transformations of polarized rays collected by the microscope objective. Each ray $\boldsymbol{\mathcal{R}'}_{(\phi_s,\theta_s)}$ emerging from the focal point, uniquely described by by its radial angle θ_s and its azimuthal angle ϕ_s in the 3D spherical coordinate system centered at the focus, will intersect the back focal plane at a specific point $(r,\theta)_{BFP}$ in the 2D polar coordinate system aligned with the back focal plane ($\theta_s \equiv \theta_{BFP}$). This point of intersection subsequently determines the transformation matrix that rotates $\boldsymbol{\mathcal{R}'}$, as well as the modified Jones matrix $\boldsymbol{\mathcal{J}}_{Obs}$ that governs its resulting polarization (equation 3.61).

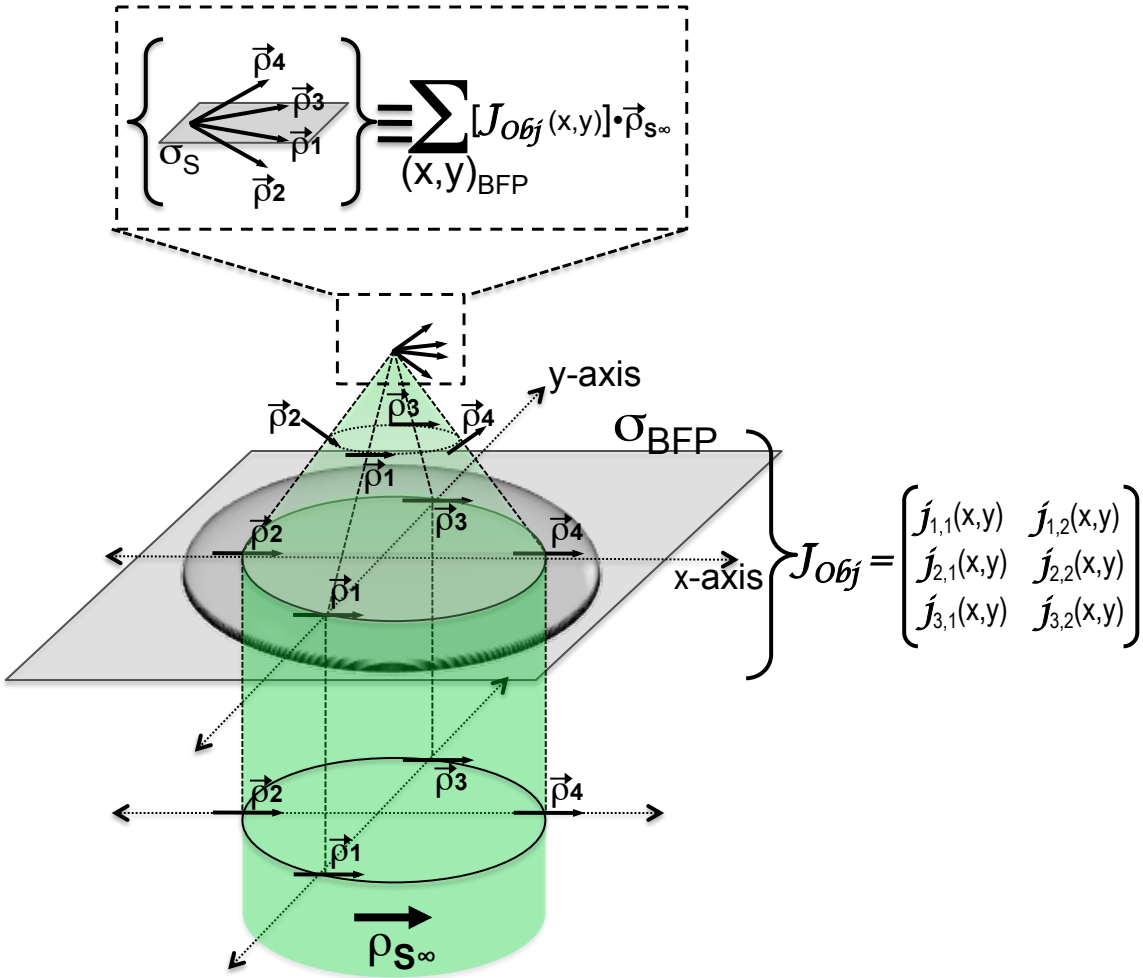

Figure 3.13: Polarized excitation by an optical system having an appreciable numerical aperture. $\vec{\boldsymbol{\rho}}_{\boldsymbol{S\infty}}$ components $\left\{\vec{\boldsymbol{\rho}}_{\mathbf{1}}, \vec{\boldsymbol{\rho}}_{\mathbf{2}}, \vec{\boldsymbol{\rho}}_{\mathbf{3}}, \vec{\boldsymbol{\rho}}_{\mathbf{4}}\right\}$ (2-vectors) are transformed individually by the *transpose* of the corresponding modified Jones matrix $\mathcal{J}_{Obj}$, which is itself a function of their point of intersection with the back focal plane. The specific Jones matrix elements $j_{(n,m)}$ may be determined using equations 3.61, 3.59 and 3.60. The net polarization vector $\vec{\boldsymbol{\rho}}_{\boldsymbol{tot}}$ at the sample plane $\boldsymbol{\sigma_S}$ is the superposition of the individually transformed polarization vectors, $\sum \vec{\boldsymbol{\rho}}_{\boldsymbol{i}}$. The inverse process, collection of 3D polarized emission, is illustrated in Figure 3.14.

In contrast, now consider the imaging of a single 3D-polarized linear dipole radiation source by the optical arrangement illustrated in Figure 3.14, the same system as used in Figure 3.13 for focusing radiation from a polarized plane wave source. A 3D-polarized emission vector $\vec{\boldsymbol{\rho}}_{\mathbf{0},\boldsymbol{\sigma_S}}$ can be separated into a $\vec{\boldsymbol{\rho}}_{\boldsymbol{z}}$ component parallel to the optical axis $\hat{\boldsymbol{z}}$ and a $\vec{\boldsymbol{\rho}}_{\boldsymbol{xy}}$ component parallel to the $xy-$plane. By analogy to the process of focusing a uniformly polarized excitation beam (Figure 3.13), $\vec{\boldsymbol{\rho}}_{\boldsymbol{xy}}$ will yield a uniformly oriented emission beam component in $\boldsymbol{S_\infty}$ parallel to $\vec{\boldsymbol{\rho}}_{\boldsymbol{xy}}$. In contrast, the $\vec{\boldsymbol{\rho}}_{\boldsymbol{z}}$ component will be transformed by the objective according to $\left[\boldsymbol{J}_{Obj}\right]^{\dagger}$, with the individual modified Jones matrix elements $j_{(n,m)}$ determined from equation 3.61). The net polarization in $\boldsymbol{\mathcal{S}_\infty}$ arising from $\vec{\boldsymbol{\rho}}_{\boldsymbol{z}}$ is zero, but there now exists an anisotropic *radial* ($\hat{\boldsymbol{r}}$) polarization component. Quantitative understanding of this transformation is essential to calculating the expected signal from a 3D-polarized dipole measured by orthogonally polarized detectors in the emission pathway (equations 3.68−3.72).

The individual elements of the modified Jones matrices may be calculated from the understanding that an infinity-corrected microscope objective transforms the vector representing every ray path originating from the central focal point (the origin of the sample plane $\boldsymbol{\sigma_s}$) to a vector parallel to the optical axis $\hat{\boldsymbol{z}}$. In general, for a ray emerging from the focus at a radial angle ϕ between 0 and 2π, and an azimuthal angle θ between 0 and $\phi_{max} = \sin^{-1}\left(\frac{NA}{n_o}\right)$, the transformation $\boldsymbol{\mathcal{J}_{Obj}}$ performed by the objective lens represents 3D rotation by angle θ about the $\hat{\boldsymbol{\phi}}_{\boldsymbol{BFP}}-$axis of the back focal plane $\boldsymbol{\sigma_{BFP}}$. Matrix representation of rotational transformation about cardinal and arbitrary axes in three dimensions is discussed in detail in appendix A.1 (p. 221).

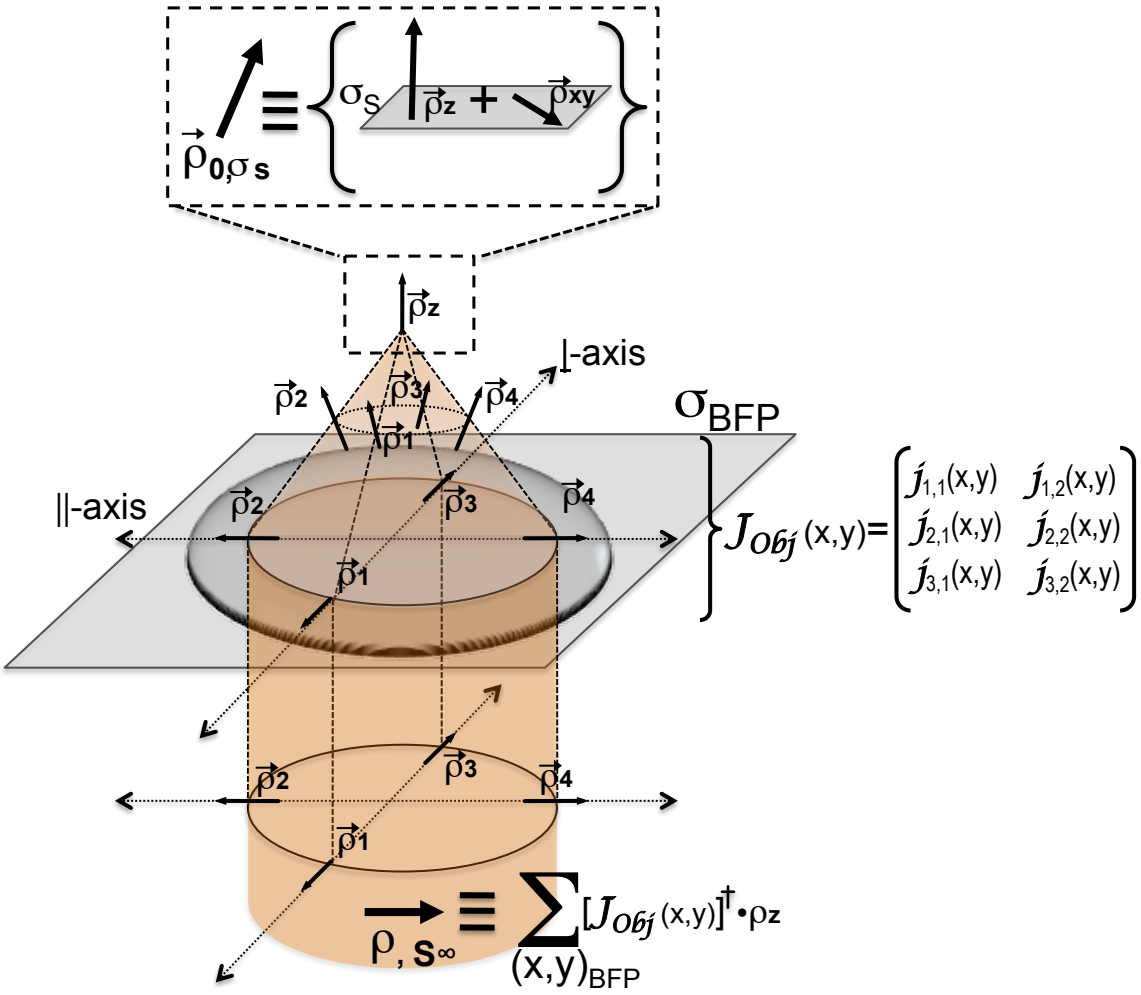

Figure 3.14: Collection of 3D-polarized light by an optical system having an appreciable numerical aperture, the inverse of the focusing process illustrated in Figure 3.13. The 3D-polarized emission vector $\vec{\boldsymbol{\rho}}_{\mathbf{0},\boldsymbol{\sigma}_S}$ can be separated into a $\vec{\boldsymbol{\rho}}_{\boldsymbol{z}}$ component parallel to the optical axis $\hat{\boldsymbol{z}}$ and a $\vec{\boldsymbol{\rho}}_{\boldsymbol{xy}}$ component parallel to the $xy-$plane. The $\vec{\boldsymbol{\rho}}_{\boldsymbol{xy}}$ component will yield a uniformly oriented emission beam polarization component in $\boldsymbol{S}_{\boldsymbol{\infty}}$ that is parallel to $\vec{\boldsymbol{\rho}}_{\boldsymbol{xy}}$. The $\hat{\boldsymbol{z}}$ component, undergoing transformation by the the modified Jones matrix $\boldsymbol{J}_{Obj}$, will yield a *radial* ($\hat{\boldsymbol{r}}$) polarization component of the emission beam in $\boldsymbol{S}_{\boldsymbol{\infty}}$. The specific Jones matrix elements $j_{(n,m)}$ may be determined using equations 3.61, 3.59 and 3.60.

Using a 3D spherical coordinate system at the sample plane, and a 2D polar coordinate system at the back focal plane, as shown in Figure 3.12, we can uniquely identify each ray $\boldsymbol{\mathcal{R}'}_{(\phi_s,\theta_s)}$ emerging from the focal point by its radial angle θ_s and its azimuthal angle ϕ_s. Without loss of generality, we can align the coordinate systems so that $\theta_s = \theta_{BFP}$. Let the 3D polarization vector of this ray be described by $\boldsymbol{\mathcal{E}}_{\boldsymbol{R'}} = (E_1\hat{\boldsymbol{x}} + E_2\hat{\boldsymbol{y}} + E_3\hat{\boldsymbol{z}})$ in the laboratory reference frame, as per equation 3.57. The point of intersection of $\boldsymbol{\mathcal{R}'}_{(\phi_s,\theta_s)}$ with $\boldsymbol{\sigma_{BFP}}$, in the polar coordinate system of the back focal plane, is given by:

$$(r_{BFP}, \theta_{BFP}) = \big(\frac{d_{BFP}}{2\tan\phi_{max}}\tan\phi_s, \theta_s\big) \tag{3.59}$$

where (d_{BFP} is the physical BFP diameter). In a 2D Cartesian coordinate system for the back focal plane, the point of intersection is given by:

$$(x_{BFP}, y_{BFP}) = \Big(\frac{d_{BFP}}{2\tan\phi_{max}}\tan\phi_s\cos\theta_s, \frac{d_{BFP}}{2\tan\phi_{max}}\tan\phi_s\sin\theta_s\Big) \tag{3.60}$$

The modified Jones transformation matrix is therefore:

$$\boldsymbol{\mathcal{J}_{Obj}}(\phi_s, \theta_s) = \begin{bmatrix} \cos\phi_s\cos^2\theta_s + \sin^2\theta_s & (\cos\phi_s - 1)\sin\theta_s\cos\theta_s \\ (\cos\phi_s - 1)\sin\theta_s\cos\theta_s & \cos\phi_s\sin^2\theta_s + \cos^2\theta_s \\ -\sin\phi_s\cos\theta_s & -\sin\phi_s\sin\theta_s \end{bmatrix}. \tag{3.61}$$

Equation 3.61 can also be reformulated in the polar coordinate system (r_{BFP}, θ_{BFP}) of the back focal plane using equation 3.59, or reformulated in the cartesian coordinate system (x_{BFP}, y_{BFP}) of the back focal plane using equation 3.60.

The 2D polarization of the collimated beam in $\boldsymbol{S_\infty}$ arising from a source with 3D polarization resulting in polarization orientation vector $\vec{\boldsymbol{\mathcal{E}}} = (E_x\hat{\boldsymbol{x}} + E_y\hat{\boldsymbol{y}} + E_z\hat{\boldsymbol{z}})$ at all points (r_{BFP}, ϕ_{BFP}) via equation 3.59 (or, equivalently (x_{BFP}, y_{BFP}) via equation 3.60) on the back focal plane may then be described by integral convolution of the polarization vector $\vec{\boldsymbol{\mathcal{E}}}_{\boldsymbol{\mathcal{R}'}}$ of every ray $\boldsymbol{\mathcal{R}'}_{(\phi_s,\theta_s)}$ transformed by the corresponding modified Jones matrix (equation 3.61). The convolution corresponds to a double integral over the radial angle $0 \leq \phi \leq 2\pi$ and the azimuthal angle $0 \leq \theta \leq \phi_{max}$.

$$\boldsymbol{\mathcal{E}}_{S_\infty} = \begin{pmatrix} E_x(r,\theta) \\ E_y(r,\theta) \end{pmatrix}_{S_\infty} = E_o \int_{\phi'=0}^{\phi_{max}} \phi' d\phi' \int_{\theta'=0}^{2\pi} d\theta' \left[\boldsymbol{\mathcal{J}}\left(\theta', \phi'\right)\right]^\dagger \cdot \begin{pmatrix} E_x \\ E_y \\ E_z \end{pmatrix} \tag{3.62}$$

Equivalently the reverse transformation corresponding to focus of a collimated beam in $\boldsymbol{S_\infty}$ with 2D polarization $\boldsymbol{\mathcal{E}}_{S_\infty} = (E_x\hat{\boldsymbol{x}} + E_y\hat{\boldsymbol{y}})$ is given by the double integral over the full angular range $0 \leq \phi \leq 2\pi$ and the radial range of the back focal plane radius $0 \leq r \leq \frac{1}{2}d_{BFP}$:

$$\boldsymbol{\mathcal{E}}_{\boldsymbol{\sigma_S}} = \begin{pmatrix} E_x \\ E_y \\ E_z \end{pmatrix} = E_o \int_{r'=0}^{r_{BFP}} r' dr' \int_{\theta'=0}^{2\pi} d\theta' \left[\boldsymbol{\mathcal{J}}\left(r', \theta'\right)\right] \cdot \begin{pmatrix} E_x(r', \theta') \\ E_y(r', \theta') \end{pmatrix} \tag{3.63}$$

The last element to include in this analysis is the 3D polarization $\boldsymbol{\mathcal{E}}_{\mathcal{R}'}$ of all rays $\boldsymbol{\mathcal{R}'}$ intersecting each point on the back focal plane, originating from a single linear dipole source $\vec{\boldsymbol{\rho}} = (\rho_x\hat{\boldsymbol{x}} + \rho_y\hat{\boldsymbol{y}} + \rho_z\hat{\boldsymbol{z}})$. The 3D polarization of a ray $\boldsymbol{\mathcal{R}'}$ with orientation (θ, ϕ) and propagation direction $\hat{\boldsymbol{k}}_{\mathcal{R}'} = (\sin\phi\cos\theta\hat{\boldsymbol{x}} + \sin\phi\sin\theta\hat{\boldsymbol{y}} + \cos\phi\hat{\boldsymbol{z}})$ is given

by:

$$\boldsymbol{\mathcal{E}}_{\mathcal{R}'} = \hat{\boldsymbol{k}}_{\mathcal{R}'} \times \vec{\boldsymbol{\rho}} \times \hat{\boldsymbol{k}}_{\mathcal{R}'}$$

$$= \begin{pmatrix} \Big[\left(\cos^2\phi + \sin^2\phi \sin^2\theta\right) \sin\Phi \cos\Theta - \sin\phi\cos\phi\cos\theta\cos\Phi \\ \qquad - \sin^2\phi \sin\theta\cos\theta\sin\Phi\sin\Theta \Big] \\ \Big[\sin^2\phi\sin\theta\cos\theta\sin\Phi\cos\Theta - \sin\phi\cos\phi\sin\theta\cos\Phi \\ \qquad + \left(\sin^2\phi\cos^2\theta + \cos^2\phi\right)\sin\Phi\sin\Theta \Big] \\ \Big[-\sin\phi\cos\phi\cos\theta\sin\Phi\cos\Theta + \sin^2\phi\cos\Phi \\ \qquad - \sin\phi\cos\phi\sin\theta\sin\Phi\cos\Theta \Big] \end{pmatrix} \tag{3.64}$$

$$\Phi = \cos^{-1}\left(\frac{\rho_z}{\|\vec{\boldsymbol{\rho}}\|}\right) \tag{3.65}$$

$$\Theta = \tan^{-1}\left(\frac{\rho_y}{\rho_x}\right) \tag{3.66}$$

Plugging equations 3.64 into the integrand of equation 3.62 results in lengthy expressions that must be solved by numerical methods. In general, however, one can make several conclusions based on the cylindrical symmetry of the optical system depicted in Figures 3.11−3.14. In particular, to focus a collimated beam the objective lens must refract rays at opposing points of the back focal plane in opposite directions, resulting in:

$$\left\langle \left[\boldsymbol{\mathcal{J}}_{Obj}(r,\theta) \cdot \boldsymbol{\mathcal{E}}_{x,y}(r,\theta)\right], \hat{\boldsymbol{z}} \right\rangle = -\left\langle \left[\boldsymbol{\mathcal{J}}_{Obj}(r,\theta+\pi) \cdot \boldsymbol{\mathcal{E}}_{x,y}(r,\theta+\pi)\right], \hat{\boldsymbol{z}} \right\rangle \tag{3.67}$$

Therefore focusing a collimated excitation source that is radially symmetric (satisfying the condition $\left\{E_x = f_X(r), E_y = f_Y(r)\right\}$) yields zero net $\hat{\boldsymbol{z}}$ polarization

component at the focal point (Figure 3.13) because the radial (ϕ') integral term in 3.63 is performed over the full angular range $0 \leq \phi' \leq 2\pi$.

From equation 3.67 it becomes clear that in order to create a $\vec{\boldsymbol{\rho}}_{\boldsymbol{z}}$ component to the excitation polarization at the objective focus it is necessary to induce a radial ($\hat{\boldsymbol{r}}$) polarization component to the excitation beam in $\boldsymbol{\mathcal{S}}_{\boldsymbol{\infty}}$. Although the experiments presented here have used only excitation sources of radially symmetric polarization, radial polarization asymmetry has been reported recently in the literature, generally induced in the excitation beam by addition of a spatially non-uniform retarder element.[279,280] This provides the potential to collect 3D orientation information from a single-dipole object in the focal volume, although the method has yet to prove experimentally fruitful.[281,282] Additionally, radially and azimuthally polarized excitation beam sources have been shown to induce point spread functions that are spatially distinct from those generated by a beam of uniform polarization.[283–285] Radially polarized excitation in particular has been proved to yield a sharper *psf* than uniformly oriented polarization.[286,287] However, the local electromagnetic field polarization at subwavelengh dimensions immediately surrounding an optical focus is spatially inhomogenous, and rigorous determination of its spatial distribution requires numerical methods.[288]

For signal collection from a single dipole source (Figure 3.14), because the $\hat{\boldsymbol{z}}$ component of $\vec{\boldsymbol{\rho}}_{\mathbf{0}}$ is transformed into a radial component of the emission beam, its *net* spatial average integrated across the entire beam is *zero*. However, if the emission beam is subsequently separated into orthogonal components using a birefringent beamsplitter, each of which is then measured in separate emission channels, the result is a signal detected in *both* channels that is proportional to ρ_z. Calculation of

the expected signal partition into orthogonally polarized emission channels I_x and I_y from a single linear dipole radiation source necessitates numerically integrating equation 3.62 containing equation 3.64 in the integrand. Using the solution presented in a recent publication by Vanden Bout *et al.*, the signal anticipated from a 1D transition dipole oriented parallel to the vector $\vec{\boldsymbol{\rho}} = (\rho_x, \rho_y, \rho_z)$ in the laboratory reference frame (Figure 3.14) is given by:[289]

$$\begin{aligned} I_x &= I_o \left(A + B\sin^2\Phi + C\sin^2\Phi\cos 2\Theta\right) \\ &= I_o \left[A + B\left(\frac{\rho_x^2+\rho_y^2}{\rho_x^2+\rho_y^2+\rho_z^2}\right) + C\left(\frac{\rho_x^2+\rho_y^2}{\rho_x^2+\rho_y^2+\rho_z^2}\right)\left(\frac{\rho_x^2-\rho_y^2}{\rho_x^2+\rho_y^2}\right)\right] \end{aligned} \tag{3.68}$$

$$\begin{aligned} I_y &= I_o \left(A + B\sin^2\Phi - C\sin^2\Phi\cos 2\Theta\right) \\ &= I_o \left[A + B\left(\frac{\rho_x^2+\rho_y^2}{\rho_x^2+\rho_y^2+\rho_z^2}\right) - C\left(\frac{\rho_x^2+\rho_y^2}{\rho_x^2+\rho_y^2+\rho_z^2}\right)\left(\frac{\rho_x^2-\rho_y^2}{\rho_x^2+\rho_y^2}\right)\right] \end{aligned} \tag{3.69}$$

$$A = \frac{1}{6} - \frac{1}{4}\cos\phi_{max} + \frac{1}{12}\cos^3\phi_{max} \tag{3.70}$$

$$B = \frac{1}{8}\cos\phi_{max} - \cos^3\phi_{max} \tag{3.71}$$

$$C = \frac{1}{48}\left(7 - 3\cos\phi_{max} - 3\cos^2\phi_{max} - \cos^3\phi_{max}\right) \tag{3.72}$$

where ϕ_{max} is governed by the objective numerical aperture and refractive index according to eq 3.29.

The most important conclusion arising from equations 3.68−3.72 is that for an optical system with nonzero numerical aperture *both* polarization channels will detect signal even if the dipole radiation source is oriented *parallel* to the optical axis. Additionally, the total signal measured between the two channels, $I_{tot} = I_x + I_y$ is strongly dependent upon the dipole orientation angle Φ relative to the optical axis.

Figure 3.15 shows the dependence of A, B and C (equations 3.70−3.72) upon the objective numerical aperture. The total signal $I_{tot} = I_x + I_y$ also increases with the numerical aperture, as discussed further in Section 5.3.2 (figure 5.13, p. 209).

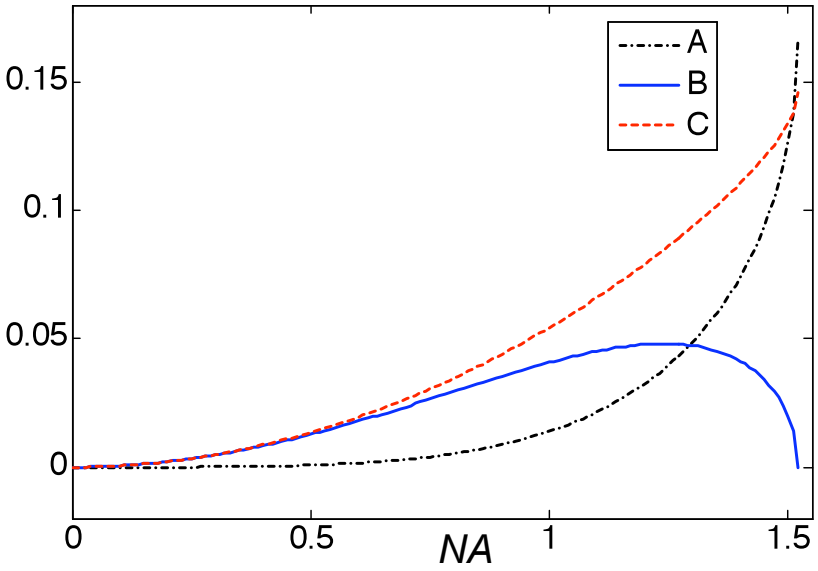

Figure 3.15: Dependence of factors A, B and C on the numerical aperture of the objective lens, calculated from equations 3.70−3.72.

In the limit of low numerical aperture ($NA \ll 1$) $\phi_{max} \approx 0$, and we can use the binomial theorem to make the approximations $\cos\phi_{max} \approx (1 - \phi_{max})$, $\cos^2\phi_{max} \approx (1 - 2\phi_{max})$, and $\cos^3\phi_{max} \approx (1 - 3\phi_{max})$. Plugging these approximations into equations 3.68−3.72 yields $A = 0$, $B = \frac{\alpha}{4}$ and $C = \frac{\alpha}{4}$ for the low-NA limit. Consequently $(I_x/I_y) = \left(\frac{1+\sin 2\theta}{1-\sin 2\theta}\right)$, and $I_{tot} \propto \cos^2\phi$, in perfect agreement with equations 3.51−3.53 derived for the zero-NA system (Figure 3.10, p. 102).

3.3 Construction of a Two-Channel Scanning Confocal Optical Microscope with Single-Photon Sensitivity

3.3.1 Optical Componentry

A schematic illustration of the optical components of the microscope is shown in figures 3.16 and 3.17. Briefly, excitation is selected from one of the available wavelengths (λ_{ex}=405nm,λ_{ex}=488nm,λ_{ex}=532nm,λ_{ex}=635nm), attenuated to the desired power, spatially filtered, and expanded to a beam of known diameter and approximately Gaussian intensity along the radial dimension (figure 3.16a). The beam is aimed by a pair of two-axis mirrors and passes through a dichroic beamsplitter (various, Chroma) before entering the back aperture of a $1.45NA$ infinity-corrected objective lens (Olympus Plan Apo 60x 1.45NA ∞/0.17 TIRFM) and focused to a diffraction-limited spot in the sample. The sample, prepared on a glass coverslip, is mounted on a custom-machined aluminum stage block mounted on a Newport 406 2-axis stage holding a piezoelectric actuator scanner (PI P-621.2CD) raster-scanned by a 2-axis close-loop amplifier (PI E-500). The large mass of the aluminum stage block provides a thermal buffer for the objective and sample, the temperature of which is measured by a thermocouple placed in direct contact with the glass coverslip $\leq$ 2mm offset from the optical axis. Fluorescence emission from the sample is collected by the same objective lens, passes through the primary dichroic beamsplitter in the opposite direction from the laser excitation source, and is focused by an imaging lens of known focal length F_I onto a confocal pinhole P_c positioned at the conjugate image plane $\boldsymbol{\sigma}_I$. The optical signal passing through the confocal pinhole is split into

two channels, each of which corresponds to a photodetector with single-photon sensitivity (SPCM-AQR-15, Perkin Elmer). The detector output is collected either by PC counter boards (MCS-pci, Ortec) for numerical post-processing in Matlab, or by hardware correlator (Flex5000, Correlator.com) for direct acquisition of auto- and cross-correlation traces. Individual optical mounts are listed in contextual context in the captions of figures 3.16 (p. 119) and 3.17 (p. 122).

Details of the spatial filter and beam expansion telescope are shown in Figure 3.16a. Spatial filtering (Thorlabs KT310, P15S and C220TME-A) of the excitation beam beam yields a radially symmetric Gaussian intensity profile free of aberration introduced by the attenuating filters (Thorlabs NE01 series) or the laser source itself. Mounting the telescope's second lens L_{t2} (Thorlabs ACN254) on an optical-axis linear translation stage (Thorlabs CT1/CT101) permits fine-tuning of the beam collimation and subsequently the z-axis position of the focus at the sample plane. The calibrated iris aperture (Thorlabs SM1D12C) permits adjustment of the beam diameter and subsequently the effective numerical aperture of the objective (Olympus Plan Apo 60x 1.45NA ∞/0.17 TIRFM). Overfilling of the objective back aperture with a beam diameter $D_l \geq 7.5$mm yields the full numerical aperture of 1.45. Reducing the beam diameter results in a non-linear but monotonically decreasing effective NA. The exact mapping of beam diameter at the objective back aperture to NA of the laser focus is determined experimentally by placing a hemispherical lens at the objective focus and manually measuring the cone angle of the emitted laser light resulting from varying beam width.

Details of the excitation pathway optically downstream of the spatial filter and beam expander are shown in figure 3.16b. Excitation wavelengths are selected from

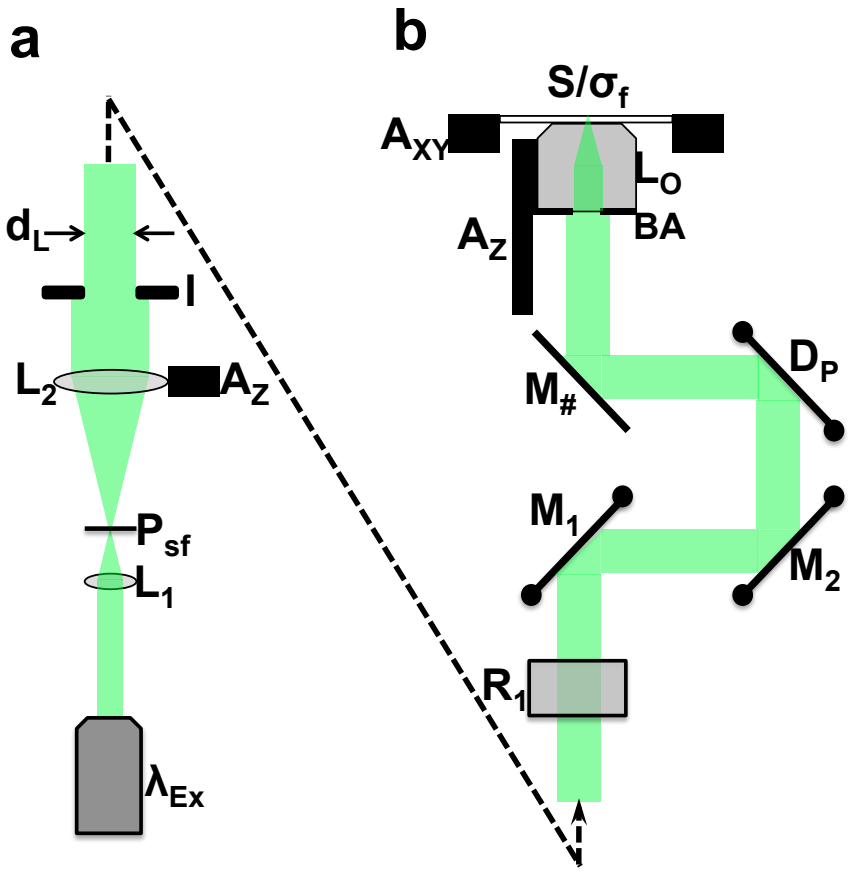

Figure 3.16: Optical microscope excitation pathway. **(a)**: The beam from a laser excitation source of wavelength λ_{ex} is first focused by a short-f.l. lens L_1 onto a spatial filter pinhole P_{sf}. The focused laser is collimated by a second lens L_2 held by an optical-axis linear translation mount. The expanded beam is sized by a calibrated iris aperture I to a known diameter d_L. **(b)**: This collimated beam of diameter d_L is assigned a desired polarization state using a variable retarder R_1, and then aimed by a pair of two-axis gimbal-mount mirrors M_1 and M_2 before reflecting off the primary dichroic D_P and a final 2" metallic mirror $M_\#$ and entering the back aperture (BA) of the objective lens L_O The objective lens is held on a single axis kinematic mount A_Z that translates it parallel to the optical axis. The sample S at the focal plane $\boldsymbol{\sigma_f}$ sits on a two-axis translation stage A_{XY}.

$\{\lambda_{ex} = 405, 488, 532, 635\}$nm using laser sources {Crystalaser 405 25mW OEM, Spectra Physics BeamLok, Intelight 12M10, Thorlabs LDM635}. The collimated laser beam is converted to either linear or circular polarization (or to any arbitrary polarization state) by a variable retarder element (New Focus 5540), and then aimed using a pair of two-axis gimbal mirror mounts (New Focus 9812) onto a 1"x2" rectangular dichroic beamsplitter (Chroma {Z405RDC, Q497lp, Z532RDC, Z633RDC} for $\{\lambda_{ex} = 405, 488, 532, 635\}$nm). The excitation beam reflects off a final 2" diameter metallic mirror (Thorlabs PF20-03-P01) before entering the back aperture of the objective lens, mounted on a stacked manual linear actuator (Thorlabs PT1) and open-loop piezoelectric linear actuator (Thorlabs AE0505D18) for adjusting the focal plane along the z-axis.

The sample sits on the custom stage and may be raster-scanned (if desired) in the x-y sample plane by a (PI P-621.2CD) 2D linear actuator via a closed-loop voltage source (PI E-500) controlled by a voltage acquisition and manipulation hardware board (National Instruments PCI-6014) and software programmed in LabView (National Instruments).

The emission pathway is illustrated in Figure 3.17. Fluorescence emitted from the sample is collected and collimated by the objective, and reflects off the common mirror before passing through the primary dichroic beamsplitter. It is then focused by an imaging lens (Thorlabs ACN254) with a focal length of 200–400mm onto a confocal pinhole P_c positioned at the conjugate image plane $\boldsymbol{\sigma}_I$ by a 3-axis manual linear translation mount (Thorlabs MT3). The magnifying power of the lens system is governed by the nominal magnification of the objective lens and the focal length of the imaging lens. The magnification of an infinity-corrected objective is defined

by the manufacturer relative to an imaging lens having 200mm focal length. In all experiments presented here a 300mm focal-length lens was used, resulting in an effective 90x magnification. For true confocality, the pinhole diameter must be equal to 1 Airy unit, calculated to be $\left(\frac{1.22\sqrt{\lambda_{ex}\lambda em}F_I M_o}{200NA}\right)\mu m$, where λ_{ex} and λ_{em} are the excitation and emission wavelengths, respectively. The exact values of λ_{ex} and λ_{em} vary for specific experiments, but in almost all cases 1 Airy unit calculated as above corresponds to $\sim 42\mu m$. A pinhole of nominal diameter $50\mu m$ (Thorlabs P50S) was used unless otherwise noted. The pinhole is mounted on a three-axis manual linear actuator (Thorlabs MT3) to facilitate alignment of the emission and excitation point spread functions in three dimensions.

The emission collection pathway optically downstream of the confocal pinhole was constructed so as to be customizable based on the needs of the experiment. The general pathway architecture, shown in Figure 3.17, consisted of a common collimating lens (Thorlabs ACN254) of focal length 60mm, a beamsplitter BS $\{$dichroic (Chroma), polarizing (Newport 05FC16PB.5), or 50:50 non-polarizing (Thorlabs BS010)$\}$ held on a kinematic mount (Thorlabs KM100P), a pair of filters (F_1, F_2) and two free-space avalanche photodiode detectors (D_1, D_2), (both SPCM-AQR-15). The filters corresponding to the two detection channels can be either spectral bandpass filters (HQ series 1" diameter, Chroma) or linear polarizers (Thorlabs LPVISB100), depending on the needs of the experiment. Each APD has a corresponding 60mm focal length lens (Thorlabs ACN254) to focus optical signal onto its active element, and is positioned manually in three dimensions by linear actuators (Thorlabs PT1) to facilitate maximum collection efficiency. For every incident photon, the APD produces a transistor-transistor logic (TTL) voltage pulse of 15ns duration and ≈2.5V amplitude for each incident photon, with quantum efficiency 60–70% across the spectral

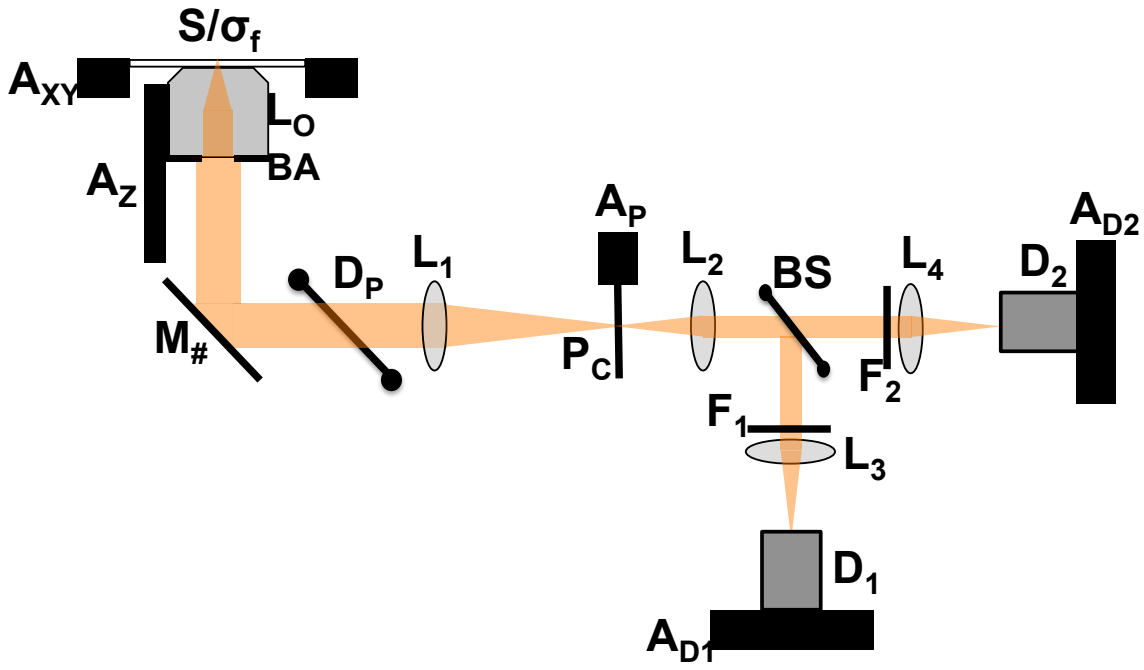

Figure 3.17: Optical microscope emission pathway. Optical signal from the sample S at the focal plane $\boldsymbol{\sigma_f}$ is collected by the same objective lens L_O as in Figure 3.16. Collected emission reflects off the 2" metallic mirror $M_{\#}$, passes through the primary dichroic D_P, and is then focused by an imaging lens L_1 onto a confocal pinhole P_C held on a 3-axis translation mount A_P at the conjugate image plane of $\boldsymbol{\sigma_f}$. The emission beam is then re-collimated by a second lens L_2 and split by a beamsplitter BS into two detection channel pathways. The reflected beam is filtered by F_1 and focused by lens L_3 onto the active element of avalanche photodiode D_1 held on a 3-axis translation mount A_{D1}. The transmitted beam is filtered by F_2 and focused by lens L_4 onto the active element of avalanche photodiode D_2 held on 3-axis translation mount A_{D2}.

range 550–800nm.

3.3.2 Computer Hardware and Software

TTL pulses from the detectors may be acquired directly as photon counts using PC counter boards (Ortec MCS-pci), or as a time correlation profile using a hardware correlator (Flex5000, Correlator.com). If collected directly as photon counts, the TTL pulses are routed via coaxial cable to a pair of synchronized counter boards operated by PC and controlled with LabView sofware (National Instruments) running on a Windows operating system. Each TTL pulse generated by detection of a single photon has a roughly 1% probability of being followed by a second pulse within $\lesssim 1\mu$s, an artifact known as 'afterpulsing.' Although this artifact has little or no effect on intensity and cross-correlation measurements because it occurs via equivalent but statistically independent stochastic processes in the two detectors, it strongly influences autocorrelation measurements from each detector at timescales $\leq 1\mu$ s.

The control and acquisition software written in LabView synchronizes photon count collection from the two detector channels with movement of the sample by specified lengths at known time intervals. The written data file consists of a list of photon counts from both detector channels for sequential time windows, and contains header information specifying user-defined parameters from the software GUI, including number of time bins (each corresponding to a pixel), raster step-size, and dwell time. Simple processing of this data file in Matlab produces the 2D intensity profile from each detector channel as an image.

Alternately, the output of both photon counters may be routed directly into the hardware autocorrelator (Flex5000, Correlator.com). The data output from the hardware correlator consists of time windows ranging from 100ns to half the duration of the experiment, each of which has a normalized auto- or cross-correlation value with arbitrary units and baseline value 1. Unfortunately, the correlator is incompatible with LabView, but may be programmed for simple automated collection by scripting in Flex5000 software provided by the manufacturer. Of notable importance is the fact that for autocorrelation measurements, values for time windows $\lesssim 1\mu$s are anomalously high due to the APD afterpulsing artifact. This effect is not present in the cross-correlation data because of the statistically independent nature of the afterpulses by the two detectors.

Chapter 4

Fluorescence Fluctuation Analysis

Abstract

This chapter begins with a literature review of fluorescence fluctuation spectroscopy, with particular emphasis on biophysical investigations. Following this is description of a series of experiments involving collection of population-resolved data collected from single Förster resonance energy transfer fluorphore pairs conjugated to DNA oligomers as they undergo cleavage by restriction endonucleases. The endonuclease enzyme Michaelis constants K_M measured for EcoRI and BglI via fluorescence burst analysis were in agreement with prior literature. The success of these experiments provide concrete confirmation of the microscope's fluorescence emission sensitivity and detection channel selectivity in the context of single-molecule experiments. The chapter concludes with description of a generalized formalism for correlation-based analysis of fluorescence signal collected using the two-channel microscopy system described in Chapter 3. Particular focus has been directed toward the theoretical auto- and cross-correlation traces anticipated from polarization-sensitive bivariate time series of photoluminescence emission from freely-rotating transition dipoles. The derived correlation trace equations provide essential mathematical models to

which the experimental data presented in Chapter 5 was subsequently fit in order to extract characteristic time constants associated with liquid-phase translation and diffusion.

4.1 Fluorescence Fluctuation Spectroscopy

4.1.1 Stochastic Fluctuations in Microscale Systems

Fluorescence fluctuation spectroscopy (FFS) represents a generalized signal-processing approach wherein statistical analysis of one or more fluorescence intensity time series reveals information regarding the nature of the underlying chemical or biological processes.[290] The powerful first-principles postulate that has provided the foundation for FFS theory and its successful evolution into a variety of derivative techniques is the understanding that the spontaneous fluctuations arising from a stochastic process fundamentally possess information content about both its underlying mechanistic architecture and the free energy landscape over which its stochastic path evolves with time. Every stochastic process can be cast in terms of a temporal sequence of random variables. When one or more of these variables expresses realized values in the form of a fluorescence signal that reports its state, statistical analysis of the resulting time series fits into the paradigm of FFS.

It is important, however, to acknowledge FFS as a special case within the broader scope of statistical time series analysis, a case for which the realized variable values are measured in the form of a fluorescence signal. Fluorescent signal sources are an experimentally convenient tool for system state measurement, particularly by virtue of their noninvasive nature and ease of introduction into biological and chemical sys-

tems, but they also represent just one possible measurement type. As the merging scientific frontiers of single-molecule measurement and stochastic nonequilibrium statistical mechanics become further intertwined, statistical assessment of spontaneous fluctuations will become a progressively more relevant analytic platform.

The spontaneous fluctuations arising from nonequilibrium systems are fundamentally distinguishable from those corresponding to equilibrium systems regardless of their scale.[171,291–301] Two nonequilibrium processes commonly encountered in fluorescence fluctuation spectroscopy are triplet-state 'blinking' of fluorescent dyes,[302,303]and quantum yield fluctuations of semiconductor nanocrystals,[304–308] both of which are photosensitive processes strongly dependent upon irradiance intensity. Concentration fluctuations displayed by components of a nonequilibrium chemical system are also distinctly different from those of a similar system operating under equilibrium conditions.[292,309–314] The smallness of scale and discreteness of components in many biological contexts magnifies the importance of these fluctuations. Stochastic fluctuation within intracellular processes is an unavoidable phenomenon and in many instances is neither subtle nor superfluous. Gene expression, for example, is a fundamentally noisy nonequilibrium process, and evolution has tended to promote organisms that benefit rather than suffer from these fluctuations.[315–334] In some cases the stochastic nature of biochemical networks can give rise to collective system-wide behavior, such as coordinated oscillations or bistability, even if the corresponding deterministic system would not exhibit that behavior.[335–338]

Single molecule interrogation represents the experimental limit of the combination of low concentration and miniscule dimensions, and the probabilistic nature of the behavior expressed by individual molecules can reveal a wealth of information otherwise

lost through averaging in a larger population. Single-molecule forced extension and relaxation experiments, carried out using both optical and mechanical force reporters on a variety of nucleic-acid and protein substrates have demonstrated free-energy dissipation processes that are absent from larger ensemble systems.[160,161,163–166,339–344] However, even at spatial and temporal scales relevant to complete cellular systems (microns and miliseconds), transient violations of the second law of thermodynamics such as net entropy consumption are commonplace.[291,345,346] These phenomena are reconciled with classical statistical mechanics, however, by the fact that the ergodic nature of the underlying system yields time- and path-averaged behavior that converges to agreement with the second law.[298,347] This is further corroborated by the experimental reconstruction of complete local equilibrium free energy landscapes solely from repeated nonequilibrium measurements.[172,293,348–350] Analogous experiments have recently been described using fluorescence state reporters in place of mechanical or optical trap force measurements, such as iterative chemically-induced unfolding and refolding of RNA containing a structurally sensitive FRET pair.[271] Similar theoretical frameworks have also been applied successfully to time series trajectories of single enzymes[351–354] and other multi-state macromolecular chemical cycles.[355,356]

4.1.2 Fluorescence Correlation Spectroscopy

Two of the most ubiquitous varieties of FFS are fluorescence correlation spectroscopy (FCS) and fluorescence cross-correlation spectroscopy (FCCS), both of which represent highly practical special cases in which the fluctuating time series signals are analyzed by numerical correlation methods.[303,357–362] Although fluorescence correlation spectroscopy was originally introduced over three decades ago as

a means of investigating spontaneous diffusion behavior of macromolecules, prior to the widespread proliferation of high-numerical-aperture confocal microscopy tools these methods were limited to relatively large observation volumes and relied upon very long integration periods to extract statistical averages from the correspondingly spontaneous concentration fluctuations.[363–368] The first FCS studies using modern confocal optics and interrogating one molecule at a time (on average) were not reported until 1994.[369]

All FCS methods utilize calculation of the auto- or cross-correlation from fluorescence time series as the numerical tool with which to assess statistical dependence of a stochastic process upon either its own history or the history of a related process. These processes may vary across broad timescales, from picoseconds for the antibunching of fluorescence emission from single photon sources,[370–375] to tens of seconds for the slow translational, orientational or structural diffusion of macromolecules in vitreous environments.[233,234,244,376–380] At the shortest timescales, FCS experiments are limited by quantization of photon emission, or by uncorrelated hardware noise overwhelming a small correlated signal. At long timescales FCS experiments are limited by either photobleaching of immobilized species or by the diffusion of free molecules away from the observation volume. Recent advances in dynamic single-particle tracking by adaptable feedback-controlled confocal optical setups have extended the timescale over which measurements of a freely-diffusing species can be made, but these methods have not yet found widespread use.[274]

When applied in a confocal microscopy context, the slowest process observable by FCS is generally statistical variation of the number of fluorophores diffusing into and out of a confocal observation volume, which occurs at a characteristic timescale

governed by the volume dimensions and the fluorophore diffusion constant. Below this timescale the number of fluorophores, and therefore also the measured optical signal tends to have a greater degree statistical predictability based on its recent history. For observation windows longer than the diffusional timescale, diffusion of fluorophores away from the observation volume and their subsequent intermingling with the indistinguishable bulk population yields statistically independent fluctuations and therefore a significant and quantifiable reduction in the signal autocorrelation. FCS has thereby proven useful for measuring translational diffusion coefficients.[191,381] Consequently it is also effective in detecting processes that induce significant changes in a fluorescent species' hydrodynamic radius, such as those induced ligand-receptor binding and dissociation. It is also used to observe translational diffusion of membrane-bound species[382–386] or reversible interactions with 2-D membrane structures.[387] Additionally, the noninvasive nature of FCS has made this experimental methodology particularly applicable to intracellular measurements *in vivo* and *in situ*.[388–394]

As fluorophores spontaneously diffuse throughout the confocal probe volume under the influence of stochastic Brownian motion, the measured fluorescence signal will fluctuate based on the number of emissive fluorophores present, as illustrated in Figure 4.1. These fluctuations rise in prominence in inverse proportion to the fluorphore concentration. When the fluorphore concentration is very low ($\lesssim$ 1nM), the probe volume will frequently contain no fluorophore, and during those time windows the fluorescence signal will be at the background level. Individual isolated spikes of fluorescence correspond to the transit of single fluorophores through the probe

volume.

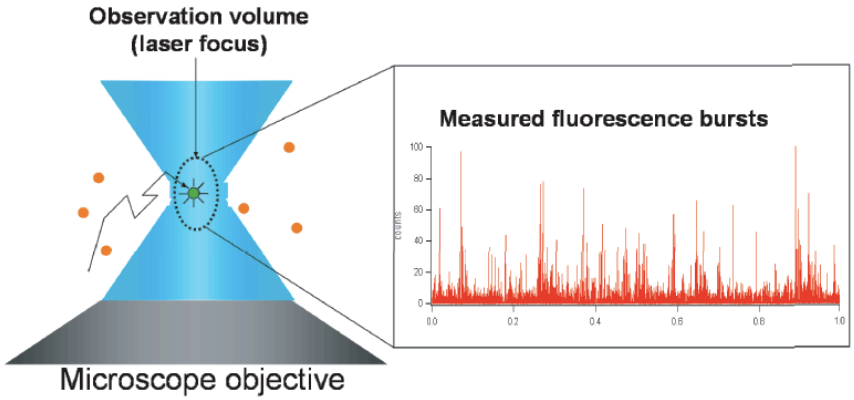

Figure 4.1: Illustration of the time-varying fluorescence signal arising from single fluorophores transiting a confocal probe volume. At sufficiently low sample concentrations the fluorescence time series (red) will display discrete bursts corresponding to the transit of single fluorophores through the probe volume.

If emission from two distinguishable fluorescence species is collected as separate time series, cross-correlation of the signals will convey whether or not the corresponding processes are statistically correlated. For example, if the signals from two spectrally distinct fluorophores are collected in separate channels of a confocal microscope, cross-correlation reveals whether the two species tend to traverse the observation volume jointly or singly. The time-dependence of the cross-correlation signal has frequently been used to observe enzymatic cleavage of nucleotides[388,395] and proteins.[390,396]

Within the characteristic time window during which a freely diffusing fluorophore tends to reside predictably within the confocal observation volume, additional stochastic processes that cause changes in the fluorescence emission will also be observable

within the correlation trace. These changes may arise from rapid molecular associations,[397–407] unimolecular transitions between fluorescent and non-fluorescent states of a molecule,[191,302,408] spontaneous structural fluctuations,[409–411] or a combination of processes. The characteristic time at which a sub-diffusional correlation motif appears in the resulting data will reveal the kinetic information of the underlying processes, and the relative magnitude of the motif is indicative of the participating fractional population as well as its impact on the measured fluorescence signal. FCS applied to fluorophore-quencher systems will frequently reveal the presence and nature of structural fluctuations.[323,412–416]

Recent years have seen significant expansion in the scope of fluorescence fluctuation analysis, and its general success as an analytic tool has also given rise to an array of derivative methods. When combined with near-field optical excitation,[220,417,418] evanescent-wave microscopy,[419] or molecular confinement within sub-wavelength physical structures,[420,421] FCS can investigate systems at significantly smaller dimensions and correspondingly higher sample concentrations than those accessible by conventional confocal microscopy.

Photon-counting histogram and fluorescence cumulant analysis (FCA) distinguish molecular species based upon their inherent brightness.[273,411,422–424] Fluorescence parameter distribution in heterogeneous systems may also be assessed using MEMFCS, in which the standard FCS model is subject to a maximum-entropy fitting routine. Time correlated single photon counting (TCSPC) yields data sets and correlation measurements that can span the full timescale range from picoseconds to thousands of seconds. This permits the subsequent extraction of all time-correlated behavior (including traditional FCS) across enormous timescales within a single experiment.

The technological tools necessary for TCSPC are, however, relatively recent and have not yet seen widespread use.[377, 425–430]

Lastly, image correlation spectroscopy (ICS), also frequently termed 'scanning FCS' is another FFS-derivative method in which spatial signal fluctuations, in addition to temporal ones are subject to correlation analysis.[431–436] The similar recently developed technique of multi-focus FCS permits accurate extraction of diffusion parameters without the necessity of prior calibration of confocal point spread function dimensions.[357, 437–442]

4.1.3 Fluorescence Burst Analysis and Förster Resonance Energy Transfer

The field of single-molecule fluorescence microscopy of chemical species includes numerous experimental methods closely related to fluorescence fluctuation spectroscopy. Coincidence analysis using two or more collection channels similarly discriminates rare events arising from sparse molecular species in the presence of significant fluorescent background.[443, 444] Fluorescence burst analysis similarly relies upon collection of the statistical distribution of the emission partition ratio into a pair of collection channels to reveal structural sub-populations of labeled macromolecules.[252, 273, 445–457]

Fluorescence coincidence analysis, fluorescence burst analysis, and numerous immobilized single-molecule experiments rely upon the phenomenon of FRET, an acronym frequently expanded as 'fluorescence resonance energy transfer', but herein always substituting for 'Förster resonance energy transfer' in reference to its original theorist. FRET is a nonradiative energy transition occurring between two fluorescent

transition dipoles separated by a small distance (typically less than 100Å), the transfer rate of which is a function of separation, dipole alignment, and the spectral resonance between the fluorescence emission dipole of the shorter-wavelength species and the excitation dipole of a longer-wavelength species. The short- and long-wavelength fluorophores constituting a FRET pair are termed the 'donor' and 'acceptor', respectively. The FRET mechanism is nonradiative and probabilistic in nature, and has a relatively straightforward derivation in quantum mechanics. A simplistic analogy is the ringing of an otherwise unexcited tuning fork held near a second mechanically-excited tuning fork with a fundamental frequency very close to that of the first. Förster's rigorous derivation of the FRET mechanism reveals a very sensitive (r^{-6}) dependence of energy transfer probability upon the donor-acceptor transition dipole separation.[458–462]

FRET has evolved into an extremely popular tool among biologists and biophysicists due to this very high spatial sensitivity as well as to the fact that the range of measurable energy-transfer dependence (roughly 2–10nm) corresponds closely with the dimensions of structural changes in enzymes, signaling proteins, allosteric regulators, catalytic nucleic acids, and other biological macromolecules. With judicious selection of the donor and acceptor fluorophores, single-pair FRET detection is feasible using common optical microscopy hardware, and has been reviewed extensively in the context of structural changes among enzymes, signaling proteins, nucleic acids and other biomacromolecules.[195,463–470] FRET microscopy approaches have also commonly been combined with the statistical tools of correlation analysis to reveal kinetic processes associated with rapid structural fluctuations or association-dissociation reactions.[251,371,403,409,428,454,456,471–477] The addition of polarization sensitivity to the excitation and emission pathways in a FRET system reveals further dynamic struc-

tural information information.[446,478,479] The use of multiple interleaved excitation pathways has demonstrated the potential to significantly extend FRET sensitivity,[265,313,480] with resolution to the degree of $< 1\%$ energy transfer efficiency being achieved for single molecule substrates by using a photo-activated donor dye,[481] or photo-switched acceptor.[482]

Among the drawbacks of biological FRET experiments, as well as those of any fluorescence investigations involving labeling with fluorescent dyes or other reporters, is the potential to interfere with the sensitive structural machinery of biological macromolecules.[483,484] FRET-labeled DNA conjugates display significant deviations from ideal behavior, dependent on the specific dyes and labeling locations.[458,460] In addition to the influence of fluorescent labels upon the native substrate behavior, the substrate itself can also alter the photophysical properties of the label, effects that are more prominent at the level of single-molecule observation than in bulk fluorescence experiments.[415,458–460,485,486] The popular Cy3 fluorescent tag, for example, exhibits fluorescence quenching via photoelectron transfer when in close proximity to guanosine nucleotides.[487] Corroborating conclusions have also been obtained from bulk anisotropy measurements of DNA aptamers,[485] and by using polypyroline helices in place of nucleic acids as the structural backbone.[488]

4.2 Confocal Fluorescence Correlation Spectroscopy of Fluorescence Dyes and Dye-Labeled Biomacromolecules

In order to test the sensitivity and accuracy of the multichannel confocal fluorescence microscopy setup described in Section 3.3, we have carried out a series of FCS, FCCS and fluorescence burst analysis experiments using restriction enzymes and DNA oligomers labeled with single fluorescent dyes and single FRET pairs. Correlation measurements confirm both the diffusive behavior of the labeled DNA and the nonequilibrium photophysics of the uorescent labels. Inclusion of a restriction endonuclease recognition sequence in the DNA oligomer located between the conjugated donor and acceptor dyes also permits observation of the changing distribution of energy transfer ratios as a means of following enzymatic cleavage of the DNA oligomer.

The autocorrelation trace collected from a single emission channel will convey the parameters governing the diffusion of fluorescent species with emission corresponding to that channel's spectral range, as well as any processes that alter fluorescence intensity of individual molecules while they diffusively transit the confocal probe volume.[302,303] Figure 4.2 illustrates the expected influence of photoinduced triplet-state fluorescence intermittency ('blinking') upon the measured autocorrelation trace.

4.2.1 Materials and Experimental Methods

The microscopy setup illustrated in Figures 3.16 (p. 119) and 3.17 (p. 122) was used with a longpass dichroic (Chroma Q497lp) for the primary dichroic mirror, a

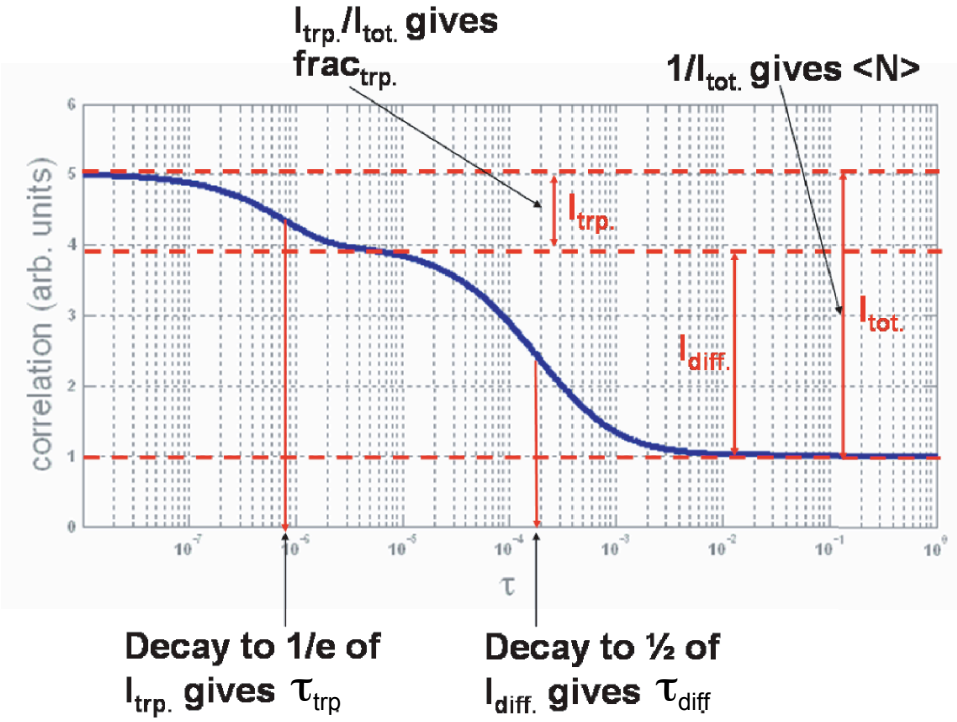

Figure 4.2: Theoretical autocorrelation trace corresponding to a single freely diffusing dye species displaying fluorescence intermittency caused by excitation-induced 'blinking'. If the timescales of diffusion and blinking are separated by two or more orders of magnitude, the components of the correlation trace corresponding to the two processes are easily distinguished both qualitatively and quantitatively as shown.

longpass dichroic (565dcxr, Chroma) for the emission beamsplitter, and bandpass filters for additional spectral filtering in the detection channels (HQ530/30bp for channel 1, HQ630/50 for channel 2). A pinhole size of $50\mu m$ was used unless otherwise noted.

Labeled DNA sequences were prepared in-house using an automated DNA synthesizer (Applied Biosystems). DNA 40-mers were labeled on complementary strands with AlexaFluor 488 succinimide and Texas Red succinimide (both from Molecular Probes/Invitrogen), with the dyes flanking a recognition sequence for the restriction endonucleases BglI (fig. 4.3) or EcoRI (not shown). The dyes were reacted with amine-modied dT bases (10-1039-90, Glen Research) incorporated into the DNA 40-mers at the appropriate sites. EcoRI and BglI were purchased from Roche Applied Science. The remaining reagents used in buffer preparation were purchased from Sigma.

DNA and uorescent dye samples were prepared in buffer containing 50mM Tris, pH 7.5, 100mM NaCl, 10mM $MgCl_2$ and 0.5mM propyl gallate (to minimize photobleaching). 25mm square #1 borosilicate glass coverslips (Corning) were prepared by sonicating for 30 minutes in 70% H_2SO_4/30%H_2O_2. After rinsing each cleaned coverslip with copious amounts of distilled deionized water and blowing dry with N_2 , a slab of poly(dimethylsiloxane) (PDMS, RTV-615, GE) of dimensions roughly 15x15x4mm with a 5mm diameter hole punched through the short axis was bonded to the coverslip overnight at 80°C. Following bonding, the PDMS wells were cleaned again by filling each well with a solution of 10% HCl/10% H_2O_2 /80% H_2O and incubating for 20 minutes at room temperature, followed by rinsing with distilled/deionized water and drying with N_2.

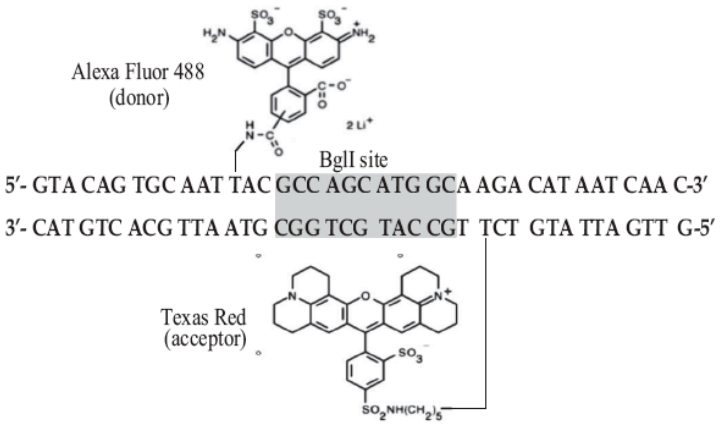

Figure 4.3: Doubly-labeled dsDNA 40bp sequence used for the experiments described in this section, showing donor and acceptor locations relative to the BglI restriction enzyme recognition site. Double stranded DNA identical in sequence to that shown above but lacking the TexasRed label was also used.

Autocorrelation traces collected from labeled DNA samples were fit to equation 4.1 expressing both translational diffusion and triplet-state blinking:[302]

$$\mathcal{G}^{(a,tot)}(\tau) = 1 + \left[1 - F + Fe^{-\left(\frac{\tau}{\tau_{trp}}\right)}\right] \frac{1}{\langle N \rangle} \left[1 + \left(\frac{\tau}{\tau_d}\right)\right]^{-1} \left[1 + \left(\frac{\tau}{a^2\tau_d}\right)\right]^{-\frac{1}{2}} \quad (4.1)$$

where τ_{trp} is the characteristic triplet-state correlation time, τ_d is the characteristic diffusion time, $\langle N \rangle$ is the average molecular occupancy of the probe volume, F is the dark triplet-state fraction, and a is the aspect ratio of the confocal probe volume.

An extended discussion regarding the rigorous derivation of equation 4.1 is presented in Section 4.3.2 (p. 154)

For doubly-labeled DNA samples, burst intensities from both emission channels were collected and processed using equation 4.2 for bursts above a specified intensity threshold to yield histograms of the Förster energy transfer efficiencies:

$$E = \frac{(A - b_A)}{\gamma * (D - b_D) + (A - b_A)} \tag{4.2}$$

where A is the acceptor channel (channel 2) photon count for that burst, D is the donor channel (channel 1) count, b_A and b_D are the acceptor and donor background signals, respectively, and γ is a term accounting for the difference in photon collection efficiencies between the donor and acceptor channels (determined empirically to be $\approx .65$). Fluorescence burst data sets were also obtained from samples of doubly-labeled DNA to which active restriction enzyme (BlgI or EcoRI) was added. The time course of enzymatic cleavage was then followed by observing the continuous population shift within a histogram of FRET efficiencies.[303]

4.2.2 Results and Discussion

Calibration of the confocal probe volume was carried out using aqueous fluorescein as a diffusion standard, for which the literature value of the translational diffusion constant D is $5.4{\cdot}10^{-6} cm^2\, s^{-1}$ at 25°C. The results yielded a minor axis diameter 2ω =437±17nm and aspect ratio a =1.86±.31, in close agreement with the values expected from the analysis of Figure 3.8.

Figure 4.4 presents the influence of excitation intensity upon the collected correlation traces for AlexaFluor 488-labeled DNA, clearly illustrating the effects of triplet-state blinking in agreement with Figure 4.2. The dark-triplet-state fraction

F is smaller at lower excitation intensity, but is present to a measurable degree even in correlation data collected at the minimum excitation power necessary to obtain adequate fluorescence signal ($\approx 1\mu W$).

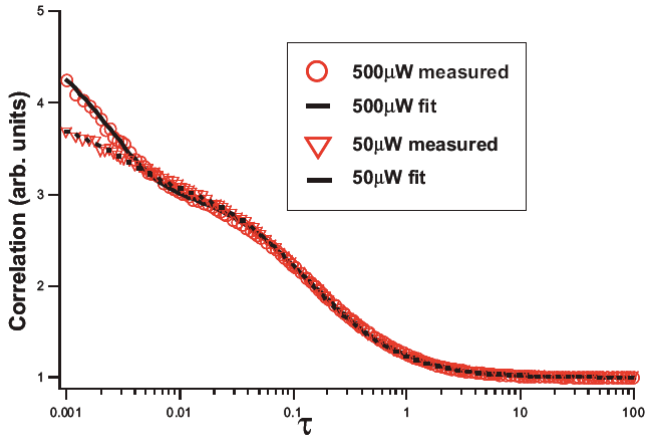

Figure 4.4: Raw data and equation 4.1 ts to autocorrelation traces collected from AlexaFluor 488 at excitation powers $50\mu W$ and $500\mu W$, each trace fit to equation 4.1. Only the triplet fraction (F) differs signicantly between ts, while the diffusion correlation time (τ_d) and other parameters remain unchanged. **Experimental Conditions:** 500pM AF488-DNA; $\lambda_{ex} = 488nm$; $Pol_{ex} : \sigma^+$; F_{em1} =HQ530/30; F_{em2} =HQ630/50; $t_{exp} = 100$s

Figure 4.5 presents the FRET efficiency population histogram measured by burst analysis for doubly-labled DNA in the absence of restriction enzyme. The center of the primary population peak occurs at $E = .51$, in agreement with that expected ($E = .54$) from the donor-acceptor separation of 14 base pairs (Figure 4.3). The small peak at $E \approx 0$ arises from DNA lacking an active acceptor fluorphore, due either to labeling inefficiency or photobleaching.[448]

For doubly-labeled DNA samples to which active restriction enzyme (EcoRI or BglI) was introduced, the time-dependence of the FRET efficiency population his-

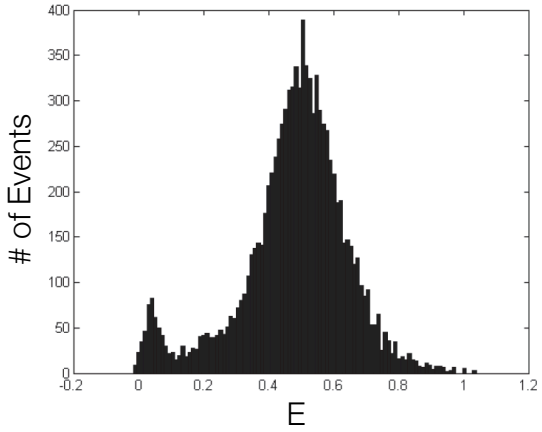

Figure 4.5: Histogram of measured FRET energy transfer efficiencies (determined from equation 4.2) for doubly-labeled DNA 40-mer. **Experimental Conditions:** 200pM AF488-DNA-TR; $\lambda_{ex} = 488nm$; $Pol_{ex} : \sigma^{+}$; $P_{ex} = 400\mu W$; F_{em1} =HQ530/30; F_{em2} =HQ630/50; $t_{exp} = 1200$s

togram was determined by defining time windows between 1 and 30 seconds, and measuring the ratio of bursts arising from active FRET pairs (unrestricted DNA, $.15 \leq E \leq .85$) to the total number of detected fluorescence bursts. A representative data set processed using two different time windows is shown in Figure 4.6 for BglI.

For restriction enzyme assays, the concentration of DNA encountered by the enzyme could be varied across a broad concentration range while still maintaining the fluorescence signal source at the optimal FRET-pair concentration for burst analysis (200pM) by adding the appropriate amount of unlabeled DNA. Because the enzyme cleaves both labeled and unlabeled DNA substrates homogeneously, the measured fraction of doubly-labeled DNA is representative of the total fraction of unrestricted DNA present in the sample.

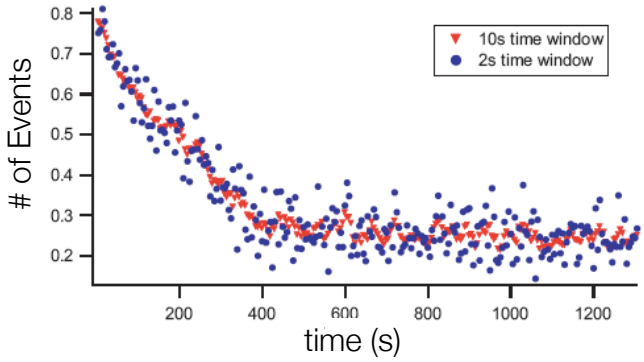

Figure 4.6: Restriction time course of 20nM DNA containing 200pM doubly-labeled DNA cut by 1U BglI. For each data point the fraction of unrestricted DNA was calculated by counting bursts from time windowsof either 10 seconds (red triangles) or 2 seconds (blue circles) in duration. **Experimental Conditions:** 200pM AF488-DNA-TR + 20nM unlabeled DNA; $\lambda_{ex} = 488nm$; $Pol_{ex} : \sigma^{+}$; $P_{ex} = 400\mu W$; F_{em1} =HQ530/30; F_{em2} =HQ630/50; $t_{exp} = 1500$s

Figure 4.7 presents data for the cleavage of varying DNA oligomer concentrations by restriction enzyme EcoRI monitored by FRET burst analysis. Figure 4.8 is the corresponding Michaelis-Menten plot, which yields $K_M = 13.9 \pm 2.8$nM and $V_{max} = .934 \pm .072$nM min^{-1}. The measured value for K_M is in agreement with reported literature values, although the measured V_{max} is low by roughly one order of magnitude. However, the V_{max} is likely to vary between enzyme samples due to differential degradation, while the K_M should remain constant. Additionally, despite passivation of the reaction vessel by PEG-silane, nonspecific adsorption of restriction enzyme to the vessel walls may occur, reducing the effective enzyme concentration by a linear factor and subsequently impacting measurement of V_{max} but not K_M.

Figure 4.9 presents reaction rate data (top row and bottom left) and corresponding Michaelis-Menten plot (bottom right) for the cleavage of varying DNA concentrations by 1U restriction enzyme BglI (622nM enzyme) in 300μl total volume. For each

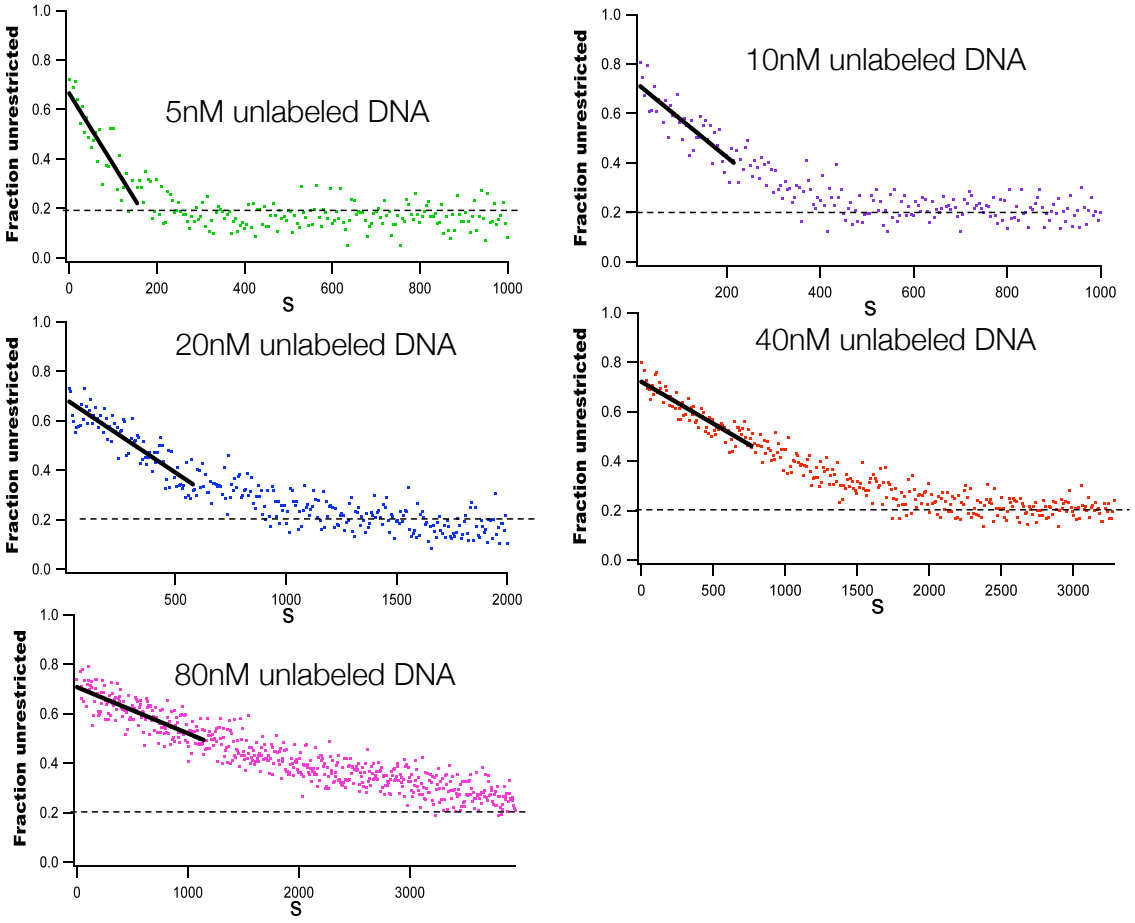

Figure 4.7: Restriction time course for 5.2nM EcoRI restriction enzyme, 200pM AF488-DNA-TR (containing an EcoRI recognition sequence) and varying concentrations of total DNA in $300\mu l$ total volume. For each data point the fraction of unrestricted DNA was calculated by counting bursts from time windows of 2–5s width. The black line in each plot represents a linear fit to the unrestricted DNA concentration to yield the initial reaction rate. **Experimental Conditions:** 200pM AF488-DNA-TR + $\{5, 10, 20, 40, 80\}$nM unlabeled DNA; $\lambda_{ex} = 488nm$; $Pol_{ex} : \sigma^{+}$; $P_{ex} = 400\mu W$; F_{em1} =HQ530/30; F_{em2} =HQ630/50; $t_{exp} = 1000 - 4000$s

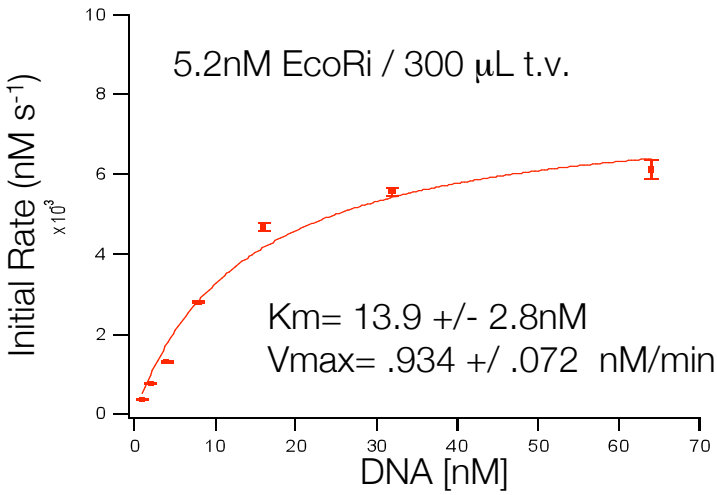

Figure 4.8: Michaelis-Menten plot for restriction enzyme EcoRI generated from the reaction data shown in Figure 4.7. The constants obtained from a Michaelis-Menten mechanism fit to the data (solid red line) are $K_M = 13.9 \pm 2.8$nM and $V_{max} = .934 \pm .072$nM min^{-1}.

reaction the fraction of unrestricted DNA was calculated for 50–500s time windows from the ratio of bursts arising from active FRET pairs (unrestricted DNA, $.15 \leq E \leq .85$) to the total number of detected fluorescence bursts. The black dotted line in each plot represents a linear fit to determine the initial reaction rate. In contrast to EcoRI, the Michaelis-Menten constant for BglI was not measurable by this method because burst analysis cannot be performed using $\lesssim$ 25pM fluorescent sample concentration. Similar difficulties have been reported for bulk assays of BglI.

Nearly identical results were obtained when the experiments described in this section were repeated using Cy3 and Cy5 dyes (Amersham) as the FRET donor and acceptor, respectively, and 532nm excitation. This corroborating fluorescence correlation and burst data provides confirmation of the sensitivity and spectral selectivity

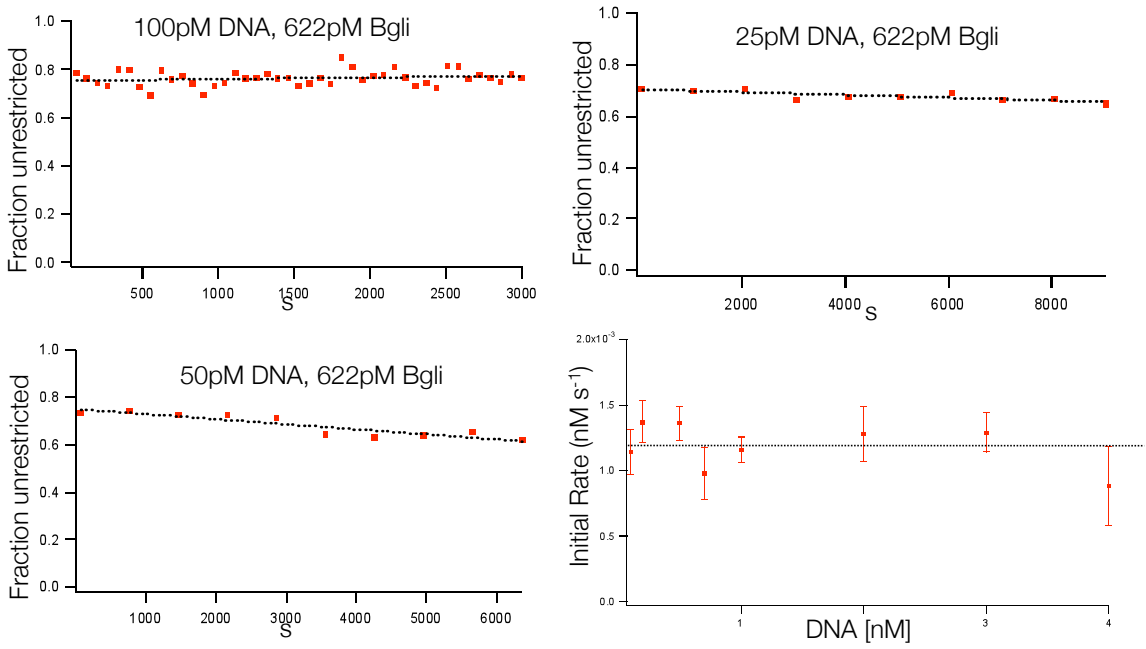

Figure 4.9: Restriction time courses (top row and bottom left) and corresponding Michaelis-Menten plot (bottom right) for .622nM BglI restriction enzyme and varying concentrations of doubly labeled DNA (containing a BglI recognition sequence) in $300\mu l$ total volume. For each data point the fraction of unrestricted DNA was calculated by counting bursts from time windows of 50–500s width. The black line in each plot represents a linear fit to the unrestricted DNA concentration to yield the initial reaction rate. **Experimental Conditions:** 200pM AF488-DNA-TR + $\{25, 50, 100\}$pM unlabeled DNA; $\lambda_{ex} = 488nm$; $Pol_{ex} : \sigma^{+}$; $P_{ex} = 400\mu W$; F_{em1} =HQ530/30; F_{em2} =HQ630/50; $t_{exp} = 1000$–4000s

of the microscope constructed as described in Section 3.3.

4.3 Fluorescence Correlation Spectroscopy Using Polarization-Sensitive Signal Collection Channels

4.3.1 Auto and Cross-Correlation Signal Processing

All fluorescence correlation spectroscopy experiments rely upon the numerical signal processing methods described in this section to generate correlation traces from the collected time series. Correlation analysis, as a result of its general formulation from conditional *expectation* values, necessarily depends upon both the observational *metrics* of the processes under investigation in addition to the statistical state distributions associated with those processes. This characteristic is one reason why correlation-based analyses inherently yield parametric models, in contrast to the non-parametric nature of models built upon information theory, a statistical approach that considers only the distribution of state and not the values of those states.[489–491] Performing statistical analysis directly from quantified measures, however, also makes correlation-based approaches much more efficient in many experimental contexts.

The most generalized approach to assessing correlation, either within a single process or between two separate ones, is to seek a quantitative metric representing the probability of measuring one specified state value having previously measured another specified state value. Stated rigorously, given two processes $\mathcal{X}$ and $\mathcal{Y}$ that consist of transitions between associated $q-$ and $p-$dimensional vector states $\boldsymbol{\xi}$ and

$\boldsymbol{\psi}$ whose domains are the state spaces $\boldsymbol{\Xi}$ and $\boldsymbol{\Psi}$, respectively:

$$\boldsymbol{\xi} = \begin{pmatrix} \xi_1 \\ \xi_2 \\ \vdots \\ \xi_q \end{pmatrix} \in \boldsymbol{\Xi} \tag{4.3}$$

$$\boldsymbol{\psi} = \begin{pmatrix} \psi_1 \\ \psi_2 \\ \vdots \\ \psi_p \end{pmatrix} \in \boldsymbol{\Psi} \tag{4.4}$$

we first require that that there exists a continuous-form mapping from each vector state to a measurable scalar value:

$$X : \boldsymbol{\xi} \mapsto X(\boldsymbol{\xi}) \in \mathbb{R}, \forall \boldsymbol{\xi} \in \boldsymbol{\Xi} \tag{4.5}$$

$$Y : \boldsymbol{\psi} \mapsto Y(\boldsymbol{\psi}) \in \mathbb{R}, \forall \boldsymbol{\psi} \in \boldsymbol{\Psi}\,. \tag{4.6}$$

These measures $X(\boldsymbol{\xi})$ and $Y(\boldsymbol{\psi})$ could, for example, represent the photon counts detected by photodiodes of an optical microscopy system when process $\mathcal{X}$ is in state ξ and process $\mathcal{Y}$ is in state ψ, respectively. Additionally, we require the existence of a probability measure P for individual states of each process as a function of an

additional parameter t:

$$P(\boldsymbol{\xi},t) = Pr\big\{\boldsymbol{\omega}\colon \boldsymbol{\xi}(t)=\boldsymbol{\omega}\big\}, \forall\boldsymbol{\omega} = \begin{pmatrix}\omega_1\\ \omega_2\\ \vdots\\ \omega_q\end{pmatrix} \in \big\{\boldsymbol{\Xi}\big\} \tag{4.7}$$

$$P(\boldsymbol{\psi},t) = Pr\big\{\boldsymbol{\nu}\colon \boldsymbol{\psi}(t)=\boldsymbol{\nu}\big\}, \forall\boldsymbol{\nu} = \begin{pmatrix}\nu_1\\ \nu_2\\ \vdots\\ \nu_p\end{pmatrix} \in \big\{\boldsymbol{\Psi}\big\} \tag{4.8}$$

When seeking time-dependent correlated behavior the parameter t will clearly represent time. However, in many cases correlation is sought for other parameters such as linear position (x) or distance between points $\|\boldsymbol{r}\|$, and so for generality t will remain unspecified.

The parameter t must also express a measure τ representing the difference between two possible parameter values: $\tau = t_\tau - t_0$. The cross-correlation $\mathcal{C}_{\mathcal{XY}}(\tau)$ between processes $\mathcal{X}$ and $\mathcal{Y}$ under metrics X and Y can then be obtained by calculating the $X-$weighted expectation value for $Y(\boldsymbol{\psi})$ at $t' = t+\tau$ conditional upon the prior measurement of a specific value $X(\boldsymbol{\xi})$ at $t' = t$, integrated over all possible process $\mathcal{X}$ states $\boldsymbol{\xi}$, all possible process $\mathcal{Y}$ states $\boldsymbol{\psi}$, and all possible initial parameter values t in the range $[t_{min}, t_{max}]$:

$$\mathcal{C}_{\mathcal{XY}}(\tau) = \int_{t_{min}}^{t_{max}} dt' \int d\boldsymbol{\xi} \int d\boldsymbol{\psi} X(\boldsymbol{\xi})\, Y(\boldsymbol{\psi}) P\big(\boldsymbol{\psi}, t'+\tau \mid \boldsymbol{\xi}, t'\big) \tag{4.9}$$

where the integrals corresponding to $d\boldsymbol{\xi}$ and $d\boldsymbol{\psi}$ are carried out over their complete state spaces.

In the context of fluorescence correlation spectroscopy, measurements of the processes of interest will always take the form of collected fluorescence signals. Assuming that $X(\boldsymbol{\xi})$ and $Y(\boldsymbol{\psi})$ represent the photon counts, the collected data will take the form of finite discrete-time series because these measurements will correspond to sums or averages over specific time windows δt defined for the experiment. An individual discrete-time series of n fluorescence intensity values A measured by a single optical detection channel $\mathcal{A}$ at regular time intervals $\left\{t_0, t_0+\delta t, t_0+2\delta t, \cdots, t_{end}-\delta t, t_{end}\right\}$ $\big($satisfying the condition $t_{end}-t_0=(n-1)\delta t\big)$can be considered as an n-element vector $\boldsymbol{\mathcal{I}_{\mathcal{A}}}$:

$$\boldsymbol{\mathcal{I}_{\mathcal{A}}} = \begin{pmatrix} A(t_0) \\ A(t_0+\delta t) \\ A(t+2\delta t) \\ \vdots \\ A(t_{end}) \end{pmatrix} = \begin{pmatrix} A_1 \\ A_2 \\ A_3 \\ \vdots \\ A_n \end{pmatrix} . \tag{4.10}$$

The difference vector $\boldsymbol{\mathcal{I}_{\Delta\mathcal{A}}}$ is simply the reformulation of the original time series vector (which contains only positive elements) in terms of the difference between each element A_i and the mean value $\langle A\rangle$, resulting in a vector that contains both positive and negative values:

$$\boldsymbol{\mathcal{I}_{\Delta\mathcal{A}}} = \begin{pmatrix} A_1-\langle A\rangle \\ A_2-\langle A\rangle \\ A_3-\langle A\rangle \\ \vdots \\ A_n-\langle A\rangle \end{pmatrix} . \tag{4.11}$$

The first step in calculating the **autocorrelation** of $\boldsymbol{\mathcal{I}_{\mathcal{A}}}$ corresponding to a characteristic positive time delay τ (which must be an integer multiple of δt, i.e., $\tau =$

$m\delta t, m \in \mathbb{N}$), is to create a τ-shifted difference vector $\boldsymbol{\mathcal{I}}_{\boldsymbol{\Delta\mathcal{A}}}(\tau)$ of length $n-m$:

$$\boldsymbol{\mathcal{I}}_{\boldsymbol{\Delta\mathcal{A}}}(\tau) = \begin{pmatrix} A_{(1+m)} - \langle A \rangle \\ A_{(2+m} - \langle A \rangle \\ A_{(3+m)} - \langle A \rangle \\ \vdots \\ A_n - \langle A \rangle \end{pmatrix} . \tag{4.12}$$

The normalized autocorrelation $\mathcal{G}^{(a)}(\tau)$[‡] is then simply the vector dot product of $\boldsymbol{\mathcal{I}}_{\boldsymbol{\Delta\mathcal{A}}}(\tau)$ and the first $(n-m)$ elements of $\boldsymbol{\mathcal{I}}_{\boldsymbol{\Delta\mathcal{A}}}$, scaled by $\left(\frac{1}{n-m}\right)$, divided by the squared norm of $\boldsymbol{\mathcal{I}}_{\boldsymbol{\Delta\mathcal{A}}}$ scaled by $\left(\frac{1}{n}\right)$:

$$\mathcal{G}^{(a)}(\tau) = \frac{\left(\frac{1}{n-m}\right) \boldsymbol{\mathcal{I}}_{\boldsymbol{\Delta\mathcal{A}}}(\tau) \cdot \boldsymbol{\mathcal{I}}_{\boldsymbol{\Delta\mathcal{A}}}{}^{(n-m)}}{\left(\frac{1}{n}\right) \|\boldsymbol{\mathcal{I}}_{\boldsymbol{\Delta\mathcal{A}}}\|^2} \tag{4.13}$$

$$= \left(\frac{n}{n-m}\right) \frac{\sum_{i=0}^{n-m} \left[\left(A_i - \langle A \rangle\right) \left(A_{(i+m)} \langle A \rangle\right)\right]}{\sum_{i=1}^{n} \left(A_i - \langle A \rangle\right)^2} . \tag{4.14}$$

If the signal source is a continuous rather than discrete time series $\big(A(t)$ rather than $[A_0, A_1, \cdots, A_N]\big)$, the summation formulation of equation 4.14 can be restated using an integral:

$$\mathcal{G}^{(a)}(\tau) = \frac{\int_{t'=t_0}^{t_{end}} \left(A(t') - \langle A(t) \rangle\right) \left(A(t'+\tau) - \langle A(t) \rangle\right)}{\int_{t'=t_0}^{t_{end}} \left(A(t') - \langle A(t) \rangle\right)^2} . \tag{4.15}$$

[‡]Equation 4.14, when not normalized by the denominator $\left\langle \|\boldsymbol{\mathcal{I}}_{\boldsymbol{\Delta\mathcal{A}}}\|^2 \right\rangle$, is sometimes also referred to as the 'second-order autocorrelation' and written as $\mathcal{G}^{(2)}(\tau)$. This is a throwback to its origins in spectral analysis of irradiance intensity, which as discussed in Section 3.2 is the square absolute magnitude of the electromagnetic field strength $\mathcal{E}$. Under that formalism the first-order (non-normalized) autocorrelation would be the numerator of equation 4.14 applied to an electromagnetic field measure $\mathcal{E}_i$ rather than a radiation intensity measure $A_i = \frac{1}{2}\mathcal{E}_i\mathcal{E}_i^*$ as we have used it.

Given a second discrete-time series of values B_i measured by a single optical detection channel $\mathcal{B}$ corresponding to the same time points as for $\mathcal{A}$, the **cross-correlation** is very similar to equation 4.14, rewritten with the τ shifted difference vector $\boldsymbol{\mathcal{I}}_{\boldsymbol{\Delta\mathcal{B}}}(\tau)$ in place of $\boldsymbol{\mathcal{I}}_{\boldsymbol{\Delta\mathcal{A}}}(\tau)$, and normalized using a dot product of the two non-shifted difference vectors in place of the squared norm of $\boldsymbol{\mathcal{I}}_{\boldsymbol{\Delta\mathcal{A}}}$:

$$\mathcal{G}^{(x)}(\tau) = \frac{\left(\frac{1}{n-m}\right)\boldsymbol{\mathcal{I}}_{\boldsymbol{\Delta\mathcal{B}}}(\tau)\cdot\boldsymbol{\mathcal{I}}_{\boldsymbol{\Delta\mathcal{A}}}{}^{(n-m)}}{\left(\frac{1}{n}\right)\boldsymbol{\mathcal{I}}_{\boldsymbol{\Delta\mathcal{B}}}\cdot\boldsymbol{\mathcal{I}}_{\boldsymbol{\Delta\mathcal{A}}}} \tag{4.16}$$

$$= \left(\frac{n}{n-m}\right)\frac{\sum_{i=0}^{n-m}\left[\left(B_i - \langle B\rangle\right)\left(A_{(i+m)} - \langle A\rangle\right)\right]}{\sum_{i=1}^{n}\left(B_i - \langle B\rangle\right)\left(A_i - \langle A\rangle\right)} \tag{4.17}$$

Restated using an integral form analogous to equation 4.15, the cross-correlation $\mathcal{G}^{(x)}(\tau)$ is:

$$\mathcal{G}^{(x)}(\tau) = \frac{\int_{t'=t_0}^{t_{end}}\left(B(t') - \langle B(t)\rangle\right)\left(A(t'+\tau) - \langle A(t)\rangle\right)}{\left[\int_{t'=t_0}^{t_{end}}\left(A(t') - \langle A(t)\rangle\right)\right]\left[\int_{t'=t_0}^{t_{end}}\left(B(t') - \langle B(t)\rangle\right)\right]} \quad . \tag{4.18}$$

4.3.2 Diffusion-Only Fluorescence Correlation Spectroscopy

In a simple one-channel FCS experiment using a confocal microscopy system, the source of each time series value is the fluorescence emission from fluorophores present in the volume defined by the confocal point spread function. If the photodetector in the emission pathway reports individual photons, then each value A_i will be the number of photons measured during the i^{th} discrete time bin of width δt. Single-photon sensitivity, however, is not necessary. Any detector that produces a signal representing a linear mapping of fluorescence signal over an intensity range relevant to the experiment will suffice.

As fluorophores spontaneously diffuse throughout the confocal probe volume under the influence of stochastic Brownian motion they will tend to spend a characteristic *average* time $\langle t_{diff} \rangle$ in its immediate vicinity before mixing irreversibly with the indistinguishable bulk population, as illustrated in the simple schematic of Figure 4.1 from the previous chapter (p. 131). This average time $\langle t_{diff} \rangle$ is determined by a combination of the confocal probe volume dimensions and the diffusion coefficient of the fluorescent species. Within the time window $\langle t_{diff} \rangle$, detection of a fluorphore in an initial time bin t_i, manifested by measurement of a characteristic signal intensity in the emission pathway, increases the statistical likelihood of detecting a fluorphore in a subsequent time bin t_j given the condition $(t_j - t_i) \lesssim \langle t_{diff} \rangle$. This is because insufficient time has transpired to allow a high probability that the initially detected fluorphore has diffused away from the probe volume vicinity and rejoin the bulk population. Similarly, if a fluorphore is *not* detected in a specified initial time bin, the statistical likelihood of detecting a fluorphore in a subsequent time bin less than $\langle t_{diff} \rangle$ time later is diminished.

Intuitively, this tendency for high signal measurements to be followed by further high signal measurements (and low signal measurements followed by further low signal measurements) for time delays shorter than the characteristic diffusion time results in a positive $\mathcal{G}^{(a)}(\tau)$ value calculated by equation 4.14 for $\tau \lesssim \langle t_{diff} \rangle$. At longer delays $\tau \gg \langle t_{diff} \rangle$, the probability of detecting a similar signal intensity is statistically independent, because the stochastic arrival of 'new' fluorphores from the indistinguishable bulk population occurs by a purely random process once the initial fluorphore has irreversibly departed. The result is that the numerator of equation 4.14 averages to zero for $\tau \gg \langle t_{diff} \rangle$.

We can now express intuitive confidence that $\mathcal{G}^{(a)}(\tau)$ is high for small values of τ and zero for large values of τ. The exact profile of the correlation trace versus τ, however, requires a significantly more rigorous analysis. First, the anticipated timescale $\tau_d \sim \langle t_{diff} \rangle$ for translational diffusion may be calculated from the translation diffusion coefficient D_T, which itself is determined using the Stokes-Einstein relation regarding stochastic Brownian motion:

$$D_T = \frac{k_B T}{6\pi\,\eta\,r_h} \tag{4.19}$$

where k_B is the familiar Boltzmann constant, T is the temperature in Kelvin, η is the solvent viscosity and r_h is the hydrodynamic radius of the diffusing particle. The diffusion coefficient D_T is closely related to the characteristic diffusional correlation time τ_d since the process driving motion of the particle toward, through and away from the confocal probe volume is stochastic Brownian motion. The characteristic duration of diffusional transit across the confocal probe volume, τ_d, will scale inversely with D_T and proportionately with the square of the probe volume's linear dimension. The exact correlation function $\mathcal{G}(\tau)$ for a fluorescence time series signal arising from a single freely diffusing species in a confocal probe volume of a 3D Gaussian spatial intensity distribution has been derived repeatedly in the literature.[359,380,381,442] If we utilize a collimated laser beam of Gaussian radial intensity profile as the excitation source, the confocal point spread function (Figure 3.8) constituting the probe volume will have an approximately Gaussian 3D intensity profile, with $\sigma_z \approx 2\sigma_\rho$ in cylindrical coordinates. The diffusion-only autocorrelation trace then takes the following form:

$$\mathcal{G}^{(a)}_{diff}(\tau) = \frac{1}{\langle N \rangle}\left(1 + \left[\frac{2k_BT}{3\pi r_h \eta \omega^2}\right]\tau\right)^{-1}\left(1 + \left[\frac{2k_BT}{3\pi r_h \eta a^2 \omega^2}\right]\tau\right)^{-\frac{1}{2}} \tag{4.20}$$

where ω is the radius of the observation volume minor axis, a is the aspect ratio determining the radius of the major axis, r_h is the effective hydrodynamic radius of the fluorphore, η is the solvent viscosity, and $\langle N \rangle$ is the average fluorophore occupancy of the observation volume. The parameters ω and a describing the physical dimensions of the confocal probe volume can be calibrated by collecting correlation traces from a fluorescent species having a known diffusion constant (e.g., fluorescein, as used in Section 4.2.2). Fits of eq.4.20 to the collected correlation traces for a well-characterized standard will yield ω and a values that can be used in subsequent measurements from novel samples.

In a two-channel detection system with no polarization sensitivity and one fluorescent species, the cross-correlation $\mathcal{G}^{(x)}(\tau)$ will be identical to equation 4.20. Equation 4.1 (p. 139) presents the modified autocorrelation trace expected for a fluorescent species exhibiting both translational diffusion and photoinduced triplet-state blinking.

4.3.3 Molecular Rotation in Condensed Matter

In the gas phase molecular rotation is inertially dominated and progresses unhindered between relatively infrequent collisions with other molecules, resulting in large sequential angular displacements and orientational decorrelation. In condensed matter, however, collisions are significantly more frequent and the resulting orientational trajectory is composed of numerous small sequential hops.[492,493] Stochastic rotation of a single molecule in condensed matter is a complex many-body problem, the full rigorous simulation of which requires intensive numerical molecular dynamics calculations.[494] However, casting the system in terms of Brownian rotational diffusion

provides a sufficient qualitative understanding of the dynamic molecular orientation behavior in homogeneous phases.[495] In complex fluids such as highly-crowded macromolecular solutions and vitreous liquids, heterogeneous rotational diffusion behavior is indicative of nanoscale structuring.[493, 496–498]

Ensemble fluorescence depolarization measurements of globular protein in aqueous solutions crowded by macromolecules of similar dimensions have exhibited rotational diffusion that is faster than expected from the bulk solvent viscosity as well as the translational diffusion that is slower than predicted.[499] This phenomenon of 'anomalous diffusion' in highly heterogeneous environments ultimately exerts strong influence on the kinetics of enzymatic reactions.[500–503] Nonlinear changes in rotational correlation time induced by macromolecular crowding disproportionately influences protein-protein association kinetics, slowing diffusional encounter rates more than expected from the viscosity changes alone.[504] These phenomena highlight the potential for single-dye and single-nanocrystal probes capable of optically reporting their nanoscale local environment.

4.3.4 Rotation-Diffusion Polarized Fluorescence Correlation Spectroscopy

For a freely rotating fluorophore in a two-channel detection system with polarization sensitivity, the full rotation-diffusion autocorrelation trace requires modification of equation 4.20 to include an additional rotational correlation term $\mathcal{G}_{rot}^{(a)}(\tau)$. As was the case for the translational diffusion coefficient (equation 4.19), the rotational correlation time τ_r can be calculated using the Stokes-Einstein-Debye relation. For an

approximately spherical molecule this is given by:

$$\tau_r = \frac{\eta V f C}{k_B T} \tag{4.21}$$

$$= \frac{4\pi\eta\, r_h^3}{3k_B T} f\, C \tag{4.22}$$

where f is a form factor governed by the shape of the molecule, and C is a parameter between 0 and 1 that accounts for the coupling strength between the solute surface and the surrounding solvent molecules. The product of parameters f and C is frequently assumed to be ~ 1, yielding $\tau_r \approx \frac{4\pi\eta\, r_h^3}{3k_B T}$.

A single freely diffusing fluorescent molecule possessing a linear transition dipole emits a spatially anisiotropic polarized signal dependent upon the dipole vector orientation $\vec{\boldsymbol{\rho}}$ (equation 3.64, p. 113), providing the potential to identify molecular rotation by observing the dipole orientation time series $\left\{\vec{\boldsymbol{\rho}}_{\mathbf{0}}, \vec{\boldsymbol{\rho}}_{\mathbf{1}}, \vec{\boldsymbol{\rho}}_{\mathbf{2}}, \cdots\right\}$. Each dipole vector $\vec{\boldsymbol{\rho}}$ can be specified by two angle variables $\left(\phi, \theta\right)$ having domains $\phi \in \boldsymbol{\Phi} \equiv \left[0, \pi\right]$ and $\theta \in \boldsymbol{\Theta} \equiv \left[0, 2\pi\right]$ that together span the full space of all possible dipole orientation states $\boldsymbol{R} \equiv \boldsymbol{\Phi} \times \boldsymbol{\Theta}$ The rigorous expression for the rotational correlation term $\mathcal{G}_{rot}^{(a)}(\tau)$ will depend on both the transition probabilities between pairs of dipole vector orientation states $\left\{(\vec{\boldsymbol{\rho}}_{\boldsymbol{i}}, \vec{\boldsymbol{\rho}}_{\boldsymbol{j}}) \in \boldsymbol{R}\right\}$ and the values the two-channel polarization-sensitive optical system measures for each state in the space $\boldsymbol{R}$. Given a functional mapping of dipole orientation to collected signal that is real-valued for all possible $\vec{\boldsymbol{\rho}}$, $\left\{\mathcal{F} : \vec{\boldsymbol{\rho}} \mapsto f(\vec{\boldsymbol{\rho}}); \forall \vec{\boldsymbol{\rho}} \in \boldsymbol{R}\right\}$ the normalized rotational autocorrelation under $\mathcal{F}$ is determined using the τ-shifted and unshifted vectors $\Delta f\left(\vec{\boldsymbol{\rho}}\right)$ defined analogously to

equations 4.11 and 4.12:

$$\mathcal{G}_{rot}^{(a)}(\tau) = \frac{\left\langle \Delta f\left(\vec{\boldsymbol{\rho}}(t+\tau)\right) \Delta f\left(\vec{\boldsymbol{\rho}}(t)\right)\right\rangle}{\left\langle \Delta f\left(\vec{\boldsymbol{\rho}}(t)\right)^2\right\rangle}\,. \tag{4.23}$$

If the measurement system uses two detection pathways, the first one expressing the mapping $\mathcal{F}$ as above and the second expressing a different signal mapping $\left\{\mathcal{H} : \vec{\boldsymbol{\rho}} \mapsto h(\vec{\boldsymbol{\rho}}); \forall \vec{\boldsymbol{\rho}} \in \boldsymbol{R}\right\}$, the rotational cross-correlation is then determined, using the same difference vector notation as above, by:

$$\mathcal{G}_{rot}^{(x)}(\tau) = \frac{\left\langle \Delta f\left(\vec{\boldsymbol{\rho}}(t+\tau)\right) \Delta h\left(\vec{\boldsymbol{\rho}}(t)\right)\right\rangle}{\left\langle \Delta f\left(\vec{\boldsymbol{\rho}}(t)\right) \Delta h\left(\vec{\boldsymbol{\rho}}(t)\right)\right\rangle}\,. \tag{4.24}$$

In all but special cases the rotational correlation functions $\mathcal{G}_{rot}^{(a)}(\tau)$ and $\mathcal{G}_{rot}^{(x)}(\tau)$ are non-analytic in nature. A theoretical investigation describing the contribution of Brownian rotational diffusion to the complete fluorescence correlation was originally reported by Aragón and Pecora in 1975, shortly following their derivation of diffusion-only FCS.[364,365] They presented a rigorous framework for correlating the anisotropy fluctuations of a small ensemble of freely rotating one-dimensional fluorescence dipoles, but were unable to perform rigorous corroborating experiments due to the technological limitations of that era.[364–367] Recent advances in confocal optics, fluorescence detection efficiency and timing of photon arrival have only very recently rendered those measurements feasible.[371,425,505]

For the two-channel microscopy system described in Section 3.3, for which each detection channel corresponds to an orthogonal polarization component, the mapping functions f and h correspond to equations 3.68 and 3.69 for the I_x and I_y channel intensities (p. 115). The exact rotational correlation function expressed by this system

must be determined from the rotational symmetry and dipole geometry and necessitates numerical methods. However, for *most* cases of molecular rotational symmetry and transition dipole geometry that are relevant to the PFCS experiments presented here (Chapter 5, p. 162), $\mathcal{G}^{(a)}_{rot}(\tau)$ may be closely approximated by a Kohlrausch-Williams-Watts (KWW) stretched-exponential rise term (equation 4.25).[495] Empirical KWW fitting models are ubiquitous across all scientific and engineering fields, particularly in systems possessing interacting response modes or representing heterogeneous systems. The smaller the value of β, the greater the system heterogeneity.[506]

$$\mathcal{G}^{(a)}_{rot}(\tau) = 1 + Fe^{\left(-\frac{\tau}{\tau_r}\right)^{\beta}} \tag{4.25}$$

F is an empirical preexponential fitting constant corresponding to the magnitude of the dipole rotation effect, and as will be discussed in subsequent sections, depends upon both the geometry of the fluorescent transition dipole and the numerical aperture of the optical system. τ_r is the characteristic rotational correlation time: $\tau_r \sim \left[\frac{4\pi\eta}{3k_BT}\right] r_h^3$ (assuming that $fC \sim 1$). The empirical KWW 'stretching' parameter β in this context represents the convolution of multiple rotational modes, and ranges from $\beta \approx .95$ for spherically symmetric molecules to smaller values for molecules with extreme rotational anisotropy or asymmetry. In most experimentally relevant cases not involving vitreous dynamics $\beta \geq .85$.

Additionally, the full rotation-diffusion cross-correlation trace must include the effect of *anti*-correlated signal intensity measured by the orthogonal polarization channels I_x and I_y of the detection pathway. The anticorrelation arises because of the mutually opposing relationship between I_x and I_y occurring as a direct consequence of equations 3.68−3.72 (p. 115). The cross-correlation $\mathcal{G}^{(x,pol)}(\tau)$ for a rotating dipole

will therefore include a KWW stretched exponential *decay* with the same parameter value set $\left\{F, \beta, \tau_r\right\}$ as the *rise* in the autocorrelation:

$$\mathcal{G}^{(a,pol)}(\tau)=\left[1+Fe^{-\left(\frac{\tau}{\tau_r}\right)^{\beta}}\right]\frac{1}{\langle N\rangle}\left[1+\left(\frac{2k_BT}{3\pi r_h\eta\omega^2}\right)\tau\right]^{-1}\left[1+\left(\frac{2k_BT}{3\pi r_h\eta a^2\omega^2}\right)\tau\right]^{-\frac{1}{2}} \quad (4.26)$$

$$\mathcal{G}^{(x,pol)}(\tau)=\left[1-Fe^{-\left(\frac{\tau}{\tau_r}\right)^{\beta}}\right]\frac{1}{\langle N\rangle}\left[1+\left(\frac{2k_BT}{3\pi r_h\eta\omega^2}\right)\tau\right]^{-1}\left[1+\left(\frac{2k_BT}{3\pi r_h\eta a^2\omega^2}\right)\tau\right]^{-\frac{1}{2}} . \quad (4.27)$$

Equations 4.26 and 4.27 can both be rewritten in a simpler form using the substitutions $\tau_d = \frac{2k_BT}{3\pi r_h\eta\omega^2}$ representing the characteristic translational diffusional correlation time:

$$\mathcal{G}^{(a,pol)}(\tau) = \left[1+Fe^{\left(-\frac{\tau}{\tau_r}\right)^{\beta}}\right]\frac{1}{\langle N\rangle}\left[1+\left(\frac{\tau}{\tau_d}\right)\right]^{-1}\left[1+\left(\frac{\tau}{a^2\tau_d}\right)\right]^{-\frac{1}{2}} \quad (4.28)$$

$$\mathcal{G}^{(x,pol)}(\tau) = \left[1-Fe^{\left(-\frac{\tau}{\tau_r}\right)^{\beta}}\right]\frac{1}{\langle N\rangle}\left[1+\left(\frac{\tau}{\tau_d}\right)\right]^{-1}\left[1+\left(\frac{\tau}{a^2\tau_d}\right)\right]^{-\frac{1}{2}} . \quad (4.29)$$

In experimental cases for which no additional time-correlated processes are prominent in the collected time series, equations 4.28 and 4.29 may be fitted directly to the collected correlation trace data. Frequently, however, additional time-correlated processes are present at timescales that overlap with τ_r or τ_d. Among these are fluorescence intermittency caused by triplet state conversion in fluorescent proteins and dyes molecules (fig.4.2, p. 137), or quantum yield fluctuations arising from various charge-transfer mechanisms in semiconductor nanocrystals, discussed in detail in Section 5.1.3 (p. 169) Many such processes are sensitive to the excitation intensity or the local environment of the fluorphore and if present at the same timescale as τ_r or τ_d will strongly interfere with calculation of τ_r and τ_d directly from the direct auto- and cross-correlation. Fortunately, however, most of these processes (and all

that were encountered in the experiments presented in Chapter 5) do not include any polarization components. For the two-channel polarization-sensitive microscope used here, by taking the *ratio* of the cross-correlation to the autocorrelation we can remove the influence of all non-polarization-sensitive correlated processes present in $\mathcal{G}^{(a,x)}(\tau)$. An additional benefit resulting from this manipulation is an empirical fitting model containing *only* the rotational correlation parameter set $\left\{F, \beta, \tau_r\right\}$.

$$\frac{\mathcal{G}^{(x,pol)}(\tau)}{\mathcal{G}^{(a,pol)}(\tau)} = \frac{1 - Fe^{\left(-\frac{\tau}{\tau_r}\right)^{\beta}}}{1 + Fe^{\left(-\frac{\tau}{\tau_r}\right)^{\beta}}} \tag{4.30}$$

Equation 4.30 was used to fit the majority of the data collected from PFCS experiments and simulations, described in Sections 5.2.4 (p. 180) and 5.3.3 (p. 213), respectively.

Chapter 5

Polarized Fluorescence Correlation Spectroscopy of Colloidal Semiconductor Nanocrystals, Dye-Labeled Phospholipids and Red Fluorescent Protein

Abstract

This chapter presents the results from a series of polarized fluorescence correlation spectroscopy experiments based upon the theoretical framework laid out in the previous chapter (Section 4.3), as well as simulated data generated by a Monte Carlo rotational diffusion numerical routine that incorporated the microscope's 3D polarization state sensitivity derived in Chapter 3 Initial PFCS were applied to a spectral series of colloidal CdSe/ZnS core-shell organic-functionalized quantum dots in hydrophobic oil solvents and CdSe/ZnS core-shell streptavidin-functionalized quantum dots in aqueous glycerol. Rotational diffusion of all quantum dot samples was readily observable in the correlation traces at microsecond timescales despite their nearly

degenerate 2D photoluminescence transition dipoles. By varying the solvent viscosity the measured τ_r values spanned the broad timescale range 5–1000μs, although the polarization factor F for each QD core size remained statistically invariant at $F \sim .12$ in agreement with simulation results. Additionally, the collected QD correlation traces qualitatively match a profile that was previously predicted from simulated data in an earlier publication but has to date not been confirmed in published experiments. Further PFCS experiments were then applied to fluorophores with 1D linear transition dipoles: the red fluorescent protein rDsRed in chilled glycerol and rhodamine-labeled phospholipid in hydrophobic oil solvents. Rotational diffusion was readily observable in the correlation data for these linear dipole samples with τ_r values spanning range in the range 10–300$\mu\, s$, although it was necessary to use the ratio-fitting method derived in Section 4.3 (equation 4.30) in order to remove the obscuring effects of triplet-state blinking dynamics that occurred at approximately the same timescale as rotational diffusion. The polarization factor F measured from for all 1D transition dipole samples was higher than that for the 2D transition dipole samples, with value $F \sim .25$, in very close agreement with simulation results. The measured parameter dependencies with respect to solvent viscosity, observation volume dimension and excitation power were all in agreement with PFCS model predictions. In particular, for the two unitless model parameters (F and β) the experimental results were in extremely close agreement with predicted values of both quantum dot and dye fluorophore samples. Parameters corresponding to time units (τ_r and τ_d) that were expected to scale linearly with solvent viscosity were found to do so with a good degree of statistical confidence.

Associated Publication

Rotational diffusion of colloidal CdSe/ZnS semiconductor nanocrystals measured by polarization-sensitive fluorescence cross-correlation spectroscopy **(Manuscript in preparation)**[507]

5.1 Photophysical Properties of Semiconductor Quantum Dots

5.1.1 Semiconductor Quantum Dots in Biology and Chemistry

Over the course of the past decade semiconductor nanocrystals, in particular those composed of a cadmium selenide core, have evolved from a model nanoscale physical system into powerful imaging and sensing tools with broad applications in biology and chemistry.[508–519] Quantum dots have been used for *in vivo* fluorescent labeling of tissues, cell membranes, and subcellular structures,[308,520–523] as well as *in situ* nucleic acid hybridization,[524] and as nanoscale sensors with single-molecule sensitivity.[525] Quantum dot FRET systems have recently been proposed for chronic *in vivo* neuronal axon staining and imaging the propagation of neuronal action potentials at millisecond temporal resolution.[526,527] Quantum dots have been utilized in FRET pairs as both acceptors[528] and donors.[513,522,525,527,529–538] However, contemporary research has only just begin to scratch the surface of their potential uses, and the remaining applications in all scientific fields are manifold.

5.1.2 Synthesis, Crystal Structures and Physical Properties of CdSe Quantum Dots

Semiconductor nanocrystals are most commonly synthesized via colloidal routes from inorganic precursors.[539–541] Precursor compounds are heated under highly controlled conditions in a low-volatility hydrophobic solvent containing a organic surfactant species, commonly trioctylphosphine oxide (TOPO), the role of which is to coat, passivate and solubilize the surface of the newly-formed quantum dots. The most synthetically and physically well-characterized colloidal quantum dots are composed of a cadmium selenide core. Often the synthetic procedure includes a final step to overcoat the CdSe core with several molecular layers of a high-bandgap semiconductor having similar crystal lattice spacing, most commonly zinc sulfide, to which the organic detergent ligand binds to yield the final colloidal product. The resulting core-shell quantum dots possess greater photostability and higher photoluminescence quantum yield than core-only dots, the putative mechanism for which is passivation of surface sites that promote nonradiative decay pathways.

CdSe nanocrystals synthesized by these methods, both core-only and over-coated with a zinc sulfide shell, adopt wurtzite crystal lattices and have C_3v point-group symmetry,[542,543] with the crystal $c-$axis aligned parallel to the C_3 axis of rotation.[544] The kinetic growth rate under most synthetic conditions is anisotropic along each crystals axis, tending to be greater along the wurtzite $c-$axis. This anisotropic growth rate tends to yield either small ($\lesssim$ 5nm-diameter) nanocrystals resembling prolate ellipsoids of aspect ratio $\lesssim 2$, or larger 'nanorods' elongated along the wurtzite $c-$axis and displaying aspect ratios as high as 30.[545] The relative rates of nucleation and growth along each crystal axis also vary anisotropically with reaction condi-

tions, a phenomenon that has been exploited to create a wide array of low-symmetry nanocrystals such as chevrons, teardrops and tetrapods.[546] The size distribution and characteristic geometry of the resulting CdSe nanocrystals is highly sensitive to the exact synthetic conditions.[547,548]

Colloidal CdSe nanocrystals universally exhibit size-dependent photoluminescence emission arising from radiative exciton decay pathways. Absorption of an incident photon of sufficient energy promotes an electron from the semiconductor valence band to the conduction band, creating a positively charged 'hole' in the valence band. The electron/hole exciton pair exists in bound states described by a wavefunction and Hamiltonian analogous to those of the electron/proton in a single H atom[†], although an exciton Bohr radius (a few nm) is significantly larger than the hydrogen atom Bohr radius (.53Å). When the CdSe crystal size is comparable to or smaller than the exciton Bohr radius, the eigenstates of the exciton Hamiltonian correspond to discrete energy levels, spaced according to their associated quantum confinement energy. These quantum confinement-induced energy level spacings correspond very closely to the eigenfunctions of the quantum mechanical model system of a particle in a 3D potential well. Smaller quantum dots therefore have discrete exciton eigenstates spaced by larger energy than larger quantum dots.

During the electron/hole excited state lifetime (ns) the exciton loses some energy by phonon-assisted nonradiative pathways, decaying to the lowest-energy conduction band eigenstate. The exciton decay that occurs when the electron drops to the highest-energy valence via a radiative charge recombination pathway releases a pho-

[†]This analogy has certain caveats associated with the nanocrystal's nature as a many-body system, but the deviations from ideal behavior based on this simplifying assumption are minimal in most contexts.

ton of wavelength corresponding to the energy gap between the lowest conduction band eigenstate and the highest valence band eigenstate. This difference represents the sum of the bulk semiconductor band gap and the quantum confinement energy. The photoluminescence frequency is therefore a function of the quantum dot dimensions, ranging from blue emission for small CdSe nanocrystals ($\approx$ 2nm diameter) to red emission for CdSe dots of larger diameter ($\gtrsim$ 5nm). Photoluminescence spectral widths are generally narrow ($\approx$ 30nm at 300K), having a lower bound determined by thermal broadening and sample heterogeneity. The emission spectral range also extends to UV/violet emission by very small CdS nanocrystals and to near-IR emission by the largest varieties of CdSe/CdTe/ZnSe nanocrystals. Photoluminescence lifetime also depends upon the nanocrystal size.[549] CdSe quantum dots have an appreciable two-photon absorption cross section, making them applicable to nonconfocal optical slicing microscopy.[308,550,551] The size-dependent photoluminescence emission from semiconductor nanocrystals, combined with their strong continuum absorption, has proven to be one of the major appeals of quantum dot fluorophores over florescent dyes in biological and chemical applications.[511]

The periodic crystal lattice structure of CdSe core-only and CdSe/ZnS core-shell nanocrystals gives rise to a permanent dipole moment aligned parallel to the C_3 symmetry axis, a property that can be calculated from partial charges and bond lengths[543,552] as well as *ab initio* numerical methods.[544] The magnitude and alignment of the permanent dipole, predicted to scale roughly with the nanocrystal volume, has been measured by a variety of experimental methods such as transient electric birefringence[548] and dielectric dispersion,[553] and has been found to agree roughly with first-principles calculations. On average, however, the predicted values have been higher than experimentally measured ones, a phenomenon that may

arise due to charged surface defect sites which tend to form in opposition to the permanent dipole.[543,554] Dielectric dispersion experiments have reported permanent dipole moments of 25 and 47 Debye for 3.4nm and 4.6nm core-diameter CdSe dots, respectively.[553]

In addition to the internal electric field associated with the permanent dipole moment, long-lived but variable internal electric fields likely caused by surface charging have been inferred from dielectric dispersion studies[543] and single-nanocrystal quantum-confined Stark Effect (QCSE) measurements under cryogenic conditions.[555–558] Exciton polarizability in core-only and core-shell CdSe nanocrystals has similarly been measured via QCSE as well as terahertz dielect response, and been found to be in good agreement with that predicted by the exciton binding energy and dielectric properties of bulk CdSe. Photoluminescence quantum yield is also highly sensitive to the local environment for a variety of nanocrystal types.[554,556,557,559–566] The putative explanation for this sensitivity will be discussed further in Section 5.1.3.

The exact geometry and orientation of the photoluminescence transition dipole moment in wurtzite CdSe quantum dots depends upon both the nanocrystals' size and their aspect ratio, as shown in Figure 5.1 (p. 170). Smaller nanocrystals (core diameter $\lesssim$ 5nm) tend to exhibit 2D non-degenerate transition dipoles, while larger quantum dots and nanorods consistently display simple 1D transition dipoles aligned with the crystal's longest dimension.[542,545,550,567–574] The two-dimensional transition dipoles exhibited by quantum dots can be considered as the superposition of a pair of orthogonal linear dipoles (Figure 5.1) which display anisotropic photoluminescence emission except in the special case where both dipoles are of exactly equal magnitude. Cadmium sulfide[575] and InGaAs[576] nanocrystals have also been reported

to have analogous transition dipole structure and anisotropy. If the quantum dot wurtzite crystal structure is asymmetric with respect to all three crystal axes, the two-dimensional transition dipole becomes non-degenerate with respect to energy in addition magnitude. The associated energy differences are just a few meV, however, necessitating cryogenic experimental conditions in order to observe them.[567,576–581]

Recent *ab initio* numerical methods have predicted that the photoluminescence transition dipole of wurtzite CdSe quantum dots may be generalized as two-dimensional elliptical, the ellipse eccentricity varying between $e = 0$ (2D circular degenerate) and $e = 1$ (1D linear) as a function of both the size and aspect ratio of the nanocrystal.[582] For a nanocrystal of diameter d_{ab} measured in the $a - b$ crystal plane and aspect ratio a (with respect to the wurtzite $c-$axis), the transition dipole is two-dimensional and aligned perpendicular to the crystal $c-$axis (fig. 5.1a) at aspect ratios below a critical value a_c. For aspect ratios $a > a_c$ the dipole is 1D, the transition at exactly $a = a_c$ passing through a state with 3D isotropic photoluminescence emission. The larger the nanocrystal diameter d_{ab} the higher the critical aspect ratio a_c. Predicted values at 100K[†] are $a_c = \{1.39, 1.57, 1.97\}nm$ for CdSe core-only quantum dots with $d_{ab} = \{4.0, 5.0, 6.0\}nm$.[571]

5.1.3 Photoluminescence Intermittency and Quantum Yield Fluctuations in Semiconductor Quantum Dots

In addition to the size-dependence of emission wavelength, one of the most prominent and ubiquitous photophysical properties exhibited by quantum dots is photoluminescence intermittency, or 'blinking'.[304] Blinking occurs for all quantum dot

[†]The critical aspect ratio a_c is predicted to have very slight temperature dependence, increasing with T.[571,582]

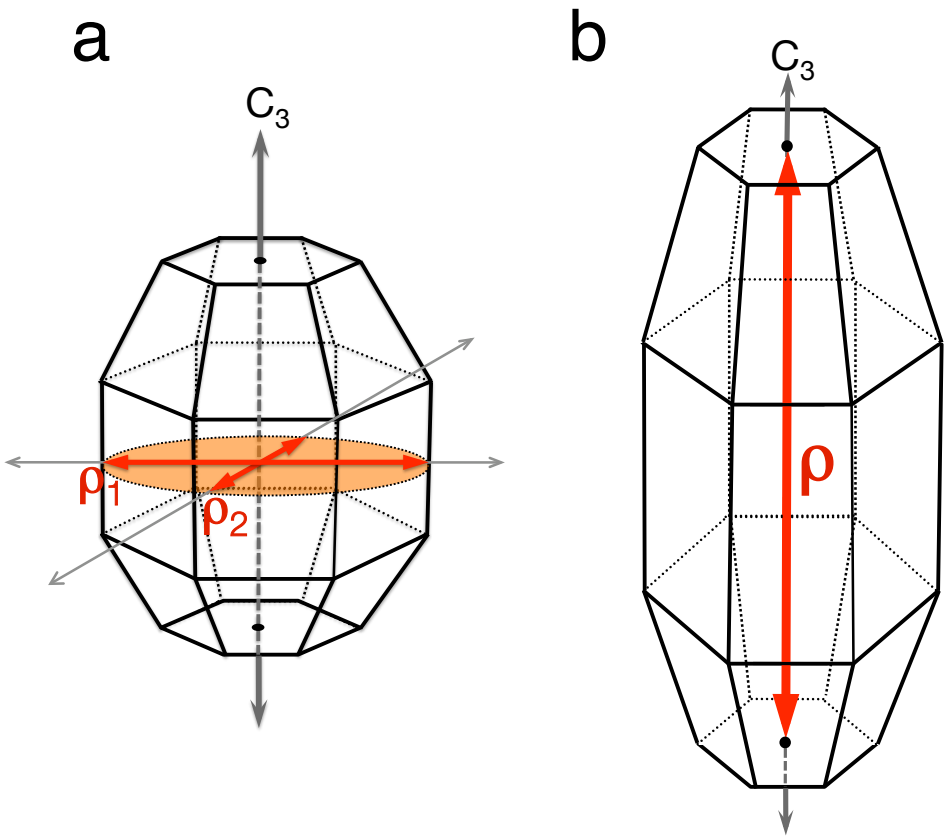

Figure 5.1: Relative geometries and transition dipole orientations for CdSe nanocrystals adopting wurtzite crystal structure. Wurtzite CdSe nanocrystals possess C_3v point group symmetry, the C_3 rotational symmetry axis being aligned with the crystal lattice $\boldsymbol{c}-$axis. **(a)** Colloidal CdSe nanocrystal with aspect ratio $\lesssim 2$. In these nanocrystals the transition dipole $\boldsymbol{\rho}$ (red) possesses anisotropic two-dimensional geometry and is oriented perpendicular to the C_3 symmetry axis. The 2D transition dipole can be considered as the superposition of two orthogonal linear dipoles $\{\boldsymbol{\rho_1}, \boldsymbol{\rho_2}\}$ in the plane of the 2D dipole, with $\langle \boldsymbol{\rho_1}, \boldsymbol{\rho_2} \rangle = 0$. If the planar transition dipole is 2D degenerate (circular) the orthogonal linear dipoles are of equal magnitude: $\|\boldsymbol{\rho_1}\| = \|\boldsymbol{\rho_2}\|$. If the 2D transition dipole is non-degenerate (elliptical with eccentricity $0 > e \leq 1$) the relative dipole magnitudes are $\|\boldsymbol{\rho_2}\| = \sqrt{1-e^2}\|\boldsymbol{\rho_1}\|$. **(b)** CdSe nanocrystals with aspect ratio $\gtrsim 2$ are considered nanorods, and have a one dimensional transition dipole aligned with the $C_3/\boldsymbol{c}-$axis.

types across broad timescales from nanoseconds to tens of seconds, generally following a simple power-law distribution of dark state duration,[234,305,562,583–593] although stretched exponential dark state distribution has also been reported.[594,595] The blinking mechanism is frequently described by charge-transfer models that involving tunneling of the exciton electron to a broad distribution of trapping potentials located on or just outside the surface of the nanocrystal.[304,585,596,597] In these models short-duration dark states arise from electron traps on the crystal surface that are quickly quenched by other relaxation pathways. Less frequent but longer duration dark states occur when the electron tunnels to a trap site well removed from the nanocrystal surface, resulting in a positively charged core for which subsequent excitons have predominantly nonradiative relaxation pathways. This hypothesis has been corroborated by scanning electronic force microscopy measurements of individual quantum dots, which have indicated that under illumination the quantum dot core frequently displays a transient elementary positive charge.[598] Nonradiant exciton relaxation pathways involving broadly distributed subsurface states have also been proposed as an explanation of blinking.[583,599]

In addition to blinking behavior, a more general phenomenon displayed by many nanocrystal types is sensitivity of the photoluminescence quantum yield to illumination. CdSe quantum dots have displayed both photo-induced dimming[584,600,601] and photo-induced brightening.[559,560,602] This photosensitivity occurs in addition to spontaneous quantum yield fluctuation[603] and spectral diffusion.[604] Spontaneous charging and spectral shifts have displayed variable statistical behavior across populations of isolated dots, suggesting sensitivity to the immediate nanoscale environment surrounding each individual quantum dot.

While this environmental sensitivity may ultimately provide pathways toward single-QD sensors it also highlights the importance of property measurements performed in homogeneous fluid media. A fluid environment, particularly one that is hydrophobic and of similar composition to the alkane arms of the passivating TOPO ligand, will minimize the presence of intermittent long-lived charge separation events promoted by proximity to a solid dielectric surface. An additional benefit of measurements acquired from a homogeneous medium, particularly in the context of polarization-sensitive measurements, is the absence of a dielectric interface. A recent publication has highlighted the differential collection efficiency for s- and p-polarization components emitted by a single transition dipole near a dielectric interface.[570] Further complicating the situation is the fact that the induced emission birefringence is different for one- and two-dimensional dipoles. In the PFCS experiments presented here, every effort was made to avoid artifacts potentially arising from dielectric boundaries or refractive index mismatch by using optical immersion oils with consistent $n_0 = 1.515$ as the solvent.

5.1.4 Fluorescence Correlation Spectroscopy of Semiconductor Nanocrystals

Fluorescence correlation spectroscopy has frequently been applied to semiconductor quantum dots, although almost exclusively in just two experimental contexts: assessing fluorescence intermittency and measuring translational diffusion coefficients.[605,606] Like all other fluorophores, correlated photoluminescence statistics at nanosecond and subnanosecond timescales are dominated by photon antibunching due to the finite excited state lifetime and quantum nature of individual dots.[372,607] FCS measurements of quantum dot photoluminescence intermittency has confirmed

the power-law dark state duration distribution in CdSe quantum dots for both single immobilized nanocrystals[234,304] and colloidal liquid-phase samples.[305–308] These studies corroborate the putative role of the high-bandgap semicondcuctor outer layers in core/shell quantum dots in improving quantum yield by reducing nonradiative exciton recombination pathways. FCS measurements of quantum dot translational diffusion measure the nanocrystals' effective hydrodynamic radii, and can be used to monitor aggregation from colloidal samples.[608,609] Under illumination conditions yielding prominent blinking effects, the measured autocorrelation function represents a convolution of statistical blinking and Brownian diffusion.[305–307]

Many publications have reported polarization-sensitive photoluminescence measurements or orientational imaging of single *immobilized* nanocrystals[542,568,570] and dye fluorophores.[610–614] Rotational measurements from freely-diffusing colloidal quantum dot preparations, however, have only recently been performed by time-resolved fluorescence anisotropy of bulk samples.[574] Single-nanocrystal transition dipole tracking has also been described for samples prepared in solid-state polymers dense enough to prevent translational diffusion while still allowing intermittent spontaneous orientational jumps.[569] Liquid-phase rotational correlation measurements have not been reported.

Rotational motion of dye fluorophores has similarly been reported for either freely-diffusing preparations via bulk fluorescence anisotropy or single-molecules embedded in supercooled vitreous matrixes that slow rotational diffusion sufficiently to permit polarization-sensitive orientational tracking,[289,493,615–619] the latter of which report the dynamic environmental heterogeneities that are ubiquitously associated with glassy materials. In general, fluorescence anisotropy and depolarization experiments

are limited to systems for which the characteristic rotation time τ_r is $\lesssim 100$ times the fluorescence excited-state lifetime.[620] Orientational tracking experiments require the duration of observation before photobleaching be $\gtrsim 100\tau_r$ in order to avoid broadening effects due to the finite trajectory length of the time series.[492,493,621,622] These timescale requirements impose a significant restriction on the space of possible experiments from which rotational measurements may faithfully be obtained.

In the following section (5.2.4) I present an experimental approach for observing time-correlated rotation of freely-diffusing CdSe/ZnS core-shell quantum dots and dyes by polarized FCS. The limitations associated with photobleaching or polarization-insensitive correlated processes obscuring the rotational timescale are eliminated by collecting both auto- and cross-correlation traces for two orthogonally polarized detection channels, then calculating the autocorrelation:cross-correlation ratio to yield measurement of exclusively polarization-sensitive correlated processes. This method accurately and effectively measures the rotational dynamics of freely-diffusing transition dipoles across a timescale range from μs to ms.

5.2 Measurement of Rotational Correlation Times for Molecules Possessing 1- and 2-Dimensional Fluorescence Transition Dipoles by Polarized FCS

5.2.1 Summary of Experiments

5.2.2 Materials

Cadium selenide quantum dots overcoated with a zinc sulfide shell (CdSe/ZnS core-shell) and coated with either trioctylphosphine oxide (TOPO) or streptavidin surface ligands were purchased from Molecular Probes (Invitrogen) in a variety of emission wavelengths (Table 5.2.2) and stored at 4°C as received until use. 'Texas Red' 1,2-dihexadecanoyl-*sn*-glycero-3-phosphoethanolamine triethylammonium salt (TR-DHPE) and 'Lissamine' Rhodamine B 1,2-dihexadecanoyl-*sn*-glycero-3- phosphoethanolamine triethylammonium salt (RB-DHPE) phospholipids were also used as obtained from Molecular Probes (Invitrogen) and stored at ≤ -20°C until use. Monomeric red fluorescent protein DsRed (rDsRed-Monomer, Clontech 632503) was used as received and stored at ≤ -60°C until use. PFCS microscopy samples were prepared on 25x25 mm Corning 0211 borosilicate #1 coverslips (VWR International) with a measured thickness range of 142–153μm.

The solvents used for preparing organic-soluble PFCS samples were selected from the range of optical immersion oils available from Cargille Laboratories (Cedar Grove, NJ), and are listed in Table 5.2.2. Cargille immersion oils were chosen for several reasons, among these primarily for their chemically inert nature, well-established optical

Name	$\lambda_{max,em}$	ϵ_{405}	ϵ_{532}	Coating	Nominal r_h	Lot
QD545	544 nm	6.4e5	9.0e4	TOPO	2.0 nm	56863A
QD565	563 nm	1.1e6	1.4e5	TOPO	2.4 nm	53263A
QD585	585 nm	2.2e6	3.1e5	TOPO	2.8 nm	53094A
QD605	609 nm	2.8e6	5.8e5	TOPO	4.5nm	465577
QD655	656 nm	5.7e6	2.1e6	TOPO	6.0 nm	399912
QD525Str	526 nm	3.6e5	–	Polymer-Str.	10.0 nm	475603
QD545Str	545 nm	6.4e6	9.0e4	Polymer-Str.	10.5 nm	57121A
QD565Str	568 nm	1.1e6	1.4e5	Polymer-Str.	11 nm	475603
QD585Str	588 nm	2.2e6	3.1e5	Polymer-Str.	12 nm	475603
QD605Str	604 nm	2.8e6	5.8e5	Polymer-Str.	13 nm	475603
QD655Str	660 nm	5.7e6	2.1e6	Polymer-Str.	15 nm	475603

Table 5.1: List of trioctylphosphine oxide- and streptavidin-coated CdSe/ZnS core-shell quantum dots obtained from Molecular Probes (Invitrogen) and used for PFCS experiments $\lambda_{max,em}$ is the wavelength of maximum fluorescence emission, measured by bulk fluorimetry. ϵ_{405} and ϵ_{532} are the extinction coefficients ($M^{-1}cm^{-1}$) at 405 nm and 532 nm, respectively. The coating is the layer of surface ligands surrounding the inorganic core and shell, either organic TOPO ligand or a Molecular Probes proprietary cross-linked polymer conjugated directly to streptavidin. r_h is the nominal hydrodynamic radius of the complete coated QD. Lot is the Molecular Probes lot number of the specific product run used to generate the PFCS data presented below.

purity, availability in a broad viscosity range (19−46000 cSt), and uniform near-exact match in refractive index (n_{589nm} =1.515) to that of the coverslips (n_{589nm} =1.523), a property that eliminates potential artifacts arising from emission birefringence near dielectric interfaces.[570] These oils are composed of varying blends of hydrogenated and non-hydrogenated terphenyls, polybutenes, and aliphatic and alicyclic hydrocarbons.

Cargille Oil Type	Viscosity (cP)	Refractive Index	Lot No.
A	1.38e2	$1.5150 \pm .0002$	100583
300	2.77e2	$1.5150 \pm .0002$	030183
HF	6.51e2	$1.5150 \pm .0002$	082078
B	1.13e3	$1.5150 \pm .0002$	071584
NVH	1.93e4	$1.5150 \pm .0002$	102481
OVH	4.22e4	$1.5150 \pm .0002$	101579

Table 5.2: List of immersion oils used as organic solvent media in PFCS experiments. Viscosities and refractive indices are nominal values at 23°C provided by Cargille.

5.2.3 Experimental Procedures

5.2.3.1 Organic Sample Preparation

Organic QD stocks (1μM in decane) were used in PFCS experiments as provided by the manufacturer without chemical modification. Excitation and emission spectra were measured prior to experimentation by bulk fluorimetry (ISS2K Fluorimeter). Fluorescence quantum yields for organic- and streptavidin-functionalized QD545, QD565 and QD585 were measured relative to Rhodamine 6G using established literature methods,[623] and found to be $\geq .6$ in all cases, whether TOPO- or streptavidin-functionalized. Quantum dots with shorter (QD525) or longer (QD605, QD655 and

QD705) wavelength emission were not assessed for quantum yield due to significant spectral separation from Rhodamine 6G, but throughout PFCS experiments these exhibited fluorescence intensity comparable to that from QD545, QD565 and QD585.

Organic TOPO-functionalized quantum dot samples were diluted from their 1μM stocks to between .05nM and 2nM in final concentration, introducing $\leq$.2% decane into the chosen oil solvent. High-viscosity oils ($\eta \geq 10^3$ cP) were warmed in an oven to $50 - 70$°C prior to addition of QD stocks, in order to facilitate thorough mixing. QD aggregation following $\geq$2 hours at room temperature was observed for samples prepared in the highest viscosity oils (NVH and OVH), and therefore care was taken to prepare all samples immediately prior to use.

Glass coverslips were cleaned by 30 minute sonication in 'Piranha' solution (30:70% H_2O_2 : H_2SO_4), stored in distilled deionized water (MiliQ), and blown dry with filtered nitrogen immediately before mounting on the microscope stage. $\approx$25μl of sample solution was placed on top of the clean coverslip. For all of the high-viscosity organic solvents used, evaporation and flow were not an issue over the duration of a typical experiment. However, in all cases the sample was covered with a clean 4cm diameter petri dish to prevent introduction of dust or other airborne contaminants.

5.2.3.2 Aqueous Sample Preparation

Streptavidin-coated quantum dot (1μM) and red fluorescent protein ($\approx$400nM) stocks were used as supplied by the manufacturers without further modification. Samples were prepared by dilution into aqueous 80–99% glycerol solutions buffered at pH 7.6 with 5mM sodium phosphate. Piranha-cleaned coverslips and Scotch adhesive tape were used to form a $\approx$25μm-thick sealed sample volume that was mounted on

the microscope stage. For reduced-temperature experiments a thermocouple was taped in contact with the top coverslip $\leq$ 2mm offset from the optical axis. The entire custom sample stage ($\approx$1.5Kg mass of machined aluminum) was gradually cooled by directing a stream of chilled nitrogen (evaporating off of a LN_2 bath) over the stage until the desired temperature was reached. This temperature remained stable within $\pm 1°C$ for $\geq$ 1000 seconds during PFCS data collection.

5.2.3.3 PFCS Microscopy

All PFCS data was collected using the microscopy setup described in Section 3.3. Optical power from the excitation laser source was attenuated from $\geq$10mW to .1-500μW and converted to clockwise circular (σ^+) polarization prior to introduction into the back aperture of the objective lens. When using the 405nm laser for excitation of the full spectrum of CdSe/ZnS quantum dots, a stacked longpass filter pair (HQ420lp + HQ500lp, Chroma) was used in the common emission pathway for all QD samples. When 532nm excitation was used for excitation of quantum dots, rDsRed or dye-labeled phospholipids, a bandpass filter (HQ series, Chroma) was selected based on the emission spectrum. Specific experimental parameters are listed in the corresponding figure captions.

PFCS data sets consisted of two autocorrelation traces and a single cross-correlation trace collected by the hardware correlator. Correlation traces were fit[§] either individually to equations 4.28 and 4.29 (p. 160), to extract parameter sets $\left\{\langle N\rangle, \tau_d, F, \tau_r\right\}$, or fit as a ratio to equation 4.30 (p. 161). Nonlinear fitting was carried out in Matlab.

[§]The hardware correlator produces traces $\mathcal{G}^{\{(a),(x)\}}(\tau)$ having baseline value of 1 in the absence of correlation. However, equations 4.28 and 4.29 assume a baseline value of 0 in the absence of correlation. This discrepancy is easily corrected by adding a constant value of 1.

5.2.4 Results

A list of salient predictions from the PFCS model presented in Section 4.3.4 are summarized in Table 5.2.4.

Parameter	Dependence
τ_d	$\propto r_h$
τ_d	$\propto \eta$
τ_d	$\propto \omega^2$
τ_r	$\propto r_h^3$
τ_r	$\propto \eta$
τ_r	$\not\propto \omega$
F	independent of sample preparation.

.

Table 5.3: List of $\mathcal{G}(\tau)$ parameter dependencies predicted from equations 4.28 and 4.29.

5.2.4.1 PFCS of 2D Transition Dipoles: Colloidal CdSe Core/Shell Quantum Dots

A representative PFCS data set collected from streptavidin-coated water-soluble quantum dots in glycerol solution is shown in Figure 5.2. A fit of the measured correlation traces to the full rotation-diffusion models (equations 4.28 and 4.29) to extract parameter sets $\left\{\langle N\rangle, \tau_d, F, \tau_r\right\}$ was straightforward because of the absence of blinking phenomena at the excitation power used. These correlation traces also closely match a theoretical trace profile that was predicted previously in the literature but has not been corroborated by experiment.[624] Fitting the cross-correlation:autocorrelation ratio to equation 4.30 provided a means by which to extract parameter subsets $\left\{F, \tau_r\right\}$ independent of $\langle N\rangle$ and τ_d.

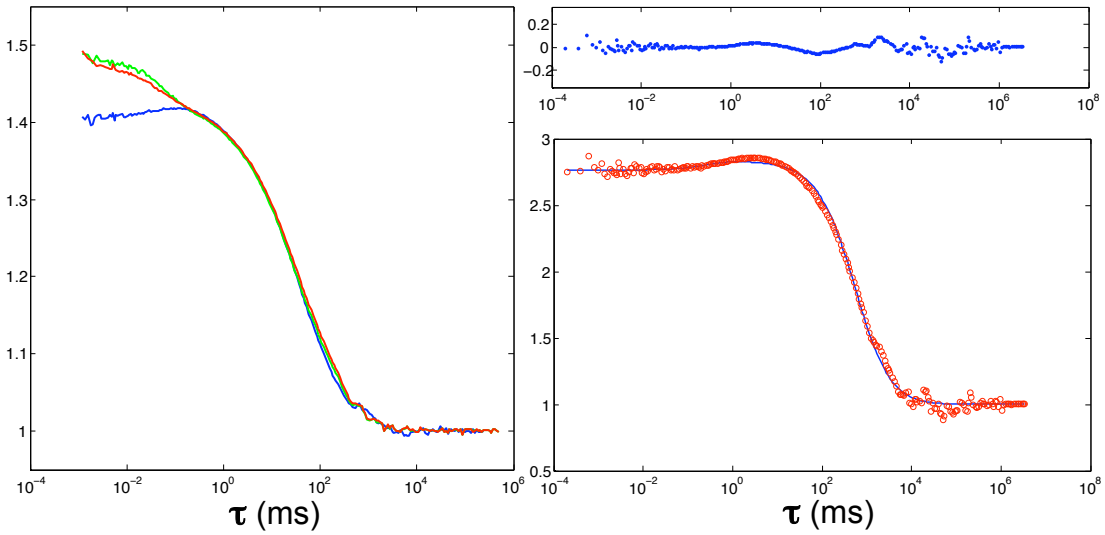

Figure 5.2: (Left): Auto- (red/green) and Cross-correlation (blue) traces collected from a sample of 1nM QD565/Streptavidin in 85% glycerol solution, 23°C (η=92cP). (Right) Cross-correlation data points (red circles) and fit to equation 4.29 (blue line), with fit residuals (blue, top) for a sample of 250pM QD565/Streptavidin in 99% glycerol solution, 23°C (η=930cP). **Experimental Conditions, Left Plot:** $\lambda_{ex} = 405nm$, $P_{ex} = 8\mu$W, $Pol_{ex} - \sigma^+$, F_{em} =HQ530lp, $T_{exp} = 900$s. **Experimental Conditions, Right Plot:** $\lambda_{ex} = 405nm$, $P_{ex} = 4\mu$W, $Pol_{ex} - \sigma^+$, F_{em} =HQ530lp, $T_{exp} = 1200$s.

The dependence of τ_r and τ_d upon observation volume size is illustrated in Figure 5.3. This experiment was carried out by varying the diameter of the collimated excitation beam by known amounts, from its full diameter of 7.5mm down to 2.0mm, in order to change the effective NA of the confocal observation volume.[†] A $150\mu m$ confocal pinhole, equivalent to ≈ 3 Airy, was used for all correlation trace collections in order that the dimensions of the resulting point spread function (Figure 3.8, p. 95) be governed predominantly by the excitation NA. In addition to the absolute dimensions of the 3D point spread function scaling inversely with NA, the relative dimensions of the probe volume will also change slightly (Figure. 3.9, p. 96). However, this effect should exert a fairly minimal influence upon τ_d and τ_r. The diffusion time constant τ_d displays a quadratic dependence on the probe volume dimensions, as expected from Table 5.2.4.

The dependence of τ_r and τ_d upon solvent viscosity for TOPO-coated organic soluble quantum dots is illustrated in Figure 5.4. Parameters F and β are invariant with respect to viscosity. Both τ_r and τ_d vary linearly with viscosity, in agreement with equations 4.19 and 4.22.

The dipole polarization magnitude parameter F was observed to be statistically independent of solvent viscosity, surface ligand composition and excitation power within the range of 80nW–200μW for 405nm excitation and 500nW–100μW for 532nm excitation, in agreement with expectations. F was found to vary slightly with QD fluorescence emission spectral range, which is itself governed by the size of the CdSe core. Table 5.4 list the measured values for F from equation 4.30 fits to each quantum dot species. From these values of F it is possible to estimate the corre-

[†]The exact mapping of beam diameter to numerical aperture is known from the calibration of input beam to output angle aided by a hemispherical lens, as described in Section 3.3

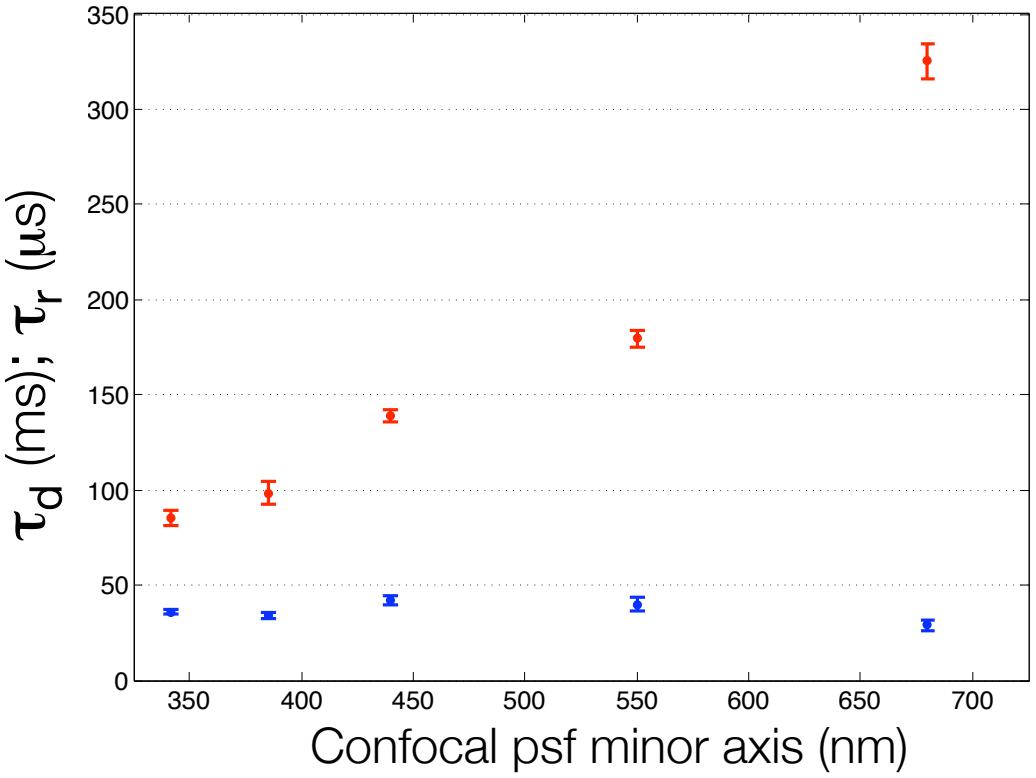

Figure 5.3: Variance of rotational and translational correlation times upon confocal probe volume size, measured using a sample of QD565Str in 85% glycerol solution. PFCS traces were fit by equation 4.29 to measure τ_d, or by equation 4.30 to measure τ_r. The x-axis is the diameter of the minor axis of the confocal probe volume, 2ω (equation 4.20, p. 154). The y-axis units are ms (for τ_d) or μs (for τ_r). The diffusion time constant τ_d displays a quadratic dependence on the probe volume dimensions, as expected from Table 5.2.4. The rotational time constant τ_r displays no dependence on probe volume, also in agreement with expectation. **Experimental Conditions:** $\lambda_{ex} = 405nm$, $P_{ex} = 50\mu$W, $Pol_{ex} - \sigma^+$, F_{em} =HQ500lp, $T_{exp} = 900$s., $d_{ph} = 150\mu m$

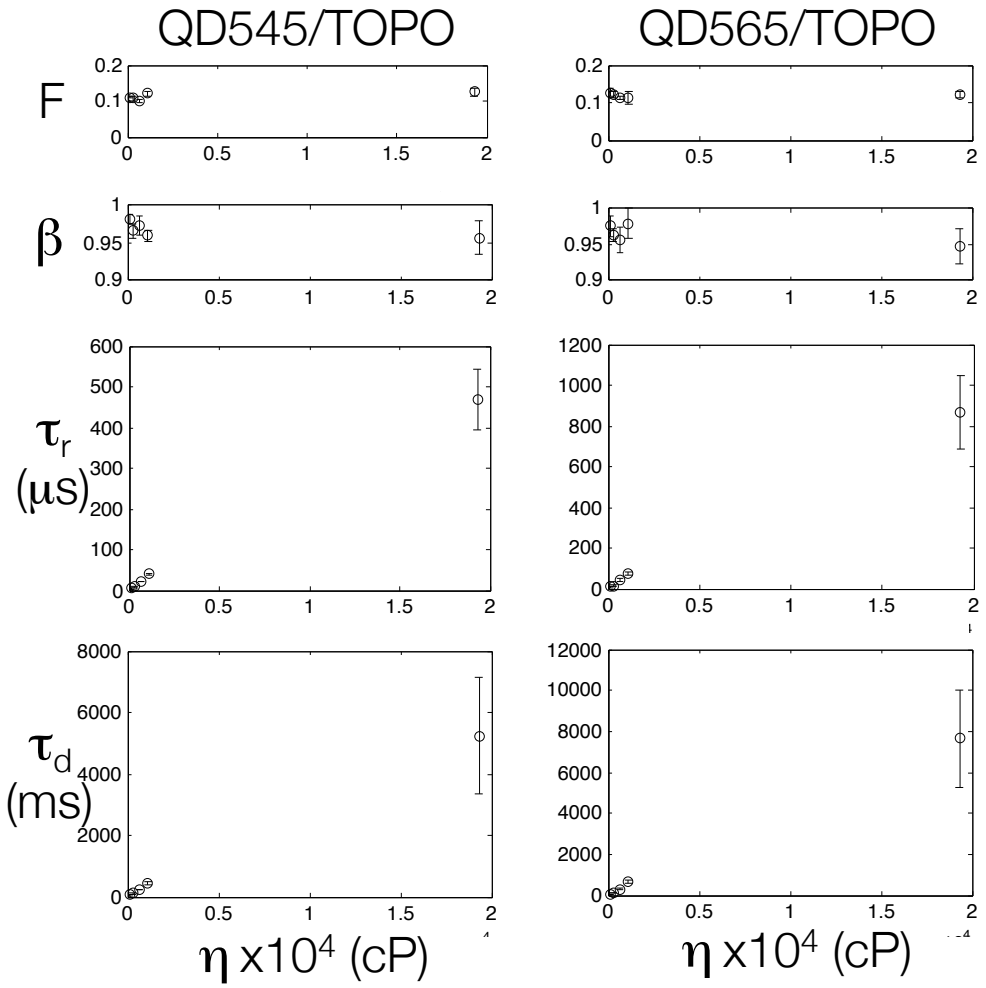

Figure 5.4: Dependence of rotational and diffusional correlation times upon solvent viscosity. Viscosity data points $\eta = \{138, 277, 651, 1130, 19300\}$ cP correspond to Cargille oils $\{$A, 300, HF, B, NVH$\}$ Parameter values represent fits to equation 4.30 (for $\{F, \tau_r, \beta\}$) or equation 4.29 for τ_d, with mean values $\pm$ one standard deviation from at least 3 data samples. **Experimental Conditions:** $\lambda_{ex} = 405nm$, $P_{ex} = \{20, 5\}\mu W$ for $\{$QD545TOPO, QD565TOPO$\}$; $Pol_{ex} = \sigma^+$, F_{em} =HQ500lp, $T_{exp} =$ 100s

sponding 2D transition dipole eccentricity, the interdependence of which is presented in Figure 5.21 of the Monte Carlo simulation section (Section 5.3.3, p. 217).

The most notable systematic phenomenon present in the data summarized in Table 5.4 is that the experimentally determined values for r_h are consistently lower when calculated based on the rotational correlation time τ_r (using equation 4.22) than when calculated based on the translational diffusion correlation time τ_d (using equation 4.19), a phenomenon that has also been observed by bulk fluorescence depolarization of globular proteins in macromolecule-crowded solutions.[499] Additionally, the r_h values calculated from τ_r are always lower than the nominally expected values. The discrepancy is much less significant for the streptavidin-coated quantum dots than for the organic TOPO-coated quantum dots. The explanation almost certainly lies in the unknown values in equation 4.22: the shape parameter f and in particular the solvent-solute coupling parameter C. The value of C can vary between 0 and 1 depending on the strength of interaction between the solvent and the surface of the quantum dot. It is reasonable to expect that the saturated alkanes comprising the octyl arms of TOPO and the saturated alkane components of the organic oil solvent will interact more weakly than will streptavidin surface ligands and an aqueous solvent. The nature of surface ligands and solvent type have previously been reported to exert varying influence on the diffusion properties of colloidal quantum dots.[602] Given the observation in this investigation that the r_h values are on average 34% lower when calculated from τ_r than when calculated from τ_d, and knowing that $\tau_r \propto Cr_h^3$, we can conclude that the coupling parameter value for TOPO/Oil is roughly one half that of streptavidin/aqueous glycerol: $C_{(TOPO-Oil)} \approx \frac{1}{3} C_{(Strept.-Aq)}$.

Quantum Dot	Nominal r_h (nm)	Experimental r_h (calc. from τ_r)	Experimental r_h (calc. from τ_d)	F	e_{2D}
QD545TOPO	3.0	2.3 ± 0.4	3.3 ± 0.3	.113±.011	$e \approx 0$
QD565TOPO	3.5	2.4 ± 0.3	3.8 ± 0.2	.128±.009	$e \leq .7$
QD585TOPO	4.0	2.9 ± 0.4	4.4 ± 0.5	.122±.010	$e \approx 0$
QD605TOPO	5.0	3.9 ± 0.7	5.6 ± 0.4	.120±.007	$e \approx 0$
QD655TOPO	6.0	4.5 ± 0.9	6.7 ± 0.6	.137±.016	$e \leq .7$
QD525Str	10 ± 1	8.9 ± 0.9	10.0 ± 0.9	.136±.021	$e \leq .7$
QD545Str	10.5 ± 1	9.2 ± 1.4	11.5 ± 2.7	.119±.027	$e \approx 0$
QD565Str	11 ± 1	9.2 ± 1.0	11.7 ± 1.3	.125±.009	$e \leq .7$
QD585Str	11.5 ± 1	9.6 ± 2.2	13.5 ± 2.2	.098±.014	$e \approx 0$
QD605Str	12 ± 1	10.7 ± 2.0	14.1 ± 2.0	.113±.020	$e \approx 0$
QD655Str	15 ± 2	12.2 ± 3.3	17.6 ± 1.7	.135±.021	$e \leq .7$

Table 5.4: Data table for streptavidin-coated aqueous colloidal quantum dots obtained from Molecular Probes (Invitrogen). Nominal hydrodynamic radii consist of the contributions from the CdSe core, the ZnS shell and the TOPO ligands. Measured values for r_h are compared to hydrodynamic radii determined experimentally from either τ_r measured by PFCS or τ_d measured by conventional FCS. Parameter values represent mean ± one standard deviation from model fits of equations 4.29 (for r_h from τ_d) or 4.30 (for r_h from τ_r and F) using data sets from at least 3 individual experiments

5.2.4.2 1D Transition Dipoles: DsRed, and Dye-Labeled Phospholipids

In order to obtain complete polarization-rotation correlation data for an emission dipole known to have simple 1D geometry, it was necessary to select a fluorescent molecule of sufficient size to yield $\tau_r \geq 1\mu s$, $1\mu s$ being the lower bound for correlation times measurable with the microscopy system described here as a result of APD afterpulsing artifacts. An additional challenge is the presence of very significant triplet-state blinking effects (discussed in Section 4.1 and Figures 4.2, p. 137, and 4.4, p. 141) in the excitation power range required to obtain sufficient fluorescence signal, effects that vitiate the results from direct fits to equations 4.28 and 4.29. Triplet-state blinking is a common issue with fluorescent protein probes uner single-molecule imaging conditions.[625–627] In these instances only ratio fits to equation 4.30 are possible.

The red fluorescent protein DsRed was found to be a suitable candidate for PFCS measurements of 1D dipole rotation, particularly when prepared in aqueous solution containing 85–99% glycerol to increase the viscosity η and correspondingly yield slower rotational diffusion. DsRed ($\lambda_{ex,max}/\lambda_{em,max}$ =556/586nm; MW 28 kDa) is available from commercial sources as a monomer of roughly spherical symmetry and r_h ≈2.3nm. The addition of glycerol to dsRed samples also permits cooling of the solution to below 0°C, further increasing solvent viscosity and τ_r.

Figure 5.5 displays representative PFCS data sets collected for dsRed. The expected rotational diffusion time assuming a hydrodynamic radius of 2.3nm is $1.3 \cdot 10^{-8}\eta$s, suggesting that in order to confidently measure a rotation component $\tau \geq 20\mu s$ by PFCS the solvent viscosity must be in excess of 10^3 centiPoise. 98% aqueous glycerol has viscosity $\eta \approx 760$cP at room temperature, therefore necessitating cooling

of the DsRed samples to further increase η. It is clear from visual examination of the dsRed cross-correlation traces (blue curves, left column of Figure 5.5) that fits to equation 4.29 are impossible with non-negative values for parameter F. This problem arises because of the significant triplet-state component of the correlation traces, which induce large positive correlation for times $\tau \lesssim 100\mu s$. Since the triplet-state-induced fluorescence intermittency does not include a polarization component, it will appear as a positive term in both the auto- and cross correlation traces and thereby obscure the dipole rotation component. Taking the cross-correlation:autocorrelation ratio, however, will remove the triplet component from the correlation traces along with the similarly polarization-insensitive diffusion component. The remaining rotation component of the correlation traces are then well fit by equation 4.30 to measure τ_r, as shown in the right column of Figure 5.5.

Data sets for DsRed monomer in 98% glycerol were acquired at four other temperatures in addition to those for which corresponding data are displayed in Figure 5.5. Figure 5.6 presents the fit parameter values collected for a sample at the temperatures $\{23.3, 14.9, 10.3, 5.6, -0.7, -4.6\} \pm 1.0°\text{C}$, at which 98% glycerol solution has viscosities $\{760, 1550, 2430, 3890, 7470, 15200\}$ centiPoise. The parameter values $\{F, \tau_r, \beta\}$ are determined from data fits to equation 4.30. Solvent viscosity was not measured directly, but inferred from the sample temperature via reference to literature sources for glycerol solution.[628] The rotational correlation time τ_r scales linearly with solvent viscosity, in agreement with expectation based on the PFCS model (Table 5.2.4). The fit parameter β is statistically invariant across the temperature range of these data sets, consistently $\beta \approx .98$, suggesting that even though the viscosity is very high at the lower temperature points, molecular orientational dynamics are not heterogeneous. The measured values for F are also statistically

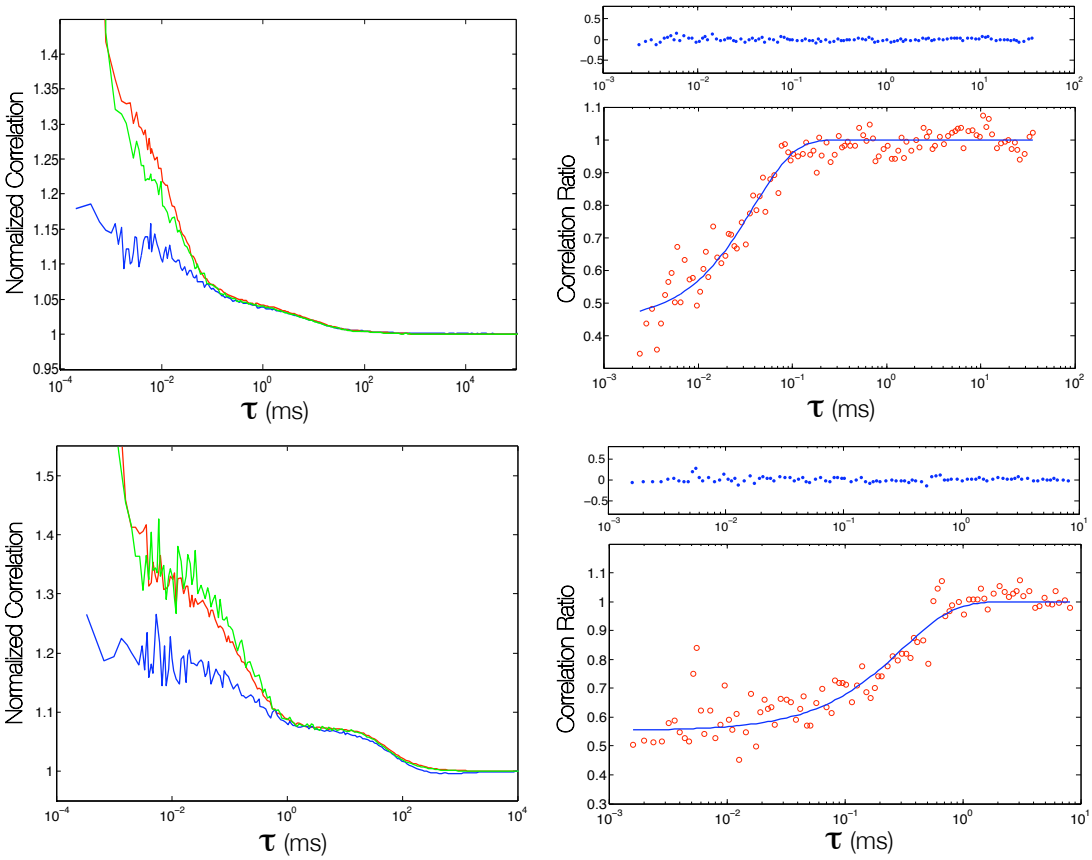

Figure 5.5: PFCS data sets and fits to equation 4.30 for a sample of DsRed monomer in 98.0% glycerol solution at two temperatures: 10.3°C (top row) and -4.6°C (bottom row). Fit parameters $\{F, \tau_r, \beta\}$ from these data sets are $\{0.253, 0.985, 0.039\mu s\}$ for the 10.3°C sample, and $\{0.238, 0.964, 0.290\mu s\}$ for the -4.6°C sample. The trace ratio profile is nearly identical to the simulated data presented in Figure 5.13 for a 1D transition dipole. (p. 209) **Experimental Conditions:** $\lambda_{ex} = 532nm$, $Pwr_{ex} = 20\mu W$, $Pol_{ex} : \sigma^+$, F_{em} =HQ595/50, $t_{exp} = 300$s

invariant across the temperature range, with mean value $\langle F \rangle = .240$, in very close agreement with the expected value for 1D dipole rotation with $NA1.45$ objective lens ($F \approx .26$). This F value will be discussed in the following Monte Carlo simulation section (see Figure 5.13, p. 209).

A linear regression fit to the data points in the bottom plot of Figure 5.6 yields a slope of $.0199\left(\frac{\mu s}{cP}\right)$. The hydrodynamic radius can be determined from $r_h = \left[\frac{3k_BT}{4\pi\eta}\right]^{\frac{1}{3}}$ by reference to the Stokes-Einstein-Debye relation (equation 4.22) (assuming $f, C \approx 1$). Plugging the slope value into this relation yields a calculated value for the hydrodynamic radius of r_h =2.7nm, slightly higher than the reported value of 2.3nm. This discrepancy is likely due to the unknown values for f and C.

Figure 5.7 illustrates the invariance of parameter values measured with laser excitation power (λ_{ex} = 532nm, σ^+ polarization) over the range 10–100μW, using a sample of DsRed in 99.5% glycerol at room temperature ($23.3°, \eta \approx 1000$cP). Excitation power below $10\mu W$ yielded insufficient signal, while excitation power above $100\mu W$ induced excessive background.

Three other commercially available GFP mutants (CFP, eGFP and YFP) were also investigated in similar PFCS experiments, however only dsRed yielded satisfactory signal-to-noise for PFCS data using the available laser excitation sources (405nm and 532nm). These proteins would likely yield PFCS data similar to that collected from dsRed if optimized microscope components were available.

Figure 5.8 depicts representative PFCS data sets and ratio fits collected from Texas Red DHPE and Rhodamine B DHPE in Cargille OVH, the highest-viscosity oil used for these experiments, having η=42,200 cP. The average parameter values measured

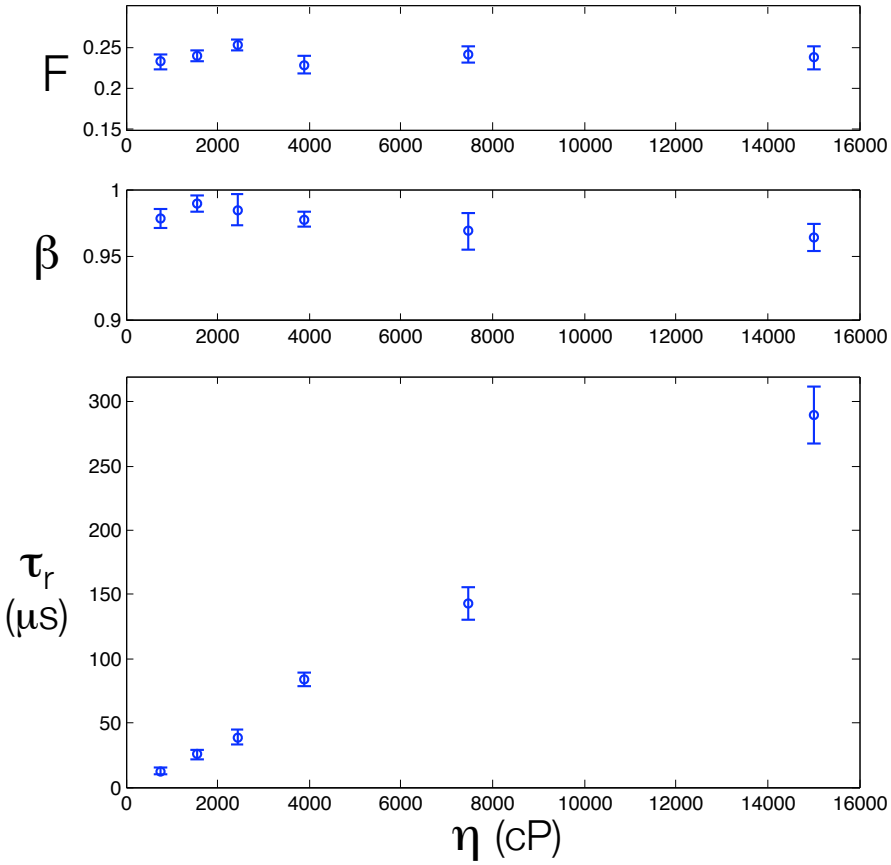

Figure 5.6: Parameter values for DsRed monomer in 98% glycerol solution at varying temperature, plotted versus solvent viscosity (in centiPoise). The top plot illustrates the invariance of parameter F versus viscosity, with mean value $\langle F \rangle = .240$. The middle plot illustrates the statistical invariance of KWW 'stretching' parameter β, with $\langle \beta \rangle = .978$. The bottom plot show the linear dependence of the rotational correlation time τ_r upon solvent viscosity. Data values are mean $\pm$ standard deviation from 3 sequential data collections. **Experimental Conditions:** $\lambda_{ex} = 532nm$, $Pwr_{ex} = 20\mu W$, $Pol_{ex} : \sigma^+$, F_{em} =HQ595/50, $t_{exp} = 300$s, $d_{ph} = 75\mu m$

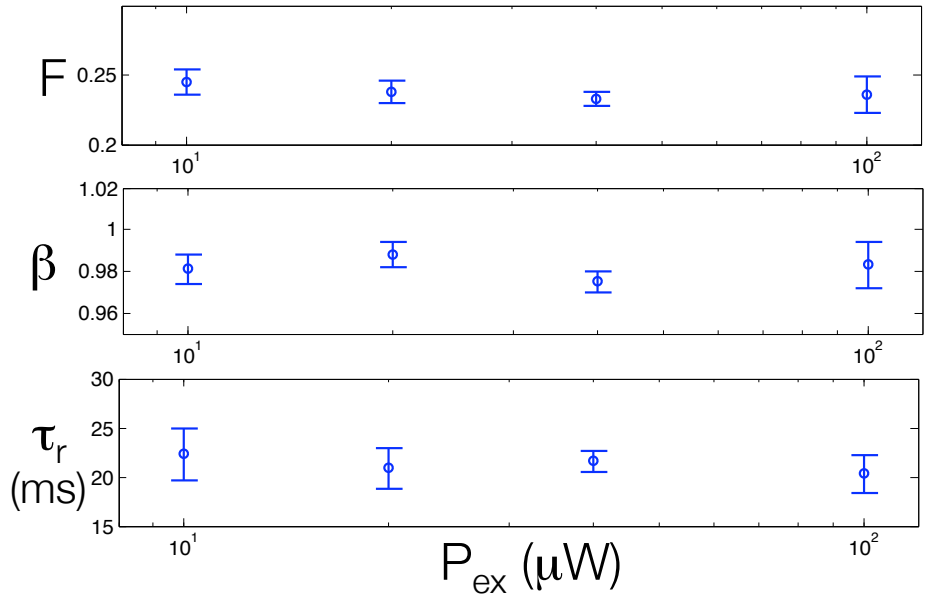

Figure 5.7: Invariance of measured fit parameters $\{F, \tau_r, \beta\}$ with respect to laser excitation power, for a sample of DsRed in 99.5% glycerol at room temperature (23.3°). Values are means ± one standard deviation from 5 collections at each power level. **Experimental Conditions** λ_{ex} = 532nm; σ_+ polarization; power=$\{10, 20, 40, 100\}\,\mu W$; F_{em} =HQ595/50, t_{exp} = 100s, $d_{ph} = 75\mu m$

for F, τ_r and β from fits to equation 4.30 for several preparations of RB-DHPE and TR-DHPE in OVH oil and NVH oil (η=19,300) are listed in Table 5.2.4.2. For both Texas Red and Rhodamine B phospholipids the measured rotational correlation times were roughly twice as fast in the NVH oil as in the OVH oil, in accordance with their expected linear dependence upon solvent viscosity. However, in both cases the measured τ_r for the Rhodamine B lipid was roughly double that of the Texas Red lipid, which may be due to differences in either dipole orientation relative to the molecular reference frame or to differences in intramolecular orientational mobility of the fluorescent dye moiety between the two species. The measured values for unitless parameters F and β were statistically indistinguishable between the two dyes and between the two solvent oils, and are both in agreement with expectations for 1D transition dipoles, as illustrated by simulation results in Section 5.3.

Dye-Phospholipd	Oil	Viscosity	F	τ_r	β
RB-DHPE	OVH	4.22e4 cP	$.220 \pm .011$	$106.8 \pm 12.0\mu$s	$.949 \pm .006$
RB-DHPE	NVH	1.93e4 cP	$.223 \pm .007$	$39.1 \pm 6.2\mu$s	$.976 \pm .011$
TR-DHPE	OVH	4.22e4 cP	$.245 \pm .008$	$58.3 \pm 10.7\mu$s	$.943 \pm .008$
TR-DHPE	NVH	1.93e4 cP	$.244 \pm .005$	$24.7 \pm 6.3\mu$s	$.953 \pm .004$

Table 5.5: Table of parameters measured for dye-labeled phospholipid samples. Parameters represent means ± one standard deviation of model fits to at least 4 individual experiments

5.2.4.3 Control Experiments

Optical control experiments were carried out by removing the polarizing beamsplitter and polarization filters from the emission pathway (Figure 3.17, p. 122) and

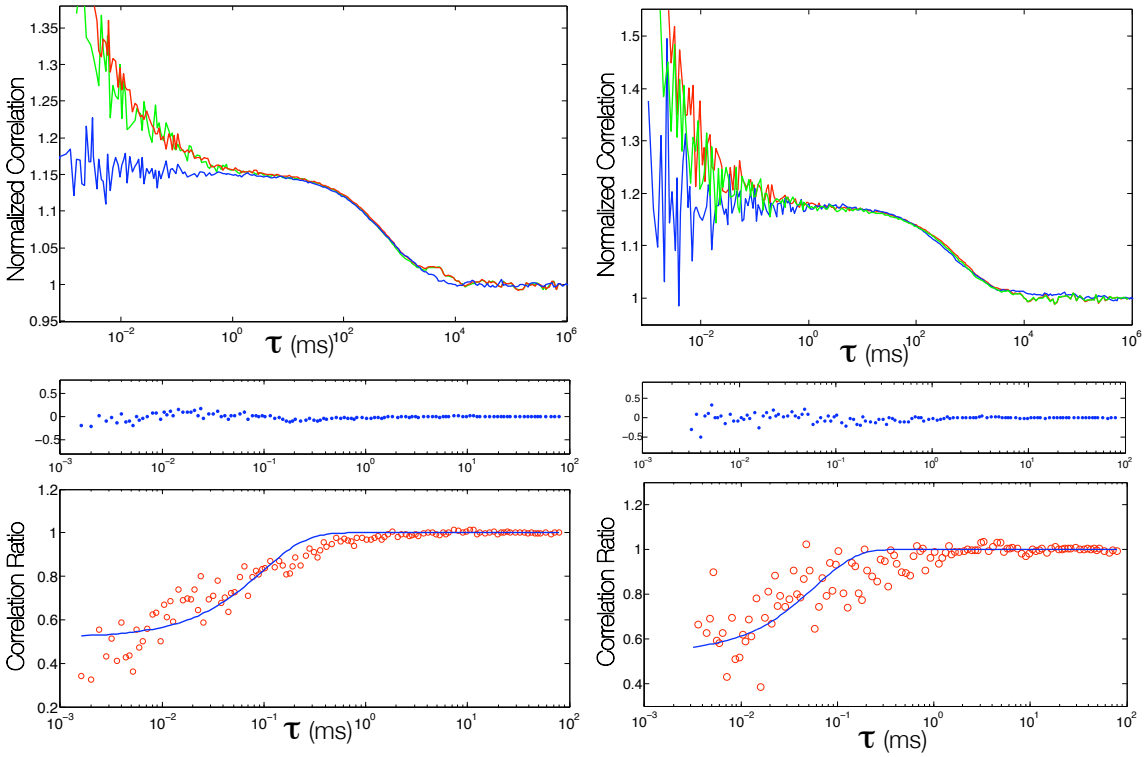

Figure 5.8: Complete PFCS data sets for RB-DHPE (left) and TR-DHPE (right) in Cargille OVH oil. The top plot in each column displays the autocorrelation traces from the horizontal (green) and perpendicular (red) polarization channels, and the cross-correlation trace (blue) for the two channels. The bottom plot in each column displays the cross-correlation:autocorrelation ratio trace (red circles) and the fit to equation 4.30 (blue line), with the fit residuals (blue dots) immediately above it. The ratio trace profile is in good agreement with the simulated results for 1D dipoles show in Figure 5.13(p. 209). Fit parameters $\{F, \tau_r, \beta\}$ from these data sets are $\{0.241, 0.954, 92.1\mu s\}$ for RB-DHPE and $\{0.231, 0.965, 55.5\mu s\}$ for TR-DHPE. **Experimental Conditions, RB-DHPE:** $\lambda_{ex} = 532nm$, $Pwr_{ex} = 50\mu W$, $Pol_{ex} : \sigma^+$, F_{em} =HQ595/50, t_{exp} = 1200s, $d_{ph} = 75\mu m$. **Experimental Conditions, TR-DHPE:** $\lambda_{ex} = 532nm$, $Pwr_{ex} = 100\mu W$, $Pol_{ex} : \sigma^+$, F_{em} =HQ630/50, $t_{exp} = 1200$s, $d_{ph} = 75\mu m$

replacing them with just a single 50:50 nonpolarizing beamsplitter. In these experiments the rotational correlation component of the auto- and cross-correlation traces was completely absent. The cross-correlation:autocorrelation ratio universally showed only the APD afterpulsing artifact at $\tau \lesssim 1\mu$s, which induces very large correlation values in the autocorrelation but has no effect on the cross-correlation, resulting in the ratio falling quickly to 0 for the shortest-time values of τ. The same profile was measured using the 50:50 nonpolarizing beamsplitter with rDsRed, Texas Red DHPE, several varieties of organic quantum dots and a bulk rhodamine 6G sample. The afterpulsing effect could potentially be mitigated or eliminated entirely by using a 4-channel hardware correlator and a system of 4 APDs in the emission pathway, with a pair of APDs each designated to one polarization channel and a 50:50 nonpolarizing beamsplitter added to each polarization pathway following the polarizing beamsplitter. The autocorrelation could then be measured free from afterpulsing artifacts collecting cross-correlation traces from each APD pair. This would reduce the lower bound for τ_r to that limited by the hardware correlator ($\approx$200 ns) but at the addition of significant expense.

Hardware control experiments included switching the photodetectors between the two collection channels, switching which PC counter board collected data from each photodetector. No differences were noted.

Data reduction control experiments involved variation of the data collection and processing methods, specifically to compare real-time output of the hardware correlator with post-processing output of the raw photon-count time series from Matlab. In particular, the endogenous Matlab function CROSSCORR produces a correlation trace with both positive and negative τ-values and a baseline correlation of 0. The hard-

ware correlator produces a trace with only positive τ-values, a baseline correlation of 1, and potentially other differences arising from algorithmic differences. However, a numerical routine custom-written in Matlab to match the hardware correlator algorithm (A.2.6, p. 240) produced correlation traces identical to those generated by the hardware alone.

Similar results to those presented here for Molecular Probes quantum dots were also obtained using core/shell quantum dots from a different manufacturer (NN Labs, AR). QDs from this supplier, however, had a significantly reduced quantum yield ($\approx$.08–.15) relative to those supplied by Molecular Probes and resulted in lower quality PFCS data (not presented).

5.3 Monte Carlo Simulations of Polarized Fluorescence Cross-Correlation Spectroscopy Applied to Freely Rotating 1- and 2-Dimensional Single-Molecule Dipoles

This section provides a description of numerical simulations of PFCS. Briefly, stochastic rotational diffusion was simulated using a Monte Carlo numerical routine consisting of sequential three-dimensional rotational matrix transformations. The transition dipole orientational trajectories collected from each simulation were used to generate the expected signals collected by horizontal and vertical polarization channels using equations 3.68–3.72 (p. 115). These simulated bivariate time series data sets were then processed using auto- and cross-correlation algorithms equiva-

lent to those performed by the hardware correlator in the microscopy setup used for the corresponding experiments (Section 3.3.2, p. 123). The simulation results presented below are in broad agreement with experimental measurements and general observation. Conclusions are enumerated in Section 5.3.4 (p. 219).

The first step in modeling experimental observation of a freely rotating single-molecular dipole using polarization-sensitive confocal microscopy involves clearly defining the molecular and laboratory (microscope) reference frames, $\boldsymbol{\mathcal{R}_{mol}}$ and $\boldsymbol{\mathcal{R}_{lab}}$, respectively, as shown in Figure 5.9. The molecular reference frame (5.9a) has scalene ellipsoidal symmetry in the right-handed Cartesian axes $\left(\hat{\boldsymbol{a}}, \hat{\boldsymbol{b}}, \hat{\boldsymbol{c}}\right)$. Rotation about each axis is described by the Euler angles (α, β, γ), respectively, with counterclockwise rotation corresponding to positive angle values. The transition dipole $\boldsymbol{\rho_0}$ has constant orientation parallel to the vector $\left(\rho_a\hat{\boldsymbol{a}} + \rho_b\hat{\boldsymbol{b}} + \rho_c\hat{\boldsymbol{c}}\right)$ in $\boldsymbol{\mathcal{R}_{mol}}$ and constant magnitude $\rho_o = \|\boldsymbol{\rho_o}\|$ (where $\|\ \|$ represents the Euclidean norm in $\mathbb{R}^{(3)}$).

The laboratory reference frame (5.9b) has right-handed Cartesian axes $(\hat{\boldsymbol{x}}, \hat{\boldsymbol{y}}, \hat{\boldsymbol{z}})$. Rotational diffusion of the transition dipole in the laboratory reference frame occurs by stochastic random-walk of each Euler angle in $\boldsymbol{\mathcal{R}_{lab}}$, with mean angular stepsize governed by a diffusion constant $(d_\alpha, d_\beta, d_\gamma)$ corresponding to each axis of rotation. Rotation of ρ_d in $\boldsymbol{\mathcal{R}_{lab}}$ can be measured by a two-channel polarization-sensitive microscopy system consisting of a beamsplitter that separates the components of $\boldsymbol{\rho_d}$ that are parallel to $\hat{\boldsymbol{x}}$ and $\hat{\boldsymbol{y}}$, each of which can then measured by an optical channel containing a polarization-insensitive photodetector. The parallel ($\parallel$) and perpendicular ($\perp$) polarization channels are arbitrarily assigned to the x- and y-axis components. The magnitude and anisotropy of the signal from $\boldsymbol{\rho_d}$ measured by two independent polarization channels describes the orientation of $\boldsymbol{\rho_0}$ in $\boldsymbol{\mathcal{R}_{lab}}$, with the

loss of information regarding the sign of ρ_z. For the purposes of measuring rotational correlation time, however, two measurement channels are sufficient.

At each point in time the complete orientation of $\boldsymbol{\rho_d}$ in $\boldsymbol{\mathcal{R}_{lab}}$ can be specified by a 3-vector $\boldsymbol{\rho_d} = (\rho_x\hat{\boldsymbol{x}} + \rho_y\hat{\boldsymbol{y}} + \rho_z\hat{\boldsymbol{z}})$ normalized under the condition $\|\boldsymbol{\rho_d}\| = \rho_o$. Alternately, it can also be described by a pair of angles (ϕ, θ) relative to the z- and x-axis, respectively, and a magnitude $\sqrt{(\rho_x^2 + \rho_y^2)} = \rho_o \sin^2\phi$, with the loss of ρ_z sign as mentioned above. The signals expected in channels I_x and I_y are given by equations 3.68–3.72 (p. 115), and are a function of variables $\rho_x, \rho_y, |\rho_z|$, and parameters ρ_o and ψ_{max}, the last of which is determined by numerical aperture of the microscope objective and the refractive index n_o of the surrounding medium.

5.3.1 Monte Carlo Polarized FCS Simulation Method

Monte Carlo simulations of polarized FCS for both linear 1D and nondegenerate 2D transition dipoles of single molecules in solution were carried out by diffusion of Eulerian angles on the surface of a hyperdimensional sphere, following a typical stochastic Wiener process. Briefly, each Euler angle is incremented by a Gaussian stepsize distribution with mean of zero and standard deviation inversely proportional to the rotational diffusion time constant for the corresponding molecular axis. The molecular reference frame is rotated about each axis using 3x3 rotational transformation matrixes calculated from the incremented angular values, and the resulting orientation of the transition dipole determined relative to the laboratory reference frame. The resulting orientation- and NA-dependent signal collected by the orthogonal polarization channels of a confocal microscope are then calculated using equations 3.68–3.72 (p. 115) for the corresponding time window to generate the sim-

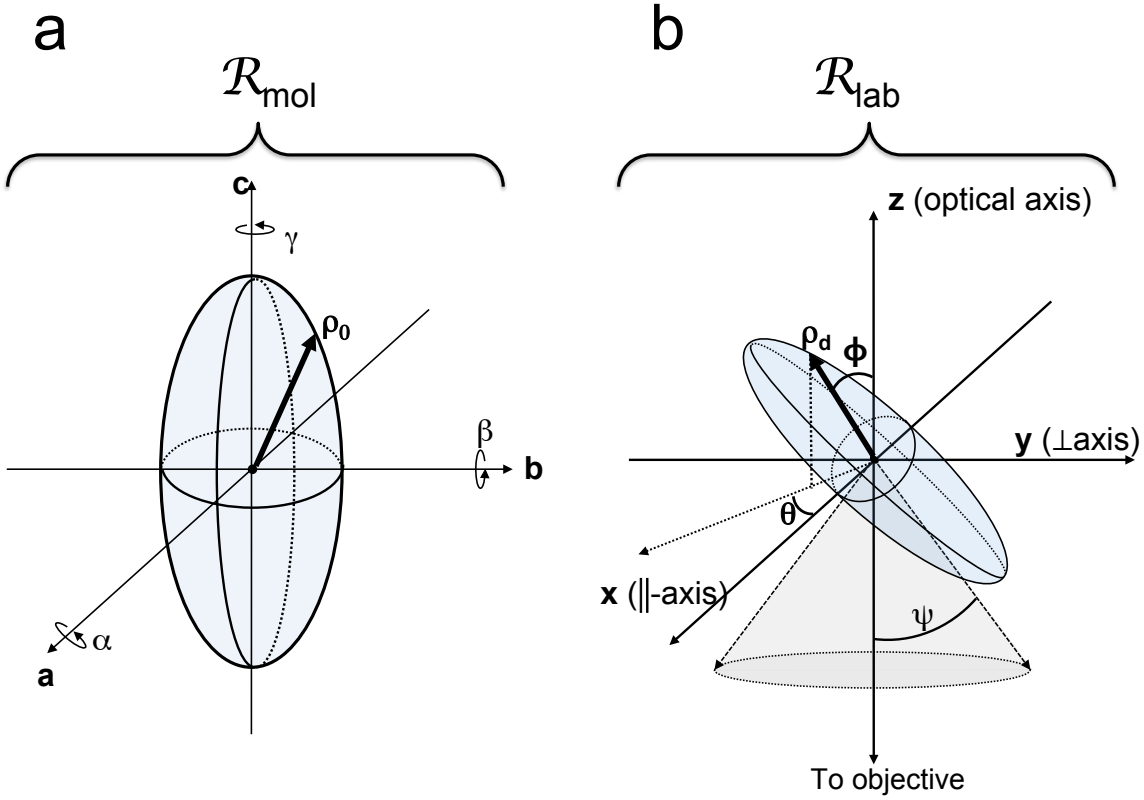

Figure 5.9: Reference frames for transition 1-D dipole diffusional rotation. **(a)**: Molecular frame of reference. Rotational diffusion occurs differentially about each of the three orthogonal axes $(\hat{\boldsymbol{a}}, \hat{\boldsymbol{b}}, \hat{\boldsymbol{c}})$ of a scalene ellipsoid by corresponding angle (α, β, γ), with clockwise defined as positive anglular values. The permanent 1-D transition dipole is assigned an arbitrary fixed vector orientation $\boldsymbol{\rho_0}$ in the molecular frame of reference. **(b)**: Laboratory frame of reference The z-axis is assigned to the optical axis of the microscope, and the x- and y-axes assigned to the perpendicular $(\perp)$ and parallel $(\|)$ polarization orientations, respectively, of the detector optics. The 1-D transition dipole $\boldsymbol{\rho_d}$ orientation in the microscope reference frame is described by equatorial angle θ and declination from the optical axis ϕ. The angular range of the photon collection cone ψ is determined from the numerical aperture (NA) of the objective lens and the refractive index of the surrounding medium (n_o) by the relation. $\psi_{max} = \sin^{-1}\left(\frac{NA}{n_o}\right)$.

ulated data set. Following completion, the time orientation and signal timecourse data are processed to yield numerical auto- and cross-correlation.

Matlab code used for these numerical simulations is presented in the appendix (Section A.2, pp. 228–240).

Rotational diffusion in three dimensions can be described by an independent real-valued Wiener process or each of the three variables (α, β, γ), corresponding to the Eulerian angles of $\boldsymbol{\mathcal{R}_{mol}}$. A Wiener process is a stochastic time series $W(t)$, characterized by the attribute that the difference in its values at two time points are described probabilistically by a normal (Gaussian) distribution $\mathcal{N}(\mu, \sigma)$ with mean zero $(\mu - 0)$ and variance equal to the time separation $(\sigma = t_i - t_j)$, as shown in equation 5.1.

$$W(t_i) - W(t_j) \sim \mathcal{N}\big(0, t_i - t_j\big) \tag{5.1}$$

Beginning from a specified initial orientation $\boldsymbol{\rho_0}$, at every discrete time step δt each variable $\{\alpha, \beta, \gamma\}$ is incremented by a corresponding random Gaussian-distributed value $\{\delta\alpha, \delta\beta, \delta\gamma\}$ with mean 0 and variance $\{\sigma_\alpha, \sigma_\beta, \sigma_\gamma\}$. These angular increments are used to determine the new orientation of the molecular reference frame $\boldsymbol{\mathcal{R}_{mol}}$, and subsequently the orientation of the permanent dipole $\boldsymbol{\rho_d}$ in the laboratory reference frame $\boldsymbol{\mathcal{R}_{lab}}$.

The numerical simulation method can be divided into one idealized and two physically realistic cases:

1. A linear transition dipole in a molecule of spherical rotational symmetry, as

illustrated in Figure 5.10.

2. A linear transition dipole in a molecule of scalene elliptical rotational symmetry, for which the dipole has an arbitrary permanent alignment $\boldsymbol{\rho_0}$ in $\boldsymbol{\mathcal{R}_{mol}}$. This situation matches the one shown in Figure 5.9 (p. 199).

3. A circular or elliptical (2D degenerate or non-degenerate, respectively) transition dipole in a molecule of scalene elliptical rotational symmetry, for which the plane of the dipole is perpendicular to one axis of molecular rotation (the wurtzite $\hat{\boldsymbol{c}}$-axis in CdSe nanocrystals). As illustrated in Figure 5.11, a 2D dipole can be treated as the superposition of two orthogonal 1D dipoles with the appropriate magnitude ratio. Figure 5.11 (p. 203) corresponds to the expected transition dipole orientation for wurtzite CdSe nanocrystals as shown in Figure 5.1 (p. 170).

In all three cases the primary mathematical object sought in each simulation time step i is a 3x3 matrix $\boldsymbol{R_{\Delta}}_i$ corresponding to the rotational diffusion steps that occur during δt_i. $\boldsymbol{R_{\Delta}}_i$ transforms the i^{th} transition dipole vector $\boldsymbol{\rho_d}_i$, to yield the $(i+1)^{\text{th}}$ vector: $\boldsymbol{\rho_{d(i+1)}} = \boldsymbol{R_{\Delta}}_i \cdot \boldsymbol{\rho_d}_i$. The difference in each of the three simulation cases is the nature and ease of constructing $\boldsymbol{R_{\Delta}}_i$. Matrix representation of rotational transformation about canonical and arbitrary axes in three dimensions is discussed in detail in appendix A.1.

Case 1. If the transition dipole $\boldsymbol{\rho_0}$ is 1-dimensional and the molecular rotation reference frame $\boldsymbol{\mathcal{R}_{mol}}$ has spherical symmetry (Figure 5.10) we can, without loss of generality, align the transition dipole with the a-axis: $\boldsymbol{\rho_o} = \hat{\boldsymbol{a}}$. Likewise, because $\boldsymbol{\mathcal{R}_{mol}}$ axes $(\hat{\boldsymbol{a}}, \hat{\boldsymbol{b}}, \hat{\boldsymbol{c}})$ are threefold degenerate, the elementary rotational diffusion steps

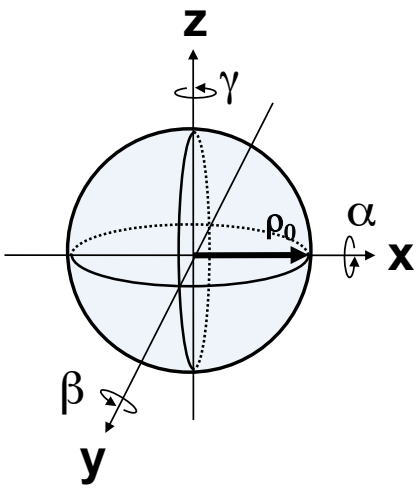

Figure 5.10: One dimensional transition dipole in a molecule with spherical roational symmetry. Without loss of generality the dipole vector may be aligned with an axis of rotation in the molecular reference frame. Rotational transformations may be performed in the laboratory reference frame due to the spherical symmetry of the molecular reference frame.

$(\delta\alpha, \delta\beta, \delta\gamma)$ can be carried using the cardinal axes $(\hat{\boldsymbol{x}}, \hat{\boldsymbol{y}}, \hat{\boldsymbol{z}})$ of instead of $(\hat{\boldsymbol{a}}, \hat{\boldsymbol{b}}, \hat{\boldsymbol{c}})$, greatly simplifying the calculation of $\boldsymbol{R}_{\boldsymbol{\Delta}_i}$. Rotation axis order may be chosen arbitrarily, and each Gaussian-distributed Eulerian angle stepsize has the same variance σ. The numerical routine for simulating **Case 1** consists of equations 5.2–5.6 iterated for the desired number of steps (N) to yield the time series $\left\{\boldsymbol{\rho_0}, \boldsymbol{\rho_1}, \cdots, \boldsymbol{\rho_N}\right\}$.

$$\boldsymbol{\rho_0} = \begin{pmatrix} 1 \\ 0 \\ 0 \end{pmatrix}$$

$$\delta\alpha_i = \sigma \cdot RN_i \tag{5.2}$$

$$\delta\beta_i = \sigma \cdot RN_i \tag{5.3}$$

$$\delta\gamma_i = \sigma \cdot RN_i \tag{5.4}$$

$$\boldsymbol{R_{\Delta i}} = \boldsymbol{R_x}(\delta\alpha_i) \cdot \boldsymbol{R_y}(\delta\beta_i) \cdot \boldsymbol{R_z}(\delta\gamma_i) \tag{5.5}$$

$$\boldsymbol{\rho}_{(i+1)} = \boldsymbol{R_{\Delta i}} \cdot \boldsymbol{\rho}_i \tag{5.6}$$

where RN_i is a Gaussian-distributed random number with mean 0 and variance 1.

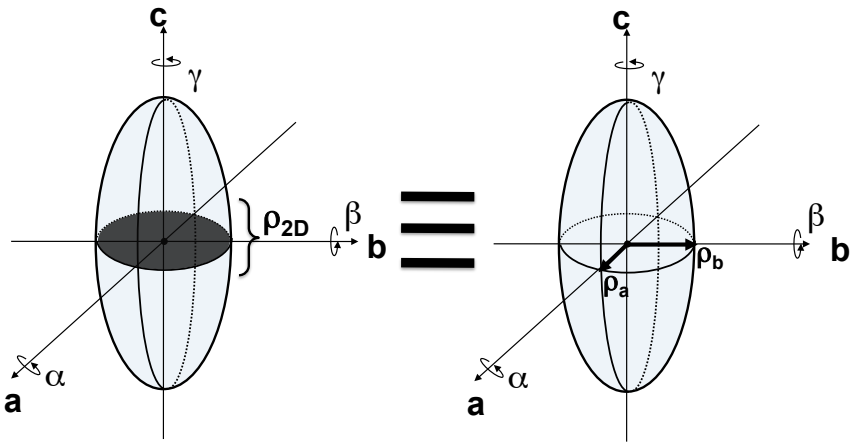

Figure 5.11: Two dimensional transition dipole oriented perpendicular to the major axis of a molecule. This case represents the expected transition dipole geometry and orientation for wurtzite CdSe nanocrystals, as shown in Figure 5.1 (p. 170). Rotational transformations are performed in the same manner as for Case 2 simulations.

Case 2. If the transition dipole $\boldsymbol{\rho_0}$ is 1-dimensional and the molecular rotation reference frame $\boldsymbol{\mathcal{R}_{mol}}$ has scalene ellipsoid symmetry, we must include additional steps corresponding to spatial rotations about the proper axes in $\boldsymbol{\mathcal{R}_{mol}}$, with a different variance of the angular stepsize for each axis: $\sigma_\alpha \neq \sigma_\beta \neq \sigma_\gamma$. Rotational axis order is still chosen arbitrarily, but during each rotational step corresponding to one molecular axis, the other two molecular axes must also undergo rotation about the other two molecular axes. The simulation for **Case 2** consists of N iterations of 5.7–5.20 to yield the dipole orientation time series $\left\{\boldsymbol{\rho_0}, \boldsymbol{\rho_1}, \cdots, \boldsymbol{\rho_N}\right\}$.

$$\boldsymbol{\rho_0} = \left(\frac{1}{\sqrt{\rho_x^2 + \rho_y^2 + \rho_z^2}}\right) \cdot \begin{pmatrix}\rho_x \\ \rho_y \\ \rho_z\end{pmatrix}$$

$$\hat{\boldsymbol{\alpha}}_0 = \begin{pmatrix}1 \\ 0 \\ 0\end{pmatrix}$$

$$\hat{\boldsymbol{\beta}}_0 = \begin{pmatrix}0 \\ 1 \\ 0\end{pmatrix}$$

$$\hat{\boldsymbol{\gamma}}_0 = \begin{pmatrix}0 \\ 0 \\ 1\end{pmatrix}$$

$$\delta\alpha_i = \sigma_\alpha \cdot RN_i \tag{5.7}$$

$$\delta\beta_i = \sigma_\beta \cdot RN_i \tag{5.8}$$

$$\delta\gamma_i = \sigma_\gamma \cdot RN_i \tag{5.9}$$

Each transformation matrix about molecular axis $\hat{\boldsymbol{a}}$, $\boldsymbol{R_{\Delta\alpha,i}}$, and the new dipole orientation $\boldsymbol{\rho_i'}$ are subsequently given by:

$$\boldsymbol{R_{\Delta\alpha,i}}(\hat{\boldsymbol{a}}_{\boldsymbol{i}}, \delta\alpha) = \left[\boldsymbol{R^{-1}_{a\to xz}} \cdot \boldsymbol{R^{-1}_{xz\to z}} \cdot \boldsymbol{R_z}(\delta\alpha) \cdot \boldsymbol{R_{xz\to z}} \cdot \boldsymbol{R_{a\to xz}}\right] \tag{5.10}$$

$$\boldsymbol{\rho'_i} = \boldsymbol{R_{\Delta\alpha,i}} \cdot \boldsymbol{\rho_i} \ . \tag{5.11}$$

The individual matrix transformation steps comprising $\boldsymbol{R_{\Delta\alpha,i}}$ are found as described in equations A.8–A.12. Similarly, the corresponding transformation matrixes for rotation about the molecular $\hat{\boldsymbol{b}}$ and $\hat{\boldsymbol{c}}$-axes, and the associated transformed dipoles $\boldsymbol{\rho''_i}$ and $\boldsymbol{\rho'''_i} = \boldsymbol{\rho_{i+1}}$ are determined from:

$$\hat{\boldsymbol{b}}'_{\boldsymbol{i}} = \boldsymbol{R_{\Delta\alpha,i}} \cdot \hat{\boldsymbol{b}}_{\boldsymbol{i}} \tag{5.12}$$

$$\boldsymbol{R_{\Delta\beta,i}}(\hat{\boldsymbol{b}}'_{\boldsymbol{i}}, \delta\beta) = \left[\boldsymbol{R^{-1}_{b'_i\to xz}} \cdot \boldsymbol{R^{-1}_{xz\to z}} \cdot \boldsymbol{R_z}(\delta\beta) \cdot \boldsymbol{R_{xz\to z}} \cdot \boldsymbol{R_{b'_i\to xz}}\right] \tag{5.13}$$

$$\boldsymbol{\rho''_i} = \boldsymbol{R_{\Delta\beta,i}} \cdot \boldsymbol{\rho'_i} \tag{5.14}$$

$$\hat{\boldsymbol{c}}'_{\boldsymbol{i}} = \boldsymbol{R_{\Delta\beta,i}} \cdot \boldsymbol{R_{\Delta\alpha,i}} \cdot \hat{\boldsymbol{c}}_{\boldsymbol{i}} \tag{5.15}$$

$$\boldsymbol{R_{\Delta\gamma,i}}(\hat{\boldsymbol{c}}'_{\boldsymbol{i}}, \delta\gamma) = \left[\boldsymbol{R^{-1}_{c'_i\to xz}} \cdot \boldsymbol{R^{-1}_{xz\to z}} \cdot \boldsymbol{R_z}(\delta\gamma) \cdot \boldsymbol{R_{xz\to z}} \cdot \boldsymbol{R_{c'_i\to xz}}\right] \tag{5.16}$$

$$\boldsymbol{\rho_{(i+1)}} = \boldsymbol{\rho'''}_{\boldsymbol{i}} = \boldsymbol{R_{\Delta\gamma,i}} \cdot \boldsymbol{\rho''_i} \tag{5.17}$$

$$\hat{\boldsymbol{a}}_{\boldsymbol{(i+1)}} = \boldsymbol{R_{\Delta\gamma,i}} \cdot \boldsymbol{R_{\Delta\beta,i}} \cdot \hat{\boldsymbol{a}}_{\boldsymbol{i}} \tag{5.18}$$

$$\hat{\boldsymbol{b}}_{\boldsymbol{(i+1)}} = \boldsymbol{R_{\Delta\gamma,i}} \cdot \hat{\boldsymbol{b}}'_{\boldsymbol{i}} \tag{5.19}$$

$$\hat{\boldsymbol{c}}_{\boldsymbol{(i+1)}} = \hat{\boldsymbol{c}}'_{\boldsymbol{i}} \, . \tag{5.20}$$

Case 3. A molecule having a two dimensional transition dipole such as a wurtzite CdSe semiconductor quantum dot (Figure 5.1, p. 170) may be modeled as the superposition of two orthogonal one dimensional dipoles, each aligned with a molecular rotational axis. In the special case for which the two orthogonal dipoles have equal

magnitude, the 2D dipole is degenerate (circular). In all other cases the transition dipole is elliptical with eccentricity e, and the minor axis dipole has a magnitude of $\sqrt{1-e^2}$ times that of the major axis dipole. As discussed in detail in Section 5.1.2 (p. 169), the transition dipole of a type II semiconductor nanocrystal quantum dot with a core smaller than ≈8nm in diameter is a 2D ellipse perpendicular to the wurtzite crystal $\hat{\boldsymbol{c}}$-axis. Physically these quantum dots have a prolate ellipsoidal shape, with the $\boldsymbol{c}$-axis corresponding to the longest dimension. This reduces the complexity of numerical simulation for **Case 3** because, without loss of generality, we can align the orthogonal components of the 2D transition dipole with the rotational $\hat{\boldsymbol{a}}$ and $\hat{\boldsymbol{b}}$-axes, and assume that $\sigma_\alpha \approx \sigma_\beta < \sigma_\gamma$.

Numerical simulation for **Case 3** then consists of N iterations of the same rotational transformations steps performed on the molecular axes as in case 2 (equations 5.7–5.20, omitting 5.11, 5.14 and 5.17). However, at each time point the two-dipole orientation is determined from $\boldsymbol{\rho_{a,i}} = \hat{\boldsymbol{a}}_{\boldsymbol{i}}$ and $\boldsymbol{\rho_{v,i}} = \sqrt{1-e^2} \cdot \hat{\boldsymbol{b}}_{\boldsymbol{i}}$ to generate the time series $\left\{(\boldsymbol{\rho_{a,0}}, \boldsymbol{\rho_{b,0}}), (\boldsymbol{\rho_{a,1}}, \boldsymbol{\rho_{b,1}}), \cdots, (\boldsymbol{\rho_{a,N}}, \boldsymbol{\rho_{b,N}})\right\}$.

In all three simulation cases, the dipole orientation in the laboratory reference frame generates a corresponding signal for the two perpendicular polarization channels in the microscope's emission pathway, $I_x(t_i)$ and $I_y(t_i)$. The dipole orientation time series $\left\{\boldsymbol{\rho_0}, \boldsymbol{\rho_1}, \cdots, \boldsymbol{\rho_N}\right\}$ is processed using equations 3.68–3.72 (derived in Section 3.2.4, p. 94) to calculate the expected signals for the horizontal ($\hat{\boldsymbol{x}}$) and vertical ($\hat{\boldsymbol{y}}$) polarization channels. These signals are then used to generate simulated auto- and cross-correlation traces for comparison with experimental data.

5.3.2 Monte Carlo Simulation Results

The dipole trajectories from typical Case 2 simulations are shown in Figure 5.12 as the trace of the 1D transition dipole vector endpoint in three dimensional space for three different values of σ_γ relative to $\sigma_\alpha = \sigma_\beta$. When the 1D transition dipole is aligned with the $\hat{\boldsymbol{a}}-$ or $\hat{\boldsymbol{b}}-$axis of the molecular reference frame all three dimensions are transited more rapidly by increasing the stepsize variance of just one molecular rotational axis (σ_γ). This effect arises because of 3D convolution of molecular axes by rotational diffusion in the laboratory reference frame. If the dipole is aligned with the same molecular axis that is subject to increasing stepsize variance (in this case the $\hat{\boldsymbol{c}}-$axis), the effect is absent because rotation of a 1D dipole about its own axis is unobservable.

The influence of objective lens numerical aperture on the total collected signal and its relative partition into the orthogonally polarized detection channels are shown in Figure 5.13. In addition to the total signal increasing for higher NA values, the relative partitioning into the I_x and I_y channels also varies.

Typical dipole trajectories from a **case 3** simulation are shown in Figure 5.14 for three different eccentricity values of a 2D transition dipole. The elliptical transition dipole major axis (blue) follows trajectories equivalent to those of a 1D transition dipole aligned with the $\hat{\boldsymbol{a}}-$axis of a molecule with prolate ellipsoidal symmetry, such as that plotted in the top row, 2nd column of Figure 5.12. Simultaneously, however, the orthogonal minor axis of the elliptical transition dipole traces a coupled trajectory (red) on the surface of smaller 3-sphere whose diameter is $\sqrt{1-e^2}$.

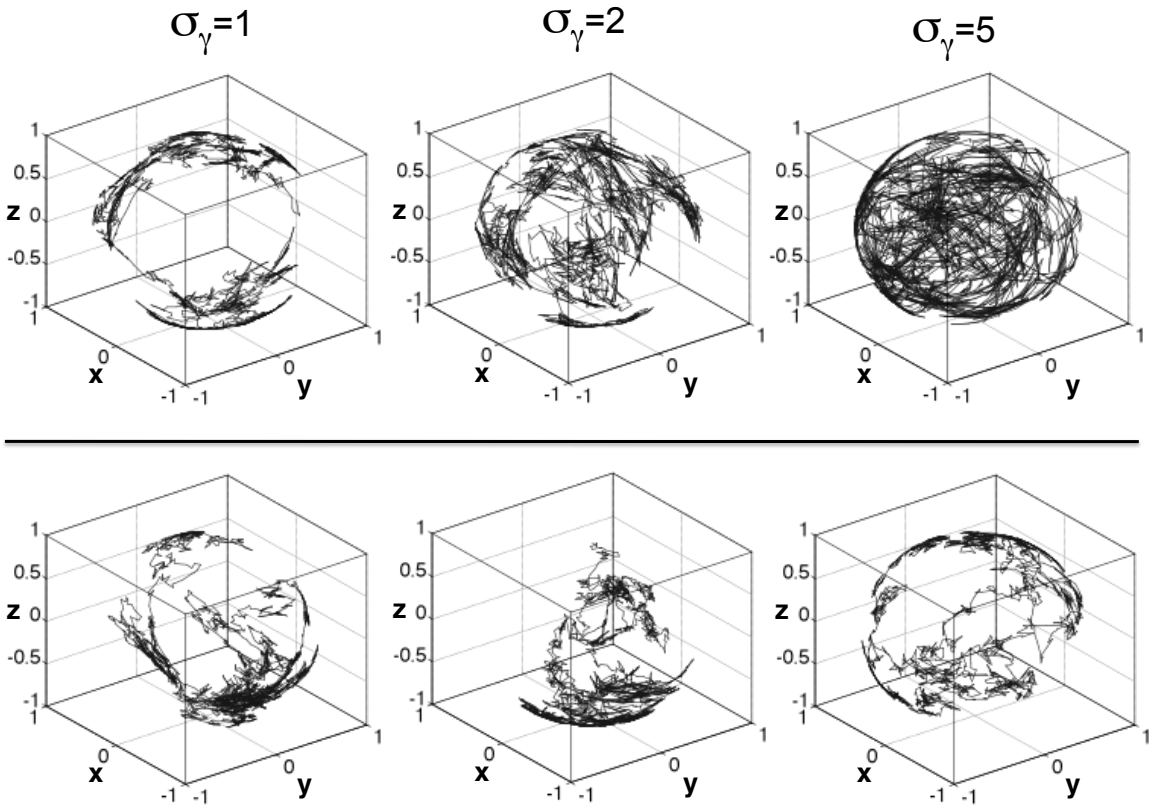

Figure 5.12: Monte Carlo simulation results for a 1D transition dipole aligned with the $\hat{\boldsymbol{a}}-$axis (top row) or the $\hat{\boldsymbol{c}}-$axis (bottom row) of a molecule with varying σ_γ values. Each plot shows the position of the normalized 1D dipole vector at sequential timesteps. Given infinite time the vector will visit every surface point on a unit 3-ball. **Simulation Conditions:** $\sigma_\gamma = \{1, 2, 5\}$; $\sigma_\alpha = \sigma_\beta = 1$; $\boldsymbol{\rho_0} = \hat{\boldsymbol{a}}$; stepsize=.1; $N = 10^3$

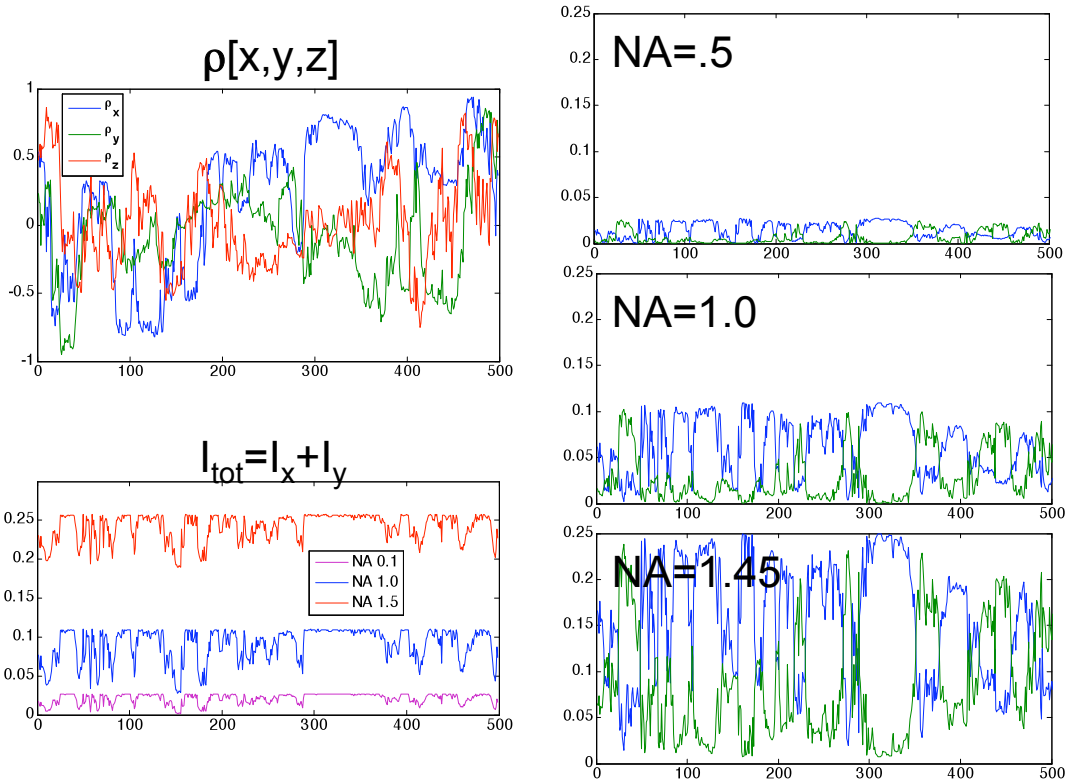

Figure 5.13: Results from a case 2 simulation. The signals I_x, I_y, and I_{tot} were calculated for three NA values from the same dipole trajectory. The (x, y, z) orientation trajectory of the dipole $\boldsymbol{\rho_d}$ is shown in the top left plot (ρ_x blue, ρ_y green, ρ_z red). The bottom left plot shows the total collected signal for $NA = \{.5, 1.0, 1.45\}$. The three plots in the right column show the I_x (blue) and I_y (green) signal for each NA value, plotted on the same scale. **Simulation Conditions:** $\sigma_\alpha = \sigma_\beta = 1$; $\sigma_\gamma = 1.5$; $\boldsymbol{\rho_a} = \left(\frac{1}{\sqrt{3}}\right)\left(\hat{\boldsymbol{a}} + \hat{\boldsymbol{b}} + \hat{\boldsymbol{c}}\right)$; stepsize=.1; $N = 500$

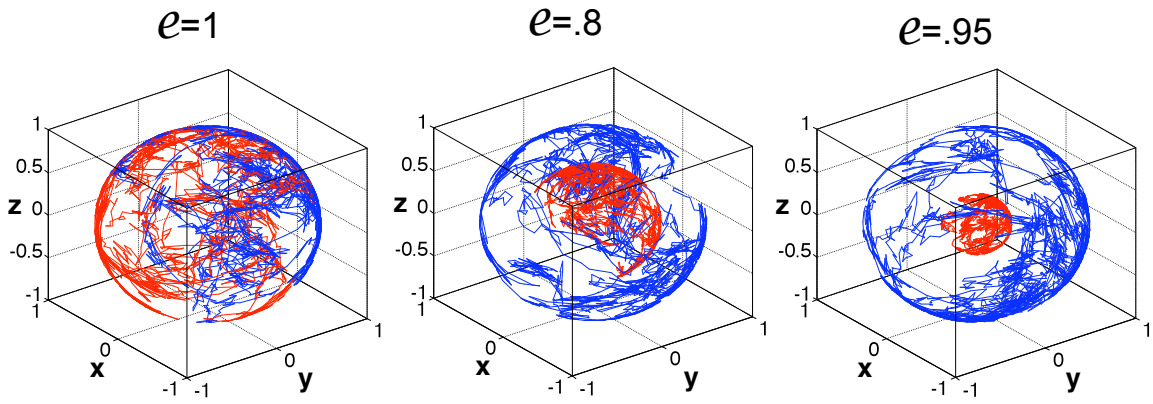

Figure 5.14: Monte Carlo simulation results for an elliptical transition dipole aligned with the major dipole axis aligned with the molecular $\hat{\boldsymbol{a}}-$axis and the minor dipole axis aligned with the molecular the $\hat{\boldsymbol{b}}-$axis. Each plot shows the position of the normalized major axis dipole vector in blue, and that of the minor axis dipole vector in red. **Simulation Conditions:** $\sigma_\alpha = \sigma_\beta = 1$; $\sigma_\gamma = 1.5$; $\boldsymbol{\rho_a} = \hat{\boldsymbol{a}}$; $\boldsymbol{\rho_b} = \sqrt{1-e^2}\hat{\boldsymbol{b}}$; stepsize=.1; $N = 10^3$.

The plots of the case 1 simulation shown in Figure 5.15 are of the ratio of normalized cross-correlation to normalized autocorrelation at each time delay $\left\{\tau = M : \left(M \in \mathbb{N}, M \leq \frac{N}{2}\right)\right\}$ in units of single time steps. No significant difference is observed upon changing the transition dipole alignment relative to the molecular axes, an invariance that is in agreement with the molecular rotational symmetry. Additionally, no significant changes are observed upon altering the molecular axis rotation order or the initial molecular reference frame alignment relative to the laboratory frame, indicating that no spatially asymmetric numerical artifacts are present the simulation. Results for simulations of case 1 at varying numerical aperture values are depicted in Figure 5.16. At higher numerical aperture the short-time plateau value rises as a result of greater collection of the dipole $\hat{\boldsymbol{z}}$ component in *both* polarization channels, in accordance with equations 3.68–3.72 (p. 115). One full rotational cycle

requires an average of $\left(\frac{2\pi}{\sigma}\right)^2$ steps, and the correlation ratio midpoint value occurs at $\tau = \tau_r \approx \frac{\pi}{6\sigma^2}$, in agreement with that expected from the Stokes-Einstein-Debye relation (equation 4.22, p. 157).

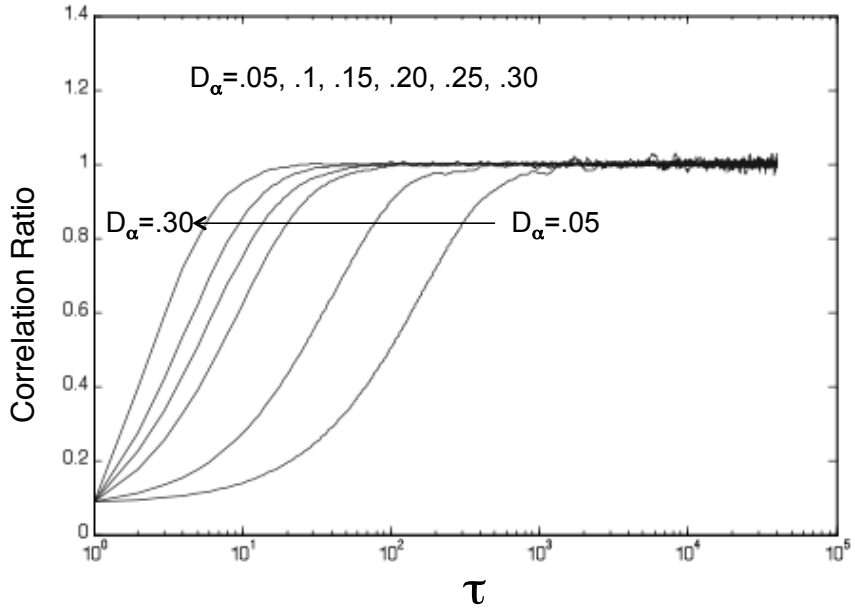

Figure 5.15: Monte Carlo polarized FCS simulation results for a 1D transition dipole in a molecule of spherical rotational symmetry at varying rotational correlation times. **Simulation Conditions:** $\sigma_\alpha = \sigma_\beta = \sigma_\gamma = \{.5, 1.0, 1.5, 2.0, 2.5, 3.0\}$; $\boldsymbol{\rho_0} = \hat{\boldsymbol{a}}$; $NA = 1.45$; $N = 10^6$; stepsize= 0.1

Normalized auto- and cross-correlation traces from a a typical simulation of case 3 are shown in Figure 5.17 for two eccentricity values of the elliptical transition dipole. In both cases the autocorrelation trace from each polarization channel rises to a plateau for $\tau < \tau_R$, with the cross-correlation trace displaying the negatively mirrored effect. The height of the plateau rises with increasing eccentricity. This phenomenon is also illustrated in Figure 5.18, which presents correlation ratios for a

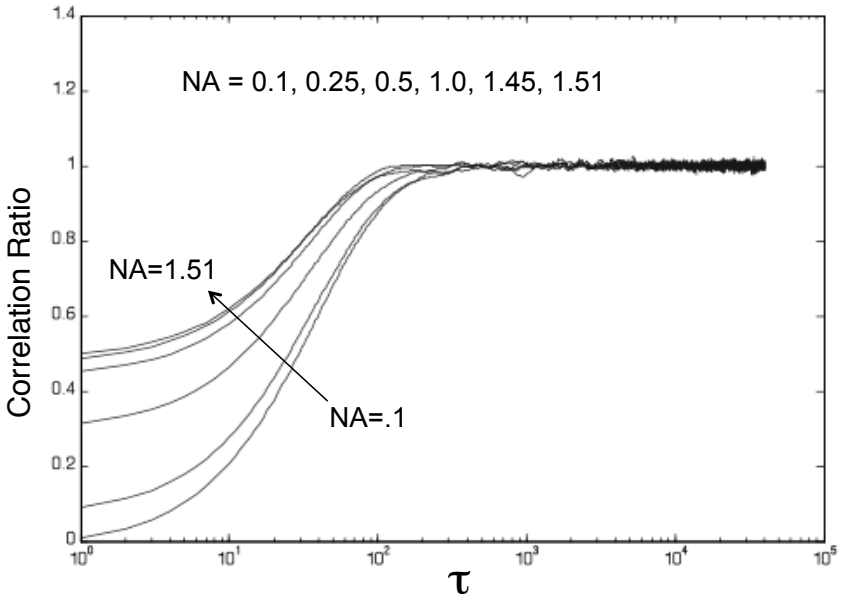

Figure 5.16: Monte Carlo polarized FCS simulation results for a 1D transition dipole in a rotational symmetric molecule with varying NA values. **Simulation Conditions:** $NA = \{0, .25, .5, 1.0, 1.45, 1.51\}$

similar 2D dipole simulation. The most significant phenomenon to note is the strong dependence of correlation ratio minimum at small time delays ($\tau \rightarrow 1$) upon the 2D dipole eccentricity e. In particular there is always a significant non-unity minimum, even in the case of a degenerate 2D dipole ($e = 1$). This latter phenomenon arises because the projected 2D dipole ellipse onto the sample plane changes its *apparent* eccentricity upon rotation about the molecular $\hat{\boldsymbol{a}}$- or $\hat{\boldsymbol{b}}$-axes (Figure 5.19).

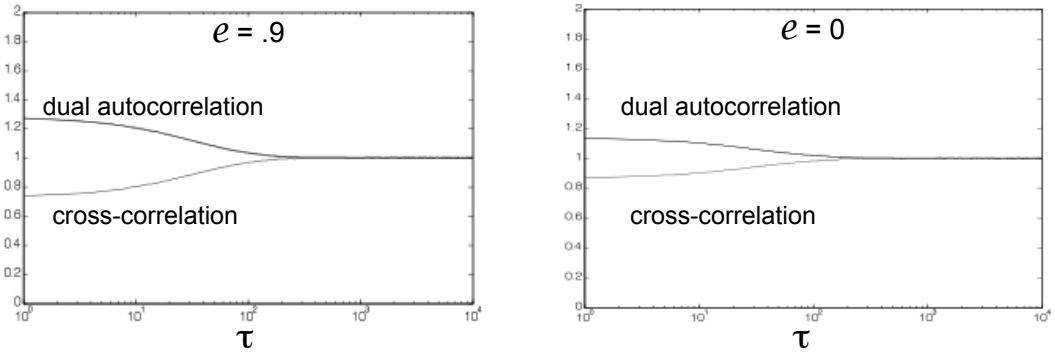

Figure 5.17: Normalized auto- and cross-correlation traces for a 2D dipole of eccentricity .9 (left), and 0 (right). **Simulation Conditions:** $\boldsymbol{\rho_{a,0}} = \hat{\boldsymbol{a}}$, $\boldsymbol{\rho_{b,0}} = \sqrt{1-e^2} \cdot \hat{\boldsymbol{b}}$; $\sigma_\alpha = \sigma_\beta = 1$; $\sigma_\gamma = 1.5$; $NA = 1.45$; $N = 10^6$; stepsize= .1.

5.3.3 Rotational Correlation Fits of Simulated PFCS Data

Simulated data correlation traces were fit by the same model as experimental data, using equation 4.30 (p. 161) to generate values for parameter sets $\{F, \tau_r, \beta\}$. Figure 5.20 presents the variation of fit parameters with isotropic stepsize parameter variance σ. In the Euler angle stochastic random walk forming the basis of the rotational diffusion simulations, each angular step has a Gaussian distribution with mean value 0. However, the average step *length* made by the rotating dipole vector ρ_d endpoint during each time window δt varies with the square of the stepsize variance,

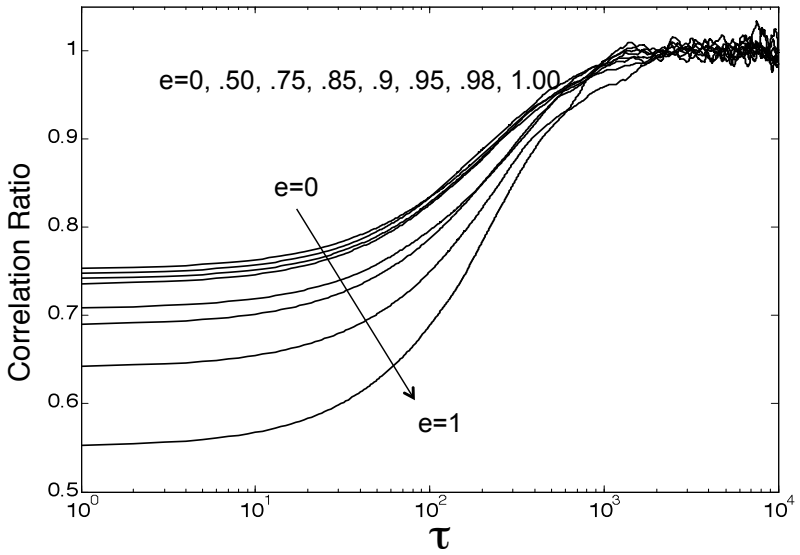

Figure 5.18: Monte Carlo polarized FCS simulation results for a 2D elliptical transition dipole with with eccentricity varying between 0 and 1. **Simulation Conditions:** $\boldsymbol{\rho_{a,0}} = \hat{\boldsymbol{a}}$; $\boldsymbol{\rho_{b,0}} = \sqrt{1-e^2} \cdot \hat{\boldsymbol{b}}$; $\sigma_\alpha = \sigma_\beta = 1$; $\sigma_\gamma = 1.5$; $e = \{0, .50, .75, .85, .90, .95, .98, 1.00\}$; $N = 1e5$

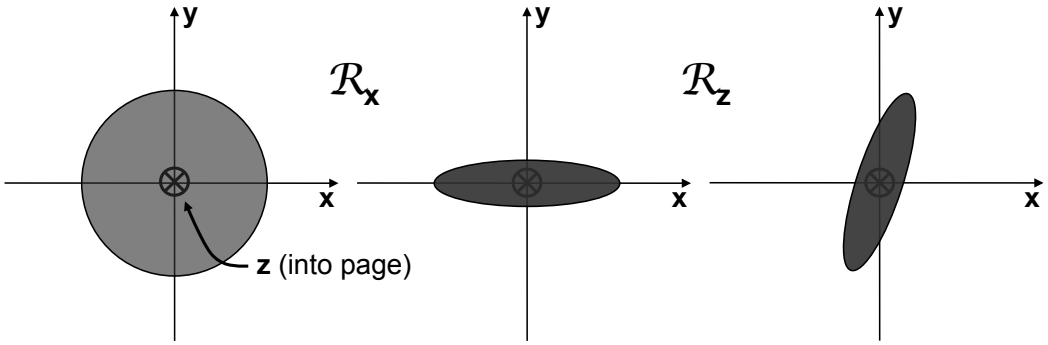

Figure 5.19: Induction of apparent non-degeneracy of a circular 2D dipole arising from rotation about a cardinal axis in the plane of the dipole

since Euler angles α, β and γ step in orthogonal directions. The result is that the rotational correlation fit parameter τ_r scales with σ^{-2}. The values of F and β from the fitting model are statistically invariant across at least the rotational correlation time range of $10 \leq \tau_r \geq 100$. $F = .255 \pm .008$, $\beta = .979 \pm .013$ for a 1D transition dipole undergoing isotropic rotational diffusion, observed by an optical system with NA =1.45, in excellent agreement with the experimentally measured parameters for Texas Red-DHPE, Rhodamine DHPE and rDsRed.

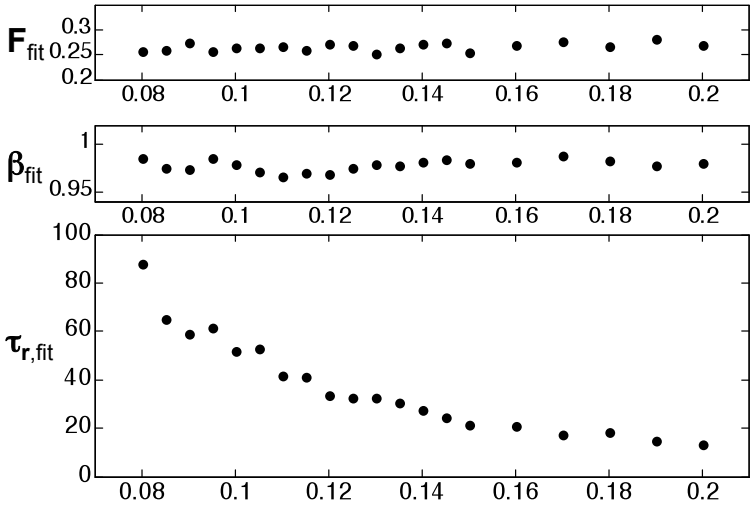

Figure 5.20: Variation of fit parameters F (top plot), β (middle plot) and τ_r (bottom plot) from equation 4.30 versus isotropic Euler angle stepsize variance σ. The measured rotational correlation time τ_r scales with the inverse square of σ. F and β are statistically invariant with respect to σ. Parameter values were obtained by fits to equation 4.30, the presented data representing average values from 12 simulations. $\sigma_\alpha = \sigma_\beta = \sigma_\gamma = 1$; NA=1.45; $N = 5e4$

Figure 5.21 presents the variation of fit parameter F with the eccentricity e of the rotating 2D fluorescence transition dipole of a molecule with slight prolate top rotationally symmetry, representative of most organic quantum dot samples examined

in the experimental section (Section 5.2.4, p. 180). For values of e ranging from zero (2D degenerate circular dipole, equivalent to orthogonal 1D dipoles of equal magnitude $\left(\|\boldsymbol{\rho_b}\| = \|\boldsymbol{\rho_a}\|\right)$ to $e \approx .85$ $\left(\|\boldsymbol{\rho_b}\| \approx .5\,\|\boldsymbol{\rho_a}\|\right)$ the value of F remains consistent at $F \approx .115$. Between $e \approx .85$ $\left(\|\boldsymbol{\rho_b}\| \leq .5\,\|\boldsymbol{\rho_a}\|\right)$ and $e = 1.00$ $\left(\|\boldsymbol{\rho_b}\| = 0\right)$ the values of F rise sharply but continuously to $F \approx .25$ the value measured for 1D fluorescence dipoles. The other two fit parameters are statistically invariant with respect to e: $\beta = .95 \pm .01$; $\tau_r = 52.3 \pm 2.1$, in agreement with expectation that only F will vary with dipole eccentricity.

Figure 5.22 presents the variation of fit parameters for anisotropic rotation of a 1D dipole that is not aligned with one molecular rotational axis. The fit parameters are plotted with respect to an 'anisotropy parameter' a, representing the degree of relative diffusion rate difference for rotation about each molecular axis. The 1D transition dipole is oriented in the molecular reference frame with equal components from each rotational axis: $\boldsymbol{\rho_0} = \frac{1}{\sqrt{3}}\left(\hat{\boldsymbol{a}} + \hat{\boldsymbol{b}} + \hat{\boldsymbol{c}}\right)$. The important conclusion is that all three parameters, $\left\{F, \beta, \tau_r\right\}$ vary when only the relative rotational rates of the axes change. From values that equal those of a 1D dipole undergoing isotropic rotation (Figure 5.20) when $a = 1$, 'degee-of-polarization' parameter F drops from $\approx .25$ to $\approx .18$ when one axis rotates twice as fast and one rotates half as fast. This change is equivalent to the 1D appearing to be a slightly eccentric 2D dipole ($e \approx .97$). Additionally the KWW 'stretching' parameter β drops from its isotropic value of $\approx .95$ to $\leq .93$, confirming its putative role as an indicator of system heterogeneity. The measured rotational correlation time τ_r rises to a value representing rotation about the fastest molecular axis.

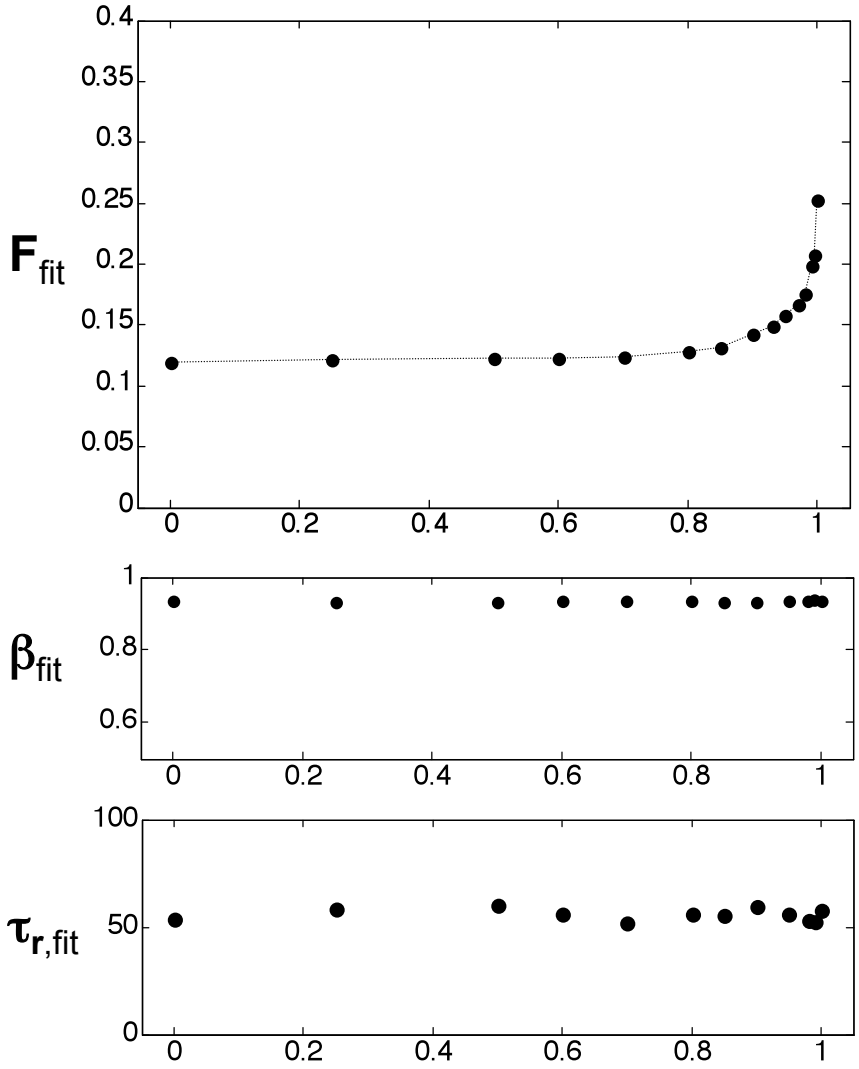

Figure 5.21: Variation of fit parameters F (top plot), β (middle plot) and τ_r (bottom plot) from equation versus 2D transition dipole eccentricity e, in a molecule with prolate top rotational symmetry. Parameter values were obtained by fits to equation 4.30, the presented data representing average values from 32 simulations. **Simulation Conditions:** $\boldsymbol{\rho_{a,0}} = \hat{\boldsymbol{a}}$, $\boldsymbol{\rho_{b,0}} = \sqrt{1-e^2} \cdot \hat{\boldsymbol{b}}$; $\sigma_\alpha = \sigma_\beta = 1$; $\sigma_\gamma = 1.5$; $0 \leq e \leq 1$; NA=1.45; $N = 1e5$

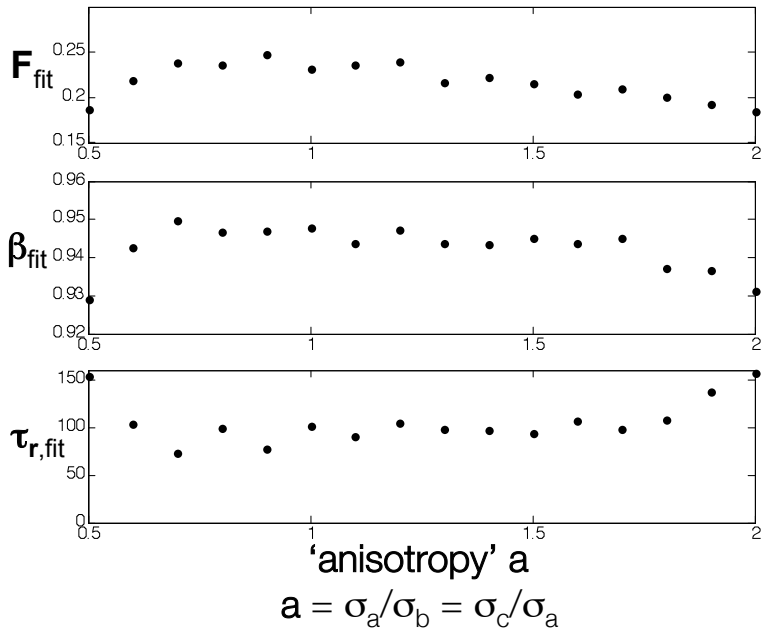

Figure 5.22: Variation of all fit parameters $\{F, \beta, \tau_r\}$ versus anisotropy parameter $\boldsymbol{a}$ for a 1D transition dipole aligned with components of all three axes. Parameter values were obtained by fits to equation 4.30, the presented data representing average values from 12 simulations. **Simulation Conditions:** $\boldsymbol{\rho_0} = \frac{1}{\sqrt{3}}(\hat{\boldsymbol{a}} + \hat{\boldsymbol{b}} + \hat{\boldsymbol{c}})$; $\sigma_\alpha = 1$; $\sigma_\beta = \frac{1}{a}$; $\sigma_\gamma = a$; $.5 \leq a \leq 2.0$; NA =1.45; $N = 5e4$

5.3.4 Conclusions

The Monte Carlo PFCS simulations presented here are in agreement with observations and experimentally collected data, and support the following conclusions.

1. Rotational diffusion of single 1D and 2D transition dipoles manifests itself in FCS data collected from two orthogonal polarization detection channels as an increase for τ values $\lesssim \tau_r$ in the autocorrelation trace, and as an equal decrease at the same timescale in the cross-correlation trace.

2. The rotational auto- and cross- correlation functions $\mathcal{C}^{(a)}(\tau)$ and $\mathcal{C}^{(x)}(\tau)$ are empirically well fit by a three-parameter Kohlrausch-Williams-Watts (KWW) stretched exponential: $1 \pm Fe^{(\tau/\tau_r)^\beta}$ (Section 4.3.4, p. 159).

3. The value of the preexponential parameter F, representing the magnitude of autocorrelation increase and cross-correlation decrease, is a function of both the nature of the rotating fluorescence transition dipole (1D linear and 2D of varying eccentricity e), and the NA of the primary objective lens. Linear transition dipoles ($e \approx 1$) result in higher values of F than elliptical dipoles $0 \leq e < 1$, and additionally higher NA optics result in lower values of F.

4. A clear rotational component is present in both the auto- and cross-correlation traces even if the fluorescence transition dipole is 2D degenerate (e=0), with preexponential parameter magnitude F ($F \approx 0.11$ for NA1.45 optics). This value for F remains consistent as the eccentricity rises to $e \approx .85$, and then increases sharply to $F \approx 0.25$ for $e = 1$ maching the F value measured for 1D dipoles. These values are in excellent agreement with the parameters measured from PFCS experiments.

5. For molecules with isotropic rotational symmetry, the characteristic rotational timescale τ_r scales with the square if the Euler angle stepsize variance simulation parameter, in agreement with expectation from random-walk models.

6. For molecules of isotropic rotational symmetry the KWW fit consistently yields a 'stretching' parameter value $\beta \sim 0.95-.98$, in excellent agreement with experimentally measured values. For molecules that exhibit anisotropic rotational diffusion relative to the fluorescence transition dipole axis, the profile of the auto- and cross-correlation traces represents the convolution of multiple rotational correlation times, and yields smaller values of β: $.90 \lesssim \beta \leq 0.95$. This is in agreement with the role of the KWW β parameter in representing progressively inhomogeneous systems at lower values.

Chapter

Appendices

A.1 Rotational Transformations in Three Dimensions

The most efficient means of describing the stochastic rotational diffusion of $\boldsymbol{\rho_d}$ is via sequential transformation matrixes $\{\boldsymbol{R_i}\}$ representing individual steps $(\delta\alpha, \delta\beta, \delta\gamma)$ about each axis (α, β, γ) in figure 5.9. In the laboratory reference frame $\boldsymbol{\mathcal{R}_{lab}}$ (or any right-handed Cartesian coordinate system), rotation about each axis by its corresponding Euler angle is described by a 3x3 matrix mapping a 3-vector $(x\hat{\boldsymbol{x}} + y\hat{\boldsymbol{y}} + z\hat{\boldsymbol{z}})$

and a scalar angular value to another 3-vector.

$$\boldsymbol{R_x} : \left\{ \begin{pmatrix} x \\ y \\ z \end{pmatrix}, \alpha \right\} \mapsto \begin{bmatrix} 1 & 0 & 0 \\ 0 & \cos\alpha & -\sin\alpha \\ 0 & \sin\alpha & \cos\alpha \end{bmatrix} \cdot \begin{pmatrix} x \\ y \\ z \end{pmatrix} \tag{A.1}$$

$$\boldsymbol{R_y} : \left\{ \begin{pmatrix} x \\ y \\ z \end{pmatrix}, \beta \right\} \mapsto \begin{bmatrix} \cos\beta & 0 & -\sin\beta \\ 0 & 1 & 0 \\ \sin\beta & 0 & \cos\beta \end{bmatrix} \cdot \begin{pmatrix} x \\ y \\ z \end{pmatrix} \tag{A.2}$$

$$\boldsymbol{R_z} : \left\{ \begin{pmatrix} x \\ y \\ z \end{pmatrix}, \gamma \right\} \mapsto \begin{bmatrix} \cos\gamma & -\sin\gamma & 0 \\ \sin\gamma & \cos\gamma & 0 \\ 0 & 0 & 1 \end{bmatrix} \cdot \begin{pmatrix} x \\ y \\ z \end{pmatrix} \tag{A.3}$$

The shorthand notations used for each transformation matrix will be $\{\boldsymbol{R_x}(\alpha), \boldsymbol{R_y}(\beta), \boldsymbol{R_z}(\gamma)\}$, and the corresponding inverse transformations $\{\boldsymbol{R_x^{-1}}(\alpha), \boldsymbol{R_y^{-1}}(\beta), \boldsymbol{R_z^{-1}}(\gamma)\}$ for each individual rotation are simply rotation by the negative of the original angle: $\{\boldsymbol{R_x}(-\alpha), \boldsymbol{R_y}(-\beta), \boldsymbol{R_z}(-\gamma)\}$.

Sequential rotation of a given 3-space vector is accomplished by left-ordered matrix multiplication of each corresponding single rotation:

$$\boldsymbol{R}_{\{\boldsymbol{x},\boldsymbol{y},\boldsymbol{z}\}}(\alpha,\beta,\gamma) \tag{A.4}$$

$$= \boldsymbol{R}_{\boldsymbol{z}}(\gamma)\cdot\boldsymbol{R}_{\boldsymbol{y}}(\beta)\cdot\boldsymbol{R}_{\boldsymbol{x}}(\alpha) \tag{A.5}$$

$$= \begin{bmatrix}\cos\gamma & -\sin\gamma & 0\\ \sin\gamma & \cos\gamma & 0\\ 0 & 0 & 1\end{bmatrix}\cdot\begin{bmatrix}\cos\beta & 0 & -\sin\beta\\ 0 & 1 & 0\\ \sin\beta & 0 & \cos\beta\end{bmatrix}\cdot\begin{bmatrix}1 & 0 & 0\\ 0 & \cos\alpha & -\sin\alpha\\ 0 & \sin\alpha & \cos\alpha\end{bmatrix} \tag{A.6}$$

$$= \begin{bmatrix}\cos\beta\cos\gamma & \cos\gamma\sin\alpha\sin\beta-\cos\alpha\sin\gamma & \cos\alpha\cos\gamma\sin\beta+\sin\alpha\sin\gamma\\ \cos\beta\sin\gamma & \cos\alpha\cos\gamma+\sin\alpha\sin\beta\sin\gamma & -\cos\gamma\sin\alpha+\cos\alpha\sin\beta\sin\gamma\\ -\sin\beta & \cos\beta\sin\alpha & \cos\alpha\cos\beta\end{bmatrix}. \tag{A.7}$$

The above transformation reads as "rotation about the x-axis by α followed by rotation about the y-axis by β followed by rotation about the z-axis by γ." Except

in special cases, rotation order *is not commutable*. For example:

$$
\begin{aligned}
&\boldsymbol{R}_{\{z,y,x\}}(\gamma,\beta,\alpha) \\
&\quad = \boldsymbol{R}_{x}(\alpha)\cdot\boldsymbol{R}_{y}(\beta)\cdot\boldsymbol{R}_{z}(\gamma) \\
&\quad = \begin{bmatrix} 1 & 0 & 0 \\ 0 & \cos\alpha & -\sin\alpha \\ 0 & \sin\alpha & \cos\alpha \end{bmatrix} \cdot \begin{bmatrix} \cos\beta & 0 & -\sin\beta \\ 0 & 1 & 0 \\ \sin\beta & 0 & \cos\beta \end{bmatrix} \cdot \begin{bmatrix} \cos\gamma & -\sin\gamma & 0 \\ \sin\gamma & \cos\gamma & 0 \\ 0 & 0 & 1 \end{bmatrix} \\
&\quad = \begin{bmatrix} \cos\alpha\cos\beta & -\cos\gamma\sin\alpha+\cos\alpha\sin\beta\sin\gamma & \cos\alpha\cos\gamma\sin\beta+\sin\alpha\sin\gamma \\ \cos\beta\sin\alpha & \cos\alpha\cos\gamma+\sin\alpha\sin\beta\sin\gamma & \cos\gamma\sin\alpha\sin\beta-\cos\alpha\sin\gamma \\ -\sin\beta & \cos\beta\sin\gamma & \cos\beta\cos\gamma \end{bmatrix} \\
&\quad \neq \boldsymbol{R}_{\{x,y,z\}}(\alpha,\beta,\gamma)\,.
\end{aligned}
$$

Equations A.1–A.3 are useful for rotating a vector about the cardinal axes of a coordinate system, but in order to describe the rotational diffusion of $\boldsymbol{\rho_d}$ in $\boldsymbol{\mathcal{R}_{lab}}$ (Figure 5.9b) we must be able to rotate $\boldsymbol{\rho_d}$ about each axis $\left(\hat{\boldsymbol{a}},\hat{\boldsymbol{b}},\hat{\boldsymbol{c}}\right)$ of $\boldsymbol{\mathcal{R}_{mol}}$ *as they are oriented in* $\boldsymbol{\mathcal{R}_{lab}}$. That is, we need to perform each rotational diffusion step $(\delta\alpha,\delta\beta,\delta\gamma)$ about an arbitrarily specified axis in $\boldsymbol{\mathcal{R}_{lab}}$.

Given any 3-space vector $\vec{\boldsymbol{v}} = (\upsilon_x\hat{\boldsymbol{x}} + \upsilon_y\hat{\boldsymbol{y}} + \upsilon_z\hat{\boldsymbol{z}})$, the general method for rotation of an object about the axis parallel to $\vec{\boldsymbol{v}}$ by an angle δ in the laboratory reference frame $\boldsymbol{\mathcal{R}_{lab}}$ can be accomplished by the following steps:

1. Rotate $\boldsymbol{\mathcal{R}_{lab}}$ about its z-axis until $\vec{\boldsymbol{v}}$ lies in the xz-plane.

2. Rotate $\boldsymbol{\mathcal{R}_{lab}}$ about its y-axis until $\vec{\boldsymbol{v}} \parallel \hat{\boldsymbol{z}}$.

3. Rotate the object about the z-axis by δ.

4. Rotate $\boldsymbol{\mathcal{R}_{lab}}$ *back* about its y-axis until $\vec{\boldsymbol{v}}$ lies in the xz-plane.

5. Rotate $\boldsymbol{\mathcal{R}_{lab}}$ *back* about its z-axis until $\vec{\boldsymbol{v}}$ is in its original orientation.

Step 1 is accomplished by left-multiplying $\vec{\boldsymbol{v}}$ by the transformation matrix $\boldsymbol{R_{v\to xz}} = \boldsymbol{R_z}(-\gamma_{v\to xz})$, where $\gamma_{v\to xz} = \tan^{-1}\left(\frac{v_x}{v_y}\right)$. However, since we already know the vector component values v_x and v_y, it is clear that $\sin(\gamma_{v\to xy}) = \frac{v_y}{\sqrt{v_x^2+v_y^2}}$ and $\cos(\gamma_{v\to xy}) = \frac{v_x}{\sqrt{v_x^2+v_y^2}}$. Therefore $\boldsymbol{R_{v\to xz}}$ is given by:

$$\boldsymbol{R_{v\to xz}} = \begin{bmatrix} \frac{v_y}{\sqrt{v_x^2+v_y^2}} & \frac{v_y}{\sqrt{v_x^2+v_y^2}} & 0 \\ -\frac{v_y}{\sqrt{v_x^2+v_y^2}} & \frac{v_y}{\sqrt{v_x^2+v_y^2}} & 0 \\ 0 & 0 & 1 \end{bmatrix}. \tag{A.8}$$

Step 2 is carried out using the transformation matrix $\boldsymbol{R_{xz\to z}} = \boldsymbol{R_y}(-\beta_{v\to xy})$ where $\beta_{v\to xy} = \tan^{-1}\left(\frac{\sqrt{v_x^2+v_y^2}}{v_z}\right)$. $\boldsymbol{R_{v\to xz}}$ is therefore:

$$\boldsymbol{R_{v\to xz}} = \begin{bmatrix} \frac{v_z}{\sqrt{v_x^2+v_y^2}} & 0 & -\sqrt{\frac{v_x^2+v_y^2}{v_x^2+v_y^2+v_z^2}} \\ 0 & 1 & 0 \\ \sqrt{\frac{v_x^2+v_y^2}{v_x^2+v_y^2+v_z^2}} & 0 & \frac{v_z}{\sqrt{v_x^2+v_y^2}} \end{bmatrix}. \tag{A.9}$$

The transformation matrix for **step 3** is determined my simply plugging the desired primary rotation angle δ into equation A.3:

$$\boldsymbol{R_z(\delta)} = \begin{bmatrix} \cos\gamma & -\sin\gamma & 0 \\ \sin\gamma & \cos\gamma & 0 \\ 0 & 0 & 1 \end{bmatrix} . \tag{A.10}$$

The transformation matrixes corresponding to **step 4** and **step 5** are the inverses $\boldsymbol{R^{-1}_{xz\to z}}$ and $\boldsymbol{R^{-1}_{v\to xz}}$ of step 2 and step 1, respectively. The inverses are easily found because both $\boldsymbol{R_{v\to xz}}$ and $\boldsymbol{R_{xz\to z}}$ are orthogonal matrixes.

$$\boldsymbol{R^{-1}_{xz\to z}} = \boldsymbol{R^{\dagger}_{xz\to z}} \tag{A.11}$$

$$\boldsymbol{R^{-1}_{v\to xz}} = \boldsymbol{R^{\dagger}_{v\to xz}} . \tag{A.12}$$

The ordered product of all 5 matrixes from equations A.8–A.12 yields the transformation matrix $\boldsymbol{R_{tot}}(\hat{\boldsymbol{v}}, \delta)$ corresponding to rotation about the axis parallel to vector $\vec{\boldsymbol{v}}$ by angle δ:

$$\boldsymbol{R}_{tot}(\hat{\boldsymbol{v}}, \delta) = \boldsymbol{R^{\dagger}_{v\to xz}} \cdot \boldsymbol{R^{\dagger}_{xz\to z}} \cdot \boldsymbol{R_z}(\delta) \cdot \boldsymbol{R_{v\to xz}} \cdot \boldsymbol{R_{v\to xz}} . \tag{A.13}$$

Lastly, the product vector $\boldsymbol{\rho'}$ arising from rotation of initial vector $\boldsymbol{\rho'}$ by angle δ about axis $\hat{\boldsymbol{v}}$ in the laboratory reference frame $\boldsymbol{\mathcal{R}_{lab}}$ is:

$$\boldsymbol{\rho'} = \boldsymbol{R}_{tot}(\hat{\boldsymbol{v}}, \delta) \cdot \boldsymbol{\rho} . \tag{A.14}$$

A.2 Matlab Code Transcripts

A.2.1 Matlab Code for Computing the 3-Dimensional Point Spread Function

Code transcript from *3dpsf.m*, which calls 3 additional functions, *izerointegrand, ioneintegrand* and *itwointegrand*.

```
function grid=3dpsf(scale,numpoints,phimax)
for j=1:numpoints
for k=1:numpoints
grid(j,k,1)=scale*(floor(.5*numpoints)-j);
grid(j,k,2)=scale*(floor(.5*numpoints)-k);
grid(j,k,3)=quad(@(a)izerointegrand(grid(j,k,1),grid(j,k,2),a,s),0,phimax);
grid(j,k,4)=quad(@(a)ioneintegrand(grid(j,k,1),grid(j,k,2),a,s),0,phimax);
grid(j,k,5)=quad(@(a)itwointegrand(grid(j,k,1),grid(j,k,2),a,s),0,phimax);
grid(j,k,6)=(abs(grid(j,k,3)))^2+2*(abs(grid(j,k,4)))^2+(abs(grid(j,k,5)))^2;
end
end
```

```
function out=izerointegrand(r,z,a,s)
out=besselj(0,r*sin(a)/s).*sqrt(cos(a)).*sin(a).*(1+cos(a)).*exp(i*z*cos(a)/s^2);
```

```
function out=ioneintegrand(r,z,a,s)
out=besselj(1,r*sin(a)/s).*sqrt(cos(a)).*((sin(a)).^2).*exp(i*z*cos(a)/s^2);
```

```
function out=itwointegrand(r,z,a,s)
```

out=besselj(2,r*sin(a)/s).*sqrt(cos(a)).*sin(a).*(1-cos(a)).*exp(i*z*cos(a)/s^2);

A.2.2 Matlab Code for Numerical Simulation of Isotropic 1D Dipole Rotational Diffusion

Code transcript from *one_dimensional_dipole_isotropic_rotation.m*

```
function [dataout,corrsout,dipole_positions]=one_dimensional_dipole_isotropic_rotation(numsteps,
stepsize, NA)
alpha=asin(NA/1.52);
A = (1/6)-(1/4)*cos(alpha)+(1/12)*(cos(alpha))^3;
B = (1/8)*(cos(alpha)-(cos(alpha))^3);
C = (1/48)*(7-3*cos(alpha)-3*(cos(alpha))^2-(cos(alpha))^3);
dataout=zeros(numsteps,2);
position=zeros(3,numsteps);
position(:,1)=[1;1;1];
randomwalksteps=randn(2,numsteps);
for i=1:numsteps-1
theta=stepsize*randomwalksteps(1,i);
phi=stepsize*randomwalksteps(2,i);
R_theta=[[1,0,0];[0,cos(theta),sin(theta)];[0,-sin(theta),cos(theta)]];
R_phi=[[cos(phi),sin(phi),0];[-sin(phi),cos(phi),0];[0,0,1]];
position(:,i+1)=R_phi*R_theta*position(:,i);
end
x=transpose(position(1,:));
y=transpose(position(2,:));
```

```
z=transpose(position(3,:));
%calculating I_0 (Ix) and I_90 (Iy) following eqns in Vanden Bout 2008 section II-A
dataout(:,1)=A + B*(x.^2+y.^2)./(x.^2+y.^2+z.^2) +
C*((x.^2+y.^2)./(x.^2+y.^2+z.^2)).*(x.^2-y.^2)./(x.^2+y.^2);

dataout(:,2)=A + B*(x.^2+y.^2)./(x.^2+y.^2+z.^2) -
C*((x.^2+y.^2)./(x.^2+y.^2+z.^2)).*(x.^2-y.^2)./(x.^2+y.^2);

dataout(isnan(dataout)) = 0; % replace any NaN values with zeros
dipole_positions=transpose(position);
corrsout=FCS_correlate(dataout);
```

A.2.3 Matlab Code for Numerical Simulation of Anisotropic 1D Dipole Rotational Diffusion

Code transcript from *one_dimensional_dipole_anisotropic_rotation.m*

```
% Ellipse orientation is described by three angles in space (alpha, beta, gamma),
% which describe the angle by which it has rotated about each of its axes
% (ra, rb, rc) relative to the origin.
% Rotational diffusion of the ellipse is determined by a random walk of
% each orientational angle (delta_alpha, delta_beta, delta_gamma) about
% each ellipse axis (ra, rb, rc) by an amount proportional to a
% user-defined stepsize and a diffusion constant for each axis (D_a, D_b,
% and D_c)
% New dipole location is then determined by rotating the permanent dipole about
% each of the ellipse's axes by the corresponding angle change.
```

```
% function r3da.m is rotation about an arbitrary vector in 3 dimensions:
% [rotated_vector]=r3da[vector_to_rotate,axis_of_rotation,angle]

function [ellipse_orientations,dipole_pos,dataout,correlations]...
=one_dimensional_dipole_anisotropic_rotation(numsteps,stepsize,...
D_a, D_b, D_c, NA, ellipse_starting_orientation, dipole_alignment)

%A_alpha = light cone collection angle (just called 'alpha' in the Vanden Bout paper)
A_alpha=asin(NA/1.518);
A = (1/6)-(1/4)*cos(A_alpha)+(1/12)*(cos(A_alpha))^3;
B = (1/8)*(cos(A_alpha)-(cos(A_alpha))^3);
C = (1/48)*(7-3*cos(A_alpha)-3*(cos(A_alpha))^2-(cos(A_alpha))^3);

%generate array of random anglular walk (delta_alpha, delta_beta, delta_gamma)
randomwalksteps=randn(numsteps-1,3);

%initialize array of polarization measurement values (Ix, Iy)
dataout=zeros(numsteps,2);

%initialize array of ellipse orientation values (alpha, beta, gamma)
ellipse_orientation=zeros(numsteps,3);
ellipse_orientation(1,:)=ellipse_starting_orientation;
alpha=ellipse_orientation(1,1);
beta=ellipse_orientation(1,2);
gamma=ellipse_orientation(1,3);
```

```
%initialize array of ellipse a-axis vector positions, [ax;ay;az]
ellipse_a_axis=zeros(3,numsteps);
ellipse_a_axis(:,1)=r3da(r3da([1;0;0],[0;0;1],gamma),r3da([0;1;0],[0;0;1],gamma),beta);

%initialize array of ellipse b-axis vector positions, [bx;by;bz]
ellipse_b_axis=zeros(3,numsteps);
ellipse_b_axis(:,1)=r3da(r3da([0;1;0],[0;0;1],gamma),r3da([1;0;0],[0;0;1],gamma),alpha);

%initialize array of ellipse c-axis vector positions, [cx;cy;cz]
ellipse_c_axis=zeros(3,numsteps);
ellipse_c_axis(:,1)=r3da(r3da([0;0;1],[1;0;0],alpha),r3da([0;1;0],[1;0;0],alpha),beta);

%intialize array of dipole-vector positions (x,y,z)
p=zeros(3,numsteps);
p(:,1)=(1/norm(dipole_alignment))*[dipole_alignment(1)*ellipse_a_axis(:,1)+...
dipole_alignment(2)*ellipse_b_axis(:,1)+dipole_alignment(3)*ellipse_c_axis(:,1)];

for i=1:numsteps-1
%Random-walk each of the ellipse orientation angles:
delta_alpha=stepsize*randomwalksteps(i,1)*D_a;
ellipse_orientation(i+1,1)=ellipse_orientation(i,1)+delta_alpha;
%delta_alpha is proportional to D_a, the rotational diffusion time
%const about ellipse's a-axis

delta_beta=stepsize*randomwalksteps(i,2)*D_b;
ellipse_orientation(i+1,2)=ellipse_orientation(i,2)+delta_beta;
```

```
%delta_beta is proportional to D_b, the rotational diffusion time
%const about ellipse's b-axis

delta_gamma=stepsize*randomwalksteps(i,3)*D_c;
ellipse_orientation(i+1,3)=ellipse_orientation(i,3)+delta_gamma;
%delta_gamma is proportional to D_c, the rotational diffusion time
%const about ellipse's c-axis

% Now find i+1th a-, b-, and c-axis unit vectors (for the next cycle)
% by transforming the ith axis unit vectors by delta_alpha, delta_beta
% and delta_gamma.

ellipse_a_axis(:,i+1)=r3da(r3da(ellipse_a_axis(:,i),ellipse_b_axis(:,i),delta_beta),ellipse_c_axis(:,i),delta_gamma);
ellipse_b_axis(:,i+1)=r3da(r3da(ellipse_b_axis(:,i),ellipse_a_axis(:,i),delta_alpha),ellipse_c_axis(:,i),delta_gamma);
ellipse_c_axis(:,i+1)=r3da(r3da(ellipse_c_axis(:,i),ellipse_a_axis(:,i),delta_alpha),ellipse_b_axis(:,i),delta_beta);
%(if the step sizes are small, the order shouldn't matter)

%Now find the actual dipole location
p(:,1)=(1/norm(dipole_alignment))*[dipole_alignment(1)*ellipse_a_axis(:,i+1)+...
dipole_alignment(2)*ellipse_b_axis(:,i+1)+dipole_alignment(3)*ellipse_c_axis(:,i+1)];

end

%calculating I_0 (Ix) and I_90 (Iy) following eqns in Vanden Bout 2008 section II-A
x1=transpose(p(1,1:numsteps));
y1=transpose(p(2,1:numsteps));
```

```
z1=transpose(p(3,1:numsteps));
dataout(:,1)=A + B*(x1.^2+y1.^2)./(x1.^2+y1.^2+z1.^2) +
C*((x1.^2+y1.^2)./(x1.^2+y1.^2+z1.^2).*(x1.^2-y1.^2)./(x1.^2+y1.^2));
dataout(:,2)=A + B*(x1.^2+y1.^2)./(x1.^2+y1.^2+z1.^2) -
C*((x1.^2+y1.^2)./(x1.^2+y1.^2+z1.^2).*(x1.^2-y1.^2)./(x1.^2+y1.^2));

dataout(isnan(dataout)) = 0; % replace any NaN values with zeros
ellipse_orientations=ellipse_orientation;
dipole_pos=transpose(p);
correlations=FCS_correlate(dataout(:,1:2));
```

A.2.4 Matlab Code for Numerical Simulation of Anisotropic 2D Dipole Rotational Diffusion

Code transcript from *two_dimensional_dipole_anisotropic_rotation.m*

```
% Same algorithm as for the 1-D dipole simulation, but for the 2D
% simulation the dipole is the superposition of two 1D dipoles, with
% relative amplitudes determined by the eccentricity e.

% Additionally, they are given a constant orientation w.r.t the ellipse
% (crystal) axes. The c-axis (WLOG, the crystal z-axis) is the 'dark
% axis', and the ab-plane (crystal xy plane) is the 'bright plane.' This
% is in accordance with published analysis of semiconductor nanocrystals.

% Ellipse orientation is described by three angles in space (alpha, beta, gamma),
% which describe the angle by which it has rotated about each of its axes
```

% (ra, rb, rc) relative to the origin.

% Rotational diffusion of the ellipse is determined by a random walk of
% each orientational angle (delta_alpha, delta_beta, delta_gamma) about
% each ellipse axis (ra, rb, rc) by an amount proportional to a
% user-defined stepsize and a diffusion constant for each axis (D_a, D_b,
% and D_c)

% New dipole location is then determined by rotating the permanent dipole about
% each of the ellipse's axes by the corresponding angle change.

% function r3da.m is rotation about an arbitrary vector in 3 dimensions:
% [rotated_vector]=r3da[vector_to_rotate,axis_of_rotation,angle]

function [ellipse_orientations,dipole_positions1, dipole_positions2,dataout,correlations]=...
two_dimensional_dipole_anisotropic_rotation(numsteps, stepsize, D_a, D_b, D_c,...
eccentricity, NA, ellipse_starting_orientation)

%A_alpha = light cone collection angle (just called 'alpha' in the Vanden
%Bout paper)
A_alpha=asin(NA/1.518);
A = (1/6)-(1/4)*cos(A_alpha)+(1/12)*(cos(A_alpha))^3;
B = (1/8)*(cos(A_alpha)-(cos(A_alpha))^3);
C = (1/48)*(7-3*cos(A_alpha)-3*(cos(A_alpha))^2-(cos(A_alpha))^3);

%generate array of random anglular walk (delta_alpha, delta_beta, delta_gamma)

```
randomwalksteps=randn(numsteps-1,3);

%initialize array of polarization measurement values (Ix, Iy)
dataout=zeros(numsteps,2);

%initialize array of ellipse orientation values (alpha, beta, gamma
ellipse_orientation=zeros(numsteps,3);
ellipse_orientation(1,:)=ellipse_starting_orientation;
alpha=ellipse_orientation(1,1);
beta=ellipse_orientation(1,2);
gamma=ellipse_orientation(1,3);

%initialize array of ellipse a-axis vector positions, [ax;ay;az]
ellipse_a_axis=zeros(3,numsteps);
ellipse_a_axis(:,1)=r3da(r3da([1;0;0],[0;0;1],gamma), r3da([0;1;0],[0;0;1],gamma),beta);

%initialize array of ellipse b-axis vector positions, [bx;by;bz]
ellipse_b_axis=zeros(3,numsteps);
ellipse_b_axis(:,1)=r3da(r3da([0;1;0],[0;0;1],gamma), r3da([1;0;0],[0;0;1],gamma),alpha);

%initialize array of ellipse c-axis vector positions, [cx;cy;cz]
ellipse_c_axis=zeros(3,numsteps);
ellipse_c_axis(:,1)=r3da(r3da([0;0;1],[1;0;0],alpha), r3da([0;1;0],[1;0;0],alpha), beta);

%intialize array of dipole-vector positions (x,y,z)
p1=zeros(3,numsteps);
```

```
p2=zeros(3,numsteps);

p1(:,1)=ellipse_a_axis(:,1);
p2(:,1)=ellipse_b_axis(:,1);

for i=1:numsteps-1
%Random-walk each of the ellipse orientation angles:

delta_alpha=stepsize*randomwalksteps(i,1)*D_a;
ellipse_orientation(i+1,1)=ellipse_orientation(i,1)+delta_alpha;
%delta_alpha is inversely proportional to D_a, the rotational diffusion time
%const about ellipse's a-axis

delta_beta=stepsize*randomwalksteps(i,2)*D_b;
ellipse_orientation(i+1,2)=ellipse_orientation(i,2)+delta_beta;
%delta_beta is inversely proportional to D_b, the rotational diffusion time—
%const about ellipse's b-axis

delta_gamma=stepsize*randomwalksteps(i,3)*D_c;
ellipse_orientation(i+1,3)=ellipse_orientation(i,3)+delta_gamma;
%delta_gamma is inversely proportional to D_c, the rotational diffusion time
%const about ellipse's c-axis

% Now find i+1th a-, b-, and c-axis unit vectors (for the next cycle)
% by transforming the ith axis unit vectors by delta_alpha, delta_beta
% and delta_gamma.
```

```
ellipse_a_axis(:,i+1)=r3da(r3da(ellipse_a_axis(:,i),ellipse_b_axis(:,i),delta_beta),ellipse_c_axis(:,i),delta_gamma);
ellipse_b_axis(:,i+1)=r3da(r3da(ellipse_b_axis(:,i),ellipse_a_axis(:,i),delta_alpha),ellipse_c_axis(:,i),delta_gamma);
ellipse_c_axis(:,i+1)=r3da(r3da(ellipse_c_axis(:,i),ellipse_a_axis(:,i),delta_alpha),ellipse_b_axis(:,i),delta_beta);
%(if the step sizes are small, the order shouldn't matter)

%Now find the dipole locations (conveniently aligned with the a- and b-axes)
p1(:,i+1)=ellipse_a_axis(:,i+1);
p2(:,i+1)=ellipse_b_axis(:,i+1);

end

%calculating I_0 (Ix) and I_90 (Iy) following eqns in Vanden Bout 2008 section II-A
x1=transpose(p1(1,1:numsteps));
y1=transpose(p1(2,1:numsteps));
z1=transpose(p1(3,1:numsteps));
x2=transpose(p2(1,1:numsteps));
y2=transpose(p2(2,1:numsteps));
z2=transpose(p2(3,1:numsteps));
```

dataout(:,1)=A + B*(x1.^2+y1.^2)./(x1.^2+y1.^2+z1.^2) + C*((x1.^2+y1.^2)./(x1.^2+y1.^2+z1.^2).*(x1.^2-y1.^2)./(x1.^2+y1.^2))+sqrt(1-eccentricity^2)*(A + B*(x2.^2+y2.^2)./(x2.^2+y2.^2+z2.^2) + C*((x2.^2+y2.^2)./(x2.^2+y2.^2+z2.^2).*(x2.^2-y2.^2)./(x2.^2+y2.^2)));

dataout(:,2)=A + B*(x1.^2+y1.^2)./(x1.^2+y1.^2+z1.^2) - C*((x1.^2+y1.^2)./(x1.^2+y1.^2+z1.^2).*(x1.^2-y1.^2)./(x1.^2+y1.^2)) +sqrt(1-eccentricity^2)*(A + B*(x2.^2+y2.^2)./(x2.^2+y2.^2+z2.^2) - C*((x2.^2+y2.^2)./(x2.^2+y2.^2+z2.^2).*(x2.^2-y2.^2)./(x2.^2+y2.^2)));

dataout(isnan(dataout)) = 0; *% replace any NaN values with zeros*

ellipse_orientations=ellipse_orientation;

dipole_positions1=transpose(p1);

dipole_positions2=transpose(p2);

correlations=FCS_correlate(dataout(:,1:2));

A.2.5 Matlab Code for 3D Rotation About an Arbitrary Axis

Code transcript from *r3da.m*

function [rotated_vector] = r3da(vector_to_rotate, axis_of_rotation, theta)

%Rotate a 3D vector ('vector_to_rotate') that passes through the origin and

%the point (x,y,z) about the axis of rotation defined by the vector

%('axis_of_rotation') that passes through the origin and the point

%(rx,ry,rz), by angle theta.

normalized_axis_of_rotation=axis_of_rotation/norm(axis_of_rotation);

```
rx=normalized_axis_of_rotation(1);
ry=normalized_axis_of_rotation(2);
rz=normalized_axis_of_rotation(3);
%step 1: rotate about z-axis to bring axis of rotation into alignment with
%the xz-plane (unless it's already aligned, i.e. ry=0)
if ry==0
R_step1=[[1;0;0],[0;1;0],[0;0;1]];
else
R_step1=[[rx/sqrt(rx^2+ry^2);ry/sqrt(rx^2+ry^2);0],[-ry/sqrt(rx^2+ry^2);rx/sqrt(rx^2+ry^2);0],[0;0;1]];
end
%step 2: rotate about the y-axis to bring the axis of rotation into
%alignment with the z-axis (unless it's already aligned, i.e. rz=1)
if rz==1
R_step2=[[1;0;0],[0;1;0],[0;0;1]];
else
R_step2=[[rz/sqrt(rx^2+ry^2+rz^2);0;-sqrt(rx^2+ry^2)/sqrt(rx^2+ry^2+rz^2)],[0;1;0],[sqrt(rx^2+ry^2)/sqrt(rx^2+ry^2+rz^2);0;rz/sqrt(rx^2+ry^2+rz^2)]];
end
%step 3: rotate about the z-axis by the desired angle theta
R_step3=[[cos(theta);sin(theta);0],[-sin(theta);cos(theta);0],[0;0;1]];
%step 4 is the inverse of step 2 (as long as R_step2 is not singular)
if det(R_step2)==0
R_step4=[[1;0;0],[0;1;0],[0;0;1]];
else
R_step4=inv(R_step2);
end
%step 5 is the inverse of step 1 (as long as R_step1 is not singular)
```

```
if det(R_step1)==0
R_step5=[[1;0;0],[0;1;0],[0;0;1]];
else
R_step5=inv(R_step1);
end
R_tot=R_step5*R_step4*R_step3*R_step2*R_step1;
rotated_vector=R_tot*vector_to_rotate;
end
```

A.2.6 Matlab Code for Generating Auto- and Cross-Correlation Traces by the Same Method as the Flex5000 Hardware Correlator

Code transcript from *FCScorrelate.m*

```
function [FCS_correlated_output] = FCS_correlate(data)
%perform auto- and cross-correlation on a pair of time series using same
%method as digital correlator box Flex5000 (Correlator.com)
%accepts Nx2 array argument 'data' and produces Nx3 array output.
numpoints=size(data,1); %determine number of time series points
numtaus=min(size(data,1),10000); %use at most 1e4 tau values
FCS_correlated_output=zeros(numtaus+1,3); %initialize array
data_mean=mean(data); normalizing_factor(1)=mean(data(:,1))2̂; % < I_1(t)^2 >
normalizing_factor(2)=mean(data(:,2))2̂; % < I_2(t)^2 >
normalizing_factor(3)=mean(data(:,1))*mean(data(:,2)); % < I_1(t) * I_2(t) >
for i=0:numtaus
```

```
corrvalue=[0,0,0];
for j=1:numpoints-i
corrvalue(1)=corrvalue(1)+(data(j,1)-data_mean(1))*(data(i+j,1)-data_mean(1));
%channel 1 autocorrelation running sum
corrvalue(2)=corrvalue(2)+(data(j,2)-data_mean(2))*(data(i+j,2)-data_mean(2));
%channel 2 autocorrelation running sum
corrvalue(3)=corrvalue(3)+(data(j,1)-data_mean(1))*(data(i+j,2)-data_mean(2));
textit%cross-correlation running sum
end
FCS_correlated_output(i+1,1)=1+corrvalue(1)/(normalizing_factor(1)*(numpoints-i));
%normalized channel 1 autocorrelation
FCS_correlated_output(i+1,2)=1+corrvalue(2)/(normalizing_factor(2)*(numpoints-i));
%normalized channel 2 autocorrelation
FCS_correlated_output(i+1,3)=1+corrvalue(3)/(normalizing_factor(3)*(numpoints-i));
%normalized cross-correlation
end
```

A.3 Proposed Formalism for Causality Inference from Bivariate Time Series

There is no universally adopted formalism for describing the flow of causal influence within a multivariate system. In this section I will present the formalism used throughout the remainder of this proposal, drawing inspiration primarily from Wiener,[629] Brockwell and Davis,[630] and Paluš *et al.*[631–634] This will be followed by illustration of some of the issues specifically associated with measuring time series data from biochemical networks in living cells. Lastly, I will present a derivation of a numerically facile causality metric (equations A.22 and A.23) which will be the functional measurement employed in potential future experiments.

A.3.1 Required Properties of a Directional Causality Metric for Stochastic Biochemical Processes

What we seek is a general causality operator $\boldsymbol{C}_{\mathcal{X}\mapsto\mathcal{Y}}$ that will tell us the magnitude of causal influence that process $\mathcal{X}$ exerts on process $\mathcal{Y}$. The stated requirements of our causality operator $\boldsymbol{C}_{\mathcal{X}\mapsto\mathcal{Y}}$ are as follows:

1. $\boldsymbol{C}_{\mathcal{X}\mapsto\mathcal{Y}}$ must employ as inputs two physically measurable discrete time series $\boldsymbol{x}_{n,m}$ and $\boldsymbol{y}_{n,m}, \forall\{n \in \mathbb{R}, m \in \mathbb{R}^{+}\}$.

2. The output of $\boldsymbol{C}_{\mathcal{X}\mapsto\mathcal{Y}}$, must convey both magnitude and direction (binary) of causal influence.

Notation	Used to describe
$\boldsymbol{T}$	Generalized set of discrete time points: $\{T_1, T_2, \cdots, T_N\}; N \in \mathbb{N}$
$\boldsymbol{T}^{n,m,\delta}$	An ordered set of N discrete time points starting at time point $T_1 = n$, ending at time $T_N = (n+m)$, $(n \in \mathbb{R}, m \in \mathbb{R}^+)$, and with consistent time spacing δ, such that $(\frac{m}{\delta}) \in \mathbb{N}$, and $N = (\frac{m}{\delta}) + 1$. $\boldsymbol{T}^{n,m,\delta}$ is equivalent to the vector $[n, n+\delta, n+2\delta, \cdots, n+m-\delta, n+m]$.
$\mathcal{X}$	An ergodic stochastic process.
X_i	Random variable representing a single state measurement of $\mathcal{X}$ at time $t = T_i$.
$x(t)$	Single realized value of a state measurement X_i performed at time $t = T_i$.
$\boldsymbol{x}$	Generalized ordered set of realized values $\{x(t); \forall t \in \boldsymbol{T}\}$ measured from $\mathcal{X}$, equivalent to the vector $[x(T_1), x(T_2), \cdots, x(T_N)]$.
Ω_{X_i}	The set of all possible realized values of single measurements X_i made on $\mathcal{X}$.
$p(x_i)$	Shorthand notation for the probability distribution of realized values of a single measurement X_i. $p(x_i) \equiv P_{X_i}(\omega) = Pr\{\omega \colon X_i = \omega\}, \forall \omega \in \Omega_{X_i}$.
$\boldsymbol{x}_{n,m}$	A contiguous N-element subsequence of $\boldsymbol{x}$ ($\boldsymbol{x}_{n,m} \subset \boldsymbol{x}$) starting at time $t_n \in \boldsymbol{T}$, ending at time $(t_n + t_m) \in \boldsymbol{T}$ and with implicit spacing $t_\delta = m/(N-1); \forall \{n \in \mathbb{R}, m \in \mathbb{R}^+\}$. $\boldsymbol{x}_{n,m}$ is equivalent to the vector $[x(n), x(n+t_\delta), x(n+2t_\delta), \cdots, x(m+n)]$.
$\boldsymbol{\Omega}_{\boldsymbol{x}_{n,m}}$	The set of all possible realized values for a subsequence $\boldsymbol{x}_{n,m}$. $\boldsymbol{\Omega}_{\boldsymbol{x}_{n,m}} \equiv \{\Omega_{X_1} \times \Omega_{X_2} \times \cdots \times \Omega_{X_N}\}$, with $\{t_i\} \in \boldsymbol{T}^{n,m,\delta}$.
$p(\boldsymbol{x}_{n,m})$	Shorthand notation for the probability distribution of subsequences $\boldsymbol{x}_{n,m} \subset \boldsymbol{x}$. $p(\boldsymbol{x}_{n,m}) \equiv P_{X_{n,m}}(\boldsymbol{\omega}) = Pr\{\boldsymbol{\omega} \colon [X_n, X_{n+t_\delta}, \cdots, X_{(n+m)}] = \boldsymbol{\omega}\}, \forall \boldsymbol{\omega} \in \Omega_{\boldsymbol{x}_{n,m}}$.
$\boldsymbol{\chi}$	A 'motif' (defined in section A.3.4) expressed by $\mathcal{X}$ within time series $\boldsymbol{x}$.

Table .1: Definitions of probability notation used throughout this proposal. The corresponding notation for additional processes $\mathcal{Y}$ and $\mathcal{Z}$ are, in the same order as above, $\{\mathcal{Y}, Y_i, y(t), \boldsymbol{y}, \Omega_{Y_i}, p(y_i), \boldsymbol{y}_{n,m}, \boldsymbol{\Omega}_{\boldsymbol{y}_{n,m}}, p(\boldsymbol{y}_{n,m}), \boldsymbol{\psi}\}$ and $\{\mathcal{Z}, Z_i, z(t), \boldsymbol{z}, \Omega_{Z_i}, p(z_i), \boldsymbol{z}_{n,m}, \boldsymbol{\Omega}_{\boldsymbol{z}_{n,m}}, p(\boldsymbol{z}_{n,m}), \boldsymbol{\zeta}\}$, respectively, with $\{\boldsymbol{T}, \boldsymbol{T}^{n,m,\delta}\}$ universal.

3. The operational method of $\boldsymbol{C}_{\mathcal{X}\mapsto\mathcal{Y}}$ must distinguish direct causal influence from time-delayed correlated behavior between $\mathcal{X}$ and $\mathcal{Y}$.

4. The method should make no requirement for prior knowledge regarding the nature or existence of processes other than $\mathcal{X}$ and $\mathcal{Y}$. In general, obtaining the output of $\boldsymbol{C}_{\mathcal{X}\mapsto\mathcal{Y}}$ should require no assumptions at all regarding the underlying structure of the system containing $\mathcal{X}$ and $\mathcal{Y}$.

We will define a generalized causality operator $\boldsymbol{C}_{\mathcal{X}\mapsto\mathcal{Y}}$ as a functional mapping of two discrete time series, $\boldsymbol{x}$ and $\boldsymbol{y}$, to a positive scalar $C_{\mathcal{X}\mathcal{Y}}$:

$$\boldsymbol{C}_{\mathcal{X}\mapsto\mathcal{Y}}\colon \{\boldsymbol{x},\boldsymbol{y}\} \mapsto C_{\mathcal{X}\mathcal{Y}} \in \mathbb{R}^{+};$$

Importantly, to meet requirement (2) it is necessary that the output of the causality operator be asymmetric with respect to processes $\mathcal{X}$ and $\mathcal{Y}$: $C_{\mathcal{X}\mathcal{Y}} \neq C_{\mathcal{Y}\mathcal{X}}$. Ideally, we would also like $\boldsymbol{C}_{\mathcal{X}\mapsto\mathcal{Y}}$ to tell us either the primary timescale, τ_c, of the causal influence, or the magnitude of causal influence with respect to time delay τ, $C_{\mathcal{X}\mathcal{Y}}(\tau)$.

A.3.2 Addressing the Stated Requirements

The processes $\mathcal{X}$ and $\mathcal{Y}$ assessed by operator $\boldsymbol{C}_{\mathcal{X}\mapsto\mathcal{Y}}$ are assumed to be both stochastic and ergodic. What is meant by stochastic is that each process possess a random component in its time evolution, making it non-deterministic in nature. The time evolution of the process is therefore best described as a sequence of random variables $\{X_1, X_2, \cdots, X_n; n \in \mathbb{N}\}$ or $\{Y_1, Y_2, \cdots, Y_n; n \in \mathbb{N}\}$ with corresponding probability distributions of individual variables $\boldsymbol{\Omega}_{X_i}$ and $\boldsymbol{\Omega}_{Y_i}$, respectively. Processes $\mathcal{X}$ and $\mathcal{Y}$ are also assumed to be ergodic, meaning that they possess some finite

memory, after which time their stochastic evolution is not influenced by initial conditions.[‡] Given sufficient time, an ergodic stochastic process will eventually revisit its initial state.

To satisfy requirement (1), we will collect simultaneous state measurements of $\mathcal{X}$ and $\mathcal{Y}$ using a consistent time step τ_{min}. This will yield $\boldsymbol{x}_{n,m}$ and $\boldsymbol{y}_{n,m}$ with element values having units depending on the physical measurement (discussed in section A.3.3). Without loss of generality (WLOG), we can define the starting time of an experiment as $T_1 = 0$, and accordingly $n = 0$. The duration of the experiment t_{exp} determines the total length of each subsequence vector as $N = (t_{exp}/\tau_{min}) + 1$. The time set $\boldsymbol{T}$ for the experiment is therefore:

$$\boldsymbol{T}^{0,m,\tau_{min}} = \left[0, \tau_{min}, 2\tau_{min}, \cdots, (\frac{t_{exp}}{\tau_{min}} - 1)\tau_{min}, t_{exp}\right] = [T_1, T_2, \cdots, T_N] \tag{A.15}$$

The individual measurements constituting $\boldsymbol{x}$ and $\boldsymbol{y}$ are:

$$\boldsymbol{x} = [x(0), x(\tau_{min}), x(2\tau_{min}), \cdots, x(t_{exp})] = [x_1, \cdots, x_N] \tag{A.16}$$

$$\boldsymbol{y} = [y(0), y(\tau_{min}), y(2\tau_{min}), \cdots, y(t_{exp})] = [y_1, \cdots, y_N] \tag{A.17}$$

A.3.3 Direct Representations of Stochastic Processes vs. Indirect Reporter Functions

The time series $\boldsymbol{x}$ and $\boldsymbol{y}$ can represent either direct state measures of the processes $\mathcal{X}$ and $\mathcal{Y}$, or be generated by **functionals** (not necessarily linear) that map each state to experimentally accessible physical values:

[‡]This is not strictly true for any biological system, because all cells and organisms age over the course of finite lifetimes, but it is sufficiently close to truth for the purposes of these experiments

$$f_{\mathcal{X}} \colon t \mapsto x(t); t \in \boldsymbol{T}$$
$$f_{\mathcal{Y}} \colon t \mapsto y(t); t \in \boldsymbol{T}$$

For example, process $\mathcal{X}$ could be the fluctuating concentration (or occupation number) of a specific fluorescent species S_X present in a confocal observation volume. Then $\{X_i\} = \{[S_X](t_i); t_i \in \boldsymbol{T}\}$. In this case $f_{\mathcal{X}}$ would be a functional that maps each concentration $[S_X](t_i)$ to the corresponding number of photons $I_X(t_i)$ counted in a specified detection channel of an optical microscope:

$$f_{\mathcal{X}} \colon t \mapsto I_X(t); t \in \boldsymbol{T}$$

Alternately, $\mathcal{X}$ could be a *single* biomolecule fluctuating between distinguishable FRET states $\{E_X\}$. Then $\{X_i\} = \{E_X(t_i); t_i \in \boldsymbol{T}\}$, and $f_{\mathcal{X}}$ would be a functional that maps each FRET state E_{X_i} to a value that is calculated from photon counts in two separate detection channels, I_{D_i} and I_{A_i}, corresponding to the donor and acceptor emission, respectively:

$$f_{\mathcal{X}} \colon t \mapsto \frac{I_A(t)}{I_A(t) + I_D(t)}; t \in \boldsymbol{T}$$

A.3.4 Time Series Motifs and Avoiding False Conclusions Regarding Causal Relationships

The following paragraphs will address requirement 3 of our method, the necessity of distinguishing directional causal influence from time-delayed correlated behavior. It is important to note that because all of the physically relevant functionals $f_{\mathcal{X}}$ and $f_{\mathcal{Y}}$ that map the states of ergodic biochemical processes to measurable fluorescence signals represent measure-preserving systems, the specific details of these functionals will not fundamentally influence an entropy-based metric.[633,635–637] In particular, for

most practical means of obtaining measurable signals from processes $\mathcal{X}$ and $\mathcal{Y}$ (such as counting photons), f will be a one-to-one mapping, implying $H[f(X)] = H[X]$ (equation A.47). Therefore WLOG, we can assume for the remainder of this section that the time series $\boldsymbol{x}$ and $\boldsymbol{y}$ are direct representations of $\mathcal{X}$ and $\mathcal{Y}$.

A given subsequence $\boldsymbol{x}_{n,m}$ is said to be a **motif**, $\boldsymbol{\chi}$, of the time series $\boldsymbol{x}$ if quantitatively similar subsequences are recurrent throughout $\boldsymbol{x}$ for many different starting times n but a consistent duration m. A time series motif is representative of some repeated behavior in the corresponding stochastic process. Neuronal action potentials measured by patch-clamp techniques provide a good example of a time series motif in an intracellular process: every action potential is slightly different, but they are easily recognized both qualitatively and quantitatively in the collected data set. Motif identification within time series is a goal common to many control, analysis and data-mining problems, and has been described extensively.[638–642] In general, motif identification frequently utilizes information-theoretic[643] or Bayesian[644] algorithms unrelated to causality inference. For the sake of brevity, in the following illustration we will use an intuitive depiction of time series motifs.

Assume that in addition to the two observable stochastic processes $\mathcal{X}$ and $\mathcal{Y}$ there exists a third unknown or unobservable stochastic process $\mathcal{Z}$, with corresponding time series $\boldsymbol{z}$. Process $\mathcal{Z}$ exerts direct causal influence over both $\mathcal{X}$ and $\mathcal{Y}$, but $\mathcal{X}$ and $\mathcal{Y}$ exert no causal influence over each other, as depicted in figure A.1a. Furthermore, the propagation of causal influence from $\mathcal{Z}$ to $\mathcal{X}$ and $\mathcal{Y}$ occurs with characteristic time delays τ_{zx} and τ_{zy}, respectively, with $\tau_{zy} > \tau_{zx}$. If a specific recurrent behavior in process $\mathcal{Z}$ generates a corresponding time series motif $\boldsymbol{\zeta}_z$ in $\boldsymbol{z}$ at time t_0, there will tend to be consistent observation of an associated motif $\boldsymbol{\chi}_{zx}$ in $\boldsymbol{x}$ at approximately

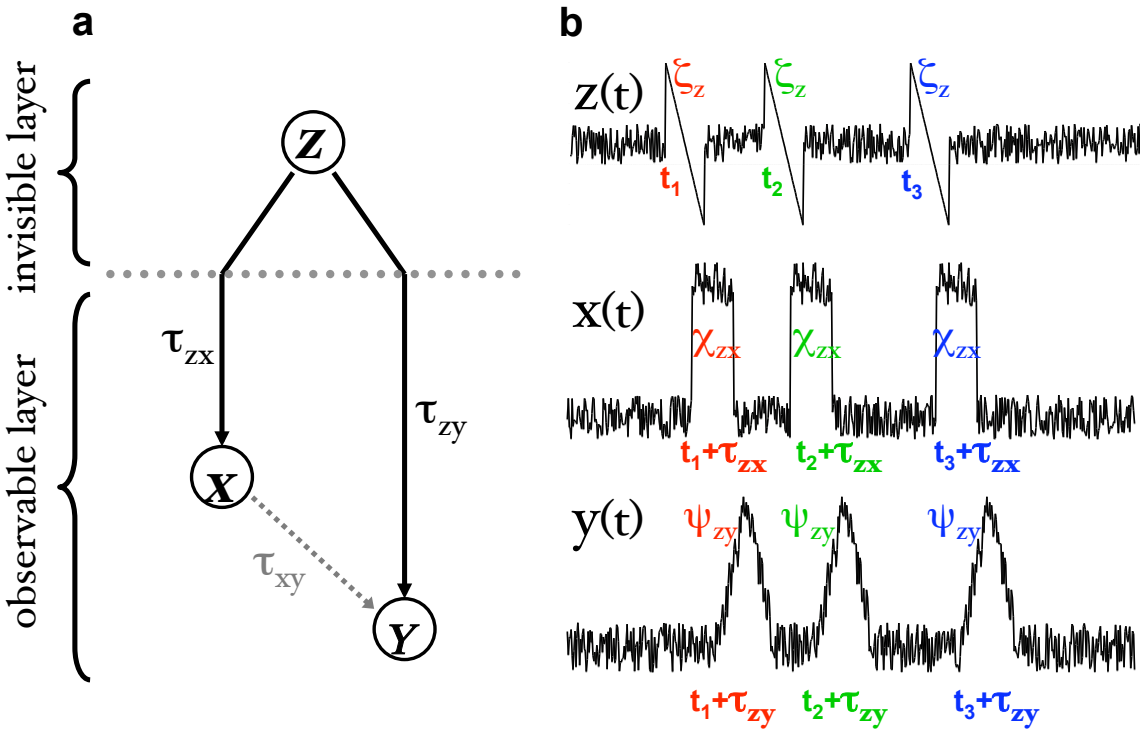

Figure A.1: **(a)** Qualitative sketch of causal influence between an unobservable controlling process (Z) and two observable responsive processes (X) and (Y) with characteristic delays times τ_{xy} and τ_{zy}, respectively. **(b)** Depiction of three occurances of motif $\boldsymbol{\zeta}_z$ in controlling time series $z(t)$, and consequent delayed occurrences of motifs $\boldsymbol{\chi}_{zx}$ and $\boldsymbol{\psi}_{zy}$ in responsive time series $x(t)$ and $y(t)$, respectively.

time $t_0 + \tau_{zx}$, as well as an associated motif $\boldsymbol{\psi}_{zy}$ in $\boldsymbol{y}$ at approximately time $t_0 + \tau_{zy}$.

For example in figure A.1b, process $\mathcal{Z}$ expresses three instances of motif $\boldsymbol{\zeta}_z$ (sawtooth waveform) at times $\{t_1, t_2, t_3\}$, each of length τ_{ζ_z}. These are subsequences $\boldsymbol{z}_{i,l}$, $\boldsymbol{z}_{j,l}$ and $\boldsymbol{z}_{k,l}$; $\{i, j, k, l\} = \{t_1, t_2, t_3, \tau_{\zeta_z}\}$. Subsequently, three associated motifs $\boldsymbol{\chi}_{zx}$ (noisy square waveform) of length $\tau_{\chi_{zx}}$ are observed at times $\{t_1+\tau_{zx}, t_2+\tau_{zx}, t_3+\tau_{zx}\}$, and three associated motifs $\boldsymbol{\psi}_{zy}$ (noisy triangle waveform) of length $\tau_{\psi_{zy}}$ are observed at times $\{t_1 + \tau_{zy}, t_2 + \tau_{zy}, t_3 + \tau_{zy}\}$. The corresponding subsequences in $\boldsymbol{x}$ are $\boldsymbol{x}_{a,d}$,

$\boldsymbol{x}_{b,d}$ and $\boldsymbol{x}_{c,d}$; $\{a,b,c,d\} = \{t_1+\tau_{zx}, t_2+\tau_{zx}, t_3+\tau_{zx}, \tau_{\chi_{zx}}\}$. The corresponding subsequences in $\boldsymbol{y}$ are $\boldsymbol{y}_{e,h}$, $\boldsymbol{y}_{f,h}$ and $\boldsymbol{y}_{g,h}$; $\{e,f,g,h\} = \{t_1+\tau_{zy}, t_2+\tau_{zy}, t_3+\tau_{zy}, \tau_{\psi_{zy}}\}$. To an observer for whom process $\mathcal{Z}$ is unknown or unobservable, it would appear that three *spontaneous* instances of motif $\boldsymbol{\chi}_{zx}$ expressed by $\mathcal{X}$ were followed consistently by $\mathcal{Y}$ expressing motif $\boldsymbol{\psi}_{zy}$ after a characteristic time delay $\tau_{xy} = \tau_{zy} - \tau_{zx}$. The observer may then erroneously conclude, both intuitively and by quantitative analysis of $\boldsymbol{x}$ and $\boldsymbol{y}$ with common time series processing tools (e.g. cross-correlation), that process $\mathcal{X}$ exerts causal influence over process $\mathcal{Y}$. This is precisely the situation that the method proposed here will avoid.

A.3.5 Direct Perturbation Approach to Inferring Causal Relationships

One technique developed by John Ross *et al.*,[645–649] to address the issue of accurately assigning causal influence within a biochemical network involves actively perturbing the network species one at a time and subsequently observing the resulting network response. Applying this technique to the simple system illustrated above, containing observable $\mathcal{X}$ and $\mathcal{Y}$ and unobservable $\mathcal{Z}$, would successfully illuminate the lack of causal connectivity between $\mathcal{X}$ and $\mathcal{Y}$. Introducing a specific perturbation at time t_0 in $\mathcal{X}$ that directly generates motif $\boldsymbol{\chi}_{zx}$ (essentially forcing a subsequence $\boldsymbol{x}_{i,j}; \{i,j\} = \{t_0, t_0+\chi_{zx}\}$ that mimics $\boldsymbol{\chi}_{zx}$ into $\boldsymbol{x}$) would demonstrate that $\boldsymbol{\psi}_{zy}$ does not appear in $\boldsymbol{y}$ at the expected time $t_0 + \tau_{xy}$, because in reality it is $\mathcal{Z}$ expressing $\boldsymbol{\zeta}_z$ that induces a subsequent $\boldsymbol{\psi}_{zy}$ in $\boldsymbol{y}$. Ross *et al.*, have demonstrated the efficacy this method for assessing causal connectivity for several different *in vitro* biochemical networks, applying concentration "pulses" of individual chemical species via microcapillary injection. However, it has yet to be undertaken in

an *in vivo* setting. One can envision constructing an *in vivo* intracellular version of this experiment free of mechanical damage by using photolytic release of caged network components. Carefully controlling the intensity profile of the photolytic laser source by acousto-optic modulation, the perturbation $\boldsymbol{x}_{i,j}$ could be 'sculpted' into a variety of useful motifs. The the current proliferation of caged biochemical species, combined with recent advances in holographic 3D-controlled photolytic uncaging, suggests a wealth of experimental opportunities. However, the intractable flaw with this approach for assessing causal relationships *in vivo* its inherently invasive nature. The induced perturbations $\boldsymbol{x}_{i,j}$, must have some non-infinitesimal magnitude in order to be of use, and this may alter natural *in vivo* cellular behavior with unexpected consequences. Furthermore, this approach necessitates prior knowledge regarding the nature of causal motifs in process $\mathcal{X}$ that are relevant to $\mathcal{Y}$, a requirement this proposal intends to obviate.

A.3.6 Noninvasive Causal Inference Based on Passive Time Series Observation

In contrast to the active perturbation methods used by Ross, *et al*, the information-theoretic time series analysis method presented here infers causal relationships solely by *passive* observation of processes $\mathcal{X}$ and $\mathcal{Y}$. No active perturbation is necessary, because $\mathcal{X}$ and $\mathcal{Y}$ exhibit continual stochastic fluctuations specific to their nonequilibrium nature.[292,301,309,311,312] If observed for a countably infinite[§] time beginning at $t = 0$, each process would express all possible subsequences $\{\boldsymbol{x}_{i,j}, \boldsymbol{y}_{k,l}, \boldsymbol{z}_{i,j}\}$ for $\{i, j, k, l, m, n\} \in \mathbb{R}^+$, including, eventually, many instances of the intended active

[§]'Countably-infinite' is mathematically more appropriate than 'infinite' in this context, because each measurement of $\mathcal{X}$ corresponds to a single random variable X_i, and the time set $\boldsymbol{T}$ of all measurements is discrete-valued rather than continuous.

perturbation $\boldsymbol{\chi}_{zx}$ in $\boldsymbol{x}$, the (falsely) anticipated response $\boldsymbol{\psi}_{zy}$ in $\boldsymbol{y}$, and the invisible motif $\boldsymbol{\zeta}_z$ in $\boldsymbol{z}$. Spontaneous (invisible) instances of $\boldsymbol{\zeta}_z$ would still tend to generate $\boldsymbol{\chi}_{zx}$ in $\boldsymbol{x}$ followed by $\boldsymbol{\psi}_{zy}$ in $\boldsymbol{y}$, but over time the hypothesis $\{\mathcal{X} \to \mathcal{Y}; \tau_c = (\tau_{zx} - \tau_{xy})\}$ would be contradicted by repeated counterexamples.

A more general information-theoretic approach, given two discrete time series of countably infinite length $\{\boldsymbol{x}_{0,\infty}, \boldsymbol{y}_{0,\infty}\}$ as inputs, would be to identify sets of every possible subsequence: $\{\boldsymbol{\Omega}_{\boldsymbol{x}_{i,j}}, \boldsymbol{\Omega}_{\boldsymbol{y}_{k,l}}; \forall\{i,j,k,l\} \in \mathbb{R}^+$ (shorthand notation $\boldsymbol{\Omega}_{\boldsymbol{x}}, \boldsymbol{\Omega}_{\boldsymbol{y}}$). Constructing the individual and joint probability distributions subsequences from these sets, $\big\{\{p(\boldsymbol{x}_{i,j}); \forall \boldsymbol{x}_{i,j} \in \boldsymbol{\Omega}_{\boldsymbol{x}}\}, \{p(\boldsymbol{y}_{k,l})); \forall \boldsymbol{y}_{k,l} \in \boldsymbol{\Omega}_{\boldsymbol{y}}\}, \{p(\boldsymbol{x}_{i,j}, \boldsymbol{y}_{k,l}); \forall (\boldsymbol{x}_{i,j} \in \boldsymbol{\Omega}_{\boldsymbol{x}}, \boldsymbol{y}_{k,l} \in \boldsymbol{\Omega}_{\boldsymbol{y}}\}\big\}$, would then permit quantification of the **conditional mutual information** (**CMI**, equation A.33) between time-shifted subsequences of $\boldsymbol{x}$ and $\boldsymbol{y}$.

Intuitively, the **CMI** measures the degree to which the future uncertainty of process $\mathcal{Y}$ is reduced by knowing the history of process $\mathcal{X}$, irrespective of the uncertainty reduction that comes from knowing history of process $\mathcal{Y}$ itself. Quantitatively, we would then define our causality metric and calculate directional influence as follows:

$$\boldsymbol{C}_{\mathcal{X} \mapsto \mathcal{Y}} \colon \{\boldsymbol{x}_{0,\infty}, \boldsymbol{y}_{0,\infty}, \tau\} \mapsto I\big[\boldsymbol{x}_{0,\infty}, \boldsymbol{y}_{\tau,\infty} \mid \boldsymbol{y}_{0,\infty}\big], \forall \tau \in \mathbb{R}^+$$
$$\boldsymbol{C}_{\mathcal{Y} \mapsto \mathcal{X}} \colon \{\boldsymbol{y}_{0,\infty}, \boldsymbol{x}_{0,\infty}, \tau\} \mapsto I\big[\boldsymbol{y}_{0,\infty}, \boldsymbol{x}_{\tau,\infty} \mid \boldsymbol{x}_{0,\infty}\big], \forall \tau \in \mathbb{R}^+$$

$$
\begin{aligned}
C_{\mathcal{XY}}(\tau) &= I\big[\boldsymbol{x}_{0,\infty}, \boldsymbol{y}_{\tau,\infty} \mid \boldsymbol{y}_{0,\infty}\big] \\
&= H[\boldsymbol{x}_{0,\infty} \mid \boldsymbol{y}_{0,\infty}] + H[\boldsymbol{y}_{\tau,\infty} \mid \boldsymbol{y}_{0,\infty}] - H[\boldsymbol{x}_{0,\infty}, \boldsymbol{y}_{\tau,\infty} \mid \boldsymbol{y}_{0,\infty}] \\
&= - \sum_{\boldsymbol{x_{i,j}} \in \boldsymbol{\Omega_x}, \boldsymbol{y_{k,l}} \in \boldsymbol{\Omega_y}} \frac{p(\boldsymbol{x_{i,j}}, \boldsymbol{y_{k,l}})}{p(\boldsymbol{y_{k,l}})} \log \left(\frac{p(\boldsymbol{x_{i,j}}, \boldsymbol{y_{k,l}})}{p(\boldsymbol{y_{k,l}})} \right) \\
&\quad - \sum_{\boldsymbol{y_{k+\tau,l}} \in \boldsymbol{\Omega_y}, \boldsymbol{y_{k,l}} \in \boldsymbol{\Omega_y}} \frac{p(\boldsymbol{y_{k+\tau,l}}, \boldsymbol{y_{k,l}})}{p(\boldsymbol{y_{k,l}})} \log \left(\frac{p(\boldsymbol{y_{k+\tau,l}}, \boldsymbol{y_{k,l}})}{p(\boldsymbol{y_{k,l}})} \right) \\
&\quad + \sum_{\boldsymbol{x_{i,j}} \in \boldsymbol{\Omega_x}, \boldsymbol{y_{k+\tau,l}} \in \boldsymbol{\Omega_y}, \boldsymbol{y_{k,l}} \in \boldsymbol{\Omega_y}} \frac{p(\boldsymbol{x_{i,j}}, \boldsymbol{y_{k+\tau,l}})}{p(\boldsymbol{y_{k,l}})} \log \left(\frac{p(\boldsymbol{x_{i,j}}, \boldsymbol{y_{k+\tau,l}})}{p(\boldsymbol{y_{k,l}})} \right) \qquad \text{(A.18)} \\
C_{\mathcal{YX}}(\tau) &= - \sum_{\boldsymbol{y_{i,j}} \in \boldsymbol{\Omega_y}, \boldsymbol{x_{k,l}} \in \boldsymbol{\Omega_x}} \frac{p(\boldsymbol{y_{i,j}}, \boldsymbol{x_{k,l}})}{p(\boldsymbol{x_{k,l}})} \log \left(\frac{p(\boldsymbol{y_{i,j}}, \boldsymbol{x_{k,l}})}{p(\boldsymbol{x_{k,l}})} \right) \\
&\quad - \sum_{\boldsymbol{x_{k+\tau,l}} \in \boldsymbol{\Omega_x}, \boldsymbol{x_{k,l}} \in \boldsymbol{\Omega_x}} \frac{p(\boldsymbol{x_{k+\tau,l}}, \boldsymbol{x_{k,l}})}{p(\boldsymbol{x_{k,l}})} \log \left(\frac{p(\boldsymbol{x_{k+\tau,l}}, \boldsymbol{x_{k,l}})}{p(\boldsymbol{x_{k,l}})} \right) \\
&\quad + \sum_{\boldsymbol{y_{i,j}} \in \boldsymbol{\Omega_y}, \boldsymbol{x_{k+\tau,l}} \in \boldsymbol{\Omega_x}, \boldsymbol{x_{k,l}} \in \boldsymbol{\Omega_x}} \frac{p(\boldsymbol{y_{i,j}}, \boldsymbol{x_{k+\tau,l}})}{p(\boldsymbol{x_{k,l}})} \log \left(\frac{p(\boldsymbol{y_{i,j}}, \boldsymbol{x_{k+\tau,l}})}{p(\boldsymbol{x_{k,l}})} \right) . \qquad \text{(A.19)}
\end{aligned}
$$

The most important aspect of the above equations to make note of is the asymmetry $C_{\mathcal{YX}}(\tau) \neq C_{\mathcal{YX}}(\tau)$, which arises by virtue of the conditional probability terms.

A.3.7 Coarse-Graining of Causal Influence for Finite Time Series

Unfortunately infinite time, countable or otherwise, is clearly not an accessible option for biological experiments. However, the ergodicity of $\mathcal{X}$ and $\mathcal{Y}$ yields a solution to this problem. Because $\mathcal{X}$ and $\mathcal{Y}$ are ergodic stochastic processes, they possess a finite 'memory' of their histories, beyond which their behavior is statistically uncorrelated with past events. This permits 'coarse graining' of their information content, essentially by measuring the Shannon entropy within finite time windows longer than the memory time of each process.[631,633,634,650] The exact analytic measure of information created by a stochastic process $\mathcal{X}$ is given by the **entropy rate** $h_{\mathcal{X}}$, defined

as the **joint entropy** (equation A.29) of a countably infinite sequence of states $\{X_i\}$ expressed by $\mathcal{X}$:

$$h_{\mathcal{X}} = \lim_{N\to\infty} \frac{1}{N} H[X_0, X_1, \cdots, X_N] \tag{A.20}$$

Intuitively, $h_{\mathcal{X}}$ is the rate (in bits per unit time) at which process $\mathcal{X}$ relinquishes certainty regarding its history, yielding new values of $X_i = x(t_i)$ that are statistically independent of prior ones. For a perfectly random process, which possesses no memory of preceding states, $h_{\mathcal{X}} = 1$ bit$/\tau_{min}$, and for a perfectly predictable deterministic process $h_{\mathcal{X}} = 0$. Again, the necessity of $N \to \infty$ in the above calculation of $h_{\mathcal{X}}$ is infeasible for biological experiments. However, we can utilize a measure of the **coarse-grained entropy rate (CER)**:

$$h_{cer,\mathcal{X}}(t, \tau_{max}) = I[\boldsymbol{x}_{(t-\tau_{max}),t-\tau_{min})}, x(t)] \tag{A.21}$$

which quantifies the degree of statistical dependence of a single measurement of process $\mathcal{X}$ at time t upon the $N = (\tau_{max}/\tau_{min})$ measurements of $\mathcal{X}$ preceding it. To identify an appropriate τ_{max}, we seek $h_{cer,\mathcal{X}}(t, \tau) \approx 0$ and $h_{cer,\mathcal{Y}}(t, \tau) \approx 0$ for $\tau \geq \tau_{max}$ at all times $0 \leq t \leq t_{exp}$. The ergodicity of $\mathcal{X}$ and $\mathcal{Y}$ assures us that such a τ_{max} exists. As an example, if $\mathcal{X}$ is a simple first-order Markov Process with memory of only the preceding state, $\tau_{max} = 2\tau_{min}$

Having examined both $\mathcal{X}$ and $\mathcal{Y}$ and identified a suitable τ_{max}, we can affect a dramatic reduction in the scale of the state spaces $\boldsymbol{\Omega}_{\boldsymbol{x}_{i,j}}, \boldsymbol{\Omega}_{\boldsymbol{y}_{k,l}}$ and $\{\boldsymbol{\Omega}_{\boldsymbol{x}_{i,j}} \times \boldsymbol{\Omega}_{\boldsymbol{y}_{k,l}}\}$ by requiring the constraints $\{j, l\} \leq \tau_{max}$ and $\{i, k\} \leq (t_{exp} - \tau_{max})$. Additionally, for time windows $\Delta t \leq \tau_{max}$ we can now calculate directional causal influence as a function of τ, $C_{\mathcal{X}\to\mathcal{Y}}(\tau)$, by the same method as for countably infinite time series

(equations A.18 and A.19), or calculate an average causal index across all $\tau_{min} \leq \tau \leq \tau_{max}$ as a function of t by using equations A.22 and A.23.

$$C_{\mathcal{X}\to\mathcal{Y}}(t) = \frac{\tau_{min}}{\Delta t} \sum_{\tau=\tau_{min}}^{\Delta t} I\left[\boldsymbol{x}_{t,\Delta t}, \boldsymbol{y}_{t+\tau,\Delta t} \mid \boldsymbol{y}_{t,\Delta t}\right]; t \leq t_{exp} - \Delta t. \tag{A.22}$$

$$C_{\mathcal{Y}\to\mathcal{X}}(t) = \frac{\tau_{min}}{\Delta t} \sum_{\tau=\tau_{min}}^{\Delta t} I\left[\boldsymbol{y}_{t,\Delta t}, \boldsymbol{x}_{t+\tau,\Delta t} \mid \boldsymbol{x}_{t,\Delta t}\right]; t \leq t_{exp} - \Delta t. \tag{A.23}$$

Most importantly $C_{\mathcal{X}\mathcal{Y}}(\tau) \neq C_{YX}(\tau)$ fulfills requirement (3) by way of asymmetry introduced in the conditional probability terms of equations A.18 and A.19, terms which are also present in equations A.22 and A.23. This asymmetry is the key ideological distinction between measures of *symmetric* time-correlated behavior $\mathcal{X} \leftrightarrow \mathcal{Y}$, and measures of asymmetric causal influence $\mathcal{X} \to \mathcal{Y}$ vs. $\mathcal{Y} \to \mathcal{X}$. Lastly, the information-theoretic basis of this causality metric fulfills requirement (4) by virtue of the fundamentally non-parametric nature of entropy.[489–491,651,652]

The formulation of $C_{\mathcal{X}\to\mathcal{Y}}(t)$ and $C_{\mathcal{Y}\to\mathcal{X}}(t)$ as coarse-grained functions of time is of practical benefit for two key reasons. First, equations A.18 and A.19 permit collection of repeated causal state measurements under consistent conditions, which can be used to assess the variability of the metric in experimental context, facilitating calculation of statistical confidence levels. Furthermore, A.18 and A.19 allow the observation of time-dependent changes in causal directionality with resolution Δt. One of the intended purposes of the work proposed here is to elucidate and quantify the means by which a single common signal transduction cascade can transmit a variety of messages. By calculating the time-dependent causal state while introducing a environmental signal change (such as receptor agonist introduction), it will be possible to identify fundamental differences in transduction network topology which

could not be assessed by conventional measurements of messenger concentration or activity.

A.4 A Starting Point for Numerical Approaches to Assess Directional Causal Influence Within Stochastic Chemical Systems

Consider a simple two-state stochastic fluctuating system describing the activation of a signaling protein X by a kinase Y. The activity state of the signaling protein and the concentration of the activating kinase vary with time according to processes $\mathcal{X}$ and $\mathcal{Y}$, respectively, yielding associated time series $x(t)$ and $y(t)$. The probability of signaling protein X being in the active state at time t is $p_X(t)$, and the parameters associated with stochastic activation and deactivation are a_X and b_X, respectively. In the absence of feedback this system is described by:

$$\begin{aligned} \frac{dp_X}{dt} &= a_X y(t) p_X(t) - b_X(1 - p_X(t)) \\ &= \big(a_X y(t) - b_X\big) p_X(t) - b_X \,. \end{aligned} \tag{A.24}$$

In this simple system we are ignoring the potential for outside influence on $\mathcal{X}$ and $\mathcal{Y}$. Therefore the causal relationship $\boldsymbol{C}_{\mathcal{Y}\mapsto\mathcal{X}}(\tau)$ can be quantified in this situation using a correlation measure.[653] What we would like to obtain is the correlation between the action of kinase Y at time t and the probability of signaling protein X being in its active state at future time $t + \tau$:

$$\begin{aligned} \boldsymbol{C}_{\mathcal{Y}\mapsto\mathcal{X}}(\tau) &= \langle x(t) p_X(t+\tau) \rangle \\ &= b_X \int_0^{t+\tau} e^{-b_X u} \left\langle Y(t) e^{\left[-a_X \int_u^{t+\tau} Y(s) ds\right]} \right\rangle du \,. \end{aligned} \tag{A.25}$$

The time-averaged term inside the first integral of equation A.25:

$$\left\langle Y(t)e^{\left[-a_X \int_u^{t+\tau} Y(s)ds\right]} \right\rangle \tag{A.26}$$

represents an infinite summation of over all possible trajectories of the kinase Y up to time $t+\tau$, and is the principle mathematical object sought in he context of simulations of the stochastic signaling protein/kinase system outlined above. The expectation value in equation A.26 can be determined using the Feynman-Kac stochastic path integral method,[654] for which an array of well-optimized numerical routines are available.[655]

A.5 Information Theory Definitions and Identities

Using the same notation as in Table A.3, for a random variable X with all possible values $x \in \Omega_X$, the **Shannon Information Entropy**[489–491,651,652] H is given by:

$$H = -K \sum_i p_i \log_b p_i \tag{A.27}$$

where p_i is probability of a discrete state X_i, b is the logarithmic base, and K is an arbitrary constant.

Omitting the arbitrary constant K assuming a consistent logarithmic base b, the **Self Entropy** of X is then stated as:

$$H[X] = -\sum_{x \in \Omega_X} p(x) \log p(x) \,. \tag{A.28}$$

Of note is the fact that $H[X]$ depends only on the distribution of values of X, and not on the actual values of X.

Similarly, given a second random variable Y with all possible values $y \in \Omega_Y$, the **Joint Entropy** of two variables is:

$$H[X, Y] = -\sum_{x \in \Omega_X, y \in \Omega_Y} p(x, y) \log p(x, y) \,. \tag{A.29}$$

Following from the conditional probability $p(x \mid y) = p(x,y)/p(y)$, the **Conditional Entropy** of X given Y is:

$$H[X \mid Y] = -\sum_{x\in\Omega_X, y\in\Omega_Y} \frac{p(x,y)}{p(y)} \log\left(\frac{p(x,y)}{p(y)}\right) . \tag{A.30}$$

The **Mutual Information** between X and Y is then defined as:

$$\begin{aligned} I[X,Y] &= H[X] - H[X \mid Y] && \text{(A.31)} \\ &= -\sum_{x\in\Omega_X} p(x)\log p(x) + \sum_{x\in\Omega_X, y\in\Omega_Y} p(x \mid y)\log p(x \mid y) . && \text{(A.32)} \end{aligned}$$

and can be interpreted as the prediction uncertainty that remains in variable X once variable Y is known. Mutual Information, alternatively written as $I(X;Y)$ or $I[X;Y]$, and sometimes called 'transinformation,' is symmetric with respect to X and Y, so knowledge of X yields the same value for the uncertainty remaining in Y.

The Mutual Information between X and Y may also be conditioned by a third variable Z, yielding the **Conditional Mutual Information**:

$$I[X,Y \mid Z] = H[X \mid Z] + H[Y \mid Z] - H[X,Y \mid Z] \tag{A.33}$$

which can be interpreted as the information shared between X and Y which is not conveyed by examining Z.

The generalized definition for **Multivariate Mutual Information**[656] yields the mutual information between X, Y and Z:

$$I[X,Y,Z] = I[X,Y] - I[X,Y \mid Z] . \tag{A.34}$$

Important Information Theory Identities are as follows:

$$H[X,Y] = H[Y,X] \tag{A.35}$$

$$H[X,Y] = H[X] + H[X \mid Y] \tag{A.36}$$

$$I[X,Y] = I[Y,X] \tag{A.37}$$

$$H[X] - H[X \mid Y] = H[Y] - H[Y \mid X] \tag{A.38}$$

$$H[X,Y \mid Z] = H[X \mid Z] + H[Y \mid X,Z] \tag{A.39}$$

$$I[X,Y \mid Z] = I[Y,X \mid Z] \tag{A.40}$$

$$= I[X,Y,Z] - I[X,Z] - I[Y,Z] \tag{A.41}$$

$$= H[X,Y] + H[X,Z] - H[Z] - H[X,Y,Z]\,. \tag{A.42}$$

For the special case in which X and Y are **statistically independent** (i.e., $Pr\{X = x \mid Y = y\} = Pr\{X = x\}$ and $Pr\{Y = y \mid X = x\} = Pr\{Y = y\}$), the following identities are also true:

$$H[X \mid Y] = H[X] \tag{A.43}$$

$$H[X,Y] = H[X] + H[Y] \tag{A.44}$$

$$I[X,Y] = 0\,. \tag{A.45}$$

Let f be a function whose domain is the set of all values for the variable X, Ω_X; i.e., $x_i \mapsto f(x_i), \forall x_i \in \Omega_X$. Then the following is true:

$$H[f(X)] \leq H[X] \tag{A.46}$$

For the special case in which f represents a *one-to-one* functional mapping from $\{x_i\}$ to $\{f(x_i)\}$, then the relation becomes a strict equality:

$$H[f(X)] = H[X]\,. \tag{A.47}$$

When Y is a **deterministic function** of X (i.e., $y_i = f(x_i), \forall x_i \in \Omega_X$), the following identities hold:

$$H[Y \mid X] = 0 \tag{A.48}$$

$$I[X, Y] = H[Y]\,. \tag{A.49}$$

Bibliography

[1] L A Wade, I R Shapiro, Z Ma, S R Quake, and C P Collier. Correlating AFM probe morphology to image resolution for single-wall carbon nanotube tips. *Nano Letters*, 4(4):725–731, 2004.

[2] L A Wade, I R Shapiro, C P Collier, M J Esplandiu, V G Bittner, and K P Giapis. Selective functionalization of carbon nanotube tips allowing fabrication of new classes of nanoscale sensing and manipulation tools. US patent 7,514,214, 2009.

[3] C J Chen. *Introduction to scanning tunneling microscopy.* Oxford University Press, 1993.

[4] M J Esplandiu. Scanning probe microscopies for analytical studies at the nanometer scale. *Contributions to Science*, 3(1):33–46, 2005.

[5] G Binning, C F Quate, and Ch Gerber. Atomic force microscope. *Physical Review Letters*, 56(9):930–933, 1986.

[6] A Engel and D J Müller. Observing single biomolecules at work with the atomic force microscopy. *Nature Structural Biologu*, 7(9):715–718, 2000.

[7] P Ringler, M Borgnia, H Stahlberg, D J Müller, P Agre, and A Engel. High resolution AFM tomographs of the *Escherichia coli* water channel aquaporin z. *EMBO Journal*, 18(18):4981–4987, 1999.

[8] J Mou, D M Czajkowsky, S Sheng, R Ho, and Z Shao. High resolution surface structure of *E coli* GroES oligomer by atomic force microscopy. *FEBS Letters*, 381:161–164, 1996.

[9] D J Müller, G Büldt, and A Engel. Force-induced conformational change of bacteriorhodopsin. *JMB*, 249:239–243, 1995.

[10] D J Müller, F A Schabert, G Büldt, and A Engel. Imaging purple membranes in aqueous solution at subnanometer resolution by atomic force microscopy. *Biophysical Journal*, 68:1681–1686, 1995.

[11] F A Schabert, C Henn, and A Engel. native *Escherichia coli* ompf porin surfaces probed by atomic force microscopy. *Science*, 268:92–94, 1995.

[12] S Scheuring, D J Müller, P Ringlet, J B Heymann, and A Engel. Imaging streptavidin 2D crystals on biotinylated lipid monolayer at high resolution with the atomic force microscope. *Journal of Microscopy*, 193:28–35, 1999.

[13] D J Müller and Y F Dufrêne. Atomic force microscopy as a multifunctional molecular toolbox in nanobiotechnology. *Nature Nanotechnology*, 3:261–268, 2008.

[14] FJ Giessibl. Atomic resolution of the silicon(111)-(7x7) surface by atomic force microscopy. *Science*, 267(5194):68, 1995.

[15] Franz J. Giessibl. Advances in atomic force microscopy. *Reviews of Modern Physics*, 75:949, 2003.

[16] F J Giessibl. A direct method to calculate tip–sample forces from frequency shifts in frequency-modulation atomic force microscopy. *Applied Physics Letters*, 78(1):123–125, 2001.

[17] F J Giessibl, M Herz, and J Mannhart. Friction traced to the single atom. *PNAS*, 99(19):12006–12010, 2002.

[18] S. Hembacher, F. J. Giessibl, J. Mannhart, and C. F. Quate. Local spectroscopy and atomic imaging of tunneling current, forces, and dissipation on graphite. *Physical Review Letters*, 94(5):056101, 2005.

[19] Y Sugimoto, P Pou, M Abe, P Jelinek, R Pérez, S Morita, and Ó Custance. Chemical identification of individual surface atoms by atomic force microscopy. *Nature*, 446:64–67, 2007.

[20] F J Giessibl. Higher-harmonic atomic force microscopy. *Surface and Interface Analysis*, 38:1696–1701, 2006.

[21] S Hembacher, F J Geissibl, and J Mannhart. Force microscopy with light-atom probes. *Science*, 305(5682):380–383, 2004.

[22] F J Giessibl, H Bielefeldt, S Hembacher, and J Mannhart. Imaging of atomic orbitals with the Atomic Force Microscope - experiments and simulations. *arXiv:cond-mat/0107195*, 2001.

[23] S Xu and M F Arnsdorf. Electrostatic force microscope for probing surface charges in aqueous solutions. *PNAS*, 92(22):10384–10388, 1995.

[24] M. Liley, D. Gourdon, D. Stamou, U. Meseth, T. M. Fischer, C. Lautz, H. Stahlberg, H. Vogel, N. A. Burnham, and C. Duschl. Friction anisotropy

and asymmetry of a compliant monolayer induced by a small molecular tilt. *Science*, 280(5361):273–275, 1998.

[25] U Kaiser, A Schwarz, and R Wiesendanger. Magnetic exchange force microscopy with atomic resolution. *Nature*, 446:522–525, 2007.

[26] C Lee, J Kwak, and A J Bard. Application of scanning electrochemical microscopy to biological samples. *PNAS*, 87:1740–1743, 1990.

[27] F-R F Fan and A J Bard. Imaging of biological macromolecules on mica in humid air by scanning electrochemical microscopy. *PNAS*, 96(25):14222–14227, 1999.

[28] T Wilhelm and G Wittstock. Analysis of interaction in patterned multienzyme layers by using scanning electrochemical microscopy. *Angewandte Chemie International Edition*, 42:2248–2250, 2003.

[29] A Kueng, C Kranz, A Lugstein, E Bertagnoli, and B Mizaikoff. Integrated AFM-secm in tapping mode: simultaneous topographic and electrochemical imaging of enzyme activity. *Angewandte Chemie International Eidition*, 42:3238–3240, 2003.

[30] Y Zu, Z Ding, J Zhou, Y Lee, and A J Bard. Scanning optical microscopy with an electrogenerated chemiluminescent light source at a nanometer tip. *Analytical Chemistry*, 73(10):2153–2156, 2001.

[31] F-R F Fan and A J Bard. Electrochemical detection of single molecules. *Science*, 267:871–874, 1995.

[32] F-R F Fan, J Kwak, and A J Bard. Single molecule electrochemistry. *JACS*, 118:9669–9675, 1996.

[33] B C Stipe, M A Rezaei, and W Ho. Single-molecule vibrational spectroscopy and microscopy. *Science*, 280:1732–1735, 1998.

[34] L J Lauhon and W Ho. Effects of temperature and other experimental variables on single molecule vibrational spectroscopy with the scanning tunneling microscope. *Review of Scientific Instruments*, 72(1):216–223, 2001.

[35] K Kim, T Komeda, and M Kawai. Single-molecule reaction and characterization by vibrational excitation. *Physical Review Letters*, 89(12):126104, 2002.

[36] J R Hahn and W Ho. Imaging and vibrational spectroscopy of single pyridine molecules on Ag(110) using a low-temperature scanning tunneling microscope. *Journal of Chemical Physics*, 124(20):204708, 2006.

[37] S Ijima. Helical microtubules of graphitic carbon. *Nature*, 363:603 – 605, 1993.

[38] S Ijima and T Ichihashi. Single-shell carbon nanotubes of 1-nm diameter. *Nature*, 354:5658, 1991.

[39] R H Baughman, A A Zakhidov, and W A de Heer. Carbon nanotubes– the route toward applications. *Science*, 297:787–792, 2002.

[40] T Chang and H Gao. Size-dependent elastic properties of a single-walled carbon nanotube via a molecular mechanics model. *Journal of the Mechanics and Physics of Solids*, 51(6):1059–1074, 2003.

[41] T Hertel, R E Walkup, and P Avouris. Deformation of carbon nanotubes by surface van der waals forces. *Physical Review B*, 50(20):13870–13873, 1998.

[42] S J Tans, M H Devoret, H Dai, A Thess, R E Smalley, L J Geerligs, and C Dekker. Individual single-wall carbon nanotubes as quantum wires. *Nature*, 386:474–477, 1997.

[43] Z Yao, C Dekker, and P Avouris. Electrical Transport Through Single-Wall Carbon Nanotubes. In M S Dresselhaus, G Dresselhaus, and P Avouris, editors, *Carbon Nanotubes*, pages 147–171, 2001.

[44] J Cao, Q Wang, and H Dai. Electromechanical properties of metallic, quasimetallic, and semiconducting carbon nanotubes under stretching. *Physical Review Letters*, 90(15):157601, 2003.

[45] J W F Wildöer, L C Venema, A G Rinzler, R E Smalley, and C Dekker. Electronic structure of atomically resolved carbon nanotubes. *Nature*, 391:59–62, 1998.

[46] M Ouyang, J-L Huang, and C M Lieber. Fundamental electronic properties and applications of single-walled carbon nanotubes. *Accounts of Chemical Research*, 35(12):1018–1025, 2002.

[47] T W Odom, J-L Huang, P Kim, and C M Lieber. Atomic structure and electronic properties of single-walled carbon nanotubes. *Nature*, 391:62–64, 1998.

[48] L C Venema, J W G Wildöer, J W Janssen, S J Tans, H L J Temminck Tuinstra, L P Kouwenhoven, and C Dekker. Imaging electron wave functions of quantized energy levels in carbon nanotubes. *Science*, 283:52–55, 1999.

[49] L C Venema, V Meunier, Ph Lambin, and C Dekker. Atomic structure of carbon nanotubes from scanning tunneling microscopy. *Physical Review B*, 61(4):2991–2996, 2000.

[50] A Jorio, R Saito, J H Hafner, C M Lieber, M Hunter, T McClure, G Dresselhaus, and M S Dresselhaus. Structural (n,m) determination of isolated single-wall carbon nanotubes by resonant raman scattering. *Physical Review Letters*, 86(6):1118–1121, 2001.

[51] P Kim, T W Odom, J-L Huang, and C M Lieber. Electronic density of states of atomically resolved single-walled carbon nanotubes: van hove singularities and end states. *Physical Review Letters*, 82(6):1225–1228, 1999.

[52] H W Ch Postma, T Teepen, Z Yao, M Grifoni, and C Dekker. Carbon nanotube single-electron transistors at room temperature. *Science*, 293:76–79, 2001.

[53] T Rueckes, K Kim, E Joselevich, G Y Tseng, C-L Cheung, and C M Lieber. Carbon nanotube-based nonvolatile random access memory for molecular computing. *Science*, 289:94–97, 2000.

[54] A Bachtold, P Hadley, T Nakanishi, and C Dekker. Logic circuits with carbon nanotube transistors. *Science*, 294:1317–1320, 2001.

[55] J H Hafner, M J Bronikowski, B R Azamian, P Nikolaev, A G Rinzler, D T Colbert, K A Smith, and R E Smalley. Catalytic growth of single-wall carbon nanotubes from metal particles. *Chemical Physics Letters*, 296:195–202, 1998.

[56] B Zheng, C Lu, G Gu, A Makarovski, G Finkelstein, and J Liu. Efficient CVD growth of single-walled carbon nanotubes on surfaces using carbon monoxide precursor. *Nano Letters*, 2(8):895–898, 2002.

[57] S Huang, M Woodson, R Smalley, and J Liu. Growth mechanism of oriented long single walled carbon nanotubes using"fast heating" chemical vapor deposition process. *Nano Letters*, 4(6):1024–1028, 2004.

[58] L X Zheng, M J O'Connell, Z K Doorn, X Z Liao, Y H Zhao, E A Akhadov, M A Hoffbauer, B J Roop, Q X Jia, R C Dye, D E Peterson, S M Huang, and J Liu. Ultralong single-wall carbon nanotubes. *Nature Materials*, 3:673–676, 2004.

[59] H Dai. Carbon nanotubes: synthesis, integration and properties. *Accounts of Chemical Research*, 35:1035–1044, 2002.

[60] H Dai. Carbon nanotubes: opportunities and challenges. *Surface Science*, 500:218–241, 2002.

[61] A M Cassell, N R Franklin, T W Tombler, E M Chan, J Han, and H Dai. Directed growth of free-standing single-walled carbon nanotubes. *JACS*, 121:7975–7976, 1999.

[62] Y Li, D Mann, M Rolandi, W Kim, A Ural, S Hung, A Javey, J Cao, D Wang, E Yenilmez, Q Wang, J F Gibbons, Y Nishi, and H Dai. Preferential growth of semiconducting single-walled carbon nanotubes by a plasma enhanced CVD method. *Nano Letters*, 4(2):317–321, 2004.

[63] M Meyyappan, L Delzeit, A Cassell, and D Hash. Carbon nanotube growth by peCVD: a review. *Plasma Sources Science and Technology*, 12:205–216, 2003.

[64] J Kong, A M Cassell, and H Dai. Chemical vapor deposition of methane for single-walled carbon nanotubes. *Chemical Physics Letters*, 292:567–574, 1998.

[65] Y Li and J Liu. Preparation of monodispersed Fe-Mo nanoparticles as the catalyst for CVD synthesis of carbon nanotubes. *Chemistry of Materials*, 13:1008–1014, 2001.

[66] P Nikolaev, M J Bronikowski, R K Bradley, F Rohmund, D T Colbert, K A Smith, and R E Smalley. Gas-phase catalytic growth of single-walled carbon nanotubes from carbon monoxide. *Chemical Physics Letters*, 313:91–97, 1999.

[67] A M Cassell, J A Raymakers, J Kong, and H Dai. Large scale CVD synthesis of single-walled carbon nanotubes. *Journal of Physical Chemistry B*, 103:6484–6492, 1999.

[68] E Joselevich and C M Lieber. Vectorial growth of metallic semiconducting single-wall carbon nanotubes. *Nano Letters*, 2(10):1137–1141, 2002.

[69] Y Li, W Kim, Y Zhang, M Rolandi, D Wang, and H Dai. Growth of single-walled carbon nanotubes from discrete catalytic nanoparticles of various sizes. *Journal of Physical Chemistry B*, 105:11424–11431, 2001.

[70] V Vinciguerra, F Buoncore, G Panzera, and L Occhipinti. Growth mechanisms in chemical vapor deposited carbon nanotubes. *Nanotechnology*, 14:655–660, 2003.

[71] S Naha and I K Puri. A model for catalytic growth of carbon nanotubes. *Journal of Physics D: Applied Physics*, 41:065304, 2008.

[72] Y Shibuta and S Maruyama. Molecular dynamics simulation of formation process of single-walled carbon nanotubes by cCVD method. *Chemical Physics Letters*, 382:381–386, 2003.

[73] J-Y Raty, F Gygi, and G Galli. Growth of carbon nanotubes on metal nanoparticles: a microscopic mechanism from *ab initio* molecular dynamics simulations. *Physical Review Letters*, 95:096103, 2005.

[74] W Yang, P Thordarson, J J Gooding, S P Ringer, and F Braet. Carbon nanotubes for biological and biomedical applications. *Nanotechnology*, 18:412001, 2007.

[75] F Balavoine, P Schultz, C Richard, V Mallouh, T W Ebbesen, and C Mioskowski. Helical crystallization of proteins on carbon nanotubes: a first step towards the development of new biosensors. *Angewandte Chemie International Edition*, 38(13/14):1912–1915, 1999.

[76] M Shim, N Wong Shi Kam, R J Chen, Y Li, and H Dai. Functionalization of carbon nanotubes for biocompatibility and biomolecular recognition. *Nano Letters*, 2(4):285–288, 2002.

[77] S S Wong, A T Woolley, E Joselevich, and C M Lieber. Functionalization of carbon nanotube AFM probes using tip-activated gases. *Chemical Physics Letters*, 306:219–225, 1999.

[78] S S Wong, A T Wooley, E Joselevich, C L Cheung, and C M Lieber. Covalently-functionalized single-walled carbon nanotube probe tips for chemical force microscopy. *JACS*, 120:8557–8558, 1998.

[79] S S Wong, E Joselevich, A T Woolley, C L Cheung, and C M Lieber. Covalently functionalized nanotubes as nanometre-sized probes in chemistry and biology. *Nature*, 394:52–55, 1998.

[80] D Shi, J Lian, P He, L M Wang, W J van Ooij, M Schulz, Y Liu, and D B Mast. Plasma deposition of ultrathin polymer films on carbon nanotubes. *Applied Physics Letters*, 81(27):5216–5218, 2002.

[81] N Tayebi, Y Narui, R J Chen, C P Collier, K Y Giapis, and Y Zhang. Nanopencil as a wear-tolerant probe for ultrahigh density data storage. *Applied Physics Letters*, 93:103112, 2008.

[82] N R Wilson and J V Macpherson. Single-walled carbon nanotubes as templates for nanowire conducting probes. *Nano Letters*, 3(10):1365–1369, 2003.

[83] J Y Chen, A Kutana, C P Collier, and K P Giapis. Electrowetting in carbon nanotubes. *Science*, 310:1480–1483, 2005.

[84] J N Barisci, G G Wallace, and R H Baughman. Electrochemical characterization of single-walled carbon nanotube electrodes. *Journal of the Electrochemical Society*, 147(12):4580–4583, 2000.

[85] P J Britto, K S V Santhanam, A Rubio, J A Alonso, and P M Ajayan. Improved charge transfer at carbon nanotube electrodes. *Advanced Materials*, 11(2):154–157, 1999.

[86] S Sotiropoulou and N A Chaniotakis. Carbon nanotube array-based biosensor. *Analytical and Bioanalytical Chemistry*, 375:103–105, 2003.

[87] X Yu, D Chattopadhyayb, I Galeska, F Papadimitrakopoulos, and J F Rusling. Peroxidase activity of enzymes bound to the ends of single-wall carbon nanotube forest electrodes. *Electrochemistry Communications*, 5(5):408–411, 2003.

[88] K Wu, J Fei, and S Hu. Simultaneous determination of dopamine and serotonin on a glassy carbon electrode coated with a film of carbon nanotubes. *Analytical Biochemistry*, 318(1):100–106, 2003.

[89] J J Davis, R J Coles, and H A O Hill. Protein electrochemistry at carbon nanotube electrodes. *Journal of Electroanalytical Chemistry*, 440:279–282, 1997.

[90] A Guiseppi-Elie, C Lei, and R H Baughman. Direct electron transfer of glucose oxidase on carbon nanotubes. *Nanotechnology*, 13:559–564, 2002.

[91] Y-D Zhao, W-D Zhang, H Chen, and Q-M Luo. Direct electron transfer of glucose oxidase molecules adsorbed onto carbon nanotube powder microelectrode. *Analytical Sciences*, 18:939–941, 2002.

[92] K Bestman, J-O Lee, F G M Weintz, H A Heering, and C Dekker. Enzyme-coated carbon nanotubes as single-molecule biosensors. *Nano Letters*, 3(6):727–730, 2003.

[93] C Cai and J Chen. Direct electron transfer of glucose oxidase promoted by carbon nanotubes. *Analytical Biochemistry*, 332:75–83, 2004.

[94] M Wang Y Liu, F Zhao, Z Xu, and S Dong. The direct electron transfer of glucose oxidase and glucose biosensor baed on carbon nanotubes/chitosan matrix. *Biosensors and Bioelectronics*, 21(6):984–988, 2005.

[95] A T Woolley, C L Cheung, J H Hafner, and C M Lieber. Structural biology with carbon nanotube AFM probes. *Chemistry & Biology*, 7:R193–R204, 2000.

[96] C V Nguyen, Q Yi, and M Meyyappan. Carbon nanotube tips for scanning probe microscopy: fabrication and high aspect ratio nanometrology. *Measurement Science and Technology*, 16:2138–2146, 2005.

[97] J H Hafner, C-L Cheung, A T Woolley, and C M Lieber. Structural and functional imaging with carbon nanotube AFM probes. *Progress in Biophysics and Molecular Biology*, 77:73–110, 2001.

[98] D Qian, G J Wagner, and W K Liu. Mechanics of carbon nanotubes. *Applied Mechanical Review*, 55(6):495–504, 2002.

[99] S S Wong, A T Woolley, T W Odom, J-L Huang, P Kim, D V Vezenov, and C M Lieber. Single-walled carbon nanotube probes for high-resolution nanostructure imaging. *Applied Physics Letters*, 73(23):3465–3467, 1998.

[100] S S Wong, J D Harper, P T Lansbury Jr., and C M Lieber. Carbon nanotube tips: high resolution probes for imaging biological systems. *JACS*, 120:603–604, 1998.

[101] G Nagy, M Levy, R Scarmozzino, R M Osgood Jr., H Dai, R E Smalley, C A Michaels, G W Flynn, and G F McLane. Carbon nanotube tipped atomic force microscopy for measurement of <100 nm etch morphology on semiconductors. *Applied Physics Letters*, 73(4):529–531, 1998.

[102] S Kuwahara, S Akita, M Shirakihara, T Sugai, Nakayama, and H Shinohara. Fabrication and characterization of high-resolution AFM tips with high-quality double-wall carbon nanotubes. *Chemical Physics Letters*, 429:581–585, 2006.

[103] J Martinez, T D Yuzivnsky, A M Fennimore, A Zettl, R García, and C Bustamante. Length control and sharpening of atomic force microscope carbon nanotube tips assisted by an electron beam. *Nanotechnology*, 16:2493–2496, 2005.

[104] C V Nguyen, K-J Chao, R M D Stevens, L Delzeit, A Cassell, J Han, and M Meyyappan. Carbon nanotube tip probes: stability and lateral resolution in scanning probe microscopy and application to surface science. *Nanotechnology*, 12:363–367, 2001.

[105] N Choi, T Uchihashi, H Nishijima, T Ishida, W Mizutani, S Akita, Y Nakayama, M Ishikawa, and H Tokumoto. Atomic force microscopy of single-walled carbon nanotubes using carbon nanotube tip. *Japanese Journal of Applied Physics*, 39:3707–3710, 2000.

[106] A J Austin, C V Nguyen, and Q Ngo. Electrical conduction of carbon nanotube atomic force microscopy tips: applications in nanofabrication. *Journal of Applied Physics*, 99(11):114304, 2006.

[107] R M D Stevens, N A Frederick, B L Smith, D E Morse, G D Stucky, and P K Hansma. Carbon nanotubes as probes for atomic force microscopy. *Nanotechnology*, 11:1–5, 2000.

[108] S Akita, H Nishijima, Y Nakayama, F Tokumasu, and K Takeyasu. Carbon nanotube tips for a scanning probe microscope: their fabrication and properties. *Journal of Physics D: Appled Physics*, 32:1044–1048, 1999.

[109] J-E Kim, J-K Park, and C-S Han. Use of dielectrophoresis in the fabrication of an atomic force microscope tip with a carbon nanotube: experimental investigation. *Nanotechnology*, 17:2937–2941, 2006.

[110] J-E Kim and C-S Han. Use of dielectrophoresis in the fabrication of an atomic force microscope tip with a carbon nanotube: a numerical analysis. *Nanotechnology*, 16:2245–2250, 2005.

[111] A Hall, W G Matthews, R Superfine, M R Falvo, and S Washburn. Simple and efficient method for carbon nanotube attachment to scanning probes and other substrates. *Applied Physics Letters*, 82(15):2506–2508, 2003.

[112] M Hulman and M Tajmar. The dielectrophoretic attachment of nanotube fibers on tungsten needles. *Nanotechnology*, 18:1045504, 2007.

[113] J Tang, G Yang, Q Zhang, A Parhat, B Maynor, J Liu, L-C Qin, and O Zhou. Rapid and reproducible fabrication of carbon nanotube AFM probes by dielectrophoresis. *Nano Letters*, 5(1):11–14, 2005.

[114] E B Cooper, S R Manalis, H Fang, H Dai, K Matsumoto, S C Minne, T Hunt, and C F Quate. Terabit-per-square-inch data storage with the atomic force microscope. *Applied Physics Letters*, 75(22):3566–3568, 1999.

[115] K Matsumoto, S Kinosita, Y Gotoh, T Uchiyama, S Manalis, and C Quate. Ultralow biased field emitter using single-wall carbon nanotube directly grown onto silicon tip by thermal chemical vapor deposition. *Applied Physics Letters*, 78(4):539–540, 2001.

[116] J H Hafner, C L Cheung, and C M Lieber. Growth of nanotubes for probe microscopy tips. *Nature*, 398:761–762, 1999.

[117] C L Cheung, J H Hafner, and C M Lieber. Carbon nanotube atomic force microscopy tips: direct growth by chemical vapor deposition and application to high-resolution imaging. *PNAS*, 97(8):3809–3813, 2000.

[118] J H Hafner, C-L Cheung, T H Oosterkamp, and C M Lieber. High-yield assembly of single-walled carbon nanotube probes for scanning probe microscopies. *Journal of Physical Chemistry B*, 105(4):743–746, 2001.

[119] N R Wilson, D H Cobden, and J V Macpherson. Single-wall carbon nanotube conducting probe tips. *Journal of Physical Chemistry B*, 106:13102–13105, 2002.

[120] C T Gibson, S Carnally, and C J Roberts. Attachment of carbon nanotube to atomic force microscopy probes. *Ultramicroscopy*, 107:1118–1122, 2007.

[121] L Chen, C L Cheung, P D Ahsby, and C M lieber. Single-walled carbon nanotube AFM probes: optical imaging resolution of nanoclusters and biomolecules in ambient and fluid environments. *Nano Letters*, 4(9):1725–1731, 2004.

[122] C L Cheung, J H Hafner, T W Odom, K Kim, and C M Lieber. Growth and fabrication with single-walled carbon nanotube probe microscopy tips. *Applied Physics Letters*, 76(21):3136–3138, 2000.

[123] C Bernard, S Marsaudon, R Boisgard, and J-P Aimé. Competition of elastic and adhesive properties of carbon nanotubes anchored to atomic force microscopy tips. *Nanotechnology*, 19:035709, 2008.

[124] I R Shapiro, S D Solares, M J Esplandiu, L A Wade, W A Goddard, and C P Collier. Influence of elastic deformation on single-wall carbon nanotube atomic force microscopy probe resolution. *Journal of Physical Chemistry B*, 108:13613–13618, 2004.

[125] S I Lee, S W Howell, A Raman, R Reifenberger, C V Nguyen, and M Meyyappan. Nonlinear tapping dynamics of multi-walled carbon nanotube tipped atomic force microcantilevers. *Nanotechnology*, 15:416–421, 2004.

[126] E S Snow, P M Campbell, and J P Novak. Single-wall carbon nanotube atomic force microscope probes. *Applied Physics Letters*, 80(11):2002–2004, 2002.

[127] H Dai, J H Hafner, A G Rinzler, D T Colbert, and R E Smalley. Nanotubes as nanoprobes in scanning probe microscopy. *Nature*, 384:147–150, 1996.

[128] S I Lee, S W Howell, A Raman, R Reifenberger, C V Nguyen, and M Meyyappan. Complex dynamics of carbon nanotube probe tips. *Ultramicroscopy*, 103:95–102, 2005.

[129] A Kutana, K P Giapis, J Y Chen, and C P Collier. Amplitude response of single-wall carbon nanotube probes during tapping mode atomic force microscopy: modeling and experiment. *Nano Letters*, 6(8):1669–1673, 2006.

[130] E S Snow, P M Campbell, and J P Novak. Atomic force microscopy using single-wall C nanotube probes. *Journal of Vacuum Science and Technology*, 20(3):822–827, 2002.

[131] D Dietzel, C Bernard, D Mariolle, A Iaia, A M Bonnot, J P Aimé, S Marsaudon, F Bertin, and A Chabli. Mechanical properties of carbon-nanotube tips and nanoneedles: a frequency modulation-atomic force microscopy comparative study. *Journal of Scanning Probe Microscopy*, 1:39–44, 2006.

[132] M C Strus, A Raman, and C V Nguyen. Imaging artifacts in atomic force microscopy with carbon nanotube tips. *Nanotechnology*, 16:2482–2492, 2005.

[133] M Stark, R W Stark, W M Heckl, and R Guckenberger. Inverting dynamic force microscopy: from signals to time-resolved interaction forces. *PNAS*, 99(13):8473–8478, 2002.

[134] A San Paulo and R García. High-resolution imaging of antibodies by tapping-mode atomic corce microscopy: attractive and repulsive tip-sample interactions. *Biophysical Journal*, 78:1599–1605, 2000.

[135] A San Paulo and R García. Unifying theory of tapping-mode atomic force microscopy. *Physical Review B*, 66(4):041406(R), 2002.

[136] R García and A San Paulo. Dynamics of a vibrating tip near or in intermittent contact with a surface. *Physical Review B*, 61(20):381–384, 2000.

[137] R García and A San Paulo. Attractive and repulsive tip-sample regimes in tapping-mode atomic force microscopy. *Physical Review B*, 60(7):4961–4967, 1999.

[138] R R Rodríguez and R García. Tip motion in amplitude modulation (tapping-mode) atomic-force microscopy: comparison between continuous and point-mass models. *Applied Physics Letters*, 80(9):1646–161648, 2002.

[139] A San Paulo and R García. Tip-surface forces, amplitude and energy dissipation in amplitude modulation (tapping-mode) force microscopy. *Physical Review B*, 64(19):193411, 2001.

[140] H Hölscher, D Ebeling, and U D Schwarz. Theory of q-controlled dynamic force microscopy in air. *Journal of Applied Physics*, 99(8):084311, 2006.

[141] S I Lee, S W Howell, A Raman, and R Reifenberger. Nonlinear dynamics of microcantilevers in tapping mode atomic force microscopy: a comparison between theory and experiment. *Physical Review B*, 66(11):115409, 2002.

[142] S I Lee, S W Howell, A Raman, and R Reifenberger. Nonlinear dynamic perspectives on dynamic force microscopy. *Ultramicroscopy*, 97:185–198, 2003.

[143] S D Solares, Y Matsuda, and W A Goddard. Influence of the carbon nanotube probe tip's angle on the effective probe stiffness and image quality in tapping-

mode atomic force microscopy. *Journal of Physical Chemistry B*, 109:16658–16664, 2005.

[144] S S Solares Rivera. *Multi-scale simulations of single-walled carbon nanotube atomic force microscopy and density functional theory characterization of functionalized and non-functionalized silicon surfaces*. PhD thesis, California Institute of Technology, 2006.

[145] S D Solares, M J Esplandiu, W A Goddard, and C P Collier. Mechanism of single-walled carbon naotube probe-sample multistability in tapping mode AFM imaging. *Journal of Physical Chemistry B*, 109:11493–11500, 2005.

[146] S D Solares. Frequency and force moduilation atomic force microscopy: low-impact tapping-mode imaging without bistabilty. *Measurement Science and Technology*, 18:L9–L14, 2007.

[147] S D Solares. Eliminating bistability and reducing sample damage through frequency and amplitude modulation in tapping-mode atomic force microscopy. *Measurement Science and Technology*, 18:592–600, 2007.

[148] N F Martínez and R García. Measuring phase shifts and energy dissipation with amplitude modulation atomic force microscopy. *Nanotechnology*, 17:S167–S172, 2006.

[149] J Tamayo and R García. Relationship betwen phase shift and energy dissipation in tapping-mode scanning force microscopy. *Applied Physics Letters*, 73(20):2926–2928, 1998.

[150] J Tamayo and R García. Deformation, contact time and phase contrast in tapping mode atomic force microscopy. *Langmuir*, 12:4430–4435, 1996.

[151] X Chen, C J Robert, J Zhang, M C Davies, and S J B Tendler. Phase contrast and attractive-repulsion transition in tapping mode atomic force microscopy. *Surface Sciences*, 519:L593–L598, 2002.

[152] R Garcia, C J Gómez, N F Martinez, S Patil, and C Dietz ad R Magerle. Identification of nanoscale dissipation processes by dynamic atomic force microscopy. *Physical Review Letters*, 97(1):016103, 2006.

[153] M Balantekin and A Atalar. Power dissipation analysis in tapping-mode atomic force microscopy. *Physical Review B*, 67(19):193404, 2003.

[154] V V Protasenko, M Labardi, and A Gallagher. Conservative and dissipative forces measured by self-oscillator atomic force microscopy at constant-drive amplitude. *Physical Review B*, 70(24):245414, 2004.

[155] H Hölscher. Theory of phase-modulation atomic force microscopy with constant-oscillation amplitude. *Journal of Applied Physics*, 103:064317, 2008.

[156] R García, R Magerle, and R Perez. Nanoscale compositional mapping with gentle forces. *Nature Materials*, 6:405–411, 2007.

[157] A Schirmeisen, H Hölscher, B Anczykowski, D Weiner, M M Schäfer, and H Fuchs. Dynamic force microscopy using the constant-excitation and constant-amplitude modes. *Nanotechnology*, 16:S13–S17, 2005.

[158] S Rast, U Gysin, P Ruff, C Gerber, E Meyer, and D W Lee. Force microscopy experiments with ultrasensitive cantilevers. *Nanotechnology*, 17:S189–S194, 2006.

[159] B Gotsmann and H Fuchs. Dynamic force spectroscopy of conservative and dissipative forces in an Al-Au(111) tip-sample system. *Physical Review Letters*, 86(12):2597–2600, 2001.

[160] J B Thompson, H G Hansma, P K Hansma, and K W Plaxco. The backbone conformational entropy of protein folding: experimental measures from atomic force microscopy. *Journal of Molecular Biology*, 322:645–652, 2002.

[161] A Irbäck, S Mitternacht, and S Mohanty. Dissecting the mechanical unfolding of ubiquitin. *PNAS*, 102(38):13427–13432, 2005.

[162] G Hummer and A Szabo. Free energy reconstruction from nonequilibrium single-molecule pulling experiments. *PNAS*, 98(7):3658–3661, 2001.

[163] P E Marszalek, H Lu, H Li, M Carrio-Vazquez, A F Oberhauser, K Schulten, and J M Fernandez. Mechanical unfolding intermediates in titin molecules. *Nature*, 402:100–103, 1999.

[164] A F Oberhauser, P E Marszalek, M Carrio-Vazquez, and J M Fernandez. Single protein misfolding events captured by atomic force microscopy. *Nature Structural Biology*, 6(11):1025–1028, 1999.

[165] M Rief, M Gautel, F Oesterhelt, J M Fernandez, and H E Gaub. Reversible unfolding of individual titin immunoglobulin domains by AFM. *Science*, 276:1109–1116, 1997.

[166] C Danilowicz, V W Cojee, C Bouzigues, D K Lubensky, D R Nelson, and M Prentiss. DNA unzipped under a constant force exhibits multiple metastable intermediates. *PNAS*, 100(22):1694–1699, 2003.

[167] C A Bippes, A D L Humphris, M Stark, D J Müller, and H Janovjak. Direct measurement of single-molecule visco-elasticity in atomic force microscope force-extension experiments. *European Biophysical Journal*, 35:287–292, 2006.

[168] H Janovjak, D J Muller, and A D L Humphrus. Molecular force modulation spectroscopy revealing the dynamic response of single bacteriorhodopsins. *Biophysical Journal*, 88:1423–1431, 2005.

[169] C Hyeon and D Thirumalai. Can energy landscape roughness of proteins and RNA be measured by using mechanical unfolding experiments? *PNAS*, 100(18):10249–10253, 2003.

[170] G Bussi, A Laio, and M Parrinello. Equilibrium free energies from nonequilibrium metadynamics. *Physical Review Letters*, 96(9):090601, 2006.

[171] C Jarzynski. Nonequilibrium equality for free energy differences. *Physical Review Letters*, 78(14):2690–2693, 1997.

[172] A B Adib. Free energy surfaces from nonequilibrium proceses without work measurement. *Journal of Chemical Physics*, 124(14):144111, 2006.

[173] J Tamayo, A D L Humphris, R J Owen, and M J Miles. High-q dynamic force microscopy in liquid and its application to living cells. *Biophysical Journal*, 81:526–537, 2001.

[174] Janos Kokavecz, Zoltan L. Horvath, and Adam Mechler. Dynamical properties of the q-controlled atomic force microscope. *Applied Physics Letters*, 85(15):3232–3234, 2004.

[175] J Tamayo, A D L Humphris, and M J Miles. Piconewton regime dynamic force microscopy in liquid. *Applied Physics Letters*, 77(4):582–584, 2000.

[176] J Tamayo, M Alvarez, and L M Lechuga. Digital tuning of the quality factor of micromechanical resonant biological detectors. *Sensors and Actuators B*, 89:33–39, 2003.

[177] Tomas R. Rodriguez and Ricardo Garcia. Theory of q control in atomic force microscopy. *Applied Physics Letters*, 82(26):4821–4823, 2003.

[178] U Durig. Interaction sensing in dynamic force microscopy. *New Journal of Physics*, 2:5, 2000.

[179] O Sahin, C F Quate, O Solgaard, and A Atalar. Resonant harmonic response in tapping-mode atomic force microscopy. *Physical Review B*, 69(16):165416, 2004.

[180] M A Lantz, H J Hug, R Hoffmann, P J A van Schendel, P Kappenberger, S Martin, A Baratoff, and H-J Güntherodt. Quantitative measurement of short-range chemical bonding forces. *Science*, 291(5513):2580–2583, 2001.

[181] R R Rodríguez and R García. Compositional mapping of surfaces in atomic force microscopy by excitation of the second normal mode of the microcantilever. *Applied Physics Letters*, 84(3):449–453, 2004.

[182] R Hillenbrand, M Stark, and R Guckenberger. Higher-harmonics generation in tapping-mode atomic force microscopy: insights into the tip-sample interaction. *Applied Physics Letters*, 76(23):3478–3480, 2000.

[183] R W Stark and W M Heckl. Higher harmonics imaging in tapping-mode atomic-force microscopy. *Review of Scientific Instruments*, 74(12):5111–5114, 2003.

[184] R W Stark. Spectroscopy of higher harmonics in dynamic atomic force microscopy. *Nanotechnology*, 15:347–351, 2004.

[185] G Chawla and S D Solares. Single-catilever dual-frequency modulation atomic force microscopy. *Measurement Science and Technology*, 20:015501, 2009.

[186] D Frenkel and B Smit. *Understanding Molecular Simulation*, pages 69–71. Academic Press; San Diego, CA, 2002.

[187] J. P. Cleveland, B. Anczykowski, A. E. Schmid, and V. B. Elings. Energy dissipation in tapping-mode atomic force microscopy. *Applied Physics Letters*, 72(20):2613–2615, 1998.

[188] I Shapiro and C P Collier. Single molecule fluorescence observation and analysis. *ACS Journal of Chemical Education*, page Manuscript in review, 2009.

[189] J W Lichtman and J-A Conchello. Fluorescence microscopy. *Nature Methods*, 2(12):910–922, 2005.

[190] D J Stephens and V J Allen. Light microscopy techniques for live cell imaging. *Science*, 300:82–85, 2003.

[191] M Böhmer and J Enderlein. Fluorescence microscopy of single molecules under ambient conditions: methodology and technology. *ChemPhysChem*, 4:792–808, 2003.

[192] W P Ambrose, P M Goodwin, J H Jett, A Van Orden, J H Werner, and R A Keller. Single molecule fluorescence spectroscopy at ambient temperature. *Chemical Reviews*, 99:2929–2956, 1999.

[193] X S Xie. Single-molecule spectroscopy and dynamics at room temperature. *Accounts of Chemical Research*, 29:598–606, 1996.

[194] X S Xie and J K Trautman. Optical studies of single molecules at room temperature. *Annual Review of Physical Chemistry*, 49:441–480, 1998.

[195] S Weiss. Fluorescence spectroscopy of single biomolecules. *Science*, 283:1676–1683, 1999.

[196] I Riven, E Kalmanzon, L Segev, and E Reuveny. Conformational rearrangements associated with the gating of the G protein-coupled potassium channel revealed by FRET microscopy. *Nuron*, 38:225–235, 2003.

[197] J K Jaiswal and S M Simon. Imaging single events at the cell membrane. *Nature Chemical Biology*, 3(2):92–98, 2007.

[198] E Chung, D Kim, and P T C So. Extended resolution wide-field optical imaging: objective-launched standing-wave total internal reflection fluorescence microscopy. *Optics Letters*, 31(7):945–947, 2006.

[199] D Axelrod. Total internal reflection fluorescence microscopy in cell biology. *Traffic*, 2:764–774, 2001.

[200] W P Ambrose, P M Goodwin, and J P Nolan. Single-molecule detection with total internal reflection excitation: comparing signal-to-background and total signals in different geometries. *Cytometry*, 36:224–231, 1999.

[201] G I Mashanov, D Tacon, A E Knight, M Peckham, and J E Molloy. Visualizing single molecules inside living cells using total internal reflection fluorescence microscopy. *Methods*, 29:142–152, 2003.

[202] A Tokunaga, K Kitamura, K Saito, A Hikikoshi, and T Yanagida. Single molecule imaging of fluorophores and enzymatic reactions achieved by

objective-type total internal reflection fluorescence microscopy. *Biochemical and Biophysical Research Communicatoins*, 235:47–53, 1997.

[203] M Ueda, Y Sako, T Tanaka, P Devreotes, and Y Yanagida. Single-molecule analysis of chemotactic signaling in *Dictyostelium* cells. *Science*, 294:865–867, 2001.

[204] D Toomre and D J Manstein. Lighting up the cell surface with evanescent wave microscopy. *Trends in Cell Biology*, 1:298–303, 2001.

[205] T Ruckstuhl and S Seeger. Attoliter detection volumes by confocal total-internal-reflection fluorescence micrscopy. *Optics Letters*, 29(6):569–571, 2004.

[206] W Tan and E S Yeung. Monitoring the reactions of single enzyme molecules and single metal ions. *Analytical Chemistry*, 69:4242–4248, 1997.

[207] Y M Wang, J O Tegenfeldt, W Riehn, X-J Guan, L Guo, I Golding, E C Cox, J Sturm, and R H Austin. Single-molecule studies of repressor-DNA interactions show long-range interactions. *PNAS*, 102(28):9796–9801, 2005.

[208] A Granéli, C C Yeykal, R B Robertson, and E C Greene. Long-distance lateral diffusion of human rad51 on double-stranded DNA. *PNAS*, 103(5):1221–1226, 2006.

[209] G Yao, X Fang, H Yokota, T Yanagida, and W Tan. Monitoring molecular beacon DNA probe hybridization at the single-molecule level. *Chemistry - A European Journal*, 9:5686–5692, 2003.

[210] F Codazzi, M N Teurel, and T Meyer. Control of astrocyte Ca^{2+} oscillations and waves by oscillating translocation and activation of protein kinase C. *Current Biology*, 11(14):1089–1098, 2001.

[211] C Bustamante, J C Macosko, and G J L Wuite. Grabbing the cat by the tail: manipulating molecules one by one. *Nature Reviews Molecular Cell Biology*, 1:131–136, 2000.

[212] K Miyakawa, H Adachi, and Y Inoue. Rotation of two-dimensional arrays of microparticles trapped by circularly polarized light. *Applied Physics Letters*, 84(26):5440–5442, 2004.

[213] D G Grier. A revolution in optical manipulation. *Nature*, 424:21–2, 2006.

[214] G Sinclair, P Jordan, J Leach, M J Padgett, and J Cooper. Defining the trapping limits of holographic optical tweezers. *Journal of Modern Optics*, 51(3):409–414, 2004.

[215] K Dholakia, P Reece, and M Gu. Optical micromanipulation. *Chemical Society Reviews*, 37:42–55, 2008.

[216] Y Roichman and D G Grier. Holographic assembly of quasicrystalline photonic heterostructures. *Optics Express*, 13(14):5434–5439, 2005.

[217] J E Curtis, B A Koss, and D G Grier. Dynamic holographic optical tweezers. *Optics Communications*, 207:169–175, 2002.

[218] H Li, D Zhou, H Browne, and D Klenerman. Evidence for resonance optical trapping of individual fluorophore-labeled antibodies using single molecule fluorescence spectroscopy. *JACS*, 128:5711–5717, 2006.

[219] T Ha, T Enderle, D F Ogletree, D S Chemla, P R Selvan, and S Weiss. Probing the interaction between two single molecules: fluorescence resonance energy transfer between a single donor and a single receptor. *PNAS*, 93:6264–6268, 1996.

[220] A Lewis, H Taha, A Strinkovski, A Manevitch, A Khatchouriants, R Dekher, and E Amman. Near-field optics: from subwavelength illumination to nanometric shadowing. *Nature Biotechnology*, 21(1):1378–1386, 2003.

[221] K Kneipp, Y Wang, H Kneipp, L T Perelman, I Itzkan, R R Dasari, and M S Feld. Single molecule detection using surface-enhanced raman scattering (SERS). *Physical Review Letters*, 78(9):1667–1670, 1997.

[222] S Nie and S R Emory. Probing single molecules and single nanoparticles by surface-enhanced raman scattering. *Science*, 275(5303):1102–1106, 1997.

[223] A Campion and P Kambhampati. Surface-enhanced raman scattering. *Chemical Society Reviews*, 27:241–250, 1998.

[224] A M Armani, R P Kulkarni, S E Fraser, R C Flagan, and K J Vahala. Label-free single-molecule detection with optical microcavities. *Science*, 317:783–786, 2008.

[225] M Kyoung, K Karunwi, and E D Sheets. A versatile multimode microscope to probe and manipulate nanoparticles and biomolecules. *Journal of Microscopy*, 225(2):137–146, 2007.

[226] M J Lang, P M Fordyce, and S M Block. Combined optical trapping and single-molecule fluorescence. *Journal of Biology*, 2(1):6, 2003.

[227] Y Sasuga, T Tani, M Hayashi, H Yamakawa, O Ohara, and Y Harada. Development of a microscopic platform for real-time monitoring of biomolecular interactions. *Genome Research*, 16:132–139, 2009.

[228] M A van Dijk, L C Kapiteln, J van Mameren, C F Schmidt, and E J G Peterman. Combining optical trapping and single-molecule fluorescence spectroscopy: enhanced photobleaching of fluorophores. *Journal of Physical Chemistry B*, 108:6479–6484, 2004.

[229] N G Walter, C-Y Huang, A J Manzo, and M A Sobhy. Do-it-yourself guide: how to use the modern single-molecule toolbox. *Nature Methods*, 5(6):475–489, 2008.

[230] A A Deniz, S Mukhopadhyay, and E A Lemke. Single molecule biophysics: at the interface of biology, physics and chemistry. *Journal of the Royal Society Interface*, 5:15–45, 2008.

[231] K C Neumann and A Nagy. Single-molecule force spectroscopy: optical tweezers, magnetic tweezers and atomic force microscopy. *Nature Methods*, 5(6):491–505, 2008.

[232] X R Bai., HJ Lee, and S R Quake. Behavior of complex knots in single DNA molecules. *Physical Review Letters*, 91(26):265506, 2003.

[233] H P Lu, L Xun, and X S Xie. Single-molecule enzymatic dynamics. *Science*, 282:1877–1882, 1998.

[234] R Verberk and M Orrit. Photon statistics in the fluorescence of single molecules and nanocrystals: correlation functions versus distributions of on- and off-times. *Journal of chemical physics*, 119(4):2214–2222, 2003.

[235] S Schuler, T Speck, C Teitz, J Wrachtrup, and U Seifert. Experimental test of the fluctuation theorem for a driven two-level system with time-dependent rates. *Physical Review Letters*, 94:180602, 2005.

[236] C Teitz, S Schuler, T Speck, U Seifert, and J Wrachtrup. Measurement of stochastic entropy production. *Physical Review Letters*, 97(5):050602, 2006.

[237] R D Smiley and G G Hammes. Single molecule studies of enzyme mechanisms. *Chemical Reviews*, 106(8):3080–3094, 2006.

[238] A Ishijima and T Yanagida. Single molecule nanobioscience. *Trends in biochemical sciences*, 26(7):438–444, 2001.

[239] S Weiss. Measuring conformation dynamics of biomolecules by single molecule fluorescence spectroscopy. *Nature Structural Biology*, 7(9):724–729, 2000.

[240] X S Xie. Single-molecule approach to enzymology. *Single Molecules*, 2(4):229–236, 2001.

[241] Y Ishii, A Ishijima, and T Yanagida. Single molecule nanomanipulation of biomolecules. *Trends in Biotechnology*, 19(6):211–216, 2001.

[242] K C Neuman, T Lionet, and J-F Allemand. Single-molecule micromanipulation techniques. *Annual Reviews in Materials Research*, 37:33–67, 2007.

[243] R D Smiley, T R L Collins, G G Hammes, and T-S Hsieh. Single-molecule measurements of the opening and closing of the DNA gate by eukaryotic topoisomerase ii. *PNAS*, 104(12):4840–4845, 2007.

[244] T-H Lee, L J Lapidus, W Zhao, K J Travers, D Herschlag, and S Chu. Measuring the folding transition time of single RNA molecules. *Biophysical Journal*, 92:3275–3283, 2007.

[245] X Zhuang, L E Bartley, H P Bbcock, R Russell, T Ha, D Herschlag, and S Chu. A single-molecule study of RNA catalysis and folding. *Science*, 288:2048–2051, 2000.

[246] C Joo, S A McKinney, M Nakamura, I Rasnik, S Myong, and T Ha. Real-time observation of RecA filament dynamics with single monomer resolution. *Cell*, 126:515–527, 2006.

[247] S Myong, I Rasnik, C Joo, T M Lohman, and T Ha. Repetitive shutting of a motor protein on DNA. *Nature*, 437:1321–1325, 2005.

[248] I Rasnik, S Myong, W Cheng, T M Lohman, and T Ha. DNA-binding orientation and domain conformation of the *E coli* rep helicase monomer bound to a partial duplex junction: single molecule studies of fluorescently labeled enzymes. *JMB*, 336:395–408, 2004.

[249] Y Harada, T Funatsu, K Murakami, Y Nonoyama, A Ishiihama, and T Yanagida. Single-molecule imaging of RNA polymerase-DNA interactions in real time. *Biophysical journal*, 76:709–715, 1999.

[250] A Coban, D C Lamb, E Zaychikov, H Heumann, and G U Nienhaus. Conformational heterogeneity in RNA polymerase oberved by single-pair FRET microscopy. *Biophysical Journal*, 90:4605–4617, 2006.

[251] D Nettels, I V Gopich, A Hoffmann, and B Schuler. Ultrafast dynamics of protein collapse from single-molecule photon statistics. *PNAS*, 104(8):2655–2660, 2007.

[252] B Schuler, E A Lipman, and W A Eaton. Probing the free-energy surface for protein folding with single-molecule fluorescence spectroscopy. *Nature*, 419:743–744, 2002.

[253] E Haas. The study of protein folding and dynamics by determination of intramolecular distance distributions and their fluctuations using ensemble and single-molecule FRET measurements. *ChemPhysChem*, 6:858–870, 2005.

[254] C Buranachai, S A McKinney, and T Ha. Single molecule nanometronome. *Nano Letters*, 6(3):496–500, 2006.

[255] S Hoihng, C Joo, and T Ha. Single-molecule three-color FRET. *Biophysical Journal*, 87:1328–1337, 2004.

[256] S Hohng, T J Wilson, E Tan, R M Clegg, D M J Lilley, and T Ha. Conformational flexibility of four-way junctions in RNA. *JMB*, 336:69–79, 2004.

[257] M K Nahas, T J Wilson, S Hohng, K Jarvie, D M J Lilley, and T Ha. Observation of internal cleavage and ligation reactions of a ribozyme. *Nature Structural & Molecular Biology*, 11(11):1107–1113, 2004.

[258] G Borinsky, D Rueda, V K Misra, M M Rhodes, A Gordus, H P Babcock, N G Walter, and X Zhuang. Single-molecule transition-state analysis of RNA folding. *PNAS*, 101(2):534–539, 2003.

[259] Z Xie, N Srividya, T R Sosnick, T Pan, and N F Scherer. Single-molecule studies highlight conformational heterogeneity in the early folding steps of a large ribozyme. *PNAS*, 101(2):534–539, 2004.

[260] A Weninger, M E Bowen, S Chu, and A T Brunger. Single-molecule studies of snare complex assembly reveal parallel and antiparallel configurations. *PNAS*, 100(25):14800–14805, 2003.

[261] S Steigmiller, B Zimmermann, M Diez, M Börsch, and P Gräber. Binding of single nucleotides to h^+-ATP synthases observed by fluorescence resonance energy transfer. *Bioelectrochemistry*, 63:79–85, 2004.

[262] M Diez, B Zimmermann, M Börsch, M König, E Schweinberger, S Steigmiller, R Reuter, S Felekyan, V Kudryavtsev, C A M Seidel, and P Gräber. Protin-powered subunit rotation in single membrane-bound F_0F_1-ATP synthase. *Nature Structural & Molecular Biology*, 11(2):135–141, 2004.

[263] T Ha, X Zhuang, H D Kim, J W Orr, J R Williamson, and S Chu. Ligand-induced conformational changes observed in single RNA molecules. *PNAS*, 96:9077–9082, 1999.

[264] Y Zhang, S Sivasankar, W J Nelson, and S Chu. Resolving cadhering interactions and binding cooperativity at the single molecule level. *PNAS*, 106(1):109–114, 2009.

[265] T A Laurence, X Kong, M Jäger, and S Weiss. Probing structural heterogeneities and fluctuations of nucleic acids and denatured proteins. *PNAS*, 102(48):17348–17353, 2005.

[266] S L Williams, L K Parkhurst, and L J Parkhurst. Changes in DNA bending and flexing due to tethered cations detected by fluorescence resonance energy transfer. *Nucleic Acids Research*, 34(3):1028–1035, 2006.

[267] J R Grunwell, J L Glass, T D Lacoste, A A Deniz, D S Chemla, and P G Schultz. Monitoring the conformational fluctuations of DNA hairpins using single-pair fluorescence resonance energy transfer. *JACS*, 123:4295–4303, 2001.

[268] H D Kim, G U Nienhaus, T Ha, J W Orr, J R Williamson, and S Chu. Mg^{2+}-dependent conformational change of RNA studied by fluorescence correlation and FRET on immobilized single molecules. *PNAS*, 99(7):4284–4289, 2002.

[269] T Ha. Structural dynamics and processing of nucleic acids revealed by single molecule spectroscopy. *Biochemistry*, 43(14):4055–4063, 2004.

[270] M C Murphy, I Rasnik, W Cheng, T M Lohman, and T Ha. Probing single-stranded DNA conformational flexibility using fluorescence spectroscopy. *Biophysical Journal*, 86:2530–2537, 2004.

[271] X Qu nd G J Smith, K T Lee, T R Sosnick, T Pan, and N F Scherer. Single-molecule nonequilibrium periodic Mg^{2+}-concentration jump experiments reveal details of the early folding pathways of a large RNA. *PNAS*, 105(18):6602–6607, 2008.

[272] I J Finkelstein and E C Greene. Single molecule studies of homologous recombination. *Molecular Biosystems*, 4:1094–1104, 2008.

[273] E Nir, X Michalet, K M Hamadani, T A Laurence, D Neuhausser, Y Kovchegov, and S Weiss. Shot-noise limited single-moleculr FRET histograms: comparison between theory and experiments. *JACS*, 110(44):22103–22124, 2006.

[274] A J Berglund, K McHale, and H Mabuchi. Feedback localization of freely-diffusing fluorescent particles ear the optical shot-noise limit. *Optics Letters*, 32(2):145–147, 2007.

[275] G S Chirikjian and A B Kyatkin. *Engineering applications of noncommutative harmonic analysis: with emphasis on rotation and motion groups*, pages 98–100. CRC Press, 2000.

[276] M Born and E Wolf. *Principles of Optics*. Cambridge University Press, 1999.

[277] R H Webb. Confocal optical microscopy. *Reports on Progress in Physics*, 59:427471, 1996.

[278] E Collett. *Field Guide to Polarization*. SPIE Press, 2005.

[279] T Colomb, E Cuche, F Montfort, P Marquet, and Ch Depursinge. Jones vector imaging by use of digital holography: simulation and experiment. *Optics Communications*, 231:137–147, 2004.

[280] P M Mejías M Martínez-Herrero and G Piquero. Overall parameters for the characterization of non-uniformly totally polarized beams. *Optics Communications*, 265:6–10, 2006.

[281] M Hashimoto, K Yamada, and T Araki. Proposition of single molecular orientation determination using polarization controlled beam by liquid crystal spatial light modulators. *Optical Review*, 12(1):37–41, 2005.

[282] R Dändliker, P Tortora, L Vaccaro, and A Nesci. Measuring the three-dimensional polarization with scanning optical probes. *Journal of Optics A: Pure and Applied Optics*, 6:S18–S23, 2004.

[283] N Bokor, Y Iketaki, T Watanabe, and M Fujii. Investigation of polarization effects for high-numerical-aperture first-order laguerre-gaussian beams by 2D scanning with a single fluorescence microbead. *Optics Express*, 13(26):10440–10448, 2005.

[284] N Lindlein, S Quabis, U Peschel, and G Leuchs. High numerical aperture imaging with different polarization patterns. *Optics Express*, 15(9):5827–5842, 2007.

[285] Y Luo and B Lü. Phase singularities of high numerical aperture radially and azimuthally polarized beams in the focal region. *Journal of Optics A: Pure and Applied Optics*, 11:015707, 2009.

[286] V V Koltyar, A A Kovalev, and S S Stafeev. Sharp focus area of radially-polarized gaussian beam propagation through an axicon. *Progress in Electromagnetics Research C*, 5:35–43, 2008.

[287] R Dorn, S Quabis, and G Leuchs. Sharper focus for a radially polarized light beam. *Physical Review Letters*, 91(23):233901, 2003.

[288] K Lindfors, A Priimagi, T Setälä, A Shevchenko, A R Friberg, and M Kaivola. Local polarization of tightly focused unpolarized light. *Nature Photonics*, 1:228–231, 2007.

[289] C Y Lu and D A Vanden Bout. Analysis of orientational dynamics of single fluorophore trajectories from three-angle polarization experiments. *The journal of chemical physics*, 128(24):244501, 2008.

[290] Z Petrášek and P Schwille. Fluctuations as a source of information in fluorescence microscopy. *Journal of the Royal Society Interface*, 6:s15–s25, 2009.

[291] C Bustamante, J Liphardt, and F Ritort. The nonequilibrium thermodynamics of small systems. *arXiv:cond-mat*, 0511629(v1), 2005.

[292] H Qian and D A Beard. Thermodynamics of stoichiometric biochemical networks in living systems far from equilibrium. *Biophysical Chemistry*, 114(2-3):213–20, 2005.

[293] E H Trepagnier, C Jarzynski, F Ritort, G E Crooks, C J Bustamante, and J Liphardt. Experimental test of Hatano and Sasa's nonequilibrum steady-state inequality. *PNAS*, 101(42):15038–15041, 2004.

[294] J Kurchan. Non-equilibrium work relations. *Journal of Statistical Mechanics*, page P07005, 2007.

[295] Y Oono and M Paniconi. Steady state thermodynamics. *Progress of Theoretical Physics Supplement*, 130:29–44, 1998.

[296] C Maes and M H van Wieren. Time-symmetric fluctuations in nonequilibrium systems. *Physical Review Letters*, 96(24):240601, 2006.

[297] F Ritort. Single molecule experiments in biophysics: exploring the thermal behavior of nonequilibrium small systems. *arXiv:cond-mat*, 0509606(v1), 2005.

[298] G E Crooks. Path-ensemble averages in systems driven far from equilibrium. *Physical Review E*, 61(3):2361–2366, 2000.

[299] D Andrieux, P Gaspard, S Ciliberto, N Garnier, S Joubaud, and A Petrosyan. Entropy production and time asymmetry in nonequilibrium fluctuations. *Physical Review Letters*, 98(7):150601, 2007.

[300] R M L Evans. Detailed balance has a counterpart in non-equilibrium steady states. *Journal of Physics A: Mathematical and General*, 38:293–313, 2005.

[301] H Qian and M Qian. Pumped biochemical reactions, nonequilibrium circulation, and stochastic resonance. *Physical Review Letters*, 84(10):2271–2274, 2000.

[302] J Widengren, U Mets, and R Rigler. Fluorescence correlation spectroscopy of triplet states in solution: a theoretical and experimental study. *J. Phys. Chem.*, 99:13368–13379, 1995.

[303] E Haustein and P Schwille. Ultrasensitive investigations of biological systems by fluorescence correlation spectroscopy. *Methods*, 29:153–166, 2003.

[304] M Lippitz, F Kulzer, and M Orrit. Statistical evaluation of single nano-object fluorescence. *ChemPhysChem*, 6:770–789, 2005.

[305] J A Rochira, M V Gudheti, T J Gould, R R Laughlin, J L Nadeau, and S T Hess. Fluorescence intermittency limits brightness in CdSe/ZnS nanoparticles quantification by fluorescence correlation spectroscopy. *Journal of Physical Chemistry C*, 111:1695–1708, 2007.

[306] R F Heuff, D T Cramb, and M Marrocco. Fluorescence correlation spectroscopy for diffusion of mobile quantum dots in dilute solutions. *Chemical Physics Letters*, 454(4-6):257–261, 2008.

[307] S Doose, J M Tsay, F Pinaud, and S Weiss. Comparison of photophysical and colloidal properties of biocompatible semiconductor nanocrystals using fluorescence correlation spectroscopy. *Analytical Chemistry*, 77:2235–2242, 2005.

[308] D R Larson, W R Zipfel, R M Williams, S W Clark, M P Bruchez, F W Wise, and W W Webb. Water-soluble quantum dots for multiphoton fluorescence imaging in vivo. *Science*, 300:1434–1436, 2003.

[309] Y Li, H Qian, and Y Yi. Oscillations and multiscale dynamics in a closed chemical reation system: second law of thermodynamics and temporal complexity. *Journal of Chemical Physics*, 129(15):154505, 2008.

[310] R D Astumian. Thermodynamics and kinetics of a brownian motor. *Science*, 276:917–922, 1997.

[311] H Qian and E L Elson. Fluorescence correlation spectroscopy with higher-order and dual-color correlation to probe nonequilibrium steady states. *PNAS*, 101(9):2828–2833, 2004.

[312] H Qian, S Saffarian, and E L Elson. Concentration fluctuations in a mesoscopic oscillator chemical reaction system. *PNAS*, 99(16):10376–10381, 2002.

[313] M Samoilov, S Plyasunov, and A P Arkin. Stochastic amplificatoin and signaling in enzymatic futile cycles through noise-induced bistability with oscillations. *PNAS*, 102(7):2310–2315, 2005.

[314] T Schmeidl and U Seifert. Stochastic thermodynamics of chemical reaction networks. *The Journal of Chemical Physics*, 126(4):044101, 2007.

[315] D Longo and J Hasty. Dynamics of single-cell gene expression. *Molecular Systems Biology*, 64:1–10, 2006.

[316] M B Elowitz, A J Levine, E D Sigga, and P S Swain. Stochastic gene expression in a single cell. *Science*, 297:1183–1186, 2001.

[317] J S van Zon, M J Morelli, S Tănase-Nicola, and P R ten Wolde. Diffusion of transcription factors can drastically enhance the noise in gene expression. *Biophys. J.*, 91:4350–4362, 2006.

[318] J Yu, J Xiao, X Ren, K Lao, and X S Xie. Probing gene expression in live cells, one protein molecule at a time. *Science*, 311:1600–1603, 2006.

[319] P S Swain, M B Elowitz, and E D Siggia. Intrinsic and extrinsic contributions to stochasticity in gene expression. *PNAS*, 99(20):12795–12800, 2002.

[320] C C Guet, M B Elowitz, W Hsing, and S Leibler. Combinatorial synthesis of genetic networks. *Science*, 296(5572):1466–1470, 2002.

[321] C V Rao, D M Wolf, and A P Arkin. Control, exploitation and tolerance of intracellular noise. *Nature*, 420:231–237, 2002.

[322] M B Elowitz and S Leibler. A synthetic oscillatory network of transcriptional regulators. *Nature*, 403:335–338, 2000.

[323] G Altan-Bonnet, A Libchaber, and O Krichevsky. Bubble dynamics in double-stranded DNA. *Physical Review Letters*, 90(13):138101, 2003.

[324] G Tkačik, T Gregor, and W Bialek. The role of input noise in transcriptional regulation. *PLoS ONE*, 3(7):e2774, 2008.

[325] H H McAdams and A Arkin. Stochastic mechanisms in gene expression. *PNAS*, 94(3):814–819, 1997.

[326] J Paulsson. Summing up the noise in gene networks. *Nature*, 427:415–418, 2004.

[327] S Rosenfeld. Origins of stochasticity and burstiness in high-dimensional biochemical networks. *EURASIP Journal on Bioinformatics and Systems Biology*, page 362309, 2009.

[328] J R Chabot, J M Pedraza, P Luitel, and A van Oudenaarden. Stochastic gene expression out-of-steady-state in the cyanobacterial circadian clock. *Nature*, 450:1249–1252, 2007.

[329] A Bar-Even, J Paulsson, N Maheshri, M Carmi, E O'Shea, Y Pilpel, and N Barkai. Noise in protein expression scales with natural protein abundance. *Nature Genetics*, 38(6):636–643, 2006.

[330] A Becskei, B B Kaufmann, and A van Odenaarden. Contributions of low molecule number and chromosomal positioning to stochastic gene expression. *Nature Genetics*, 37:937–944, 2005.

[331] J M Raser and E K O'Shea. Control of stochasticity in eukaryotic gene expression. *Science*, 304:1811–1814, 2004.

[332] J R Chubb, T Trcek, S M Shenoy, and R H Singer. Transcriptional pulsing of a developmental gene. *Current Biology*, 16:1018–1025, 2006.

[333] A Raj, C S Peksin, D Tranchina, D Y Vargas, and S Tyagi. Stochastic mRNA synthesis in mammalian cells. *PLoS Biology*, 4(10):1707–1719, 2006.

[334] I Golding, J Paulsson, S M Zawilski, and E C Cox. Real-time kinetics of gene activity in individual bacteria. *Cell*, 123:1025–1035, 2005.

[335] D Bratsun, D Volfson, L S Tsimring, and J Haty. Delay-induced stochastic oscillations in gene regulation. *PNAS*, 102(41):14593–14598, 2005.

[336] M O Vlad, F Moran, F M Schneider, and J Ross. Memory effects and oscillations in single-molecule kinetics. *PNAS*, 99(20):12548–12555, 2002.

[337] D Bray. Bacterial chemotaxis and the question of gain. *PNAS*, 99(1):7–9, 2002.

[338] C Suguna and S Sinha. Cellular dyamics in noisy environment. *Fluctuation and Noise Letters*, 2(4):L313–L326, 2002.

[339] F Ritort, C Bustamante, and I Tinoco Jr. A two-state kinetic model for the unfolding of single molecules by mechanical force. *PNAS*, 99(21):13544–13548, 2002.

[340] C Danilowicz, Y Kafri, R S Control, V W Coljee, J weeks, and M Prentiss. Measurement of the phase diagram of DNA unzipping in the temperature-force plane. *Physical Review Letters*, 93(7):078101, 2004.

[341] C P Calderon, W-H Chen, K-J Lin, N C Harris, and C-H Kiang. Quantifying DNA melting transitions using single-molecule force spectroscopy. *Journal of Physics: Condensed Matter*, 21:034114, 2009.

[342] O K Dudko, G Hummer, and A Szabo. Intrinsic rates and activation free energies from single-molecule pulling experiments. *Physical Review Letters*, 96(10):108101, 2006.

[343] G Hummer and A Szabo. Free energy surfaces from single-molecule force spectroscopy. *Accounts of Chemical Research*, 38:504–513, 2005.

[344] S Kirmizialtin, L Huang, and D E Makarov. Topography of he free-energy landscape probed via mechanical unfolding of proteins. *Journal of Chemical Physics*, 122(23):234915, 2005.

[345] G M Wang, E M Sevick, E Mittag, D J Searles, and D J Evans. Experimental demonstration of violations of the second law of thermodynamics for small systems and short time scales. *Physical Review Letters*, 89(5):050601, 2002.

[346] D M Carberry, J C Reid, G M Wang, E M Sevick, D J Searles, and D J Evans. Fluctuations and irreversability: an experimental demonstration of a second-law-like theorem using a colloidal particle held in an optical trap. *Physical Review Letters*, 92(14):140601, 2004.

[347] G E Crooks. Entropy production fluctuation theorem and the nonequilibrium work relation for free energy differences. *Physical Review E*, 60(3):2721–2726, 1999.

[348] G Hummer and A Szabo. Free energy reconstructoin from nonequilibrium single-molecule pulling experiments. *PNAS*, 98(7):3658–3661, 2001.

[349] G Hummer and A Szabo. Kinetics from nonequilibrium single-molecule pulling experiments. *Biophysical Journal*, 85:5–15, 2003.

[350] J Liphardt, S Dumont, S B Smith, I Tinoco, and C Bustamante. Equilibrium information from nonequilibrium measurements in an experimental test of Jarzynski's inequality. *Science*, 296:1832–1835, 2002.

[351] W Min, L jiang, J Yu, S C Kou, H Qian, and X S Xie. Nonequilibrium steady state of a nanometric biochemical system: determining the thermodynamic driving force from single enzyme turnover time traces. *Nano Letters*, 5(12):2373–2378, 2005.

[352] H Qian and X S Xie. Generalized haldane equation and fluctuation theorem in the steady-state cycle kinetics of single enzymes. *Physical Review E*, 74(1):010902R, 2006.

[353] D A Beard and H Qian. Relationship between thermodynamic driving force and one-way fluxes in reversible chemical reactions. *arXiv:q-bio.SC*, 0607020(v1), 2006.

[354] H Qian. Equations for stochastic macromolecular mechanics of single proteins: equilibrium fluctutations, transient kinetics, and nonequilibrium steady-state. *Journal of Physical Chemistry B*, 106:2065, 2002.

[355] H Qian. Nonequilibrium potential function of chemically driven single macromolecules via Jarzynski-type log-mean-exponential heat. *Journal of Physical Chemistry B*, 109:23624–23628, 2005.

[356] H Wian and D A Beard. Thermodynamics of stoichiometric biochemical networks in living systems far from equilibrium. *Biophysical Chemistry*, 114(2-3):213–220, 2004.

[357] L C Hwang and T Wohland. Recent advances in fluorescence cross-correlation spectroscopy. *Cell biochemistry and biophysics*, 49(1):1–13, 2007.

[358] S Maiti, U Haupts, and W W Webb. Fluorescence correlation spectroscopy: diagnostics for sparse molecules. *PNAS*, 94:11753–11757, 1997.

[359] N L Thompson, A M Lieto, and N W Allen. Recent advances in fluorescence correlation spectroscopy. *Curr. Op. Struct. Biol.*, 12:634–641, 2002.

[360] S T Hess, S Huang, A A Heikal, and W W Webb. Biological and chemical applications of fluorescence correlation spectroscopy: a review. *Biochemistry*, 42(3):697–705, 2002.

[361] A Van Orden, K Fogarty, and J Jung. Fluorescence fluctuation spectroscopy: a coming of age story. *Applied Specroscopy*, 58(5):122A–137A, 2004.

[362] O Krichevsky and G Bonnet. Fluorescence correlation spectroscopy: the technique and its applications. *Reports on Progress in Physics*, 65:251–297, 2002.

[363] D Magde, E Elson, and W W Webb. Thermodynamic fluctuations in a reacting system— measurement by fluorescence correlation spectroscopy. *Physical Review Letters*, 29(11):705–708, 1972.

[364] S R Aragón and R Pecora. Fluorescence correlation spectroscopy as a probe of molecular dynamics. *The Journal of Chemical Physics*, 64(4):1791–1803, 1975.

[365] S R Aragón and R Pecora. Fluorescence correlation spectroscopy and brownian rotational diffusion. *Biopolymers*, 14:119–138, 1975.

[366] P Kask, P Piksarv, M Pooga, Ü Mets, and E Lippmaa. Separation of the rotational contribution in fluorescence correlation experiments. *Biophysical Journal*, 55:213–220, 1989.

[367] P Kask, P Piksarv, Ü Mets, M Pooga, and E Lippmaa. Fluorescence correlation spectroscopy in the nanosecond time range: rotational diffusion of bovine carbon anhydrase a. *European Biophysics Journal*, 14:257–261, 1987.

[368] K Peck, L Stryer, A N Glazer, and R A Mathies. Single-molecule fluorescence detection: autorrelation criterion and experimental realization with phycoerythrin. *PNAS*, 86:4087–4091, 1989.

[369] S Nie, D T Chiu, and R N Zare. Probing individual molecules with confocal fluorescence microscopy. *Science*, 266:1018–1021, 1994.

[370] P Kask, P Piksarv, and Ü Mets. Fluorescence correlation spectroscopy in the nanosecond time range: photon antibunching in dye fluorescence. *European Biophysics Journal*, 12:163–166, 1985.

[371] J W Borst, S P Lapentok, A H WEstphal, R Kühnemuth, H Hornen, N V Visser, S Kalinin, J Aker, A van Hoek, C A M Seidel, and A J W G Visser. Structural changes of yellow chameleon domains observed by quantitative FRET analysis and polarized fluorescence correlation spectroscopy. *Biophysical Journal*, 95:5399–5411, 2008.

[372] B Lounis, H A Bechtel, D Gerion, P Alivisatos, and W E Moerner. Photon antibunching in single CdSe/ZnS quantum dot fluorescence. *Chemical Physics Letters*, 329(5-6):399–404, 2000.

[373] A J Berglund, A C Doherty, and H Mabuchi. Photon statistics and dynamics of fluorescence resonance energy transfer. *Physical Review Letters*, 89(6):068101, 2002.

[374] G O Ariunbold, G S Agarwal, Z Wang, M O Scully, and H Walther. Nanosecond dynamics of single-molecule fluorescence resonance energy transfer. *Journal of Physical Chemistry A*, 108:2402–2404, 2004.

[375] A K Luong, C C Gradinaru, D W Chandler, and C C Hayden. Simultaneous time- and wavelength-resolved fluorescence microscopy of single molecules. *Journal of Physical Chemistry B*, 109:15691–15698, 2005.

[376] H Qian and E L Elson. On the analysis of high order moments of fluorescence fluctuations. *Biophys. J.*, 57:375–380, 1990.

[377] H Yang, G Luo, P Karnchanaphanurach, T-M Louie, I Rech, S Cova, L Xun, and X S Xie. Protein conformational dynamics probed by single-molecule electron transfer. *Science*, 302(5643):262–266, 2003.

[378] H Yang and X S Xie. Probing single-molecule dynamics photon-by-photon. *Journal of Chemical Physics*, 117(24):10965–10979, 2002.

[379] X S Xie. Single-molecule approach to dispersed kinetics and dynamical disorder: probing conformational fluctuation and enzymatic dynamics. *Journal of Chemical Physics*, 117(24):11024–11032, 2002.

[380] S Saffarian and E L Elson. Statistical analysis of fluorescence correlation spectroscopy: the standard deviation and bias. *Biophys. J.*, 84:2030–2042, 2003.

[381] J Enderlein, I Gregor, D Patra, T Dertinger, and U B Kaupp. Performance of fluorescence correlation spectroscopy for measuring diffusion and concentration. *ChemPhysChem*, 6:2324–2336, 2005.

[382] K Bacia, D Scherfeld, N Khaya, and P Schwille. Fluorescence correlation spectroscopy relates rafts in model and native membranes. *Biophysical Journal*, 87:1034–1043, 2004.

[383] L Rusu, A Gambhir, S McLaughlin, and J Radler. Fluorescence correlation spectroscopy studies of peptide and protein binding to phospholipid vesicles. *Biophys. J.*, 87:1044–1053, 2004.

[384] J Widengren and P Thyberg. FCS cell surface measurements– photophysical limitations and consequences on molecular ensembles with heterogenic mobilities. *Cytometry A*, 68A:101–112, 2005.

[385] J Korlach, P Schwille, W W Webb, and G W Feigenson. Characterization of lipid bilayer phases by confocal microscopy and fluorescence correlation microscopy. *PNAS*, 96:8461–8466, 1999.

[386] M K Doeven, J H A Folgering, V Krasnikov, E R Geertsma, G van den Bogaart, and B Poolman. Distribution, lateral mobility and function of membrane proteins incorporated into giant unilamellar vesicles. *Biophysical Journal*, 88:1134–1142, 2005.

[387] C Fradin, A Abu-Arish, R Granek, and M Elbaum. Fluorescence correlation spectroscopy close to a fluctuating membrane. *Biophys. J.*, 84:2005–2020, 2003.

[388] K G Heinze, A Koltermann, and P Schwille. Simultaneous two-photon excitation of distinct labels for dual-color fluorescence crosscorrelation analysis. *PNAS*, 97(19):10377–10382, 2000.

[389] P Schwille and K G Heinze. Two-photon fluorescence cross-correlation spectroscopy. *ChemPhysChem*, 2:269–272, 2001.

[390] T Kohl, K G Heinze, R Kuhlemann, A Koltermann, and P Schwille. A protease assay for two-photon crosscorrelation and FRET analysis based solely on fluorescent proteins. *PNAS*, 99(19):12161–12166, 2002.

[391] K Bacia, S A Kim, and P Schwille. Fluorescence cross-correlation spectroscopy in living cells. *Nature methods*, 3(2):83–89, 2006.

[392] K Bacia and P Schwille. A dynamic view of cellular processes by in vivo fluorescence auto- and cross-correlation spectroscopy. *Methods*, 29:74–85, 2003.

[393] K Bacia and P Schwille. Practical guidelines for dual-color fluorescence cross-correlation spectroscopy. *Nature Protocols*, 2(11):2842–2856, 2007.

[394] T Ohrt, J Mütze, W Staroske, L Weinmann, J Höck, K Crell, G Meister, and P Schwille. Fluorescence correlation spectroscopy and fluorescence cross-correlation spectroscopy reveal the cytoplasmic origination of loaded nuclear RISC *in vivo* in human cells. *Nucleic Acids Research*, pages 1–11, 2008.

[395] U Kettling, A Koltermann, P Schwille, and M Eigen. Real-time enzyme kinetics monitored by dual-color fluorescence cross-correlation spectroscopy. *PNAS*, 95:1416–1420, 1998.

[396] T Kohl, E Haustein, and P Schwille. Determining protease activity in vivo by fluorescence cross-correlation analysis. *Biophysical Journal*, 89:2770–2782, 2005.

[397] L C Hwang, M Gösch, T Lasser, and T Wohland. Simultaneous multicolor fluorescence cross-correlation spectroscopy to detect higher order molecular interactions using single wavelength laser excitation. *Biophysical journal*, 91:715–727, 2006.

[398] E Thews, M Gerken, R Eckert, J Zäpfel, C Tietz, and J Wrachtrup. Cross talk free fluorescence cross correlation spectroscopy in live cells. *Biophysical journal*, 89:2069–2076, 2005.

[399] C Tang, J Iwahara, and M Clore. Visualization of transient encounter complexes in protein-protein association. *Nature*, 444:383–386, 2006.

[400] D C Daniel, M Thompson, and N W Woodbury. Fluorescence intensity fluctuations of individual labeled DNA fragments and a DNA bindinG protein in solution at the single molecule level: A comparison of photobleaching, diffusion and binding dynamics. *J Phys. Chem. B*, 104:1382–1390, 2000.

[401] D C Daniel, M Thompson, and N W Woodbury. DNA-binding interactions and conformational fluctuations of tc3 transposase DNA binding domain examined with single molecule fluorescence spectroscopy. *Biophys. J.*, 82:1654–1666, 2002.

[402] H Xu, J Frank, U Trier, S Hammer, W Schröder, J Behlke, M Schäfer-Korting, J F Holzwarth, and W Saenger. Interaction of fluorescence labeled single-stranded DNA with hexameric DNA-helicsase RepA: A photon and fluorescence correlation spectroscopy study. *Biochemistry*, 40:7211–7218, 2001.

[403] G Li, M Levitus, C Bustamante, and J Widom. Rapid spontaneous accessibility of nucleosomal DNA. *Nature Structural & Molecular Biology*, 12(1):46–53, 2005.

[404] R Strohner, M Wachsmuth, K Dachauer, J Mazurkiewicz, J Hochstatter, K Rippe, and G Längst. A 'loop recapture' mechanism for acf-dependent nucleosome modeling. *Nature Structural & Molecular Biology*, 12:683–690, 2005.

[405] A E Miller, A J Fischer, T Laurence, C W Hollars, R J Saykally, J C Lagarias, and T Huser. Single-molecule dynamics of phytochrome-bound fluorophores probed by fluorescence correlation spectroscopy. *PNAS*, 103(30):11136–11141, 2006.

[406] P Rigler and W Meier. Encapsulation of fluorescent molecules by functionalized polymeric nanocontainers: investigation by confocal fluorescence imaging and fluorescence correlation spectroscopy. *JACS*, 128:367–373, 2006.

[407] H Neuweiler, A Schultz, M Böhmer, J Enderlein, and M Sauer. Measurement of submicrosecond intermolecular contact formation in peptides at the single-molecule level. *JACS*, 125:5324–5330, 2003.

[408] P Tinnefeld, J Hofkens, D-P Herten, S Masuo, T Vosch, M Cotlet, S Habuchi, K Müllen, F C De Schryver, and M Sauer. Higher-excited-state photophysical pathways in multichromophoric systems revealed by single-molecule fluorescence spectroscopy. *ChemPhysChem*, 5:1786–1790, 2004.

[409] L Ying, W I Wallace, and D Klenerman. Two-state model of conformational fluctuation in a DNA hairpin loop. *Chemical Physics Letters*, 334:145–150, 2001.

[410] J Jung and A Van Orden. Folding and unfolding kinetics of DNA hairpins in flowing solution by multiparameter fluorescence correlation spectroscopy. *Journal of Physical Chemistry B*, 109:3648–3657, 2005.

[411] J Jung and A Van Orden. A three-state mechanism for DNA hairpin folding characterized by multiparameter fluorescence fluctuation spectroscopy. *JACS*, 128:1240–1249, 2006.

[412] K Chattopadhyay, E L Elson, and C Frieden. The kinetics of conformational fluctuations in an unfolded protein measured by fluorescence methods. *PNAS*, 102(7):2385–2389, 2005.

[413] G Bonnet, O Krichevsky, and A Libchaber. Kinetics of conformational fluctuations in DNA hairpin loops. *PNAS*, 95:8601–8606, 1998.

[414] H Neuweiler, S Doose, and M Sauer. A microscopic view of miniprotein folding: enhanced folding efficiency through formation of an intermediate. *PNAS*, 102(46):16650–16655, 2005.

[415] J Kim, S Doose, H Neuweiler, and M Sauer. The initial step of DNA hairpin folding: a kinetic analysis using fluorescence correlation spectroscopy. *Nucleic Acids Research*, 34(9):2516–2527, 2006.

[416] T Ambjörnsson and R Metzler. Blinking statistics of a molecular beacon triggered by end-denaturation of DNA. *Journal of Physics: Condensed Matter*, 17:S4305–S4316, 2005.

[417] M J Levene, J Korlach, S W Turner, H G Craighead, and W W Webb. Zero-mode waveguides for single-molecule analysis at high concentrations. *Science*, 299(5607):682 – 686, 2003.

[418] D Vobornik, D S Banks, Z Lu, C Fradin, R Taylor, and L D Johnston. Fluorescence correlation spectroscopy with sub-diffraction-limited resolution using near-field optical probes. *Applied Physics Letters*, 93(16):163904, 2008.

[419] J Ries, E P Petrov, and P Schwille. Total internal reflection fluorescence correlation spectroscopy: effects of lateral diffusion and surface-generated fluorescence. *Biophysical Journal*, 95:390–399, 2008.

[420] C-Y Kung, M D Barnes, N Lerner, W B Whitten, and J M Ramsey. Confinement and manipulation of individual molecules in attoliter volumes. *Analytical Chemistry*, 70:658–661, 1998.

[421] D Stamou, C Duschl, E Delamarche, and H Vogel. Self-assembled microarrays of attoliter molecular vesicles. *Angewandte Chemie International Edition*, 42:5580–5583, 2003.

[422] B Wu and J D Müller. Time-integrated fluorescence cumulant analysis in fluorescence fluctuation spectroscopy. *Biophysical Journal*, 89:2721–2735, 2005.

[423] J D Müller. Cumulant analysis in fluorescence fluctuation spectroscopy. *Biophysical Journal*, 86:3981–3992, 2004.

[424] B Wu, Y Chen, and J D Müller. Dual-color time-integrated fluorescence cumulant analysis. *Biophysical Journal*, 91:2687–2698, 2006.

[425] S Felekyan, R Kühnemuth, V Kudryavtsev, C Sandhagen, W Becker, and C A M Seidel. Full correlation from picoseconds to seconds by time-resolved and time-correlated single photon counting. *Review of scientific instruments*, 76:083104, 2005.

[426] M Wahl, R-J Rahn, R Erdmann, and J Enderlein. Dead-time optimized time-correlated single photon counting instrument with synchronized, independent timing channels. *Review of Scientific Instruments*, 78(3):033106, 2007.

[427] A Benda, M Hof, M Wahl, M Patting, R Erdmann, and P Kapusta. TCSPC upgrade of a confocal FCS microscope. *Review of Scientific Instruments*, 76:033106, 2005.

[428] J H Werner, R Joggerst, R B Dyer, and P M Goodwin. A two-dimensional view of the folding energy landscape of cytochrome C. *PNAS*, 103(30):11130–11135, 2006.

[429] M Prummer, B Sick amd A Renn, and U P Wild. Multiparameter microscopy and spectroscopy for single-molecule analytics. *Analytical Chemistry*, 76:1633–1640, 2004.

[430] M Wahl, H-J Rahn, T Röhlicke, G Kell, D Nettels, F Hillger, B Schuler, and R Erdmann. Scalable time-correlation photon counting system with multiple independent input channels. *Review of Scientific Instruments*, 79(12):123113, 2008.

[431] Z Petrášek and P schwille. Scanning fluorescence correlation spectroscopy. In H Vogel and R Rigler, editors, *Single molecules and nanotechnology*, volume 12 of *Springer Series in Biophysics*, chapter 4, pages 83–105. Springer Berlin Heidelberg, 2008.

[432] A Amediek, E Haustein, D Scherfeld, and P Schwille. Scanning dual-color cross-correlation analysis for dynamic co-localization studies of immobile molecules. *Single Molecules*, 3(4):201–210, 2002.

[433] P Wiseman, J Squier, M Ellisman, and K Wilson. Two-photon image correlation spectroscopy and image cross-correlation spectroscopy. *Journal of Microscopy*, 200:14–25, 2000.

[434] D L Kolin, D Ronis, and P W Wiseman. k-space image correlation spectroscopy: a method for accurate transport measurements independent of fluorophore photophysics. *Biophysical Journal*, 91:3061–3075, 2006.

[435] B Hebert, S Costantino, and P W Wiseman. Spatiotemporal image correlation spectroscopy (STICS) theory, verification, and application to protein velocity mapping in living cells. *Biophysical Journal*, 88(5):3601–3614, 2005.

[436] J W D Comeau, S Costantino, and P W Wiseman. A guide to accurate fluorescence microscopy colocalization measurements. *Biophysical Journal*, 91:4611–4622, 2006.

[437] J Ries and P Schwille. New concepts for fluorescence correlation spectroscopy on membranes. *Physical Chemistry Chemical Physics*, 10:3487–3497, 2008.

[438] T Dertinger, V Pacheco, I von der Hocht, R Hartmann, I Gregor, and J Enderlein. Two-focus fluorescence correlation spectroscopy: A new tool for accurate and absolute diffusion measurements. *ChemPhysChem*, 8:433–443, 2007.

[439] J Ries and P Schwille. Studying slow membrane dynamics with continuous wave scanning fluorescence correlation spectroscopy. *Biophysical Journal*, 91:1915–1924, 2006.

[440] Q Ruan, M A Cheng, M Levi, E Gratton, and W W Mantulin. Spatial-temporal studies of membrane dynamics: scanning fluorescence correlation spectroscopy (SFCS). *Biophysical Journal*, 87:1260–1267, 2004.

[441] Y Xiao, V Buschmann, and K D Weston. Scanning fluorescence correlation spectroscopy: a tool for probing microsecond dynamics of surface-bound fluorescent species. *Anal. Chem.*, 77:36–48, 2005.

[442] Y Korlann, T Dertinger, X Michalet, S Weiss, and J Enderlein. Measuring diffusion with polarization-modulation dual-focus fluorescence correlation microscopy. *Optics Express*, 16(19):14609–14616, 2008.

[443] T Winkler, U Kettling, A Kolterman, and M Eigen. Confocal fluorescence coincidence analysis: an approach to ultra high-throughput screening. *PNAS*, 96:1375–1378, 1999.

[444] H Li, L Ying, J J Green, S Balasubramanian, and D Klenerman. Ultrasensitive coincidence fluorescence detection of single DNA molecules. *Analytical Chemistry*, 75:1664–1670, 2003.

[445] C Eggeling, J R Fries, L Brand, R Gunther, and C A M Seidel. Monitoring conformational dynamics of a single molecules by selective fluorescence spectroscopy. *PNAS*, 95:1556–1561, 1998.

[446] C Eggling, S Berger, L Brand, J R Fries, J Schaffer, A Volkmer, and C A M Seidel. Data registration and selective single-molecule analysis using multiparameter fluorescence detection. *Journal of Biotechnology*, 86:163–180, 2001.

[447] M Jäger, E Nir, and S Weiss. Site-specific labeling of proteins for single-molecule FRET by comining chemical and enzymatic modification. *Protein Science*, 15:640–646, 2006.

[448] A D Deniz, M Dahan, J R Grunwell, T Ha, A E Faulhaber, D S Chemla, S Weiss, and P G Schultz. Single-pair fluorescence resonance energy transfer on freely diffusing molecules: observation of Förster dstance dependence and subpopulations. *PNAS*, 96:3670–3675, 1999.

[449] M A Morgan, K Okamoto, J D Kahn, and D S English. Single-molecule spectroscopic determination of lac repressor-DNA loop conformation. *Biophysical Journal*, 89:2588–2596, 2005.

[450] M Dahan, A A Deniz, T Ha, D S Chemla, P G Schultz, and S Weiss. Ratiometric measurement and identification of single diffusing molecules. *Chemical Physics*, 247:85–106, 1999.

[451] Y Ishii, T Yoshida, T Funatsu, T Wasawa, and T Yanagida. Fluorescence resonance energy transfer between single fluorophores attached to a coiled-coil protein in aqueous solution. *Chemical Physics*, 247:163–173, 1999.

[452] G Pljevaljčić, D P Millar, and A A Deniz. Freely diffusing single hairpin ribozymes provide insights into the role of secondary structure and partially folded states in RNA folding. *Biophysical Journal*, 87:457–467, 2004.

[453] E A Lipman, B Schuler, O Bakajin, and W A Eaton. Single-molecule measurements of protein folding kinetics. *Science*, 301:1233–1235, 2003.

[454] R Liu, D Hu, X Tan, and H P Lu. Revealing two-state protein-protein interactions of calmodulin by single-molecule spectroscopy. *JACS*, 128(31):10034–10042, 2006.

[455] B D Slaughter, M W Allen, J R Unruh, R J B Urbauer, and C K Johnson. Single-molecule fluorescence resonance energy transfer and fluorescence correlation spectroscopy of calmodulin in solution. *Journal of Physical Chemistry B*, 108:10388–10397, 2004.

[456] H Lui, X Ren, L Ying, S Balasubramanian, and D Klenerman. Measuring single-molecule nucleic acid dynamics in solution by two-color filtered ratiometric fluorescence correlation spectroscopy. *PNAS*, 101(40):14425–14430, 2004.

[457] K M Hamadani and S Weiss. Nonequilibrium single molecule protein folding in a coaxial mixer. *Biophysical Journal*, 95:352–365, 2008.

[458] C R Sabanayagam, J S Eid, and A Meller. Using fluorescence resonance energy transfer to measure distances along indivudal DNA molecules: corrections due to nonideal transfer. *Journal of Chemical Physics*, 122(6):061103, 2005.

[459] D G Norman, R J Grainger, D Uhrín, and D M J Lilley. Location of cyanine-3 on double stranded DNA: importance for fluorescence resonance energy transfer studies. *Biochemistry*, 39:6317–6324, 2000.

[460] C R Sabanayagam, J S Eid, and A Meller. Long time scale blinking kinetics of cyanine fluorophores conjugated to DNA and its effect on Förster resonance energy transfer. *Journal of Chemical Physic*, 123(22):224708, 2005.

[461] A Dietrich, V Buschmann, C Müller, and M Sauer. Fluorescence resonance energy transfer (FRET) and competing processes in donor-acceptor substituted DNA strands: a comparative study of ensemble and single-molecule data. *Reviews in Molecular Biotechnology*, 82:211–231, 2002.

[462] A Iqbal, S Arslan, B Okumus, T J Wilson, G Giraud, D G Norman, T Ha, and D M J Lilley. Orientation dependence in fluorescent energy transfer between cy3 and cy5 terminally attached to double-straned nucleic acids. *PNAS*, 105(32):11176–11181, 2008.

[463] C Joo and T Ha. Single molecule FRET with total internal reflection microscopy. In *Single-Molecule Techniques; A Laboratory Manual*, chapter 2, pages 3–36. Cold Spring Harbor Laboratory Press, 2008.

[464] C Joo, H Balci, Y Ishitsuka, C Buranachai, and T Ha. Advances in single-molecule fluorescence methods for molecular biology. *Annual Reviews in Biochemistry*, 77:51–76, 2008.

[465] R Roy, S Hohng, and T Ha. A practical guide to single-molecule FRET. *Nature Methods*, 5(6):507–516, 2008.

[466] A Hillisch, M Lorenz, and S Diekmann. Recent advances in FRET: distance determination in protein-DNA complexes. *Current Opinion in Structural Biology*, 11:201–207, 2001.

[467] I Rasnik, S A McKinney, and T Ha. Surfaces and orientations: much to FRET about? *Accounts of Chemical Research*, 38:542–548, 2005.

[468] E A Jares-Erijman and T M Jovin. FRET imaging. *Nature Biotechnology*, 21(1):1387–1395, 2003.

[469] T Ha. Single-molecule fluorescence resonance energy transfer. *Methods*, 25:78–86, 2001.

[470] E A Jares-Erijman and T M Jovin. Imaging molecular interactions in living cells by FRET microscopy. *Current Opinion in Chemical Biology*, 10:409–416, 2006.

[471] E F Y Hom and A S Verkman. Analysis of coupled biomolecular reaction kinetics and diffusion by two-color fluorescence correlation spectroscopy: enhanced resolution of kinetics by resonance energy transfer. *Biophysical Journal*, 83:522–546, 2002.

[472] M I Wallace, L Ying, S Balasubramanian, and D Klenerman. FRET fluctuation spectroscopy: exploring the conformational dynamics of a DNA hairpin loop. *Journal of Physical Chemistry B*, 104(48):11551–11555, 2000.

[473] M I Wallace, L Ying, S Balasubramanian, and D Klenerman. Non-arrhenius kinetics for the loop closure of a DNA hairpin. *PNAS*, 90(10):5584–5589, 2001.

[474] G Harms, G Orr, and H P Lu. Probing ion channel conformational dynamics using simultaneous single-molecle ultrafast spectroscopy and patch-clamp electric recording. *Applied Physics Letters*, 84(10):1792–1794, 2004.

[475] M Margittai, J Widengren, E Schweinberger, G F Schröder, S Felekyan, E Haustein, M König, D Fasshauer, H Grubmüller, R Jahn, and C A M Seidel. Single-molecule fluorescence resonance energy transfer reveals a dynamic equilibrium between closed and open conformations of syntaxin 1. *PNAS*, 100(26):15516–15521, 2003.

[476] P D Smolen and D A Baxter andJ H byrne. Fluorescence probes of protein dynamics and conformations in freely diffusing molecules: Single-molecule resonance energy transfer and time-resolved fluorescence methods. In *Reviews in Fluorescence*, pages 239–259. Springer US, 2006.

[477] S A Kim, K G Heinze, M N Waxham, and P Schwille. Intracellular calmodulin availability accessed with two-photon cross-correlation. *PNAS*, 101(1):105–110, 2004.

[478] A L Mattheyses, A D Hoppe, and D Axelrod. Polarized fluorescence resonance energy transfer. *Biophysical Journal*, 87(4):2787–2797, 2004.

[479] M A Rizzo and D W Piston. High-contrast imaging of fluorescent protein FRET by fluorescence polarization microscopy. *Biophysical Journal: Biophysical Letters*, pages L14–L16, 2004.

[480] B K Müller, E Zaychikov, C Bräuchle, and D C Lamb. Pulsed interleaved excitation. *Biophysical Journal*, 89:3508–3522, 2005.

[481] S Mao, R K P Benninger, Y Yan, C Petchprayoon, D Jackson, C J Easley, D W Piston, and G Marriott. Optical lock-in detection of FRET using synthetic and genetically encoded optical switches. *Biophysical Journal*, 94:4515–4524, 2008.

[482] M Bates, T R Blosser, and X Zhuang. Short-rage spectroscopic ruler based on a single-molecule optical switch. *Physical Review Letters*, 94(10):108101, 2005.

[483] E J Bjerneld, S Földes, M Käll, and R Rigler. Single-molecule surface-enhanced raman and fluorescence correlation spectroscopy of horseradish peroxidase. *Journal of Physical Chemistry B*, 106:1213–1218, 2002.

[484] A N Kapanidis and S Weiss. Fluorescent probes and bioconjugation chemistries for single-molecule fluorescence analysis of biomolecules. *Journal of Chemical Physics*, 117(24):10953–10964, 2002.

[485] J R Unruh, G Golkulrangan, G H Lushington, C K Johnson, and G S Wilson. Orientational dynamics and dye-DNA interactions in a dye-labeled DNA aptamer. *Biophysical Journal*, 88:3455–3465, 2005.

[486] T Wazawa, Y Ishii, T Funatsu, and T Yanagida. Spectral fluctuation of a single fluorophore conjugated to a protein molecule. *Biophysical Journal*, 78:1561–1569, 2000.

[487] J J Han, W Wang, and A D Q Li. Folding and unfolding of chromophoric foldamers show unusual colorful single molecule spectral dynamics. *JACS*, 128:672–673, 2006.

[488] B Schuler, E A Lippman, P J Steinbach, M Kumke, and W A Eaton. Polyproline and the"spectroscopic ruler" revisited with single molecule fluorescence. *PNAS*, 102(8):2754–2759, 2005.

[489] C E Shannon. A mathematical theory of communication. *The Bell System Technical Journal*, 27:379–423, 623–656, 1948.

[490] C E Shannon and W Weaver. *The mathematical theory of communication*. The University of Illinois Press, Urbana, IL, 1949.

[491] T M Cover and J A Thomas. *Elements of Information Theory*, chapter 4. John Wiley & Sons, Inc. Hoboken, NJ, 2nd edition, 2006.

[492] C-Y Lu and D A Vanden Bout. Effect of finite trajectory length on the correlation function analysis of single molecule data. *The Journal of chemical physics*, 125(12):124701, 2006.

[493] L A Deschenes and D A Vanden Bout. Heterogeneous dynamics and domains in supercooled o-terphenyl: A single molecule study. *Journal of Physical Chemistry B*, 106(44):11438–11445, 2002.

[494] R A L Valleé, W Paul, and K Binder. Single molecule probing of the glass transition phenomenon: simulations of several types of probes. *The Journal of Chemical Physics*, 127(15):154903, 2007.

[495] G Hinze, G Dietzmann, and Th Bashe. Rotational correlation functions of single molecules. *Physical Review Letters*, 93(20):203001, 2004.

[496] H Sanabria, Y Kubota, and M N Waxham. Multiple diffusion mechanisms due to nanostructuring in crowded environments. *Biophys. J.*, 92:313–322, 2007.

[497] M C Konopka, I A Shkel, S Cayley, M T Record, and J C Weisshaar. Crowding and confinement effects on protein diffusion in vivo. *J. Bacteriol.*, 188:6115–6123, 2006.

[498] S A Tatarkova and D A Berk. Probing single DNA mobility with fluorescence correlation spectroscopy. *Physical Review E*, 71(4):041913, 2005.

[499] S Zorilla, M A Hink, A J W G Visser, and M P Lillo. Translational and rotational motions of proteins in a protein crowded environment. *Biophysical chemistry*, 125:298–305, 2007.

[500] S Schnell and T E Turner. Reaction kinetics in intracellular environments with macromolecular crowding: simulations and rate laws. *Prog. Biophys. Mol. Biol.*, 85:235–260, 2004.

[501] R Kopelman. Fractal reaction kinetics. *Science*, 241:1620–1626, 1988.

[502] I Y Wong, M L Gardel, D R Reichmann, E R Weeks, M T Valentine, A R Bausch, and D A Weitz. Anomalous diffusion probes microstructure dynamics of entangled f-actin networks. *Phys. Rev. Lett.*, 92:178101, 2004.

[503] H Berry. Monte carlo simulations of enzyme reactions in two dimensions: fractal kinetics and spatial segregation. *Biophysical Journal*, 83:1891–1901, 2002.

[504] Y Y Kuttner, N Kozer, E Segal, G Schreiber, and G Haran. Separating the contribution of translational and rotational diffusoin to protein association. *JACS*, 127:15138–15144, 2005.

[505] R A L Vallée, T Rohand, N Boens, W Dehaen, G Hinze, and T Basché. Analysis of the exponential character of single molecule rotational correlation functions for large and small fluorescence collection angles. *The Journal of Chemical Physics*, 128(15):154515, 2008.

[506] P G Debenedetti and F H Stillinger. Supercooled liquids and the glass transition. *Nature*, 410:259–267, 2001.

[507] I Shapiro and C P Collier. Rotational diffusion of colloidal semiconductor nanocrystals measured by polarization-sensitive fluorescence cross-correlation spectroscopy, 2009.

[508] M Bruchel, M Moronne, P Gin, S Weiss, and AP Alivisatos. Semiconductor nanocrystals as fluorescent biological labels. *Science*, 281(5385):2013–2016, 1998.

[509] A Fu, W Gu, C Larabell, and A P Alivisatos. Semiconductor nanocrystals for biological imaging. *current opinion in neurobiology*, 15:568–575, 2005.

[510] Aihua Fu, Weiwei Gu, Benjamin Boussert, Kristie Koski, Daniele Gerion, Liberato Manna, Mark Le Gros, Carolyn A. Larabell, and A. Paul Alivisatos. Semiconductor quantum rods as single molecule fluorescent biological labels. *Nano Letters*, 7(1):179–182, 2007.

[511] R C Somers, M G Bawendi, and D G Nocera. CdSe nanocrystal based chem-/bio- sensors. *Chemical Society Reviews*, 36:579–591, 2007.

[512] I L Medintz, H T Uyeda, E R Goldman, and H Mattoussi. Quantum dot bioconjugates for imaging, labeling and sensing. *Nature Materials*, 4:435–446, 2005.

[513] I L Medintz, A R Clapp, H Mattoussi, E R Goldman, B Fisher, and J M Mauro. Self-assembled nanoscale biosensors based on quantum dot FRET donors. *Nature Materials*, 2:630–638, 2003.

[514] X Michalet, F F Pinaud, L A Bentolila, J M Tsay, S Doose, J J Li, G Sundaresan, A M Wu, S S Gambhir, and S Weiss. Quantum dots for live cells, in vivo imaging, and diagnostics. *Science*, 307:538–544, 2005.

[515] A M Smith, G Ruan, M N Rhyner, and S Nie. Engineering luminescent quantum dots for *in vivo* molecular and cellular imaging. *Annals of Biomedical Engineering*, 34(1):3–14, 2006.

[516] N Kaji, M Tokeshi, and Y Baba. Quantum dots for single bio-molecule imaging. *Analytical Sciences*, 23:21–24, 2007.

[517] W J Parak, D Gerion, T Pellegrino, D Zanchet, C Micheel, S C Williams, R Bodreau, M A Le Gros, C A Larabel, and A P Alivisatos. Biological applications of colloidal nanocrystals. *Nanotechnology*, 14:R15–R27, 2003.

[518] A P Alivisatos, W Gu, and C Larabell. Quantum dots as cellular probes. *Annual Reviews in Biomedical Engineering*, 7:55–76, 2005.

[519] Z B Li, W Cai, and X Chen. Semiconductor quantum dots for in vivo imaging. *Journal of Nanoscience and Nanotechnology*, 7(8):2567–2581, 2007.

[520] B Dubertret, P Skourides, D J Norris, V Noireaux, A H Brivanlou, and A Libchaber. In vivo imaging of quantum dots encapsulated in phospholipid micelles. *Science*, 298:1759–1762, 2002.

[521] S Pathak, E Cao, M C Davidson, S Jin, and G A Silva. Quantum dot applications to neuroscience: new tools for probing neurons and glia. *Journal of Neuroscience*, 26(7):1893–1895, 2006.

[522] S Geissbuehler, R Hovius, K L Martinez, M Adrian, K R Thampi, and H Vogel. Lipid-coated nanocrystals as multifunctionalized luminescent scaffolds for

supramolecular biological assemblies. *Angewandte Chemie International Edition*, 44:1388–1392, 2005.

[523] G Gopalkrishnan, C Danelon, P Izewska, M Prummer, P-Y Bolinger, I Geissbühler, D Demurtas, J Dubochet, and H Vogel. Multifunctional lipid-quantum dot hybrid nanocontainers for controlled targeting of live cells. *Angewandte Chemie International Edition*, 45:5478–5483, 2006.

[524] S-M Xie, X Zhao, Z-L Zhang, H-Y Xie, Z-Q Tian, J Peng, Z-X Lu, D-W Pang, and Z-X Xie. Quantum-dot-labeled DNA probes for fluorescence in situ hybridization (FISH) in the microorganism *Escherichia coli*. *ChemPhysChem*, 7:1062–1067, 2006.

[525] C-Y Zhang, H-C Yeh, M T Kuroki, and T-H Wang. Single-quantum-dot-based DNA nanosensor. *Nature Materials*, 4:826–831, 2005.

[526] J L Nadeau, S J Clarke, C A Hollmann, and D M Bahcheli. Quantum-dot FRET systems for imaging of neuronal action potentials. pages 833–858. IEEE EMBS Annual International Conference, 2006.

[527] J A Kloepfer, N Cohen, and J L Nadeau. FRET between CdSe quantum dots in lipid vesicles and water- and lipid-soluble dyes. *Journal of Physical Chemistry B*, 108:17042–17049, 2004.

[528] M-K So, C Xu, A M Loening, S S Gambhir, and J Rao. Self-illuminating quantum dot conjugates for *in vivo* imaging. *Nature Biotechnology*, 24(3):339–343, 2005.

[529] S Hohng and T Ha. Single-molecule quantum-dot fluorescence resonance energy transfer. *ChemPhysChem*, 6:956–960, 2005.

[530] A R Clapp, I L Medintz, and H Mattoussi. Förster resonance energy transfer investigations using quantum-dot fluorophors. *ChemPhysChem*, 7:47–57, 2006.

[531] A R Clapp, I L Medintz, J M Mauro, B R Fisher, M G Bawendi, and H Mattoussi. Fluorescence resonance energy transfer between quantum dot donors and dye-labeled protein acceptors. *JACS*, 126:301–31–, 2003.

[532] I L Medintz, L Berti, T Pons, A F Grimes, D S English, A Alessandrini, P Facci, and H Mattoussi. A reactive peptidic linker for self-assembling hybrid quantum dot-DNA assemblies. *Nano Letters*, 7(6):1741–1748, 2007.

[533] H Peng, L Zhang, T H M Kjällman, C Soeller, and J Travas-Sejdic. DNA hybridization detection with blue luminescent quantum dots and dye-labeled single-stranded DNA. *JACS*, 129:3048–3049, 2007.

[534] D M Willard and. CdSe-ZnS quantum dots as resonance energy transfer donors in a model protein-protein binding assay. *Nano Letters*, 1(9):469–474, 2001.

[535] T Pons, I L Medintz, X Wang, D S English, and H Mattoussi. Solution-phase single quantum dot fluorescence resonance energy transfer. *JACS*, 128:15324–15331, 2006.

[536] F Müller, S Gotzinger, N Gaponik, H Weller, J Mlynek, and O Benson. Investigation of energy transfer between CdTe nanocrystals on polystyrene beads and dye molecules for FRET-SNOM applications. *Journal of Physical Chemistry B*, 108:14527–14534, 2004.

[537] I L Medintz, J H Konnert, A R Clapp, I Stanish, M E Twigg, H Mattoussi, J M Mauro, and J R Deschamps. A fluorescence resonance energy transfer-

derived structure of a quantum dot-protein bioconjugate nanoassembly. *PNAS*, 101(26):9612–9617, 2004.

[538] D Zhou, J D Piper, C Abell, D Klenerman, D-J Kang, and L Ying. Fluorescence resonance energy transfer between and quantum dot donor and a dye acceptor attached to DNA. *Chemical Communications*, pages 4807–4809, 2005.

[539] C. B. Murray, D. J. Norris, and M. G. Bawendi. Synthesis and characterization of nearly monodisperse CdE (E = sulfur, selenium, tellurium) semiconductor nanocrystallites. *Journal of the American Chemical Society*, 115(19):8706–8715, 1993.

[540] A P Alivisatos. Perspectives on the physical chemistry of semiconductor nanocrystals. *The Journal of Physical Chemistry*, 100(31):13226–13239, 1996.

[541] L Qu and X Peng. Control of photoluminescence properties of CdSe nanocrystals in growth. *Journal of the American Chemical Society*, 124(9):2049–2055, 2002.

[542] D Patra, I Gregor, J Enderlein, and M Sauer. Defocused imaging of quantum dot angular distribution of radiation. *Applied Physics Letters*, 87:101103, 2005.

[543] M Shim and P Guyot-Sionnest. Permanent dipole moment and charges in colloidal semiconductor quantum dots. *Journal of Chemical Physics*, 111(15):6955–6964, 1998.

[544] E Rabani. Structure and electrostatic properties of passivated CdSe nanocrystals. *Journal of Chemical Physics*, 115(3):1493–1497, 2001.

[545] J Hu, L-S Li, W Yang, L Manna, L-W Wang, and A P Alivisatos. Linearly polarized emission from colloidal semiconductor quantum rods. *Science*, 292:2060–2063, 2001.

[546] L Manna, E C Scher, A P, and Alivisatos. Synthesis of soluble and processable rod-, arrow-, teardrop-, and tetrapod-shaped CdSe nanocrystals. *JACS*, 122(51):12700–12706, 2000.

[547] X Peng, L Manna, W Yang, J Wickham, E Scher, A Kadavanich, and AP Alivisatos. Shape control of CdSe nanocrystals. *Nature*, 404:59–61, 2000.

[548] E C Scher, L Manna, and A P Alivisatos. Shape control and applications of nanocrystals. *Royal Society of London Philosophical Transactions Series A*, 361:241–257, 2003.

[549] A F van Driel, G Allan, C Delerue, P Lodahl, W L Vos, and D Vanmaekelbergh. Frequency-dependent spontaneous emission rate from CdSe and CdTe nanocrystals: Influence of dark states. *Physical Review Letters*, 95(23):236804, 2005.

[550] H E Grecco, K A Lidke, R Heintzmann, D S Lidke, C Spagnuolo, O E Martinez, E A Jares-Erijman, and T M Jovin. Ensemble and singe particle photophysical properties (two-photon excitation, anisotropy, FRET, lifetime, spectral conversion) of commercial quantum dots in solution and in live cells. *Microscopy research and technique*, 65:169–179, 2004.

[551] J L Swift, R Heuff, and D T Cramb. A two-photon excitation fluorescence cross-correlation assay for a model ligand-receptor binding system using quantum dots. *Biophys. J.*, 90:1396–1410, 2006.

[552] T Nann and J Schneider. Origin of permanent electric dipole measurements in wurtzite nanocrystals. *Chemical Physics Letters*, 384:150–152, 2004.

[553] S A Blanton, R L Leheny, M A Hines, and P Guyot-Sionnest. Dielectric dispersion measurements of CdSe nanocrystal colloids: observation of a permanent dipole moment. *Physical Review Letters*, 79(5):865–868, 1997.

[554] E Rabani, H Hetényi, B J Berne, and L E Brus. Electronic properties of CdSe nanocrystals in the absence and presence of a dielectric medium. *Journal of Chemical Physics*, 110(11):5355–5369, 1999.

[555] S A Empedocles and M G Bawendi. Quantum-confined stark effect in single CdSe nanocrystallite quantum dots. *Science*, 278:2114–2117, 1997.

[556] J Seufert, M O M Scheibner, Na A Gippius, G Bacher, A Forchel, T Passow, K Leonardi, and D Homel. Stark effect and polarizability in a single CdSe/ZnS quantum dot. *Applied Physics Letters*, 79(7):1033–1035, 2001.

[557] E Rochenberg, M Kazes, E Shaviv, and U Banin. Electric field induced switching of the fluorescence of single semiconductor quantum rods. *Nano Letters*, 5(7):1581–1586, 2005.

[558] J W Robinson, J H Rice, K H Lee, J H Na, R A Taylor, D G Hasko, R A Oliver, M J Kappers, C J Humphreys, and G A D Briggs. Quantum-confined stark effect in a single InGaN quantum dot under a lateral electric field. *Applied Physics Letters*, 86(21):213103, 2005.

[559] A Y Nazzai, X Wang, L Qu, W Yu, Y Wang, X Peng, and M Xiao. Environmental effects on photoluminescence of highly luminescent CdSe and CdSe/ZnS

core/shell nanocrystals in polymer thin films. *Journal of Physical Chemistry B*, 108:5507–5515, 2004.

[560] J A Kloepfer, S E Bradforth, and J L Nadeau. Photophysical properties of biologically compatible CdSe quantum dot structures. *Journal of Physical Chemistry B*, 109:9996–10003, 2005.

[561] C Wang, M Shim, and P Guyot-Sionnest. Electrochromic nanocrystal quantum dots. *Science*, 291:2390–2392, 2001.

[562] D E Gómez, M Califano, and P Mulvaney. Optical properties of single semiconductor nanocrystals. *Physical Chemistry Chemical Physics*, 8:4989–5011, 2006.

[563] R Verberk, J W M Chon, M Gu, and M Orrit. Environment-dependent blinking of single semiconductor nanocrystals and statistical aging of ensembles. *Physica E*, 26:19–23, 2005.

[564] S-J Park, S Link, W L Miller, and A Gesquiere. Effects of electric field on the photoluminescence intensity of single CdSe nanocrystals. *Chemical Physics*, 341:169–174, 2007.

[565] M Shim, C Wang, and P Guyot-Sionnest. Charge-tunable optical properties in colloidal semiconductor nanocrystals. *Journal of Physical Chemistry B*, 205:2369–2373, 2001.

[566] F Wang, J Shan, M A Islam, I P Herman, M Bonn, and T F Heinz. Exciton polarizability in semiconductor nanocrystals. *Nature Materials*, 5:861–864, 2006.

[567] H Htnoon, M Furis, S A Crooker, S Jeong, and V I Klimov. Linearly polarized 'fine structure' of the bright exciton state in individual CdSe nanocrystal quantum dots. *Physical Review B*, 77(3):035328, 2008.

[568] F Koberling, U Kolb, G Philipp, I Potapova, T Basché, and A Mews. Fluorescence anisotropy and crystal structure of individual semiconductor nanocrystals. *Journal of Physical Chemistry B*, 107(30):7463–7471, 2003.

[569] I Chung, K T Shimizu, and M G Bawendi. Room temperature measurements of the 3D orientation of single CdSe quantum dots using polarization microscopy. *Proceedings of the National Academy of Sciences*, 100(2):405–408, 2003.

[570] X Brokmann, L Coolen, J-P Hermier, and M Dahan. Emission properties of single CdSe/ZnS quantum dots close to a dielectric interface. *Chemical Physics*, 318:91–98, 2005.

[571] X W Zhang and J B Xia. Effects of shape and magnetic field on the optical properties of wurtzite quantum rods. *Physical Review B*, 72(20):205314, 2005.

[572] S A Empedocles, R Neuhauser, and M G Bawendi. Three-dimensional orientation measurements of symmetric single chromophores using polarization micriscopy. *Nature*, 399:126–129, 1999.

[573] V L Kolvin, K L Cunningham, and A P Alivisatos. Electric field modulation studies of optical absorption in CdSe nanocrystals: dipolar character of the excited state. *Journal of Chemical Physics*, 101(8):7122–7138, 1994.

[574] S S Narayanan, R Sarkar, S S Sinha, F Dias, A Monkman, and S K Pal. Luminescence depolarization dynamics of quantum dots: is it hydrodynamic

rotation or exciton migration? *Journal of Physical chemistry C*, 112:3243–3428, 2008.

[575] J Qi, C Mao, J M White, and A M Belcher. Optical anisotropy in individual CdS quantum dot ensembles. *Physical Review B*, 68(12):125319, 2003.

[576] A Muller, Q Q Wang, P Bianucci, C K Shih, and Q K Xue. Determination of anisotropic dipole moments in self-assembled quantum dots using rabi oscillations. *Applied Physics Letters*, 84(6):981–983, 2004.

[577] G V Astakhov, T Kiessling, A V Platanov, T Slobodskyy, S Mahapatra, W Ossau, G Schmidt, K Brunner, and L W Molenkamp. Circular-to-linear and linear-to-circular coversion of optical polarization in semiconductor quantum dots. *Physical Review Letters*, 96(2):027402, 2006.

[578] G Jundt, L Robledo, A Högele, S Fält, and A Imamoğlu. Obervation of dressed excitonic states in a single quantum dot. *Physical Review Letters*, 100(17):177401, 2008.

[579] B Patton, U Woggon, and W Langbein. Coherent control and polarization readout of individual excitonic states. *Physical Review Letters*, 95(26):266401, 2005.

[580] U Woggon. Single semiconductor nanocrystals: physics and applications. *Journal of Applied Physics*, 101:081727, 2007.

[581] A Högele, B Alén, F Bickel, R J Warburton, P M Petroff, and K Karrai. Exciton fine structure splitting of InGaAs self-assembled quantum dots. *Physica E*, 21:175–179, 2004.

[582] X W Zhang and J B Xia. Effects of magnetic field on the electronic structure of wurtzite quantum dots: Calculations using effective-mass envelope function theory. *Physical Review B*, 72(7):075363, 2005.

[583] P A Frantsuzov and R A Marcus. Explanation of quantum dot blinking without the long-lived trap hypothesis. *Physical Review B*, 72(15):155321, 2005.

[584] J Tang and R A Marcus. Single particle versus ensemble average: From power-law intermittency of a single quantum dot to quasistretched exponential fluorescence decay of an ensemble. *The Journal of Chemical Physics*, 123(20):204511, 2005.

[585] R Verberk, A M van Oijen, and M Orrit. Simple model for the power-law blinking of single semiconductor nanocrystals. *Physical Review B*, 66(23):233202, 2002.

[586] I Chung, J B Witkoskie, J Cao, and M G Bawendi. Description of the fluorescence intensity time trace of collections of CdSe nanocrystal quantum dots based on single quantum dot blinking statistics. *Physical Review E*, 73(1):011106, 2006.

[587] I Chung and M G Bawendi. Relationship between single quantum-dot intermittency and fluorescence intensity decays from collections of dots. *Physical Review B*, 70(16):165304, 2004.

[588] I Chung, J B Witkoskie, J P Zimmer, J Cao, and M G Bawendi. Extracting the number of quantum dots in a microenvironment from ensemble fluorescence intensity fluctuations. *Physical Review B*, 75(4):045311, 2007.

[589] J Yao, D R Larson, H D Vishwasrao, W R Zipfel, and W W Webb. Blinking and nonradiant dark fraction of water-soluble quantum dots in aqueous solution. *PNAS*, 102(40):14284–14289, 2005.

[590] M Kuno, D P Fromm, F H Hamann, A Gallagher, and D J Nesbitt. Nonexponential "blinking" kinetics of single CdSe quantum dots: a universal power law behavior. *Journal of Chemical Physics*, 112(7):3117–3119, 2000.

[591] K T Shimizu, R G Neuhauser, C A Leatherdale, S A Empedocles, W K Woo, and M G Bawendi. Blinking statistics in single semiconductor nanocrystals. *Physical Review B*, 63(20):205316, 2001.

[592] M Pelton, D G Grier, and P Guyot-Sionnest. Characterizing quantum-dot blinking using noise power spectra. *Applied Physics Letters*, 85(5):819–821, 2004.

[593] C Margolin and E Barkai. Aging correlation functions for blinking nanocrystals, and other on-off stochastic processes. *Journal of Chemical Physics*, 121(3):1556–1577, 2004.

[594] S Ito, N Toitani, L Pan, N Tamai, and H Miyasaka. Fluorescence correlation spectroscopic study on water-soluble cadmium telluride nanocrystals: fast blinking dynamics in the microsecond-milisecond region. *Journal of Physics: Condensed Matter*, 19:486208, 2007.

[595] A Y Kobitski, C D Heyes, and G U Nienhaus. Total internal reflection fluorescence microscopy: a powerful tool to study single quantum dots. *Applied Surface Science*, 234:86–92, 2004.

[596] X Brokmann, L Coolen, M Dahan, and J P Hermier. Measurement of the radiative and nonradiative decay rates of single CdSe nanocrystals through a controlled modification of their spontaneous emission. *Physical Review Letters*, 93(10):107403, 2004.

[597] A Issac, C von Borczyskowski, and F Cichos. Correlation between photoluminescence intermittency of CdSe quantum dots and self-trapped states in dielectric media. *Physical Review B*, 71(16):161302, 2005.

[598] T D Krauss and L E Brus. Charge, polarizability and photoionization of single semiconductor nanocrystals. *Physical Review Letters*, 83(23):4840–4843, 1999.

[599] J Tang and R A Marcus. Determination of energetics and kinetics from single-particle inermittency and ensemble-averaged fluorescence intensity decay of quantum dots. *The Journal of Chemical Physics*, 125(4):044703, 2006.

[600] A Komoto and S Maenosono. Photoinduced fluorescence intensity oscillation in a reaction-diffusion cell containing a colloidal quantum dot dispersion. *Journal of Chemical Physics*, 125(11):114705, 2006.

[601] W Wang, L Qu, J Zhang, X Peng, and M Xiao. Surface-related emission of highly luminescent CdSe quantum dots. *Nano Letters*, 3(8):1103–1106, 2003.

[602] C Dong, X Huang, and J Ren. Characterization of water-soluble luminescent quantum dots by fluorescence correlation spectroscopy. *Annals of the NY Academy of Sciences*, 1130:253–261, 2008.

[603] J Müller, J M Lupton, A L Rogach, J Feldman, D V Talpin, and H Weller. Monitoring the surface charge migration in the spectral dynam-

ics of single CdSe/ZnS nanodot/nanorod heterostructures. *Physical Review B*, 72(20):205339, 2005.

[604] S A Empedocles and M G Bawendi. Influence of spectral diffusion on the line shapes of single CdSe nanocrystallite quantum dots. *The Journal of Physical Chemistry B*, 103:1826–1830, 1999.

[605] R F Heuff, J L Swift, and D T Cramb. Fluorescence correlation spectroscopy using quantum dots: advances, challenges and opportunities. *Physical Chemistry Chemical Physics*, 9:1870–1880, 2007.

[606] M J Murcia, D L Shaw, E C Long, and C A Naumann. Fluorescence correlation spectroscopy of CdSe/ZnS quantum dot optical bioimaging probes with ultrathin biocompatible coatings. *Optics Communications*, 281:1771–1780, 2008.

[607] G Massin, J P Hemier, E Giacobino, P Desbiolles, and M Dahan. Bunching and antibunching in the fluorescence of semiconductor nanocrystals. *Optics Letters*, 26(23):1891–1893, 2001.

[608] T Leidl, S Keller, F C Simmel, J O Rädler, and W J Parak. Fluorescent nanocrystals as colloidal probes in complex fluids measured by fluorescence correlation spectroscopy. *Small*, 1(10):997–1003, 2005.

[609] P Zhang, L Li, C Dong, H Qian, and J Ren. Sizes of water-soluble luminescent quantum dots measured by fluorescence correlation spectroscopy. *Analytical Chemica Acta*, 546:46–51, 2005.

[610] A Débarre, R Jaffiol, C Julien, D Nutarello, A Richard, P Tchénio, F Chaput, and J P Boilot. Quantitative determination of the 3D dipole orientation of single molecules. *The European physical journal D*, 28:67–77, 2004.

[611] D Patra, I Gregor, and J Enderlein. Image analysis of defocused single-molecule images for three-dimensional molecule orientation studies. *Journal of Physical Chemistry A*, 208:6836–6941, 2004.

[612] W Schroeyers, R Vallée, D Patra, F Jofkens, S Habuchi, T Vosch, M Cotlet, K Müller, J Enderlein, and F C De Schryver. Fluorescence lifetimes and emission patterns probe the 3D orientation of the emitting chromophore in a multichromophoric system. *JACS*, 126:14310–14311, 2004.

[613] E Toprak, J Enderlein, S Syed, S A McKinney, R G Petschek, T Ha, Y E Goldman, and P R Selvin. Defocused orientation and position imaging (DOPI) of myosin v. *PNAS*, 103(17):6495–6499, 2006.

[614] T Ha, J Glass, T Enderle, D S Chemla, and S Weiss. Hindered rotational diffusion and rotational jumps of single molecules. *Physical Review Letters*, 80(10):2093–2096, 1998.

[615] A P Bartko, K Xu, and R M Dickson. Three-dimensional single molecule rotational diffusion in glassy state polymer films. *Physical Review Letters*, 89(s):026101, 2002.

[616] A Adhikari, N A Capurso, and D Bingemann. Heterogeneous dynamics and dynamic heterogeneities at the glass transition probed with single molecule spectroscopy. *Journal of Chemical Physics*, 127(11):114508, 2007.

[617] R A L Vallée, M Baruah, J Hofkens, F C De Schryver, N Boens, and M Van der Auweraer. Fluorescence lifetime fluctuations of single molecules probe the local environment of oligomers around the glass transition temperature. *Journal of Chemical Physics*, 126:184902, 2007.

[618] R Zondervan, F Kulzer, F C G Berkhout, and M Orrit. Local viscosity of supercooled glycerol near t_g probed by rotational diffusion of ensembles and single dye molecules. *PNAS*, 104(31):12628–12633, 2007.

[619] M F Gelin and D S Kosov. What can be learned about molecular reorientation from single molecule polarization microscopy. *The journal of chemical physics*, 125:054708, 2006.

[620] R Zondervan, F Kulzer, H van der Meer, J A J M Disselhorst, and M Orrit. Laser-driven microsecond temperature cycles analyzed by fluorescence polarization microscopy. *Biophysical journal*, 90:2958–2969, 2006.

[621] C-Y J Wei, C-Y Lu, Y H Kim, and D A Vanden Bout. Determining if a system is heterogeneous: the analysis of single molecule rotational correlation functions and their limitations. *Journal of Fluorescence*, 17:797–804, 2007.

[622] K A Lidke, B Rieger, D S Lidke, and T M Jovin. The role of photon statistics in fluorescence anisotropy imaging. *IEEE Transactions on Image Processing*, 14(9):1237–1245, 2005.

[623] D Madge, R Wong, and P G Seybold. Fluorescence quantum yields and their relation to lifetimes of rhodamine 6G and fluorescein in nine solvents: improved absolute standards for quantum yields. *Photochemistry and Photobiology*, 75(4):327–334, 2002.

[624] M L Barcellona, S Gammon, T Hazlett, M A Digman, and E Gratton. Polarized fluorescence correlation spectroscopy of DNA-DAPI complexes. *Microscopy research and technique*, 65:205–217, 2004.

[625] B Seefeldt, R Kasper, T Seidel, P Tinnefeld, K-J Dietz, M Heilmann, and M Sauer. Fluorescent proteins for single-molecule fluorescence applications. *Journal of Biophotonics*, 1(1):74–82, 2008.

[626] A Müller-Taubenberger and K I Anderson. Recent advances using green and red fluorescent protein variants. *Applied Microbiology and Biotechnology*, 77(1):1–12, 2007.

[627] N C Shaner, G H Patterson, and M W Davidson. Advances in fluorescent protein technology. *Journal of Cell Science*, 120(24):4247–4260, 2007.

[628] http://www.dow.com/glycerine/resources/viscosity.htm.

[629] N Wiener. *Time Series*, pages 1–28. M.I.T University Press, Cambridge, MA, 1964.

[630] P J Brockwell and R A Davis. *Time Series: Theory and Methods*, pages 8–37. Springer, NY, 1991.

[631] M Paluš and A Stefanovska. Direction of coupling from phases of interacting oscillators: an information-theoretic approach. *Physical Review E*, 67(5):055201, 2003.

[632] M Paluš, A Stefanovska, and M Veber. Causality between the amplitude and frequency of cardiac oscillations. *Cardiovascular Engineering*, 4(2):127–133, 2004.

[633] K Hlaváčková-Schindler, M Paluš, M Vejmelka, and J Bhattacharya. Causality detection based on information-theoretic approaches in time series analysis. *Physics Reports*, 441:1–41, 2007.

[634] M Vejmelka and M Paluš. Inferring the directionality of coupling with conditional mutual information. *Physical Review E*, 77(2):026214, 2008.

[635] K Petersen. *Ergodic Theory*, pages 3–43. Cambridge University Press, Cambridge, 1989.

[636] M Paluš. Coarse-grained entropy rates for characterization of complex time series. *Physica D*, 93:64–77, 1996.

[637] R A H Lorentz. On the entropy of a function. *Journal of Approximation Theory*, in press, 2008.

[638] J Lin, E Keogh, S Lonardi, and P Patel. *Finding motifs in time series*, pages 53–68. 2002.

[639] B Chiu, E Keogh, and S Lonard. *Probabilistic discovery of time series motifs*, pages 493–498. 2003.

[640] Y Tanaka and K Uehara. *Discover motifs in multi-dimensional time-series using the principal component analysis and the MDL principle*, pages 297–322. Springer Berlin Heidelberg, 2003.

[641] Y Tanaka, K Iwamoto, and K Uehara. Discovery of time-series motif from multi-dimensional data based on mdl principle. *Machine Learning*, 58:269–300, 2005.

[642] S J Loutridis. An algorithm for the characterization of time-series based on local regularity. *Physica A*, 381:383–398, 2007.

[643] H Akaike. A new look at the statistical model identification. *IEEE Transactions on Automatic Control,*, 19(6):716–723, 1974.

[644] G Schwarz. Estimating the dimension of a model. *The Annals of Statistics*, 6(2):461–464, 1978.

[645] M Samoilov, A Arkin, and J Ross. On the deduction of chemical reaction pathways from measurements of time series concentrations. *Chaos*, 11(1):108–114, 2001.

[646] M O Vlad, A Arkin, and J Ross. Response experiments for nonlinear systems with application to reaction kinetics and genetics. *PNAS*, 101(19):7223–7228, 2004.

[647] W Vance, A Arkin, and J Ross. Determination of causal connectivities of species in reaction networks. *PNAS*, 99(9):5816–5821, 2002.

[648] A S Torralba, K Yu, P Shen, P J Oefner, and J Ross. Experimental test of a method for determining causal connectivities of species in reactions. *PNAS*, 100(4):1494–1498, 2003.

[649] J Ross. From the determination of complex reaction mechanisms to systems biology. *Annual Review of Biochemistry*, 77:479–494, 2008.

[650] M Paluš, V Komarek, Z Hrncir, and K Sterbova. Synchronization as adjustment of information rates: detection from bivariate time series. *Physical Review E*, 63(4):046211, 2001.

[651] E T Jaynes. Information theory and statistical mechanics. *Physical Review*, 106(4):620–630, 1957.

[652] E T Jaynes. Information theory and statistical mechanics ii. *Physical Review*, 108(2):171–190, 1957.

[653] H Qian. Personal communication, 2006.

[654] H Kleinert. *Path integrals in quantum mechanics, statistics, polymer physics, and financial markets*. World Scientific, 2004.

[655] A Balaž, I Vidanović, and A Bogojević. Accelerated path integral calculations for many-body systems. *Journal of Physics Conference Series*, 128(1):012048, 2008.

[656] R M Fano. *Transmission of Information: A Statistical Theory of Communication*, pages 57–59. MIT Press, Cambridge, MA, 1961.